Master of Science Thesis

Preliminary multi-mission UAS design

H.C.M. Veerman B.Sc.

August 23, 2012

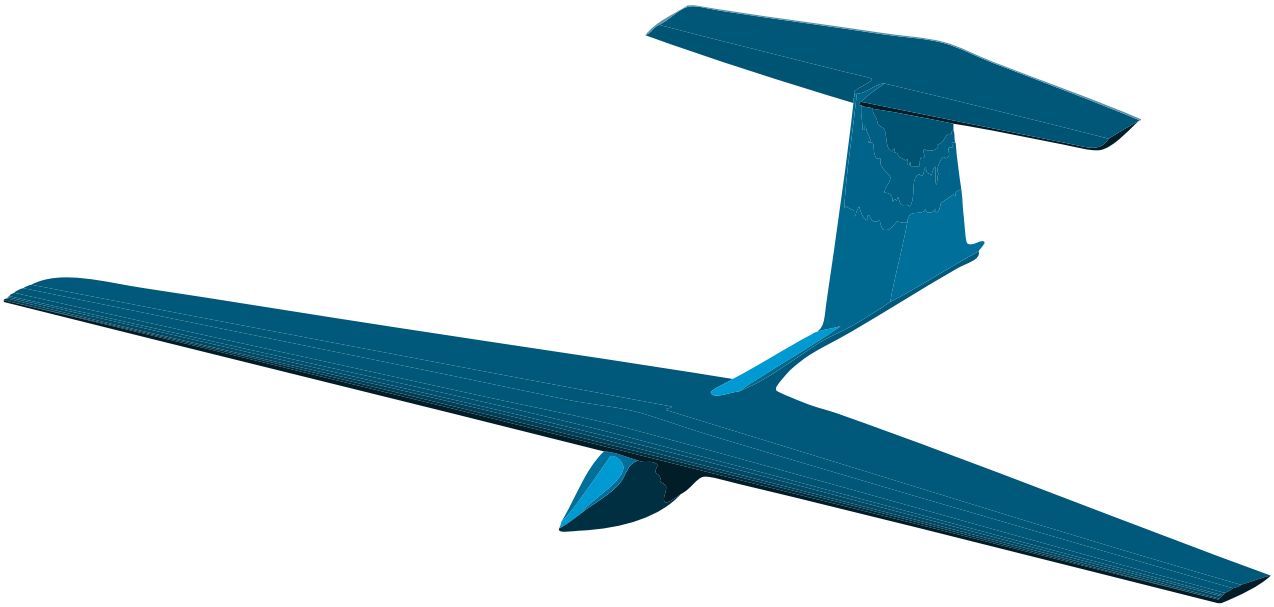

Faculty of Aerospace Engineering · Delft University of Technology

TU Delft

Preliminary multi-mission UAS design

Master of Science Thesis

For obtaining the degree of Master of Science in Aerospace Engineering at Delft University of Technology

H.C.M. Veerman B.Sc.

August 23, 2012

Faculty of Aerospace Engineering · Delft University of Technology

Delft University of Technology

Delft University Of Technology
Department Of Flight Performance & Propulsion
Design, Integration and Operations of Aircraft and Rotorcraft

The undersigned hereby certify that they have read and recommend to the Faculty of Aerospace Engineering for acceptance a thesis entitled **"Preliminary multi-mission UAS design"** by **H.C.M. Veerman B.Sc.** in partial fulfillment of the requirements for the degree of **Master of Science**.

Dated: August 23, 2012

Graduation professor and Supervisor: _____
Prof.dr.ir. John Stoop

Supervisor: _____
Drs. Gerald Poppinga

Reader: _____
Dr.ir. Dries Visser

Reader: _____
Prof.dr.ir. Serge Hoogendoorn

Summary

The goal of this thesis was to create a preliminary design of a multi-mission UAS by using off-the-shelf systems. This UAS must be able to perform both low and high speed missions. These missions are based on the requirements defined by the faculty of Civil Engineering at Technical University Delft, the Dutch National Aerospace Laboratory (NLR) and the Dutch National Police (KLPD). The mission objectives include providing support during fire and rescue operations, collecting aerial footage and conducting traffic monitoring, surveillance and reconnaissance.

To reach the stated goal several sub-goals were defined. A clear overview of all requirements had to be created first. The requirements were obtained by interviewing the above stated parties. This was followed by extensive market research in order to get an overview of the performance of current UAS designs. This market research was captured in a database containing over 400 entries. Based on the requirements in combination with the obtained database, all UAS classes and configurational options have been evaluated. The evaluation revealed that a new fixed wing electrical powered mini UAS design may be able to comply with the all UAS requirements.

The preliminary UAS design was initiated by estimating all Maximum Take-Off Weight (MTOW) components. The MTOW of an UAS consists of the empty weight, payload weight and fuel weight. The empty weight includes the structural weight, propulsion system weight and fixed equipment weight. The structural weight is defined by the weight of the fuselage, wing an tail. The fixed equipment weight is build up from the avionic instrumentation weight, communication system weight and the flight control system weight. In order to estimate these weight components, existing Weight Estimation Relationships (WERs) are often used in preliminary aircraft design. For this UAS design, however, the existing WERs could not be used. At present, there are no WERs available for mini UAS design. Therefore, new WERs have been derived for preliminary mini UAS design. These WERs were based on the available data in the database that was created. From this it was concluded concluded that most UASs are equipped with an electrical or piston powered propulsion system. The effect of the two different propulsion systems was investigated. This analysis was based on relations from Roskam[1], Kundu[2],

Raymer[3] and Ruijgrok[4] in combinations with the derived WERs. It was concluded that an electric propulsion system results in a UAS design that has a lower MTOW, higher power to weight ratio, power to price ratio and payload to Maximum Take Off Weight (MTOW) ratio. Therefore, the remainder of the design was based on the obtained results for a UAS with an electric propulsion system.

After obtaining all weight parameters, the constraints of the preliminary UAS design were tested. Evaluation of the stall, loiter, cruise and cruise back speed was conducted. Also the climb rate and gradient were evaluated. This resulted in a new design point. Based on this new design point, the wing design was initiated. After evaluating the different wing design options, a high wing configuration was selected. Subsequently, a quasi-3D optimizer was used to optimize the wing shape of the UAS. This optimizer combines a vortex lattice method (AVL) with viscous airfoil data (XFOIL). In order to initiate the wing optimizer, an airfoil had to be selected. Over 1500 airfoils were analyzed by using XFOIL. After analyzing the airfoils, three optimal airfoils were chosen. This choice was based on the highest performance at loiter speed and the capability to produce the required amount of lift during the other flight conditions. Subsequently, the wing was optimized for all three airfoils. Based on the performance and geometry of the three optimized wings, the wing with the naca23012 airfoils was chosen for this UAS wing design. This was followed by revising the obtained weight parameters.

The next step in the preliminary design was to create a tail design. After evaluating the different tail design options, a conventional single boom tail was chosen with a high horizontal tail. Both horizontal and vertical tail designs were created by using volume coefficients. Based on the obtained wing parameters and reference UASs parameters in combinations with these volume coefficients, the tail design was defined. During the tail design, the effects of two typical symmetrical airfoil types were compared. Based on the performance of both airfoils, the naca0010 airfoil was selected for this tail design.

After creating the wing and tail design, the effect of the wing on the tail was investigated. The focus was in particular on the wake of the wing at stall conditions. XFLR5 was used for investigating this effect. XFLR5 is an analysis tool for planes operating at low Reynolds numbers. From this analysis was concluded that the horizontal tail is not in the wake of the wing at stall conditions. This allows the horizontal tail to maneuver the UAS back into normal flight conditions while the wing is in stall conditions.

Subsequently, the stability of the UAS was addressed. AVL was used in order to compute the primary static and dynamic stability derivatives of the UAS. From the obtained stability derivatives was concluded that the UAS is both statically and dynamically stable. In longitudinal direction the UAS may be even too stable. When, after detailed analysis, is concluded that this is the case, the horizontal tail design needs to be revised.

Next, the UAS material options for the structure were evaluated. During this evaluation a new manufacturing technique, 3D printing, was tested. Based on the results was concluded that this manufacturing method is not yet suitable for creating UAS designs. Therefore, it is recommended to create the UAS structure

out of EPP in combination with carbon fiber reinforcements/carbon rods. If, in a later stage of the design, it appears that this structure is not strong enough, a composite structure can be considered. After constructing the UAS by using 3D software, the structural weight of the UAS was estimated. The evaluation revealed that the initial structural weight was slightly underestimated. A structural weight of 500 [g] was anticipated while in reality the structural weight is approximately 524 [g].

After obtaining the structural weight of the UAS, the propulsion system of the UAS was designed. The UAV Propulsion Development Kit (UPDK) was used to estimate the performance of a propeller and electrical engine combination. The initial UPDK simulated the flow through the propeller by using blade element momentum theory. The electrical engine was modeled by using analytical equations for electrical engines. The results were used in analyzing the engine-propeller combination for a certain flight range and airframe input. During this thesis, the UPDK was extended in collaboration with the developer of the program. 1700 Additional engines with more than 7000 test data records were implemented in the program together with 40 additional propellers. Besides that, the engine and propeller modeling module were revised and a batch mode in combination with a multi-core functionality was implemented.

After preselection of the engines and propellers, the UPDK was used to analyze the remaining combinations. Based on the evaluation of the top five combinations, the Scorpion HK3026-1600KV electrical engine in combination with the Graupner CAM 10x6 propeller were chosen for this preliminary UAS design. From this selection was concluded that the required power for the UAS was underestimated in the preliminary UAS design. This was caused by overestimating the efficiency of the engine and propeller. A loiter power of 8 [W] was determined while the actual amount of loiter power is 14 [W]. Instead of an actual required cruise power of 326 [W], a cruise power of 201 [W] was calculated in the preliminary design.

Next, the Thunder Power 11.1V 2100mAh 25C battery Lithium Polymer battery was selected based on the total amount of required energy capacity. The required energy capacity was calculated for two mission profiles. The first mission profile describes the climb of the UAS to the operating altitude and a 30 [min] loiter mission. The second mission profile consists out of a climb period, cruise period of 2 [min], cruise back period at optimum speed and loiter period for the remainder of the 30 [min]. Based on the most energy intensive mission profile, mission profile two, the battery capacity was selected. The weight of this battery was also underestimated because of overestimating the efficiency of the engine and propeller. A battery weight of 121 [g] was anticipated while in reality the battery weight was determined to be 147 [g].

Subsequently, the UAS subsystems were selected. These subsystems included the autopilot, control station, camera(s), datalink and videolink. Based on the specifications of the hardware and software, the Lisa/L autopilot was chosen. A Motion computing J3500 tablet was selected for running the autopilot software. Selecting an off the shelf camera that respects all requirements proved to be difficult. The GoPro Hero 2 was selected as an observation camera. The composite video out

connection of the camera is used for streaming purposes. An additional Caspa FS camera was selected to catch the infrared part of the light spectrum. This camera can easily be connected to the autopilot which allows onboard processing of the images. For the datalink, a long range low data rate Xbee-PRO 868 module was selected while for the videolink a short range high data rate Xbee 868LP module was selected. When the range and/or data rate of videolink is not sufficient an additional TurboWifi v2 directional antenna can be used to improve the link. From these results, the payload weight was derived. In this case the weight was overestimated. A payload weight of 500 [g] was assumed while the WERs estimated a payload weight of 270 [g]. In reality the payload weight was determined to be 113 [g].

After all subsystems were selected, the UAS design characteristics were evaluated. From this it was concluded concluded that the fuel and structural weight were underestimation while the payload weight was overestimated. The large wing span, in comparison with the reference UASs, resulted in a higher structural weight causing it to differ from the result of the WER. The payload weight was intentionally overestimated in order to have some freedom in the payload selection. The WER however, did not accurately estimate the actual payload weight for the UAS. It was concluded that the reference UASs are equipped with heavier or additional payloads. Fortunately, part of this overestimated payload weight could be used to compensate the underestimated weights. After this compensation there was still a relatively large rest weight. This rest weight can be used for an increase in battery capacity or for additional payloads.

Next, the UAS design was evaluated based on the requirements. From this evaluating was concluded that the UAS complies with most requirements. Despite the fact that the UAS is able to achieve a maximum speed of 145 [km/h], it is not able to fly with a head wind of 4 [Bft]. Note that the engine has enough access power to achieve a higher maximum speed. The UPDK revealed that flying at a higher speed is limited by the performance of the propeller. Note that structural analysis was not performed during this thesis. Therefore nothing can be stated about the structural resistance against wind forces. Furthermore, the videolink may not be capable of streaming images at the edge of the UAS range. In order to increase the range of the videolink, a directional antenna can be used on the ground. The resistance of the UAS against precipitation, the ability to operate within 10 [min] and in conditions with dust and smoke could not be tested. However, an additional infrared camera was selected in order to allow navigation in poor visibility. Also was concluded that the observation camera limits the maximum observation altitude to 480 [m]. This is caused by its “low” resolution. Note that the maximum field of view of this camera is 170°. Due to that, and the fact that the camera has a single image sensor, the GoPro camera exhibits some fisheye distortion around the edges of the frame. Besides that, the GoPro camera does not have the required global shutter, which can result in motion artifacts. The camera also does not have the ability to zoom. However, by changing the field of view in 1080p mode, one can shorten the focal distance, effectively zooming in the camera. One final remark can be made about the ground station requirements. The J3500 tablet has an internal protection resistance of only 52 instead of 54. This means that the ground station

is less resistance against water and dust.

Overall can be concluded that it is possible to create a preliminary mini UAS design based on the derived WERs. Together with off-the-shelf systems it was possible to create a design that is able to comply with most requirements. In future research should be kept in mind that predicting the efficiency of the propulsion system greatly affects the resulting weight estimation outcomes. Also finding a suitable camera proved to be difficult. Not one of the considered off-the-shelf cameras were able to comply with all requirements.

Acknowledgements

This graduation project would not have been possible without the help of some people, so I would like to take this opportunity to thank them.

I express sincere appreciation to my supervisor at the TU Delft faculty of Aerospace Engineering: John Stoop and to my supervisor at the NLR: Gerald Poppinga for their guidance and insight throughout my graduation project. To my family and girlfriend, I offer sincere thanks for their continuous support and patience during this period.

Jeroen Veerman, Delft, August 23, 2012

Contents

List of Figures

List of Tables

Nomenclature

Latin Symbols

A	Aspect ratio	$[-]$
$A_{frontal}$	Frontal area	$[m^2]$
A_{H-tail}	Aspect ratio horizontal tail	$[-]$
A_{max}	Maximum cross-sectional area	$[m^2]$
$A_{propeller\,disk}$	Propeller disk area	$[m^2]$
b	Wing span	$[m]$
b_{H-tail}	Horizontal tail span	$[m]$
b_{V-tail}	Vertical tail span	$[m]$
C	Capacitance	$[F]$
c	Wing chord	$[m]$
c_{flap}	Flap chord	$[m]$
$C_{battery}$	Battery capacity	$[Wh]$
C_{D_i}	Induced drag coefficient	$[-]$
$C_{d_{naca0010}}$	Drag coefficient naca0010 at loiter	$[-]$
$C_{d_{naca0012}}$	Drag coefficient naca0012 at loiter	$[-]$
C_{D_0}	Zero-lift/Parasite drag coefficient	$[-]$
C_{D_w}	Wave drag coefficient	$[-]$
C_f	Skin friction coefficient	$[-]$
c_{HT}	Horizontal tail volume coefficient	$[-]$
C_L	Wing lift coefficient	$[-]$
$C_{l_{design}}$	Design lift coefficient	$[-]$
$C_{L_{max\,clean}}$	Maximum clean lift coefficient	$[-]$

$C_{L_{max\,landing}}$	Maximum landing lift coefficient	$[-]$
$C_{L_{tail}}$	Tail lift coefficient	$[-]$
$C_{L_{wing}}$	Wing lift coefficient	$[-]$
C_{m_0}	Airfoil zero lift moment coefficient	$[-]$
c_{mean}	Wing mean aerodynamic chord length	$[m]$
$c_{mean_{H-tail}}$	Horizontal tail mean aerodynamic chord length	$[m]$
$c_{mean_{V-tail}}$	Vertical tail mean aerodynamic chord length	$[m]$
$C_{m_{naca0010}}$	Moment coefficient naca0010 at loiter	$[-]$
$C_{m_{naca0012}}$	Moment coefficient naca0012 at loiter	$[-]$
$C_{m_{wing}}$	Wing pitching moment coefficient	$[-]$
c_p	Specific fuel consumption of a propeller engine	$[kg/J]$
$C_{p_{electrical\,engine}}$	Specific fuel consumption electrical engine	$[kg/s]$
C_{req}	Required capacity	$[Wh]$
$C_{req\,cruise}$	Required cruise capacity	$[Wh]$
$C_{req\,cruise\,back}$	Required cruise back capacity	$[Wh]$
$C_{req\,loit}$	Required loiter capacity	$[Wh]$
$c_{root_{H-tail}}$	Horizontal tail root chord length	$[m]$
$c_{root_{V-tail}}$	Vertical tail root chord length	$[m]$
$c_{tip_{H-tail}}$	Horizontal tail tip chord length	$[m]$
$c_{tip_{V-tail}}$	Vertical tail tip chord length	$[m]$
c_{VT}	Vertical tail volume coefficient	$[-]$
D	Drag	$[N]$
d_{to}	Take-off distance	$[m]$
$\Delta C_{D_{0_{flap}}}$	Miscellaneous drag coefficient due to flaps	$[-]$
ΔC_{D_i}	Induced drag coefficient increment	$[-]$
$\Delta C_{D_{0_{lg\,and\,aft\,fus}}}$	Miscellaneous drag coefficient due to landing gear	$[-]$
$\Delta C_{D_{0_{unfeathered\,props}}}$	Miscellaneous drag coefficient due to unfeathered props	$[-]$
$\Delta C_{L_{flap}}$	Diff. max clean lift coefficient and max take-off lift coefficient	$[-]$
D_{min}	Minimum drag	$[N]$
D_p	Propeller diameter	$[m]$
D/q	Drag reference area	$[m^2]$
D_v	Vehicle diameter	$[m]$
E	Endurance	$[h]$
e	Oswald span efficiency factor	$[-]$
E_{cruise}	Maximum endurance at cruise speed	$[min]$
E_{loiter}	Maximum endurance at loiter speed	$[min]$
$E_{max\,speed}$	Maximum endurance at maximum speed	$[min]$
$e_{straight\,wing}$	Oswald span efficiency factor straight wing	$[-]$

$e_{swept\,wing}$	Oswald span efficiency factor swept wing	$[-]$
f	Equivalent parasite drag area	$[m^2]$
FF	Component form factor	$[-]$
FF_{engine}	Form factor engine	$[-]$
$FF_{fuselage}$	Form factor fuselage	$[-]$
F_{flap}	Flap coefficient	$[-]$
$FF_{wing\,and\,tail}$	Form factor wing and tail	$[-]$
f_{ratio}	Fineness ratio	$[-]$
f_{sqft}	Equivalent parasite area	$[ft^2]$
H	Ceiling	$[m]$
h	Distance to the center of gravity	$[m]$
h_0	Distance to the aerodynamic center of the wing	$[m]$
h_g	Height above ground	$[m]$
i_0	No load current	$[A]$
I_{cruise}	Current at cruise	$[A]$
I_e	Electrical current	$[A]$
$I_{e_{motor}}$	Electrical current motor	$[A]$
$I_{e_{subsystems}}$	Electrical current subsystems	$[A]$
I_{loit}	Current at loiter	$[A]$
i_t	Tail incidence angle	$[deg]$
i_w	Wing incidence angle	$[deg]$
K	Drag due to lift factor	$[m^2]$
k_f	Flap induced drag factor	$[-]$
K_v	Engine back EMF constant	$[rad/s]$
L	Lift	$[N]$
l	Distance between the ac of the wing and the ac of the horizontal tail	$[m]$
l_c	Component length	$[m]$
$(L/D)_{cruise}$	Lift over drag ratio during cruise	$[-]$
$(L/D)_{cruise\,back}$	Lift over drag ratio during cruise back	$[-]$
$(L/D)_{loiter}$	Lift over drag ratio during loiter	$[-]$
l_{engine}	Length engine	$[m]$
L_{tail}	Tail lift	$[N]$
l_{tail}	Distance between the cg and the ac of the horizontal tail	$[m]$
l_v	Distance between the ac of the wing and the ac of the vertical tail	$[m]$
l_{v-tail}	Distance between the cg and the ac of the vertical tail	$[m]$
L_{wing}	Wing lift	$[N]$
MAC	Mean Aerodynamic Chord	$[m]$

M_{wing}	Pitching moment of the wing	$[Nm]$
N	Number of available data sets	$[-]$
n	Load factor	$[-]$
P	Engine power	$[W]$
P_a	Available power	$[W]$
P_{br}	Brake horse power	$[W]$
P_{cruise}	Cruise power	$[W]$
$P_{e_{motor}}$	Power electrical motor	$[W]$
P_{loit}	Loiter power	$[W]$
P_r	Required power	$[W]$
$P_{r_{min}}$	Minimum power	$[W]$
$P_{r_{motor}}$	Required power electrical motor	$[W]$
Q	Component interference factor	$[-]$
Q_{engine}	Component interference factor engine	$[-]$
$Q_{fuselage}$	Component interference factor fuselage	$[-]$
$Q_{tail_{clean\,vtail}}$	Component interference factor tail clean vtail	$[-]$
$Q_{tail_{conventional}}$	Component interference factor conventional	$[-]$
Q_{wing}	Component interference factor wing	$[-]$
R	Electrical resistance	$[\Omega]$
R	Range	$[km]$
RC	Rate of climb	$[m/s]$
RC_{max}	Maximum rate of climb	$[m/min]$
R_{cruise}	Required cruise range	$[m]$
$R_{cruise\,back}$	Maximum range at cruise back speed	$[km]$
R_e	Reynolds number	$[-]$
R_{engine}	Radius engine	$[m]$
E_{loit}	Required loiter range	$[m]$
R_m	Main rotor diameter	$[m]$
$R_{datalink}$	Maximum range based on datalink (theoretical)	$[km]$
$R_{max\,speed}$	Maximum range at maximum speed	$[km]$
$R_{videolink}$	Maximum range based on videolink (theoretical)	$[km]$
RPM_{cruise}	RPM at cruise	$[rev/min]$
RPM_{loit}	RPM at loiter	$[rev/min]$
RPM_{max}	Maximum propeller RPM at cruise speed	$[rev/min]$
R_t	Tail rotor diameter	$[m]$
S_{flap}	Flap area	$[m^2]$
$S_{fuselage_{side}}$	Area fuselage side	$[m^2]$
$S_{fuselage_{top}}$	Area fuselage top	$[m^2]$

S_{H-tail}	Horizontal tail area	$[m^2]$
s_{land}	Landing distance	$[m]$
S_r	Rotor disk area	$[m^2]$
S_{ref}	Wing reference area	$[m^2]$
S_{V-tail}	Vertical tail area	$[m^2]$
S_{wet}	Wetted area	$[m^2]$
$S_{wet_{engine}}$	Wetted area estimation engine	$[m^2]$
$S_{wet_{fuselage}}$	Wetted area estimation fuselage	$[m^2]$
$S_{wet_{sqft}}$	Wetted area	$[ft^2]$
$S_{wet_{wing\,and\,tail}}$	Wetted area estimation wing and tail	$[m^2]$
T_{cruise}	Required propeller thrust at cruise speed	$[N]$
u	Upsweep angle of the aft fuselage	$[rad]$
U_{cruise}	Voltage at cruise	$[V]$
$U_{e_{motor}}$	Voltage electrical engine	$[V]$
U_{loit}	Voltage at loiter	$[V]$
V_{cruise}	Cruise speed	$[km/h]$
$V_{cruise\,back}$	Cruise back speed	$[m/s]$
$V_{D_{min}}$	Velocity for minimum drag	$[m/s]$
V_{eff}	Effective velocity	$[m/s]$
V_∞	Free-stream velocity	$[m/s]$
V_{loit}	Loiter speed	$[km/h]$
V_{max}	Maximum speed	$[km/h]$
V_{min}	Minimum speed	$[m/s]$
$V_{P_{r_{min}}}$	Velocity for minimum power	$[m/s]$
V_{st}	Stall speed	$[km/h]$
$W_{battery}$	Battery weight	$[N]$
$W_{cruise\,back\,fuel}$	Required cruise back fuel	$[N]$
$W_{cruise\,fuel}$	Required cruise fuel	$[N]$
$W_{e_{electrical}}$	Empty weight electrical powered UAS	$[N]$
W_{empty}	Empty weight	$[N]$
$W_{empty\,excl}$	Empty weight (excluding subsystems)	$[N]$
W_{engine}	Engine weight	$[g]$
$W_{e_{piston}}$	Empty weight piston powered UAS	$[N]$
W_f	Weight ratio between landing weight and take-off weight	$[-]$
W_{feq}	Fixed equipment weight	$[N]$
W_{fuel}	Fuel weight	$[N]$
$W_{fuel\,electrical}$	Fuel weight electrical powered UAS	$[N]$
$W_{loiter\,fuel}$	Required loiter fuel	$[N]$

W/P	Power loading	$[N/W]$
$W_{payload}$	Payload weight	$[N]$
$(W/P)_{Climb\,gradient}$	Power loading for climb gradient requirement	$[N/W]$
$(W/P)_{Climb\,rate}$	Power loading for climb rate requirement	$[N/W]$
$W_{pl_{electrical}}$	Payload weight electrical powered UAS	$[N]$
$W_{pl_{piston}}$	Payload weight piston powered UAS	$[N]$
$W_{propulsion}$	Propulsion system weight	$[N]$
W/S	Wing loading	$[N/m^2]$
$(W/S)_{Cruise\,back}$	Wing loading at cruise back speed	$[N/m^2]$
$(W/S)_{Loit}$	Wing loading at loiter speed	$[N/m^2]$
$(W/S)_{Stall}$	Wing loading at stall speed	$[N/m^2]$
W_{TO}	Maximum take-off weight	$[N]$
$W_{TO_{initial}}$	Initial MTOW	$[N]$
$W_{TO_{lb}}$	Maximum take-off weight in pounds	$[lb]$

Greek Symbols

α_f	Fuselage angle of attack	$[deg]$
Λ_{H-tail}	Sweep angle horizontal tail	$[deg]$
λ_{H-tail}	Taper ratio horizontal tail	$[-]$
$\alpha_{naca0010}$	naca0010 required loiter angle of attack	$[deg]$
$\alpha_{naca0012}$	naca0012 required loiter angle of attack	$[deg]$
α_{twist}	Wing twist	$[deg]$
Λ_{V-tail}	Sweep angle vertical tail	$[deg]$
λ_{V-tail}	Taper ratio vertical tail	$[-]$
δ_{flap}	Flap angle	$[deg]$
ϵ	Downwash angle	$[deg]$
ϵ_{wing}	Wing tip twist	$[\%]$
$\eta_{p_{cruise}}$	Propeller efficiency at cruise speed	$[-]$
$\eta_{com_{cruise}}$	Combined efficiency at cruise speed	$[-]$
$\eta_{com_{loit}}$	Combined efficiency at loiter speed	$[-]$
$\eta_{e_{cruise}}$	Engine efficiency at cruise speed	$[-]$
$\eta_{e_{loit}}$	Engine efficiency at loiter speed	$[-]$
η_p	Propeller efficiency	$[-]$
η_{tot}	Total efficiency motor	$[-]$
$\eta_{p_{cruise}}$	Propeller efficiency at cruise speed	$[-]$
$\eta_{p_{loit}}$	Propeller efficiency at loiter speed	$[-]$
Λ_m	Sweep maximum thickness line	$[rad]$

$\Lambda_{\bar{c}/4}$	Sweep at quarter mean aerodynamic chord	$[deg]$
λ	Taper ratio	$[-]$
Λ_{LE}	Sweep angle leading edge	$[deg]$
ν	Kinematic viscosity	$[m^2/s]$
ρ	Air density	$[kg/m^3]$
$\rho_{cruise\ altitude}$	Air density at cruise altitude	$[kg/m^3]$
σ	Propeller solidity	$[-]$

Abbreviations

AESA	Active Electronically Scanned Array
AFA	Adaptive Frequency Agility
AVL	Athena Vortex Lattice
BACN	Battlefield Airborne Communications Node
BEM	Blade Element Momentum
BLDC	BrushLess Direct Current
BLOS	Beyond Line Of Sight
BSFC	Brake Specific Fuel Consumption
CAA	Civil Aviation Authority
CAS	Close Air Support
COM	Computer-On-Module
CS-VLA	Certification Specifications - Very Light Aircraft
CS-VLR	Certification Specifications - Very Light Rotorcraft
CSAR	Combat Search And Rescue
CS	Certification Specification
DSP	Digital Signal Processor
ECCM	Electronic Counter-CounterMeasures
ECM	Electronic CounterMeasures
EO	Electro-Optical
EPP	Expanded PolyPropyleen
EPS	Expanded PolyStyrene
ESC	Electrical Speed Controller
ESC	Electronic Speed Controller
ESM	Electronic Support Measures
FC	Fuel Consumption
GMTI	Ground Moving Target Indicator
GPS	Global Positioning System
GSM	Global System for Mobile communications

HALE	High Altitude Long Endurance
HSPA	High-Speed Packet Access
IAI	Israeli Aircraft Industry
IBS	Integrated Broadcast System
ICAO	International Civil Aviation Organization
IMU	Inertial Measurement Unit
IR	Infra-Red
ISR	Intelligence, Surveillance and Reconnaissance
LBT	Listen Before Talk
LOS	Line Of Sight
LVR	LuchtVerkeersRegelement
MAC	Mean Aerodynamic Chord
MALE	Medium Altitude Long Endurance
MAV	Micro Aerial Vehicle
MIPS	Millions of Instructions Per Second
MP-RTIP	Multi-Platform Radar Technology Insertion Program
MTOW	Maximum Take-Off Weight
MUAV	Mini Unmanned Aerial Vehicle
OEF	Operation Enduring Freedom
PGM	Precision Guided Munition
PHM	Prognostics and Health Management
RADAR	RAdio Detection And Ranging
SADL	Situation Airborne Data Link
SAM	Surface-to-Air Missile
SAR	Synthetic Aperture Radar
SATCOM	SATellite COMmunication
SFC	Specific Fuel Consumption
TDL	Tactical Data Link
TUAV	Tactical Unmanned Aerial Vehicle
UAS	Unmanned Aircraft System
UAV	Unmanned Aerial Vehicle
UCAV	Unmanned Combat Air Vehicles
UHF	Ultra High Frequency
UMTS	Universal Mobile Telecommunications System
UPDK	UAV Propulsion Development Kit
VFR	Visual Flight Rules
VHF	Very High Frequency
WASP	Wide Area Surveillance Projectile

WER	Weight Estimating Relationships
WFD	Work-Flow Diagram
WIFI	WIreless FIdelity
WIMAX	Worldwide Interoperability for Microwave Access

Introduction

Unmanned vehicles are important when it comes to performing a desired task in a dangerous or inaccessible environment. Unmanned robots have been successfully used for many years. More recently, a growing interest in Unmanned Aircraft Systems (UASs) has arisen. UASs consist of an Unmanned Aerial Vehicle (UAV) and a control station interconnected via a datalink. A UAV can be controlled by a pilot, autonomously or a combination of the two. UAVs that can be hand launched or have the capability to take-off vertically, which are highly maneuverable and stable, are an important contribution to the field of aerial robotics.

UASs offer major advantages over manned aircraft when used for reconnaissance, aerial surveillance, monitoring and inspection in dangerous and complex environments. The low risks combined with the high confidence in mission success fuels the continuous expansion of the use of UASs. Besides that, also technological, economic and political factors encourage the development and use of UASs. From a technological perspective it can be observed that the sensors, microprocessors and propulsion systems are smaller, lighter and more capable than ever before. This leads to endurance, efficiency and autonomy levels that exceed the capabilities of manned flight. Due to the successful deployment in many missions, more funding and a large number of production orders have been realized. Market studies predict that the worldwide UAS market will expand significantly in the next decade. According to "Homeland Security and Commercial Unmanned Aircraft Systems (UAS) Market Shares, Strategies and Forecast worldwide, 2011 to 2017", the UAS markets are forecasted to reach $2.3 billion dollars, worldwide by 2017[5].

The demand for UASs arises from the low manufacturing and operational costs. A large number of successful designs have been created by several universities, commercial companies and research agencies. Due to the wide variety of applications, several configurational concepts have been developed. As a result, most UAS designs are optimized for a dedicated task. In order to perform different tasks, users need to have access to multiple UASs. This means that manufacturers and users have to maintain production and support lines for multiple UASs. From this the question arises:

Is it possible to design a UAS that can be used for a variety of low and high speed missions?

The biggest advantages of a multi-mission design in comparison with dedicated designs are higher cost efficiency, less complexity and an increase operational time. This increases both mission effectiveness and cost effectiveness of such a system.

This aim of this thesis is to create a preliminary design of a multi-mission UAS capable of providing support during fire and rescue operations, collecting aerial footage and conducting traffic monitoring, surveillance and reconnaissance. These missions purposes are derived from the demand expressed by the faculty Civil Engineering at Technical University of Delft, the Dutch National Aerospace Laboratory (NLR) and the Dutch National Police (KLPD).

The faculty of Civil Engineering has an interest in using a UAS for traffic monitoring. The NLR and KLPD are searching for a UAS capable of providing support during calamities, surveillance and reconnaissance. Note that these missions expect the UAS to be capable of flying at both high and low speeds. This preliminary UAS design required an expansion of current weight estimation techniques and relationships. These techniques and relationships are developed for manned aircraft and are therefore not yet applicable to UASs.

The structure of this thesis report is as follows. An overview of the thesis context and outline is presented in Chapter 1. In Chapter 2, the background on UASs is given. This chapter includes the definition of a UAS, typical UAS components and the applications of UASs. Chapter 3 presents the customer expectations and design requirements for the UAS. After that, the preliminary UAS design is discussed in Chapter 4. Chapter 5 describes the UAS characteristics derived from the preliminary UAS design. Finally, conclusions and recommendations are presented in Chapter 6.

Chapter 1

Thesis context and outline

This chapter describes the thesis context and outline. First, the project was organized in order to create a structured and systematic design process. This was initiated by stating the objective in Section 1.1, followed by a description of the goals and delimitations of the project in Section 1.2. After that, the project approach is described in Section 1.3. At the end of this section, an overview of the tasks that needed to be performed is shown in a so called Work-Flow Diagram (WFD).

1.1 Objective

The main objective of this thesis is to create a preliminary design of a multi-mission UAS by using off-the-shelf components. This preliminary design must be capable of providing support during fire and rescue operations, collecting aerial footage and conducting traffic monitoring, surveillance and reconnaissance.

1.2 Goals and delimitations

The main goal of this thesis is to create a preliminary design of a multi-mission UAS by using off-the-shelf systems. This UAS must be able to execute both low speed missions and high speed missions. After conducting a coarse analysis the preliminary design procedures and current UAS designs, detailed sub-goals were set for the UAS design. These goals are listed below.

- Identify the UAS requirements.
- Perform a market research in order to get an overview of the performance of current UAS designs.
- Capture this market research in a database. In processing the data for the database, the UASs are not separated based on their applications.
- Based on the UAS database, derive weight estimation relationships for preliminary mini UAS design.
- Use the weight estimation relationships to conduct preliminary aerodynamic and performance analysis of the UAS design.

- After obtaining the design point, optimize the wing for loiter conditions.
- Create a preliminary tail design for the UAS.
- Address the wing-tail effects, stability and materials briefly.
- Analyze UAS propulsion systems. This analysis focussed on existing off-the-shelf propulsion systems. Find the optimum propulsion system for this preliminary UAS design.
- Find the required subsystems for this preliminary UAS design.
- Evaluate the weight estimation relationships and the preliminary UAS design.

1.3 Approach

This section roughly describes each phase of the graduation project. The design process that is used during this project is based on the aircraft design process of Roskam[1] and Raymer[3].

1.3.1 Discovery phase

Organizing the project was the first task. This started by creating an objective followed by a description of the goals and delimitations. Tasks to be done were put into a Work-Flow Diagram (WFD) indicating the order in which they should be performed. Simultaneously, a background study was performed in order to obtain pre-knowledge about UASs. During this background study knowledge was gained about UASs design. This was used to form the project approach. The results of this phase are all presented in the literature research report.

1.3.2 Creative phase

This phase is started with a functional analysis. During the functional analysis all parties involved were consulted in order to obtain the required UAS functions. From the UAS function description, the performance requirements were derived. Together with the airworthiness requirements this formed the overall UAS requirements. Next, a UAS database was created. Based on the UAS database, weight estimation relationships for preliminary mini UAS design were derived. These relationships were used for the UAS configurational analysis and the UAS weight estimation. After investigating the technical and operational feasibility, the compliance with respect to the requirements was checked. This resulted in a UAS configuration decision. Subsequently, the UAS database was used again to decide on the UAS propulsion system. Every step performed during this phase is shown in the base-line thesis report.

1.3.3 Technical phase

In this phase the selected UAS configuration was analyzed in more detail. Optimization of the wing was performed. This was followed by a tail design. Next, the

wing-tail effects were addressed. After that, the stability characteristics of the UAS were analyzed. This was followed by an evaluation of the material options for the structure. Subsequently, the propulsion system design was performed. At the end of this technical phase the additional subsystems were selected. All steps performed in this phase are presented in the mid-term thesis report.

1.3.4 Review phase

After the preliminary UAS design was completed, the effectiveness of the design was determined by evaluating the UAS design. The results from this review phase are described in the final thesis report. After the final report is checked and corrected, the final results are presented during the graduation presentation.

1.3.5 Work-Flow Diagram

All phases that have been discussed in this section contain tasks that needed to be performed during this project. The Work Flow Diagram shows these tasks in a chronological order. This diagram can be found in Figure A.1 of Appendix A.

This concludes the section on the thesis approach. In the next chapter the UASs background is presented.

Chapter 2

Background

Before discussing the design requirements, it is necessary to provide some background information about Unmanned Aircraft Systems (UASs). In Section 2.1 the definition of a UAS is stated first. Section 2.1 also includes a small historical overview of UASs. After that, in Section 2.2, an overview of the existing UASs in the market is presented. Typical UASs components are discussed in Section 2.3. The last section, Section 2.4, shows the most common UAS applications.

2.1 UAS definition and history

2.1.1 UAS definition

Unmanned Aircraft Systems (UASs) typically consist of an Unmanned aerial vehicle (UAV), a control station and a communication system.

A UAV can be defined as:

A powered, aerial vehicle that does not carry a human operator, uses aerodynamic forces to provide vehicle lift, can fly autonomously or be piloted remotely, can be expendable or recoverable, and can carry a lethal or non-lethal payload. Ballistic or semi ballistic vehicles, cruise missiles, and artillery projectiles are not considered unmanned aerial vehicles[6].

More detailed elaboration about the break-up of a UAS is presented in Section 2.3.

2.1.2 UAS history[7]

In 1884, Nikola Tesla introduced the concept of unmanned flight in his dissertation. He described an armed, pilotless aircraft designed to defend the United States. The first UAS was manufactured by Elmer Ambrose Sperry in 1916 (see Figure 2.1a). During a competition in Paris he demonstrated his gyrostabilized seaplane. Safety pilots were onboard in order to perform the takeoffs and landings. By November, 30 mile flights with accuracy errors of 2 miles were being achieved.

A few years later in September of 1924 the British successfully launched, flew and landed the "RAE 1921 Target". The UAS flew under remote control (radio controlled) and achieved a flight time of 40 minutes. In the 1930s target drones were introduced. They were used in the training of anti-aircraft crews. The Fairey Queen is such a target drone and can be seen in Figure 2.1b.

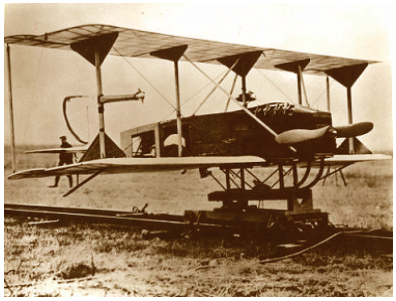

a: Gyrostabilized Curtiss N-9 seaplane[8]

b: Radio controlled Fairley Queen[8]

Figure 2.1: Gyrostabillized Curtiss N9 and Radio controlled Fairley Queen

In 1943 the first Precision Guided Munition (PGM) was successfully demonstrated. Despite over two decades of work developing the technology for unmanned flight in the US and Britain, it was Germany that deployed the first operational PGMs and cruise missiles. During the second world war the FX-1400, better known as the Frits X, was developed. In Figure 2.2a the Frits X is shown. The Frits X served as a guided anti-ship bomb.

During the 1950s, technological breakthroughs and innovations led to the development of reconnaissance UASs equipped with advanced navigational systems. The SD-1 Observer, alias MQM-57 Falconer, was the first tactical reconnaissance UAS developed by Northrop Gruman (see Figure 2.2b). The US army used this basis configuration to further develop UAS target drones into effective reconnaissance and surveillance aircraft.

a: Fritz X[9]

b: MQM-57 Falconer[10]

Figure 2.2: Fi 103 “V1” and MQM-57 Falconer

The world’s first free flight of an unmanned helicopter was realized by Gyrodyne Helicopters. Their QH-50 was capable of carrying a torpedo (Mark 43 homing torpedo). The QH-50 is presented in Figure 2.3a. The helicopter was remote controlled.

The US air force made an important step in UAS development by introducing the Lightning Bug in the 1960s. The design was based on the BQM-34 Firebee (see Figure 2.3b). The Firebee demonstrated to be successful as a photo/reconnaissance aircraft. The Firebee was slightly modified in order to improve endurance and to increase the flight altitude. The Lightning Bug was mainly used during the Vietnam war.

a: Gyrodyne QH-50[11]

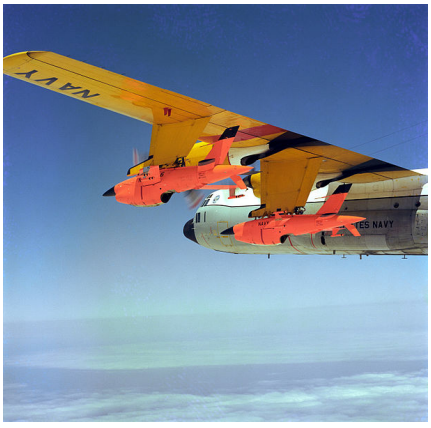

b: BQM-34 Firebee[12]

Figure 2.3: Gyrodyne QH-50 and BQM-34 Firebee installed on the wing

Despite many successful operations, the US government decided not to expend research and development into UASs after the Vietnam war. Therefore, UASs were not significantly used in US military operations until the 1990s. The Israeli government on the other hand, invested heavily in UAS research and design. This resulted in the Israeli Aircraft Industry's (IAI) Scout UAS (see Figure 2.4a). The UAS was developed from scratch and has adequate sensors and stable electrooptic systems that ensured proper operation. During the 1982 Lebanon War, the Israelis were confronted by Syrian Surface-to-Air Missiles (SAMs). The Scout was used for reconnaissance and therefore had a major contribution in destroying all SAM sites. After the success of the Scout, the US realized that UASs in warfare are indispensable. In August of 1990 the Gulf War started. UASs proved their crucial role once again. Their main task during the war was to perform reconnaissance missions.

In August of 1998 a UAS called the Laima completed a flight across the Atlantic Ocean. This was the first crossing of the Atlantic Ocean by a UAS. At the time, it was also the smallest aircraft ever to cross the Atlantic. The flight was performed without external control at an altitude of 5500 ft. The Laima manufactured by Aerosonde is shown in Figure 2.4b.

a: IAI Scout[13]

b: Aerosonde Laima[14]

Figure 2.4: IAI Scout and Aerosonde Laima

Since the Global Hawk's first flight in 1998, it has flown thousands of hours in support of combat operations worldwide (see Figure 2.5a). The Global Hawk made history in 2001 by completing the first unmanned powered flight across the Pacific Ocean. The Global Hawk also collected valuable reconnaissance on hundreds of targets in Afghanistan during Operation Enduring Freedom (OEF) and still continues to support current global operations.

In the same year, 2001, Aerosonde achieved a record flight with their solar powered Helios. This UAS, as presented in Figure 2.5b, reached an altitude of almost 100.000 feet. It was a world record for sustained horizontal flight by a winged aircraft. Unfortunately, the Helios broke up and fell in the Pacific in 2003 during a checkout flight in preparation for an endurance test. Exceeding the nominal flight speed caused the UAS to crash.

a: Global Hawk[15]

b: Helios[16]

Figure 2.5: Global Hawk and Helios

Currently, the main research and development for UASs aims at pushing the limits/boundaries of the flight envelope and also the vehicle's size. Most ongoing research in the field of UASs is conducted into Unmanned Combat Air Vehicles (UCAV) with high speed and high maneuverability or Micro Aerial Vehicles (MAVs) with insect-like size and performance.

2.2 Existing UASs

In the past decades various UAS configurations with different sizes, capabilities and endurance levels were developed. In this section an attempt is made to classify the different UASs.

2.2.1 Classification

As discussed in Subsection 2.1.1, UAS typically consist of a UAV, a ground station and a communication system. UAVs are generally divided in different classes[17]. In the following list, an overview of the different UAV classes is presented:

- *Nano UAVs* - Weight class less than 0.1 kg. The vehicle has an endurance of minutes and can generally not be flow beyond visual line of sight. The maximum flight altitude is below 100 ft. An example of a nano UAV is the DelFly Micro. The DelFly Micro is developed by TU Delft and is presented in Figure 2.6a.
- *Micro UAVs* - Weight class between 0.1 and 1.0 kg with a flight altitude typically below 500 ft. The range of such a UAV is up to 10 km while the endurance is generally up to one hour. The Wasp developed by AeroVironment is an example of a micro UAV and is shown in Figure 2.6b.
- *Mini UAVs (MUAVs)* - Weight class between 1.0 and 20 kg, flight altitude below 5000 ft with a range up to about 30 km. A UAV in this class has an endurance up to two hours. Figure 2.7a represents a Raven mini UAV and is also developed by AeroVironment.

- *Small UAVs* - Weight class between 20 and 150 kg, flight altitude below 20 000 ft with an operating range up to about 500 km. An endurance up to 10 hours can often be achieved. The Fulmar, which is developed by Aerovision, is a typical UAV in this class. It is presented in Figure 2.7b.
- *Tactical UAVs (TUAVs)* - Weight class between 150 and 1000 kg, flight altitude below 30 000 ft with a typical range up to 1000 km. A tactical UAV has an endurance up to 24 hours. An example of a tactical UAV is the Predator. The predator is developed by General Atomics and is presented in Figure 2.8a.
- *Medium Altitude Long Endurance (MALE) UAVs* - Weight class between 1000 and 6000 kg, flight altitude typically below 45 000 ft and an endurance up to 24 hr. Generally the range is up to 1500 km. A famous MALE UAV is the Reaper which is also developed by General Atomics. This UAV can be seen in Figure 2.8b.
- *High Altitude Long Endurance (HALE) UAVs* - Weight class above 6000 kg, flight altitude up to 65 000 ft and 24+ hr endurance. Such a UAV has an operating range of more than 1500 km. The Global Hawk is a typical HALE UAV. This UAV is developed by Northrop Grumman and is shown in Figure 2.9.

In Table 2.1 one can see a tabular overview of the above mentioned UAV classes and their specifications.

Table 2.1: Overview specifications UAV classes

Class:	MTOW [kg]:	Ceiling [ft]:	Range [km]:	Endurance [h]:
Nano	<0.1	<100	Visual LOS	<1
Micro	<1.0	<500	10	<2
Mini	<20	<5000	30	<10
Small	20 - 150	<20000	500	<24
Tactical	150 - 1000	<30000	1000	<24
MALE	1000 - 6000	<45000	1500	<24
HALE	>6000	<65000	>1500	>24

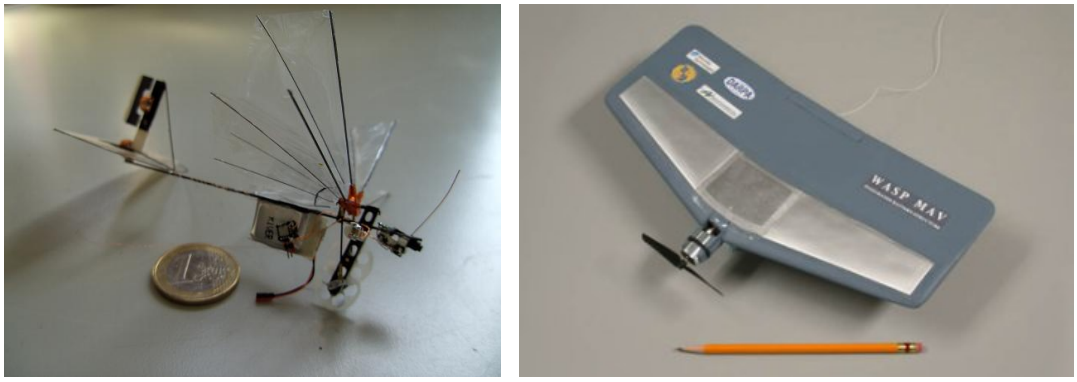

a: DelFly Micro[18] b: Wasp[19]

Figure 2.6: DelFly Micro and Wasp

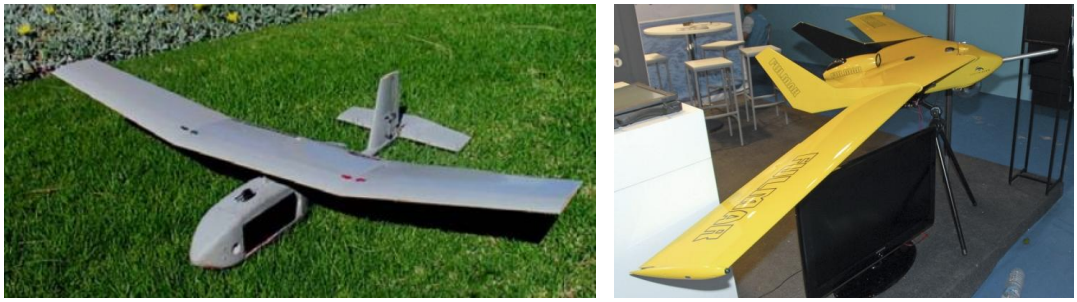

a: Raven[20] b: Fulmar[21]

Figure 2.7: Raven and Fulmar

a: Predator[22] b: Reaper[23]

Figure 2.8: Predator and Reaper

Figure 2.9: Global Hawk[15]

The upcoming subsection gives a brief overview of the UAS system characteristics that were used as an example for the UAV classes.

2.2.2 System characteristics example UASs

Nano: DelFly The DelFly Micro[18] only weighs 3 grams and has a wing span of only 10 cm. It is the smallest flying, camera carrying ornithopter in the world. The UAV has a range of 50 meters and is powered by a 30 mAh lithium polymer battery. This gives the UAV enough power for a three minute flight. The wings flaps 30 times per second. The DelFly Micro is controlled by a remote-control joystick. This UAV can contribute in advancing the understanding of the aerodynamics of an ornithopter. Simulations showed that there is still no clear understanding. The ultimate goal of the DelFly is to achieve flight without intervention of a pilot.

Micro: Wasp A slightly bigger UAV is the Wasp[19]. Developed by AeroVironment, the Wide Area Surveillance Projectile (WASP) MAV, weighs only 430 grams. Propulsion is delivered by a battery powered electric motor. The WASP is capable of flying for approximately 45 minutes and has a range of 5 km. It has successfully flown from sea level up to 5,000 feet, can withstand 40 degrees Celsius and is waterproof. The normal operations are between 50 and 500 ft. The maximum speed of the UAV is approximately 65 km/h. The payload of the WASP consists of fixed, forward, and side looking color daylight cameras with a real time video downlink. The latest development WASP, the Block III version, includes a swappable night vision camera. The WASP was designed for use over land and sea. The aircraft can be manually flown or programmed with GPS navigation to perform day or night missions. Its purpose includes reconnaissance and surveillance for Naval support and light infantry military operations on urban terrain. The WASP is relatively cost efficient at 5,000 dollars per unit[24]. WASP vehicles have been flown by the U.S. Navy and the platform is in full production.

Mini: Raven The Raven[20], developed by AeroVironment, is a 1.9 kg mini-UAV. The Raven can be hand launched and is propelled by an electric motor that is powered by rechargeable lithium ion batteries. The endurance of this UAV is approximately 80 minutes. Normal altitude of operations is between 100 and 500 feet but the maximum altitude of the UAV is 15.000 feet. The Raven has a range of 8-12 km and a maximum speed of 95 km/h. A single Raven costs about $ 25.000-35.000 and the total system costs about $ 250.000[25]. This system consists of three aircraft, a ground control station and a remote video terminal. The Raven provides "over the hill" intelligence at the tactical level. It carries a dual forward and side-looking pan/tilt/zoom Electro-Optical (EO) camera and an Infra-Red (IR) camera and is capable of broadcasting live video or providing images. The aircraft can be manually flown or programmed with GPS-based autonomous navigation to perform day or night reconnaissance and surveillance missions at low altitude. The Raven has been extensively used in Afghanistan and Iraq over the past few years. On average, a Raven can land approximately 200 times before it required maintenance[25].

Small: Fulmar Developed by Aerovision[21], this UAV can be catapult launched from a ship or ashore. The weight of the Fulmar is approximately 20 kg. One single-

cylinder two-stroke engine, driving a two-blade pusher propeller propels the UAV. The maximum operating altitude of the Fulmar is approximately 16.500 feet. The vehicle has a maximum range up to 400 km and the maximum speed of the platform is 150 km/h. An endurance of approximately 8 hours can be achieved. The Fulmar system is man-portable by two persons and can be setup in less than 30 minutes. The UAV can be equipped with a gyrostabilized two-axis gimbal mounting under the nose for an 360° pan-tilt daylight camera or a 14 megapixel digital camera with optional IR filter. A real-time 2.4 GHz video downlink is possible. The Fulmar is pre-programmed and flies fully automatic including take-off and landing. GPS waypoint navigation is used in order to guide the platform.

Tactical: Predator The Predator is an armed, multi-role, UAS[22]. A four-cylinder, four stroke engine provides the variable-pitch pusher propeller with 115 HP. Using this engine it is possible to propel the 1000 kg Predator to a maximum speed of 220 km/h. The operating altitude of this UAV is between 10.000 and 20.000 feet. The maximum operating altitude of the UAV is 25.000 feet, the range is up to 1100 km and a maximum operating endurance of 24 hours can be achieved. Typical payloads of the Predator are EO/IR camera's, laser target marker, laser illuminator and signal intelligence payloads. The UAV can employ two laser guided Hellfire missiles. The UAS can be deployed for worldwide operations. The Predator can be disassembled and loaded into a C-130 Hercules together with the ground station. The unit cost is approximately $20 million (2009 dollars)[26]. USAF pilots fly this UAV by one of three methods. These methods are: manual flying, semi-autonomous monitored flight and pre-programmed flight. With two data link options, Predators can be flown Line Of Sight (LOS) within approximately 250 km of the launch and recovery base. LOS refers to the radio horizon (the farthest possible point of propagation of radio waves). Besides LOS the platform can also be flown in Beyond Line Of Sight (BLOS) via satellite datalinks. The range can then be extended to approximately 1100 km. Predators are used primarily for performing the following missions and tasks: intelligence, surveillance, reconnaissance, Close Air Support (CAS), Combat Search And Rescue (CSAR) support and precision strikes.

MALE: Reaper The Reaper is an armed, MALE UAS[27]. A turboprop engine with 900 HP allows the 4760 kg UAV to reach a maximum speed of 480 km/h. It's maximum altitude is approximately 50.000 feet. Normal operations occur between 25.000 and 30.000 feet. An operational endurance of approximately 18 hours can be achieved with a maximum range of 1600 km. The Reaper carries an EO/IR camera payload, laser target marker, laser illuminator and Synthetic Aperture Radar (SAR). Seven external points allow a variety of weapon and payloads to be carried. A maximum of four laser guided Hellfire missiles can be employed by this UAV. This platform can also be disassembled and loaded into a C-130 Hercules. The unit costs of this system are around $53 million (2006 dollars)[28]. USAF pilots are able to fly these aircraft in the same matter as the Predator: manual flying, semi-autonomous monitored flight and pre-programmed flight. With two data link options, Reapers can be flown LOS within approximately 160 km of the launch and recovery base or flown BLOS via satellite datalinks. This increases the range to approximately 1600

km. The Reaper performs the following missions and tasks: Intelligence, Surveillance and Reconnaissance (ISR), CAS, CSAR support and precision strike. Reapers are used primarily for strike functions while possessing loiter time for ISR functions as well.

HALE: Global Hawk The Global Hawk is a HALE UAV[29]. This UAV has a turbofan engine that can deliver 7600 pounds of thrust. With a weight of approximately 14500 kg it is still able to reach a maximum speed of 800 km/h. It is able to fly at a maximum altitude of 65000 feet. A mission endurance up to 36 hours can be achieved with this UAV. A maximum range of 25000 km can be achieved. The Global Hawk can be equipped with a large range of payloads. EO, IR, and SAR sensors integrated on the UAV. A Battlefield Airborne Communications Node (BACN) can also be implemented on the Global Hawk. BACN provides a Tactical Data Link (TDL) gateway between the Situation Airborne Data Link (SADL) and the Integrated Broadcast System (IBS). BACN makes it possible for users to share information and form a common tactical picture. Furthermore, BACN provides an Internet Protocol based networking capability so military networks can share content across internet connections. BACN also allows soldiers on foot, or platforms without advanced communications systems to connect via cell phones, existing narrow band radios, or even an airborne 802.11 to the battle field network. The Global Hawk can also have the Multi-Platform Radar Technology Insertion Program (MP-RTIP) payload. Capabilities of this system includes Active Electronically Scanned Array (AESA) radar with high-resolution imagery, high-range-resolution imagery, and robust Ground Moving Target Indicator (GMTI) data. The unit cost of the system are between $55 and $81 million[30]. This includes a ground station. The ground stations consist of a launch and recovery element and the mission control element. The crew exists out of two pilots (one for launch and recovery and one for mission and control), one sensor operator, and additional support that include one quality control manager and one communications technician. The Global Hawk has a maximum range of 15.000 km and provides near continuous all weather wide area surveillance. As much as 100.000 square kilometer of terrain a day can be surveyed.

2.2.3 UAS categories

Besides the different UAS classes, the UASs can also be divided into UAS types. In this subsection the main categories are presented.

UASs are typically divided into the following categories:

- Fixed wing
- Rotary
- Convertible
- Flapping wing
- Blimps

Fixed wing Most UAS designs are from this category. The first UASs were fixed wing UASs and since then a lot of research is conducted into this category. Within the fixed wing UAS category there is also variation. A UAS can have a so called "high wing", as presented in Figure 2.7a. A "low wing" as shown in Figure 2.9 is used in most UAS designs. Research is currently conducted into the flying wing (blended wing) and joined wing (Prandtl Plane) concepts. An example of a flying wing can be seen in Figure 2.10a while a joined wing is presented in Figure 2.10b.

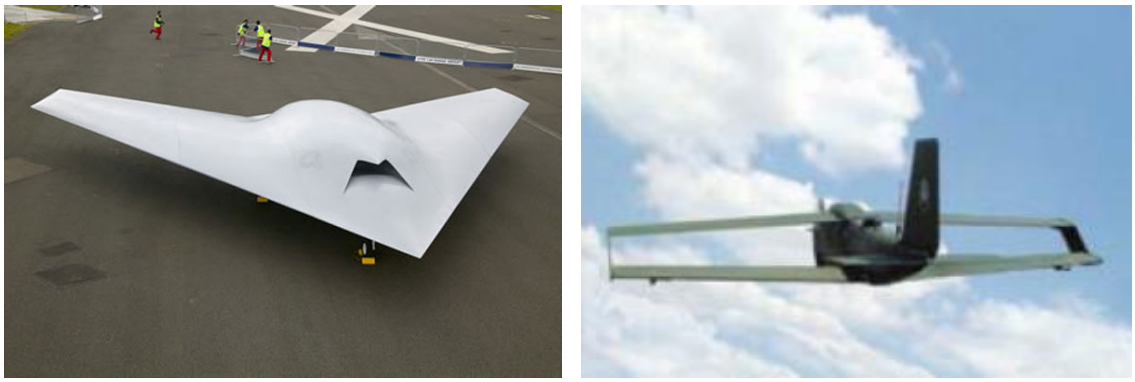

a: Boeing X-45[31] b: Buster[32]

Figure 2.10: Boeing X-45 and Buster

Rotary A large part of commercial UAVs require the vehicle to fly at relatively low speeds (up to 100 km/h). Besides that, often the ability to hover is requirement for the UAV (for incident control by police e.g.). In this case a helicopter configuration can offer the most efficient performance. Due to its high blade loading it is the most insensitive of all aircraft types to turbulence. A high maneuverability is also one of the advantages of this UAS kind.

Within the rotary aircraft category there are several configurational types. In the following list an overview of all rotary configurations is presented:

- Conventional rotary aircraft (see Figure 2.11b)
- Coaxial (see Figure 2.12a)
- Tandem (see Figure 2.12b)
- Multirotor (see Figure 2.13a and Figure 2.13b)

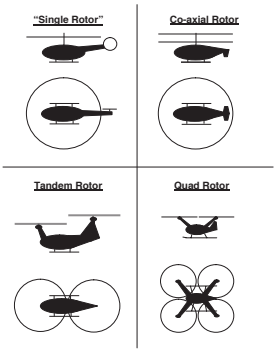

a: Overview rotary UAVs[17]

b: Camcopter S-100[33]

Figure 2.11: Overview rotary UAVs and Camcopter S-100

a: EADS Sharc[34]

b: Dragonfly DP-6[35]

Figure 2.12: EADS Sharc and Dragonfly DP-6

a: AscTec Pelican[36]

b: AscTec Falcon 8[37]

Figure 2.13: AscTec Pelican and AscTec Falcon 8

Convertible Convertible aircraft configurations provide a compromise between the requirement to take off and land vertically while flying its mission as a conventional fixed wing. This can be achieved by using a tilt-rotor, tilt-wing, tilt-wing-body or shrouded/ducted fan configuration (see Figure 2.14a). The rotors are used

to lift the vehicle in the air vertically. Next, the rotor/wing/vehicle is converted such that horizontal flight can be achieved. In Figure 2.14b such a convertible UAV is shown.

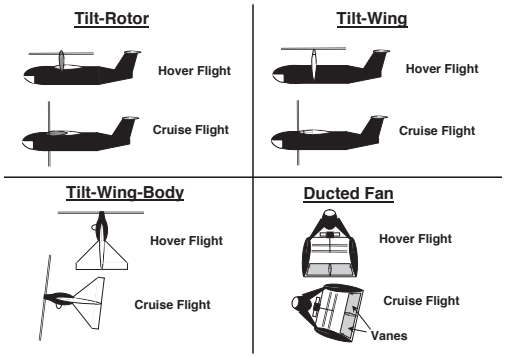

a: Convertible UAVs[17]

b: Panther[38]

Figure 2.14: Convertible UAVs and Panther

Flapping wing A UAV based on flapping wings has a high degree of aerodynamic efficiency. Propulsion and lift are achieved by the flapping motion of the wings. An example of such a UAV is shown in Figure 2.6a. A more complicated flapping wing UAV is the SmartBird and is presented in Figure 2.15. This UAV uses active torsion to further increase the aerodynamic efficiency.

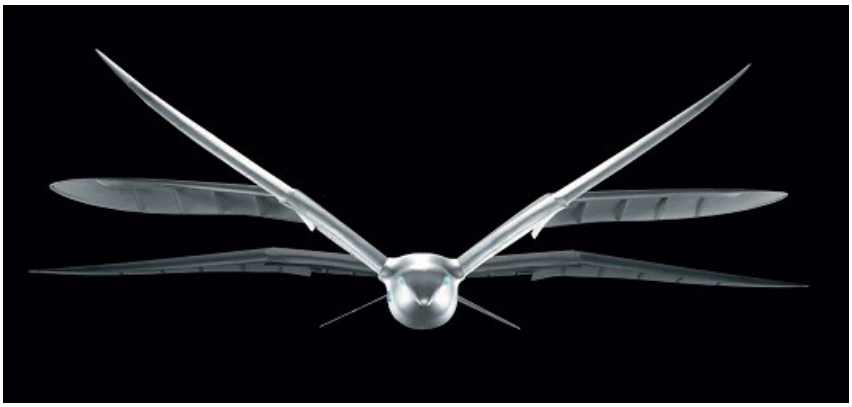

Figure 2.15: Festo SmartBird[39]

Blimps An airship or balloon (lighter than air vehicle) is a versatile and relatively low cost platform that can be used to carry payloads. This category of UASs generally has a long endurance and operates at low speeds. Therefore it is perfect for static measurements. The downside of blimps are their large size and their limited maneuverability. In Figure 2.16 an example of an airship is shown.

Figure 2.16: T-Blimp[40]

From this subsection can be concluded that there is a large variety in UAS categories. The next section describes the decomposition of a typical UAS.

2.3 UAS components

A modern autonomous UAS has a complex architecture. There is a lot of interaction between the different components. In Subsection 2.1.1, a brief overview of the UAS components was presented. In the next overview this overview is extended:

- Air vehicle
- Communications
- Launch and Recovery equipment
- Payloads
- Transportation
- Control station

Every component is addressed in a separate subsection.

2.3.1 Air vehicle

The airborne part of the system is also called the air vehicle. The type and performance of the air vehicle is determined by the needs of the mission. The main task of the vehicle is to carry the payload to its point of application. This also includes subsystems that are required to operate the vehicle. These subsystems include a flight control unit, the structure, propulsion unit, power systems and controls. Payload is also a part of the air vehicle but is treated separately. Significant determinants in the design of the air vehicle are the operational range, the airspeed and endurance demanded by the the requirements of the mission.

Flight control The flight control unit of an air vehicle provides flight control of the platform. The operator is connected to this unit through a communication device. Nowadays such a control unit can be equipped with an additional development board. Communication devices, sensors and other payloads can connected to this board. Such a development board is shown in Figure 2.17. This board is equipped with an Atom based microprocessor and provides much more computing power than a classical flight control unit. As a result this board allows onboard data processing of the attached units.

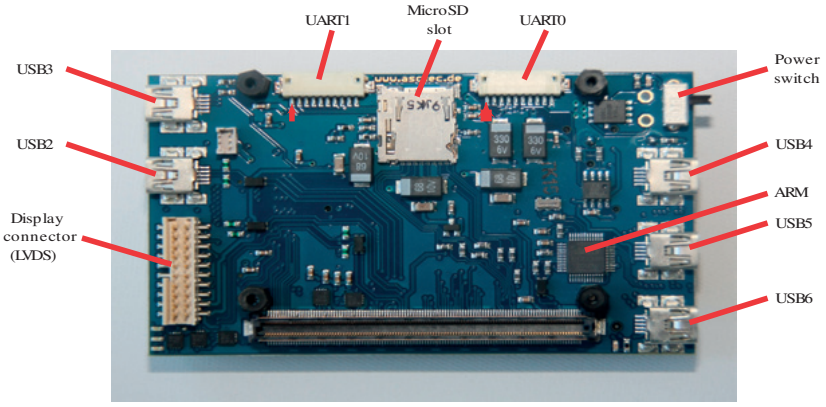

Figure 2.17: Ascending Technologies Atom Processor Board[41]

Structure The structure of a UAV can be constructed out of a variety of materials. Examples are: metal alloys like aluminum or steel, organics like bio-fibres or wood, polymers like nylon or polyvinyl and composites like metal matrix composite or fiber reinforced plastics. Nowadays, most small UAV structures are based on a composite materials structure. This technology enables the structure/airframe of the UAV to be lighter, more efficient and lower in cost.

Propulsion unit In order to propel UAVs there are several types of propulsion possible. Some small sized propulsion systems are listed below[42]:

- *Electrical engines (battery, solar or fuel cell powered)* - The efficiency and reliability of electrical engines has been improved significantly over the past few years. Therefore, this engine type has become an interesting energy resource for UASs. UASs from the nano class up to the small class with a maximum speed up to 150 km/h are generally equipped with this type of engine. The power required for the electrical engine can be provided by either batteries, solar cells or fuel cells. A typical brushless electrical engine is shown in Figure 2.18a. This engine has an efficiency of 88% and can provide approximately 0.6 HP. The weight of such an electrical engine is approximately 500 grams.
- *Internal combustion 2 stroke piston engine* - This kind of piston engines are used since the beginning of aviation. The reliability of these engines is very high and therefore they are still used in aviation today. Combustion engines are especially adapted for UAS applications. This engine type is generally used in mini and small UASs with a maximum speed up to 150 km/h. The

BGX-1 3500 RN engine produced by O.S. Engine is an example of such a 2 stroke engine and is presented in Figure 2.18b. This engine delivers 4.1 HP and weighs about 1.3 kg.

- *Wankel engines* - A wankel engine is an internal combustion engine using a rotary design instead of pistons. Such a design generates more power when compared to a piston engine of the same size. Besides that, it also has a better efficiency (lower Specific Fuel Consumption (SFC)) and power to weight ratio than a classical 2 or 4 stroke piston engine. A wankel engine is generally found in the UAS class small and tactical. These UASs have a maximum speed up to 250 km/h. In Figure 2.19a a wankel engine is presented. This engine weighs 335 grams and delivers 1.3 HP.
- *Internal combustion 4 stroke piston engine* - 4 stroke piston engines have also been used since the beginning of aviation. As with the 2 stroke piston engine this type has also a very high efficiency. A 4 stroke engine has a higher efficiency (SFC) than a 2 stroke engine. Besides that, a 4 stroke engine produces less noise and vibrations, which is preferable. Tactical UASs with a maximum speed up to 250 km/h are generally equipped with this engine type. Figure 2.19b represents such a small 4 stroke engine. It provides 4 HP and weighs approximately 1.8 kg.
- *Turboprop engines* - Turboprop engines for UAVs are often an adaption of existing engines from manned commercial and military aircraft. In Figure 2.20a however, a specially UAS designed turboprop is shown. It provides a power output of 7.5 HP and weighs approximately 400 grams. This engine uses a combustion chamber to generate a mass flow which drives a turbine that in turn drives the shaft to which the propeller is attached. MALE UASs with a maximum speed up to 500 km/h are generally equipped with this engine type.
- *Turbofan and Turbojet engines* - Turbofan and Turbojet engine designs for UAVs are also based on existing engines from manned commercial and military aircraft. Such a design is shown in Figure 2.20b. This figure shows a turbine that is often used in model aircraft. The turbojet can deliver 160 Newton of thrust and only weighs 410 grams. This engine produces thrust by generating a mass flow with a certain velocity in the combustion chamber of the engine. Generally, UASs of the type HALE that can achieve a maximum speed up to 800 km/h are equipped with this engine type. Assuming that the engine can deliver this 160 Newtons at 800 km/h results in approximately 45 HP that can be delivered by this engine. In reality the engine produces much less power at high speeds.

a: AXI 4130/20 electrical engine[43]

b: BGX-1 3500 RN 2 Stroke Engine[44]

Figure 2.18: AXI 4130/20 Goldline electrical engine and BGX-1 3500 RN O.S. 2 Stroke Engine

a: 49-PI Type II .30 Wankel Engine[45]

b: FT-300 O.X. 4 Stroke Engine[46]

Figure 2.19: 49-PI Type II .30 Wankel Engine and FT-300 O.X. 4 Stroke Engine

a: Wren 44 Turboprop[47]

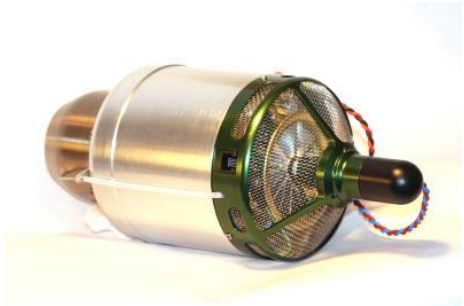

b: Wren 160 Pro Turbojet[48]

Figure 2.20: Wren 44 Turboprop and Wren 160 Pro Turbojet

In Table 2.2 all above mentioned specifications of propulsion types are presented in a clear overview.

Table 2.2: Overview specifications propulsion types

Propulsion type:	Used in UAS class:	Max. speed UAS [km/h]:	Power [HP]:	Weight [g]:
Electrical	Nano-Small	150	0.6 HP	500
2 stroke piston	Mini-Small	150	4.1 HP	1300
Wankel	Small-Tactical	250	1.3 HP	335
4 stroke piston	Tactical	250	4.0 HP	1800
Turboprop	MALE	500	7.5 HP	400
Turbofan/Turbojet	HALE	800	45 HP	410

2.3.2 Communications

The UAV is an unmanned aircraft, and as such it needs a remote operator in order to control it or at least to supervise its activities (in autonomous flight). One of the most demanding requirements for the communication system is the up and down link between the control station and the air vehicle. There are two main categories of communication:

Line Of Sight communication (antennae communication) - For small and medium sized UASs this way of communication is most common, even though its range is limited. Range limitation can vary from a few dozens of meters for micro/nano systems to several hundred kilometers for more sophisticated systems. Communication equipment together with a antennae is required at the control station. The UAV itself obviously requires an antennae as well. Examples of line of sight communication are Ultra High Frequency (UHF), Very High Frequency (VHF), WIreless FIdelity (WIFI) and Bluetooth.

Beyond Line Of Sight - Large MALE and HALE UASs generally use this type of communication. This communication type ranges up to worldwide coverage. Communication equipment together with an antennae is in this case also required onboard of the UAV and at the control station. Examples of beyond line of sight communication include Universal Mobile Telecommunications System (UMTS), High-Speed Packet Access (HSPA), Worldwide Interoperability for Microwave Access (WIMAX),Global System for Mobile Communications (GSM), SATellite COMmunication (SATCOM) and airborne ad hoc network (wireless network). In Figure 2.21 an overview of a UAS communication system as a whole is presented. Figure 2.22 shows the differences in speed versus mobility of the LOS and BLOS communications that were mentioned previously.

Besides the link between the control station and the UAV it is also possible to have communications with other sources. For example, when a UAV is performing a surveillance mission operated by the military, it can receive tasks from the military control station but it can also report specific information back to other users.

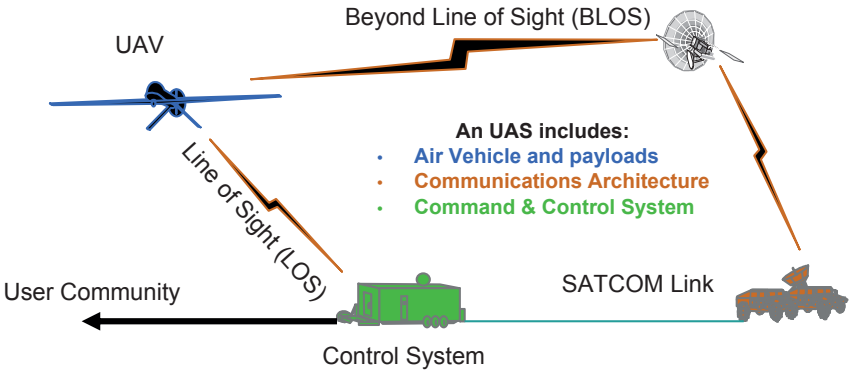

Figure 2.21: UAS Communication System

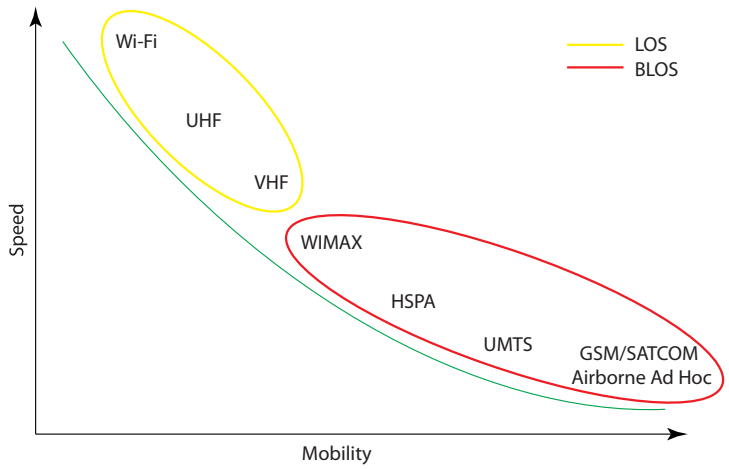

Figure 2.22: Communication mobility vs speed

2.3.3 Launch and Recovery equipment

There are various methods to launch and recover a UAV. In the next paragraphs the different methods are presented.

Launch Generally there are three methods of launching a UAV:

- Horizontal take-off by using a wheeled undercarriage. In this case a prepared surface needs to be available.
- Catapult, hand or rocket powered launched. This method can be used when the UAV has no vertical take-off capabilities or the operating circumstances do not allow it to take of horizontally (e.g. due to harsh terrain).
- Vertical take-off.

When a wheeled undercarriage is used to take-off, the runway length is an important parameter in designing the UAV. This will in a great extend determine the employability. In areas where no (long) take-off strip is available, the UAV might not be able to take-off. A UAV designed for a short take-off length is different from a UAV designed for a moderate take-off length.

When no airstrip is available and the UAS is required to be mobile, catapult or hand launching the vehicle is a possibility. The UAV is catapulted into the air with sufficient acceleration to achieve the required minimum flight speed. This method achieves the aim of mobility although it does require transportation of a catapult system in addition to the UAV and control station unit(s). Launching a vehicle can range from hand-launching, bungee-powered launching to pneumatic powered launching.

Taking off vertically allows a UAV to take off at almost any type of terrain. No runway or catapult system is required. This allows the system to have an even higher mobility factor than a catapult launched system or wheeled take-off system. The required power for such a vehicle on the other hand is much higher than a wheeled take-off or catapult launched vehicle. This results in a higher energy consumption. Therefore a vertical take-off vehicle is generally used for close range applications.

Recovery A UAV with a wheeled undercarriage obviously touches down onto its undercarriage at a runway or airstrip. Long range UAVs, such as the Global Hawk (see Figure 2.9), have the ability to take-off and land completely automated by using GPS. Smaller UAV types can be landed by making use of a forward looking camera. This allows the operator to see the runway during the landing phase of the mission.

Catapult launched UAVs generally do not have a wheeled undercarriage. Therefore other means of landing are required. In this case skid or belly landing can be used. The WASP, as presented in Figure 2.6b, is a UAV that lands by means of a belly landing. A catchment net can also be used to land the UAV. This method is not often used because the chance of missing the catchment net is too large resulting in the UAV striking the ground. Besides that, the rapid deceleration of the UAV can seriously damage the vehicle. Another means of landing is by using a parachute in combination with an energy absorbing system (airbag e.g.). A disadvantage of this method is the unpredictability of the point of touch down. In a worse case scenario the vehicle lands in a tree, in water or hits another obstacle resulting in serious damage.

Recovering a UAV that is able to take-off and land vertically is simple. Small UAVs can be landed manually by using a remote control. GPS assisted landing is also possible. The vehicle can be directed to a certain GPS position at a predetermined altitude. Subsequently, automated landing can be performed.

2.3.4 Sensors and payloads

Sensors are an essential part of a UAS design. Without them, the platform is not able to fly on its own. The sensor types and performances are derived from the operational requirements. Besides essential sensors, there are also sensors that can be seen as payloads. Payloads can also include cargo and armament. In the next few paragraphs the most common sensor and payload types are highlighted. Note that sensors will be considered as essential parts of the UAS and payloads not.

Sensors

Inertial Measurement Unit The Inertial Measurement Unit (IMU) is one of the most important parts of the flight control system of the UAV. It determines the position, velocity and altitude of the platform using accelerometers, magnetometers and gyroscopes. Accelerations measured with the accelerometer are used by the IMU to determine in which direction the platform is moving. When a certain maximum acceleration is set, the IMU makes sure that the platform will not accelerate faster than allowed. Besides that, also the velocity of the platform can be derived from the measured accelerations. In order to get a more accurate reading additional airspeed sensors can be used. The magnetometers are used to determine the position and attitude of the UAV. Gyroscopes are mechanical or optical devices that maintain orientation based on angular momentum while in motion. Gyroscopes are fairly accurate initially, but orientation tends to drift over time due to external forces exerted on the gyroscope. This results in an unreliable reading of position over time and is also called precession. It can be suppressed by using state of the art technology. For example, ring laser gyros can be used. In this type of gyros two laser beams counter rotate around the same gyroscopic axis. When forces act on the gyroscope the wavelength of the beam changes indicating a rotation[49]. The precision of the measured beam changes determines the accuracy of the gyroscopes and the level of precession. Although ring laser gyros significantly increased IMU accuracy over time, it still does not eliminate precession altogether. In order for UAVs to be used for long endurance and precise missions, a more consistent navigational system was needed. The answer came in the form of embedded GPS and IMU, developed for redundancy which proved extremely reliable while minimizing inaccuracies. Also a barometric pressure measurement device can be used in order to obtain a more accurate altitude reading.

Payloads

Global Positioning System Global reach of UAVs today is largely possible due to the navigational capabilities of GPS. GPS allows UAVs to be guided and controlled from anywhere at any time. Currently GPS receivers are accurate to within meters. This is crucial because precision and accuracy are important for executing operations. The application of GPS in UAS operations is critical to navigation and control. Prior to GPS, an IMU singly enabled airborne navigation. Nowadays, GPS assists the IMU in its measurements allowing the system to navigate more precisely.

RADAR RAdio Detection And Ranging (RADAR) analyzes the properties of reflected electromagnetic waves emitted by the onboard transmitter and is used to detect and track targets obstacles in its surrounding area. The radar system used for ground target surveillance is known as a Synthetic Aperture Radar (SAR). Metallic objects “light up” when hit with the radio frequency waves of the SAR, and show up bright in the images that are created by the SAR. SAR can be used at night and can “see” through dust, fog, rain and sandstorms, making it particularly useful for surveillance and reconnaissance. Besides that, it can also be used for search and rescue, fire line location and tracking through smoke, iceberg detection, ice pack analysis and the detection of debris or oils spills on the ocean. In order to achieve

higher-resolution images, the sensor can take multiple images of a target scene from different angles. An example of a SAR system can be seen in Figure 2.23a. Besides active RADAR it is also possible to use passive RADAR. Passive RADAR uses radio signals already present in the environment such as commercial broadcast and communications signals. This can be used to avoid detection by enemy forces.

Acoustic sensors Acoustic sensors can provide means of detecting and tracking the passage of objects. Therefore this type of sensors can also be used for navigation purposes. Obstacle avoidance is an example of such a navigation purpose. In combination with GPS and barometric sensors it can provide an accurate system that allows automated landing. Landing based on acoustic sensors only cannot be performed in every case. Grass, for example, is a difficult surface type for the acoustic sensors. The acoustic waves are diffused in the grass resulting in incorrect measurements. Therefore a combination of sensors must be used. In Figure 2.23b an ultrasonic range finder is shown. Such an acoustic sensor is relatively light (a few grams) and can provide sufficient navigation when combined with other sensors (stereo vision e.g.). For indoor navigation purposes this is very important since no GPS is available indoor.

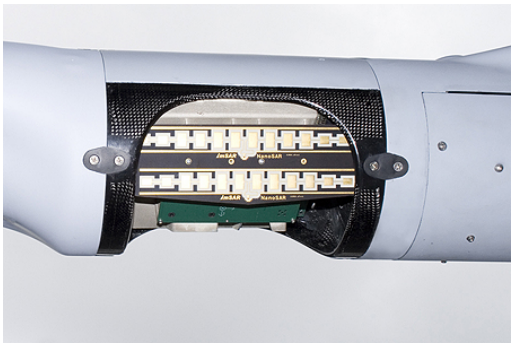

a: Nanosar SAR[50]

b: Ultrasonic Rangefinder[51]

Figure 2.23: Nanosar SAR and Ultrasonic Rangefinder

Electro Optic and InfraRed sensors One of the most commonly used sensors are electro optical sensors. They range from simple cameras to multi-spectral systems. Electromagnetic radiation emitted from an object can be collected with an EO sensor. A simple camera has the ability to create an image from received light with a wavelength range between $0.4 - 0.7\,\mu m$. During night situations there is not enough light for a normal camera to create images. In that case an IR sensor can be used (see Figure 2.24a). Such a sensor has the ability to determine the temperature of objects emitting $0.7 - 1000\,\mu m$ wavelengths. In Figure 2.24b such an infrared image is shown. Besides these sensors it is also possible to analyze the environment by using a 3D camera (stereo vision e.g.) or a laser scanner. Data on the shape and appearance of an environment can be collected by making use of such a sensor.

The resolution of an image depends upon the amount of pixels of the receptor. More pixels receiving light from a target improves the sharpness of the image. To be able to focus on a certain area of interest one can choose for a sensor that is able

to zoom-in. In order to ensure a sufficiently sharp image additional stabilization is often required. Detecting, recognizing and tracking objects requires in many cases even more additional systems. This can significantly increase the complexity and weight of the system as a whole.

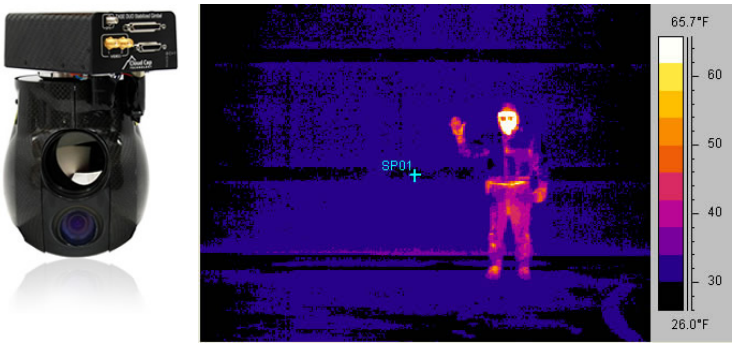

a: TASE 200 Gimbal EO sensor and IR sensor[52]

b: IR image[53]

Figure 2.24: TASE 200 Gimbal and Infrared Image

Experimental and Scientific payloads In order to perform scientific/experimental missions, a UAV can be equipped with a variety of different sensors. It can include dynamic and static pitot tubes measurement devices in order to perform various meteorological and agricultural measurements. Numerous other payload types can be thought of.

Sensors for weapons of mass destruction A UAV is able to fly in harsh conditions. Especially in dangerous environments this comes in hand. Equipping a UAV with sensors, in stead of a "normal" manned aircraft, that can measure the presence of chemical, biological and nuclear weapons of mass destruction would eliminate the risk of pilots getting harmed.

Electronic warfare Electronic warfare refers to action involving the use of electromagnetic spectrum to control the spectrum, attack an enemy or counteract enemy assaults via the spectrum. Generally there are three categories of electronic warfare. Electronic Support Measures (ESM), Electronic CounterMeasures (ECM) and Electronic Counter-CounterMeasures (ECCM). All are used for collecting electronic information and counter-measuring enemy's electronic systems that attempts to disrupt systems. Enemy emitters can be detected and identified in order to collect and record traffic.

ESM gathers intelligence through passive "listening" to electromagnetic radiations of interest. ECM are actions to reduce or prevent the enemy's use of the electromagnetic spectrum. It is designed to trick or deceive radar, sonar or other detection systems like IR or lasers. It is used to protect aircraft from guided missiles. ECCM

are actions to ensure friendly use of the electromagnetic spectrum against electronic warfare. The main objective of such a system is to eliminate or reduce the efficiency of the enemy's ECM. It is often called a means of resistance to jamming.

Psyops Psychological operations impact the behavior of the enemy. Like non-lethal weapons, the intent is not to kill a target. Potential objectives include convincing an enemy force to surrender or preventing ambushes of friendly forces. Psychological operations can eliminate the enemy's will to fight. Examples of payloads are: air-drop leaflets, megaphones or radio broadcasts.

Armament and cargo payloads This type of payload includes ammunition or explosives for an attack mission and containers with supplies for cargo missions. As presented in Paragraph 2.2.2, the Reaper can carry up to a maximum of four laser guided Hellfire missiles. The SnowGoose, as shown in Figure 2.25, is an example of a cargo UAV. This UAV is able to carry a payload of approximately 35 kg over a distance of 300 km.

Figure 2.25: MMIST CQ-10 SnowGoose[54]

2.3.5 Transportation

Transportation means for UASs are obviously dependent on the size and weight of the system. Nano and micro UASs can often be transported in one or two backpacks. Mini and small UASs are often fitted in a single trailer. In Figure 2.26a the transport boxes for the Raven mini UAS are shown. This UAV does not require a catapult ramp to take-off. Therefore this system is very transportable. The ScanEagle tactical UAS, on the other hand, does require a catapult ramp (see Figure 2.26b) which decreases it's transportability. Tactical, MALE and HALE UASs often require multiple vehicles and trailers or even airplanes for transportation.

a: Transport boxes Raven[55]

b: Catapult launcher Scaneagle[56]

Figure 2.26: Transport boxes Raven and Catapult launcher Scaneagle

2.3.6 Control station

The control station is the operational control center of the UAS. It's primary means is to control, track and operate the UAV. The control station is also used for displaying and processing video, command and other data from the UAV and its sensors. It may also include mission planning, video instruments, ground data and communication equipment. A control station may be based on the ground, aboard of a ship or aboard of a parent airplane. The sophistication and amount of crew members of a control station depends on the size of the UAV and the profile of the mission(s). Small UASs such as a Raven for example (see Figure 2.7a), can be operated by using a small ground station with only one crew member. A laptop can serve as a ground station while a small data link antenna can provide communication. Large UASs, like the Global Hawk (see Figure 2.9), require a crew of minimal six in order to operate one UAV. In Figure 2.27 part of a Global Hawk ground station is shown.

Figure 2.27: Global Hawk ground station[57]

This concludes the overview of UAS components. In the next section the different UAS applications are presented.

2.4 UAS applications

One can imagine that the market for UASs is still in devolopment. In order to get an idea about the different applications of UASs, the applications are arranged into four segments. These segments are: the military, research institutes (universities e.g.), the government and commercial & civil. In the upcoming subsections an overview of the different applications of UASs for each segment is presented.

2.4.1 Military

This subsection addresses the military applications of UAS's. In the following table a small overview of some applications is shown:

Table 2.3: Overview military applications

Applications:
Air combat
Intelligence, Reconnaissance and Surveillance
Aerial targets
Elimination of unexploded bombs
Airfield base security
Research & rescue
Air strikes
Psyops
Signal intelligence
Electronic warfare
Cargo delivery

2.4.2 Research institutes

Besides military applications, also scientific applications can be thought of. The next table presents a small overview of these scientific applications:

Table 2.4: Overview scientific applications

Applications:
Traffic monitoring
Atmospheric monitoring (near space e.g.)
Hurricane research
Volcano research
Remote sensing
Extraterrestrial exploration
Atmospheric research

2.4.3 Government

UASs are also used by governments. Table 2.5 gives a small overview of the government applications for UASs.

Table 2.5: Overview government applications

Applications:
Traffic monitoring
Infrastructure monitoring
Aerial imaging
Terrain mapping
Agriculture and forestry
Surveillance
Law enforcement
Crisis management
Search and Rescue
Fire fighting support
Tsunami watch
Port security
Meteorology
Border patrol

2.4.4 Commercial & civil

Nowadays there is a growing commercial market for UASs. Table 2.6 gives a small overview of some commercial applications for UASs.

Table 2.6: Overview commercial applications

Applications:
Aerial photography
Crop monitoring
Crop spraying
Fishing support
Inspections (pipeline inspections e.g.)
Mining exploration
Fishery application
Agricultural applications
Security applications
Telecommunications
News and Media broadcasting
Cargo

As one can see there are endless possibilities for UASs today. The military has the most dominant role in UAS design today. UASs components become smaller, lighter and more accurate every day. When operating a UAS becomes less difficult, the market is likely to expand drastically.

This concludes the chapter on UAS definition, existing UAS types, UAS components and the applications of UASs. In the next chapter, the UAS requirements are discussed.

Chapter 3

Requirements

In this chapter the customer expectations and requirements of the UAS design are presented. First, the customer expectations and mission description are shown in Section 3.1. The expectations together with the mission description gives a clear overview of the expected capabilities of the platform. These capabilities are presented as functional requirements for the UAS. Subsequently, from these functional requirements the performance requirements were derived. Both functional and performance requirements are shown in Section 3.2. This is followed by Section 3.3 on constraints and airworthiness requirements. Finally, all requirements summarized in Section 3.4.

3.1 Customer expectations and mission description

This section describes the customer expectations and the mission description for the UAS. The expectations were obtained by interviewing the different parties.

3.1.1 Customer expectations

This subsection describes the expectations of the different customers. A short description of their expectations is given. The considered customers were the faculty Civil Engineering at the Technical University of Delft, the Dutch National Aerospace Laboratory (NLR) and the Dutch National Police (KLDP). Each customer is addressed separately.

Expectations Civil Engineering

Currently, Civil Engineering is gathering traffic data by performing manned helicopter flights above the highway while recording the traffic flow. This is an expensive way of gathering data. Therefore, a UAS must be designed that is able to provide the same recordings in a more efficient way. In the following list the expectations of Civil Engineering are presented:

- The quality of the images obtained by the onboard camera must be equal or better than the obtained images from the camera of the manned helicopter.
- If multiple platforms can be used simultaneously, this would create additional value.
- The UAS must be easy to operate. One person should be able to operate the platform without requiring to much training.
- The recording time of the camera must also be equal or larger than was achieved with the manned helicopter.
- The recorded observation area must also at least be be equal to that of the manned helicopter.

Expectations NLR/KLPD

Nowadays, there is an increase in need for UASs to perform police tasks. The KLPD together with the NLR are currently exploring the capabilities of UASs. From a UAS design they expect the following:

- It must be a robust and reliable system.
- It must be possible to employ the system fast.
- It is desired that one person is able to operate the UAS. The education and training must be minimal.
- The system must be employable in most weather conditions.
- It must be possible to attach different payloads to the UAS (camera e.g.) without having to worry about airworthiness regulations.
- The manufacturer of the UAS should have a clear development plan (including upgrades). Upgrading the platform should be easy and low costs.
- Maintenance should be minimal. This maximizes the operational time.
- It is desired to have one UAS that can perform all desired tasks instead of a few UASs that each performs a different task.
- Existing organizational structure should be sufficient. No additional facilities should be required in order to operate and maintain the UAS.

3.1.2 Mission description

Besides the UAS expectations there are also a number of mission descriptions defined for the UAS. Again this was defined for both parties (Civil Engineering and NLR/KLPD).

Mission description Civil Engineering

As presented in the previous subsection, the faculty of Civil Engineering is planning on using the UAS for traffic monitoring purposes. The UAS must be able to monitor traffic on highways. Besides this mission, it is also desired to use the platform for crowd monitoring. The second mission description is not a priority for the design. If this mission can be achieved by using minimal effort this would be desired. It should not be the main aim of the UAS design.

Mission description NLR/KLPD

The NLR/KLPD has described a number of scenarios which represent the kind of tasks that a UAS should be able to perform. The scenarios/missions are described as follows:

- In case of an international meeting of VIPS e.g., monitor movements in a specified area and provide information regarding those movements to the desired parties.
- In an industrial area it is expected that drugs are cultivated. In this case the UAS must be able to observe and analyze the area in order to find the expected location of the drugs.
- The Champignons League final is taking place and both clubs are well known for their aggressive supporters. Monitor the environment during the event and report suspicious movement in the area to the desired parties.
- A car-bomb exploded at a marketplace in the city center. In this case, the UAS must be able to provide high quality recordings from every desired angle and reconstruct the expected trajectory of the car.
- A chemical factory is exploded and hazardous substances are released. The task of the UAS is to take samples of the hazardous substances in the air and to determine the wind direction and speed in the different layers of air.
- In case of a fire the UAS must be able to determine the location the fire and provide color and thermal images to the desired parties (also in segregated airspace).

3.2 Functional and performance requirements

The customer expectations and the mission description for the UAS was the starting point in deriving the UAS requirements. The requirements were split into requirements for the UAV, the camera and the ground station. Subsequently, the requirements were subdivided into functional requirements and performance requirements.

3.2.1 UAV requirements

UAV functional requirements Civil Engineering

- Preferably, the UAV must be able to follow the "shockwave" within a traffic stream. This "shockwave" is created when congestion occurs and moves against the traffic stream.
- In order to comment on the behavior of a vehicle, the UAV should be able to track a vehicle for at least two minutes.
- No real-time analysis of traffic motion is possible yet, so the high resolution images/video do not need to be processed in real-time.
- The UAV should be able to observe/monitor a certain area of highway. The platform is not required to hover at a particular spot in order to record the area of interest. During this period it is desired to record high quality video while

streaming low quality video to a ground station. This allows the operator to see what the platform is seeing.
- Images created under a variety of angles should be possible. This is required because the Department of Waterways and Public Works does not allow platforms to fly above the highway. Therefore the platform needs to fly besides the highway.

UAS functional requirements NLR/KLPD

The dutch national police (KLPD) and the NLR have described the demand for UASs by means of eleven scenario's[58]. These scenarios can be translated to functional/operational demands. In this subsection, the UAS requirements derived from the described scenarios are presented. An overview of these requirements is presented in the following list:

- Observe urban and non-urban environments (including buildings and roads) during day and night time operations.
- Information regarding the observed object(s) and the direction of movement should be forwarded to the required stakeholders. This can be done by providing a live stream of low quality video. The high quality video can be recorded such that more detailed analysis is possible afterwards.
- In case of a disaster, provide high quality recordings of the area from every desired angle.
- In case of a fire, the UAV must be able to provide thermal images to the desired parties.

Besides the "normal" requirements, there are also some optional requirements. When possible, these requirements can be implemented as well. The optional requirements are enlisted below:

- Detect and recognize objects and their direction of movement by means of real time analysis of the UAV images (onboard the UAV or on the ground station).
- In case of hazardous substances in the air, the UAV should be able to determine the wind direction and wind speed in the different layers of air. Taking samples of the substances in the air is also required (analysis of the samples onboard is not required).

UAS performance requirements Civil Engineering

In the previous subsection the functional requirements for the UAV were described. These requirements had to be translated to performance requirements in order to have "measurable" requirements which can be used for the design. In the following list, the performance requirements for are shown:

- The UAV must preferably be able to follow the "shockwave" within a traffic stream. This "shockwave" moves against the traffic stream with approximately 30 [km/h].
- The UAV must be able to track traffic. In order to comment on the behavior of a vehicle, the UAV must be able to track such a vehicle for at least two minutes at flight speeds between 90 [km/h] and 130 [km/h].
- Tracking a car for two minutes at a maximum speed of 130 [km/h] requires a range of at least 4.5 [km].
- In order to match the current recording time of the manned helicopter, the UAV must have an endurance of at least 30 minutes.
- It is desired to fly at an altitude between 300 [m] and 490 [m]. Flying at 490 [m] allows a traffic view of also 490 [m] (when using a wide angle camera). This is preferred over an altitude of 300 [m], which allows a traffic view of only 300 [m].
- Currently a manned helicopter is used to record data. Flight costs are around €8000,- for three hours of flight. Effectively this creates about 90 minutes of usable images. Two to three flights per year were performed because of those high costs. In the past five years this resulted in about €100.000,- of costs (not including the costs of two additional operators). The operating costs of the new UAS design must therefore be lower than €20.000,- per year (assuming an operating period of five years).

UAS performance requirements NLR/KLPD

As for the performance requirements of Civil Engineering, also for the NLR/KLPD the performance requirements had to be determined. Besides translating the functional requirements, also a survey[59] conducted within the KLPD was used to determine the performance requirements (see Appendix B). The following list gives an overview of the performance requirements:

- Time between planning the deployment and deployment is generally between one hour and one day.
- The system should be operational within 5-10 minutes after arrival on location.
- An endurance of minimal 20 minutes is required.
- Maintenance should be required after at least 4 deployments (more deployments are desired). Prognostics and Health Management (PHM) can be used to manage the lifecycle of the UAS. In case maintenance is required, spare parts should be available on short basis. Besides that, additional facilities in order to maintain the UAS should not be required.
- An operating range of at least 250 [m] is desired.

- An operating ceiling of 120 [m] would be excellent.
- The total system costs should be €10.000,- to €20.000,- maximum.
- The areas in which the system will be deployed is in most cases uncultivated, above buildings or between buildings.
- In order to transport the system a medium sized car must be sufficient.
- With respect to payload, it is expected that a daylight-camera together with an IR-camera is required in most cases. Combining different sensors would be ideal.
- The platform must be able to observe an area of interest from a distance of at least 10 [m].
- With respect to the video stream, the system must at least be able to store an HD stream onboard of the platform and send a low resolution (PAL) stream to the ground station.
- In order to fly in most weather conditions the vehicle must be able to withstand a wind force of 4 [Bft].
- Besides resistance against wind, the system should also be resistant against precipitation to a certain extent. Resistance against 0.1 mm precipitation per hour must be possible.
- The UAS must be able to operate in areas with dust and smoke. It is also desired that the system can operate in areas that contain flammable, explosive and corrosive gases.
- In visibility below 100 [m] the system should at least be operable.
- In case of electromagnetic disturbances the system is allowed to change its mission (in order to prevent the magnetic compass or GPS signal to be disturbed). The mission may even be aborted if the datalink or videolink is disturbed.
- With respect to noise, it is desired that the platform produces a minimum amount of noise.

3.2.2 Camera requirements

The camera is an essential part of the UAS design and therefore a separate set of requirements for the camera was derived. Most functional requirements for the camera were already discussed in the previous subsections. Therefore, it is decided not to repeat those requirements but to present the performance requirements for the camera. Again, first the requirements of Civil Engineering are presented.

Camera performance requirements Civil Engineering

Currently, Civil Engineering is gathering traffic data by performing manned helicopter flights above the highway while recording the traffic flow with a camera. The following camera performance requirements were derived based on conducted interviews:

- An accuracy of 20-25 [cm] within the recorded images is required. Using this requirement, it is possible to determine the camera requirements. At a flight altitude of 490 [m], the view of the camera must also be approximately 490 [m] wide (assuming a wide angle camera). Using Figure 3.1 and the previous assumptions it can be said that the camera angle of view should at least be

equal to $\beta = 59°$. In order to assure the accuracy of 20-25 [cm] at the upper bound of the operating requirements, 490 [m], the camera must at least have a resolution of $\frac{490}{.25} = 1960$ pixels in the direction parallel to the traffic stream. Currently a Prosilica GC 2450[60] camera with 2448x2050 pixels is used onboard of the manned helicopter. Note that in case the UAV is flying at an altitude of 300 [m] with a camera angle of view equal to $\alpha = 45°$ this will result in a higher accuracy (assuming the same camera is used in both cases). In this case the accuracy will be $\frac{1}{\frac{2000}{300}} = 0.15$ [cm]. The field of view is reduced to 300 [m] in this case.

- Preferably non-interlaced video/progressive-scan video[61] is desired. Progressive scanning (alternatively referred to as noninterlaced scanning) is a way of displaying, storing, or transmitting moving images in which all lines of each frame are drawn in sequence. This is in contrast to interlaced video, used in traditional analog television systems, where only the odd lines are drawn alternately.
- A short exposure time is required. The purpose of exposure adjustment is to control the amount of light emitted/reflected from the subject that is allowed to fall on the film, so that "significant" areas of shadow and highlight detail do not exceed the film's useful exposure range. This ensures that no "significant" information is lost during capture.
- The camera must deliver at least 10-15 frames per second.
- A camera recording time of 10 to 30 minutes is sufficient for now.
- Accurate time reference is desired. A DCF77[62] receiver can be used for example. This is a long-wave time signal radio station. This signal can be picked up by a simple, low cost and low weight, device and used as a time reference.
- A low resolution video stream must be send to the ground station in order to "see" what the camera is "seeing". The camera must therefore be able to deliver a video stream.
- A camera road view of approximately 490 [m] is desired. It is possible to increase the view by using a large angle camera (software gives the ability to compensate for possible deformation in the pictures)
- Low image compression is desired in order to maintain as much information as possible.
- The camera must be free of high frequent vibrations (above 5 [Hz]). These vibrations can not be compensated for and reduces the quality of the images. Low frequent vibrations (below 5 [Hz]) are allowed.

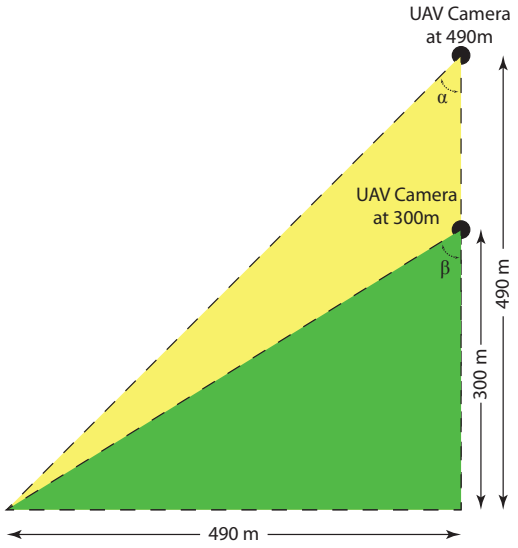

Figure 3.1: Camera view at 300 [m] and 490 [m]

Camera performance requirements NLR/KLPD

Based on interviews and the survey[59] conducted within the KLPD, the following camera requirements were established:

- The camera should be as light as possible.
- A resolution of at least 1280 x 720 (720p) is desired. The resolution of a daylight camera should at least be 14 [mm/pixel].
- Preferably auto focus should be available.
- Optical/digital zoom can be an additional option.
- The ability to stream video is required. This may also be done by using additional onboard hardware.
- An H264 compressed stream converted to transport stream or MPEG2 converted to transport stream is desired in order to easily get the video stream in the video exploration system of the ASSP department of the NLR. Metadata should be included in each frame as well.
- A global shutter is desired. Such a shutter does not suffer from motion artifacts (motion in a picture).
- A multi-sensor camera[63] (360° field of view) in combination with sensors is desirable for future purposes.
- 3D modeling[64] of the environment is an interesting feature for future purposes.

3.2.3 Ground station requirements

This subsection describes the ground station functional and performance requirements. First, the functional requirements of each party is presented after which the performance requirements are stated.

Ground station functional requirements Civil Engineering

- The UAS must be operable without requiring to much training time, therefore the interface of the ground station should be straightforward and easy to control.
- The video stream that is send from the UAV must be displayed on the ground station.

Ground station functional requirements NLR/KLPD

- A programmable software interface is required. This allows the user to adjust the interface to their own needs.

Ground station performance requirements Civil Engineering

- In order provide control of the UAV, the ground station must be able to have an operational time equal or larger than the operational time of the flying platform.

Ground station performance requirements NLR/KLPD

- In order to provide control of the UAV, the ground station must be able to have an operational time equal or larger than the operational time of the flying platform.
- An example of a desired ground station interface is presented in Figure 3.2.
- The ground station must be operable by at most two operators.
- Interoperability with PAL video, digital video (MPEG2), digital video with position information, exchangeable sensors and exchangeable ground stations should be possible.
- The ground station must be portable. A tablet PC[65] would be perfect.
- With respect to resistance to dust and water, it is required that the system has an Internal Protection (IP) resistance of at least 54 (see Table **??**).

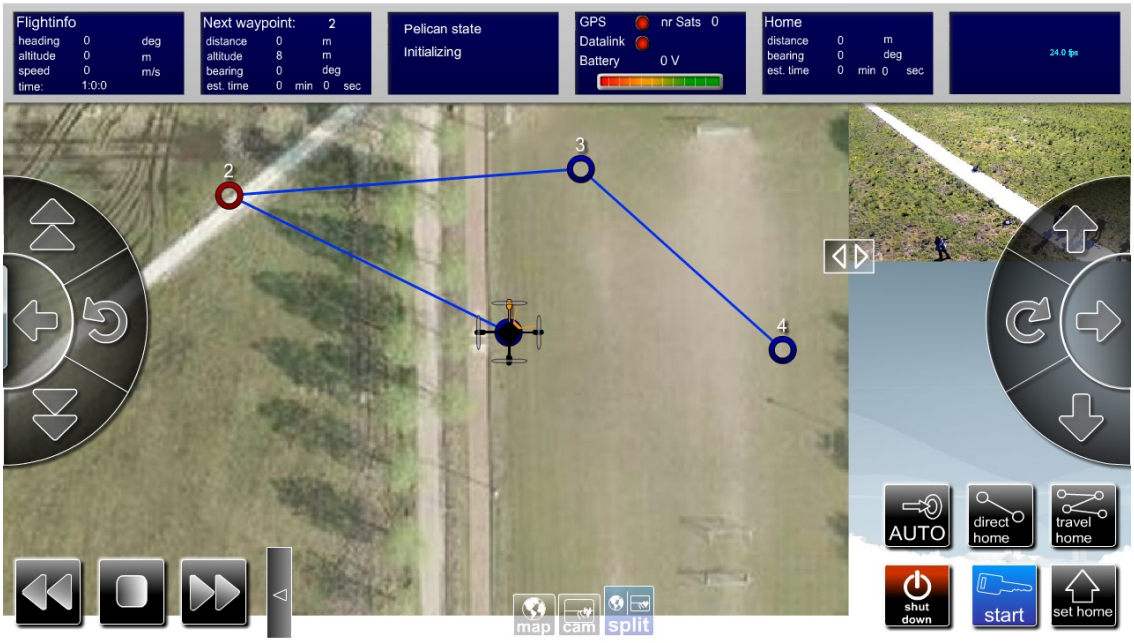

Figure 3.2: Example ground station interface[66]

This concludes the section on functional and performance requirements. The next section describes the regulations to which an UAS design is subjected.

3.3 UAS airworthiness requirements

Besides the UAV, camera and ground station requirements that were determined by the clients, there are also certain constraints on the UAS design. These constraints include for example airworthiness requirements. The regulations for model aircraft are described first. After that, the proposed/future regulations regarding aircraft lighter than 150 [kg] are presented.

Currently there are requirements for UASs heavier than 150 [kg]. For all UASs internationally, the convention of Chicago (International Civil Aviation Organization doc 7300)[67] and the ICAO Circular 328[68] applies. In Europe the so called Regulations EC determined by EASA apply to UASs heavier than 150 [kg][69]. UASs up to 25 [kg] that are used for recreational purposes fall under the category model aircraft. Up till now, there are no clear regulations for UASs that are heavier than 25 [kg] and lighter than 150 [kg] or UASs that are used for non-recreational purposes. Besides that, the existing regulations stated in the Circular of ICAO are not binding yet. The Dutch government is free to decide if the content of the Circular is incorporated in the national regulations. For now it is expected that the UAS design will not be heavier than 150 [kg]. From Section 4.2 was derived that the UAS design will be of the mini class. Therefore the design is not expected to be heavier than 20 [kg]. This section therefore focusses on the regulations regarding UASs up to 20 [kg].

3.3.1 Regulations model aircraft

In the following list, the regulations regarding model aircraft are presented[70]:

- The MTOW can not exceed 25 [kg].
- Flights can only be conducted under good visibility conditions (clear definition about the visibility conditions are not stated).
- The UAV should be in line of sight at all times.
- An altimeter is not required.
- Acrobatic flight is allowed.
- It is prohibited to closely approach other aircraft as this can cause the vehicles to collide.
- The controller of the UAV should take measures in order to prevent collisions. Aircraft that are not model aircraft should be given precedence.
- No flight plan is required.
- The maximum altitude within Class G airspace is 1000 [ft] (see Figure 3.3). Provided that the vehicle flies within a 3 [km] range of an uncontrolled airspace or an area for which an exemption was issued. In areas that allow low altitude flights there must be a second person observing the airspace to warn for other air vehicles.
- Flights within an aerodrome traffic zone of military terrain are allowed up to 1500 [ft].
- Flights within airspace Class C are allowed if a covenant has been agreed with the local air traffic management.
- Radio connection with air traffic management is not required.
- Rules for navigation and telecommunication installations in order to perform Visual Flight Rules-flights (VFR-flights) do not apply.

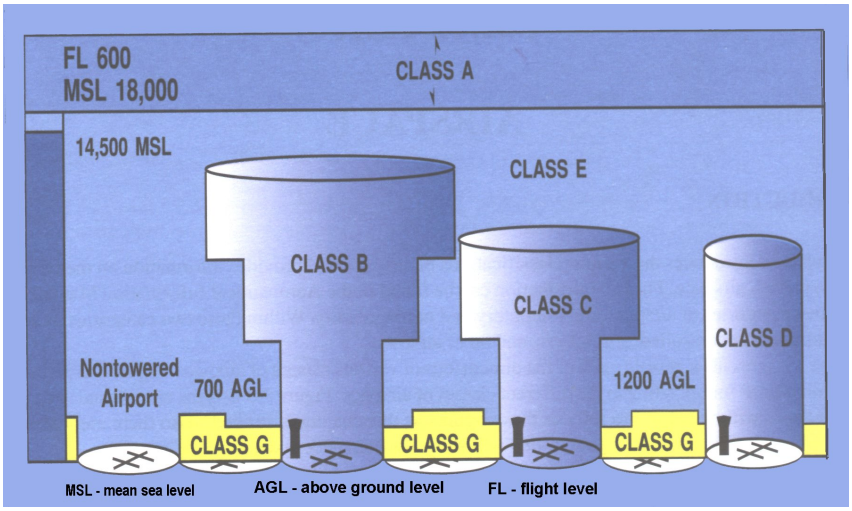

Figure 3.3: Airspace Classes[71]

Currently, the dutch Civil Aviation Authority (CAA) is adjusting current UAV regulations, the so called LuchtVerkeersRegelement (LVR), in order to incorporate light UASs. These light UASs weigh between 0 [kg] and 150 [kg], have a maximum speed below 130 [km/h], an impact energy below 66 [Joule] (depends on maximum

speed and weight) and are to be used for non-recreational purposes. The certification will be derived from CS-VLA and CS-VLR. Common european rules for UASs below 150 [kg] will be developed based on the work of the JAA and EUROCAE. They developed rules for two different classes. These classes are described in the following subsection.

3.3.2 Light UAS classes

Operation class I This class should enable easy OPS licensing and easy technical allowance. There are some restrictions. These are enlisted in the following overview:

- Maximum altitude is 120 [m].
- Maximum range is 500 [m].
- LOS operations.
- Daytime operations.
- Do not fly above people and buildings.

In order to operate a UAS in this class, training is required. An operating license is required for the organization before one is allowed to operate a UAS of this class. Details about the certificate still need to be worked out.

Operation class II For this class the same restrictions apply as for operation class 1, except for the fact that one or even more of those restrictions can be discarded. It should therefore be possible to fly at higher than 120 [m] and beyond a range of 500 [m]. Certification with respect to airworthiness and noise emission are required. These certifications will be derived from manned Certification Specification-regulations determined by EASA. CS for light unmanned aircraft will be derived from Certification Specifications - Very Light Aircraft (CS-VLA). CS for light unmanned rotorcraft will be derived from Certification Specifications - Very Light Rotorcraft(CS-VLR). For this class it is also required to have a certificate in order to operate the UAS.

The requirements of both classes will, in a later stage, be supplemented by certifications relating the ground station and detect, sense and avoid. Also requirements related to the design, production and maintenance of the UAS will be formulated in the near future.

The GC-201 produced by Geocopter[72] is an example of a UAS that has a class I approval. A class II approval has been provided to the dutch military for flying the Raven[73]. Currently, special permits are provided to other parties that want to perform flights. They have to satisfy the following requirements:

- Appropriate pilot license and medical license (2 or 3).
- Certificate of airworthiness.
- Maintenance performed by a qualified organization or persons.
- UAS registered in official aircraft register.
- Nationality and registration marks.

- Permit of the Provence to fly above a certain terrain.
- Respect the rules of the air.
- Respect the rules for operations.
- Respect the rules for giving information about incidents and accidents.

From this section can be concluded that there are no clear airworthiness requirements for UASs yet. Developing those rules is in progress. For now special permits need to be requested before it is allowed to fly with UASs that are used for non-recreational purposes. This concludes the section on UAS airworthiness requirements. The following section gives an overview of all requirements that were discussed in this chapter.

3.4 Conclusion

In order to obtain the requirements for the UAS design first the customer expectations and mission descriptions were defined. These were translated to functional requirements. Subsequently, by using the functional requirements the performance requirements for the UAS design could be derived. Besides these requirements the UAS design is also subjected to certain airworthiness requirements. This section gives an overview of the requirements that are considered in the UAS design.

The requirements of both parties were combined in order to get a general overview of the requirements. First, the UAV requirements are shown (see Table 3.1).

Table 3.1: Overview UAV requirements

UAV requirements:
Flight regime between 30 [km/h] and 130 [km/h]
Range of 4500 [m]
30 [min] endurance
Flight altitude between 300 [m] and 490 [m]
Operating cost below €20.000,- per year with maximum purchasing costs between €10.000,- and €20.000,-.
Operable within 10 [min]
Withstand a wind force of 4 [Bft]
Resistant against 0.1 [mm] precipitation per hour
Operate in dust and smoke with visibility below 100 [m]
Least amount of noise emission

Next, the requirements for the camera are presented in Table 3.2.

Table 3.2: Overview camera requirements

Camera requirements:
EO and/or IR sensor(s)
At least 1960 pixels in the direction parallel to the traffic stream at an operating altitude of 490 [m]
Non-interlaced video
Global shutter
10-15 [fps]
10-30 [min] high resolution recording time and 10-30 [min] simultaneous low resolution streaming time
Low image compression
Optical/digital zoom
Auto focus

Subsequently, an overview of the ground station requirements is shown in Table 3.3.

Table 3.3: Overview ground station requirements

Ground station requirements:
Portable
IP resistance of at least 54 (see Table **??**)
Simple and programmable interface
Operational time of more than 30 minutes
Capable of supporting different video streams (PAL and MPEG2)

Finally, an overview of current airworthiness requirements is presented in Table 3.4. The new airworthiness requirements for each class are shown in Table 3.5.

Table 3.4: Overview current airworthiness requirements

Current airworthiness requirements
Appropriate pilot license and medical license (2 or 3)
Certificate of airworthiness
Maintenance performed by a qualified organization or persons
UAS registered in official aircraft register
Nationality and registration marks
Permit of the Provence to fly above a certain terrain
Respect the rules of the air
Respect the rules for operations
Respect the rules for giving information about incidents and accidents

Table 3.5: Overview new airworthiness requirements

Operation class I:	Operation class II:
Maximum altitude of 120 [m]	No maximum altitude restrictions
Maximum range of 500 [m]	No maximum range restrictions
LOS operations are allowed	BLOS operations are allowed
Daytime operations only	Both daytime and nighttime operations
Not allowed to fly above people and buildings	Allowed to fly above people and buildings
Operating license required	Operating license required

From these requirements can be seen that in order to respect the UAV requirements, the UAS design must comply with operation class II airworthiness requirements. This concludes the chapter on requirements. Next, the requirements are used to initiate the preliminary UAS design. This is described in Chapter 4.

Chapter 4

Preliminary UAS design

After the UAS requirements were defined, a UAS database had to be created. Before this was done, first the vehicles that were implemented in this database were described in Section 4.1. In this first section also the database structure is presented. This is followed by Section 4.2 on evaluation of the performance of current UASs, making use of the created database. After that, the mission profiles were presented and a weight estimation was performed in Section 4.3. In order to complete the weight estimation, an estimation of the drag was required. This is discussed in Section 4.4. By combining the drag and weight estimation in Section 4.5, it was possible to conduct a rough performance analysis. Subsequently, these results were used as a starting point for the weight convergence procedure. After that, the results needed to be evaluated by means of Section 4.6 on preliminary sizing. Next, all results were combined and used as an input for Section 4.7 that describes the wing design. The section on wing design is followed by a Section 4.8 on tail design. After that, Section 4.9 describes the effect of the wing on the tail. This is followed by Section 4.10 on stability of the UAS. In Section 4.11, the design possibilities with respect to materials for the UAS structure is discussed. This is followed by Section 4.12 on propulsion system design. Finally, Section 4.13 describes the remaining UAS subsystems.

4.1 UAS database

This section describes the structure of the UAS database. The types of UASs that were included in the database are also presented in this section. In Chapter 3 the requirements for the UAS were described. These requirements formed the basis for the UAS database. From these requirements, the desired parameters were derived. The following table shows the derived parameters that were included in the database:

Table 4.1: Overview derived parameters

Description:	Symbol:	Unit:
Maximum take-off weight	W_{TO}	[N]
Endurance	E	[h]
Range	R	[km]
Maximum speed	V_{max}	[km/h]
Stall speed	V_{st}	[km/h]
Ceiling	H	[m]
Payload weight	$W_{payload}$	[N]

In addition to those parameters, the following table of parameters can be useful at a later stage of the design and were therefore also incorporated in the database:

Table 4.2: Overview other useful parameters

Description:	Symbol:	Unit:
Empty weight	W_{empty}	[N]
Wing span	b	[m]
Main rotor diameter	R_m	[m]
Tail rotor diameter	R_t	[m]
Propeller diameter	D_p	[m]
Vehicle diameter	D_v	[m]
Cruise speed	V_{cruise}	[km/h]
Loiter speed	V_{loit}	[km/h]
Wing surface area	S_{ref}	[m^2]
Rotor disk area	S_r	[m^2]
Aspect ratio	A	[-]
Engine power	P	[W]
Maximum rate of climb	RC_{max}	[m/min]
Take-off distance	d_{to}	[m]
Take-off and landing means	-	[-]

The next step was to determine which UAS categories and types to include in the database. In Subsection 2.2.3 the different UAS categories and types were already presented. Using Subsection 2.2.3 in combination with the available data, it was decided to include all UAS categories except for the flapping wing aircraft and blimps. This was done because data regarding flapping wing UASs and blimps was not as extensive as for the other categories. Besides that, it is also expected that blimps and flapping wing UASs are not able to comply with the maximum speed requirement of at least 130 [km/h].

Within the remaining categories; fixed wing, rotary and convertible UASs; the following types were included in the database:

Table 4.3: Overview database included UAS types

Configurations:
Fixed wing
Conventional rotary wing
Coaxial rotary wing
Multi-rotary wing
Shrouded/Ducted fan rotary wing
Tilt rotor/Tilt wing/Tilt body

From Table 4.3 can be seen that the tandem rotary UAS type was also not included. Again this decision was based on the lack of available data.

Before creating the database one final limit had to be set, the Maximum Take Off Weight (MTOW). As discussed in Section 3.3 it is expected that the UAS design weight will not exceed 150 [kg], therefore the MTOW limit was set to 150 [kg]. This means that the nano, micro, mini and small UAS classes had to be considered for the database. Subsequently, the database was created. Data for the database was mainly derived from the Janes all the world UAVs website[74]. Janes is well known in the aircraft design business and has a good reputation. Besides information from Janes, also contact with manufacturers was used to fill in the open gaps in the data. Based on engineering judgement and common sense, the veracity of the data was determined. The created database consists of more than 400 entries. ±200 fixed wing, ±100 conventional rotary wing, 6 coaxial, ±50 shrouded rotary wing/ ducted fan, ±50 multi-rotary wing and 15 tilt rotor/tilt wing/tilt body UASs were included in the database. The next section describes which UAS type and category was chosen, based on the requirements and the data from the created database.

4.2 UAS configuration analysis

After creating the database, the data had to be analyzed. The most important parameters of the database were presented in Table 4.1. Therefore the focus was on these parameters. Based on the UAS classes that were discussed in Table 2.1, the data is presented. The available data for these classes determined if a UAS was included in the analysis.

The database with over 400 entries is not complete for all parameters. Therefore a filter had to be applied before analysis could be performed. The filter was based on the availability of all required data (see Table 4.1). As an example, some UAS data included MTOW but no range. Therefore this UAS was not included in the analysis. Applying this filter caused the nano UAS class to drop out. This class did not contain all required parameters.

Since the UAS will be deployed near highways, above fires and disaster areas it is desired to have a low weight design. If, somehow, the system fails and comes down this will result in a minimum amount of damage. Therefore it is decided to use MTOW as a fixed x-variable in the plots while changing the y-variables according

to the parameters in Table 4.1. Every analysis is discussed in a different subsection. Note that if a configuration does not occur in a figure, it does not mean that this configuration is impossible. In that case, the availability of data is lacking for that particular configuration.

4.2.1 MTOW versus endurance

First, the endurance of the different classes were analyzed. From Section 3.4 can be seen that an endurance of at least 30 minutes is required. In Figure 4.1a through Figure 4.1c, the MTOW versus endurance is presented for each UAS class. From Figure 4.1a can be seen that for micro UASs not much data was present. Also can be concluded that only fixed wing UASs are able to comply with the endurance requirement. For mini UASs, as presented in Figure 4.1b, a lot more data was present. From this figure can be seen that all UAS types have a sufficient endurance. Small UASs were presented in Figure 4.1c. Again from this figure can be seen that all UAS types comply with the endurance requirement.

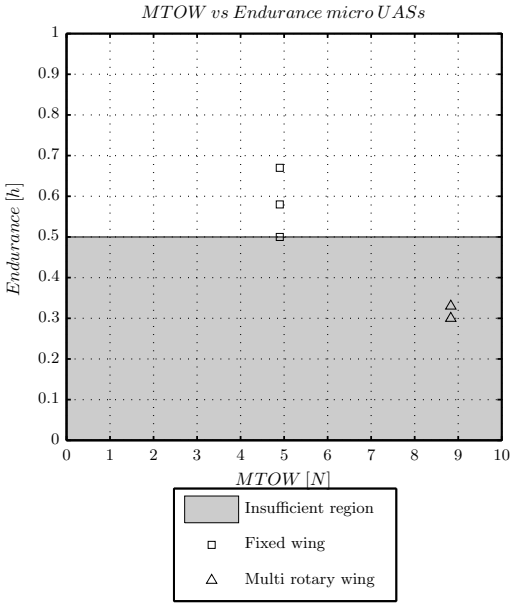

a: MTOW vs Endurance micro UAS

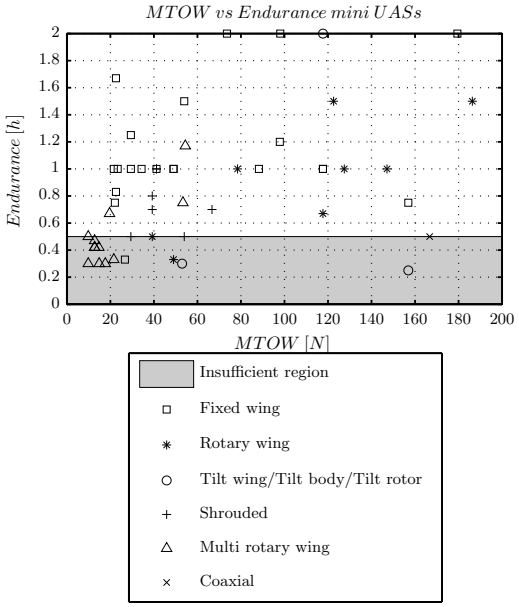

b: MTOW vs Endurance mini UAS

Figure 4.1: MTOW vs Endurance micro, mini and small UAS

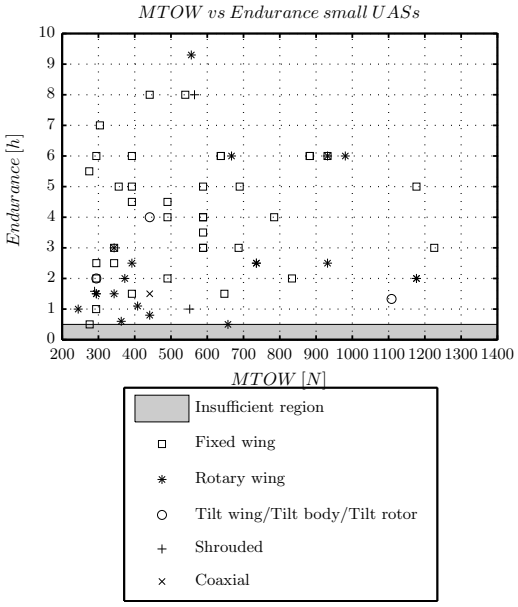

c: MTOW vs Endurance small UAS

Figure 4.1: MTOW vs Endurance micro, mini and small UAS (cont'd)

4.2.2 MTOW versus range

Next, range for the different classes had to be analyzed. The required range, as presented in Section 3.4, is at least 4.5 [km]. Figure 4.2d through Figure 4.2f, represent the MTOW versus range for each UAS class. Again can be seen that for micro UASs not much data was present. From the available data can be concluded that only the fixed wing UASs are able to comply with the range requirement. The multi rotary wing micro UASs have a range up to 3 [km]. From Figure 4.2e can be seen that all presented UAS types are able to comply with the range requirement. All small UASs, as presented in Figure 4.2f, also have a sufficient range.

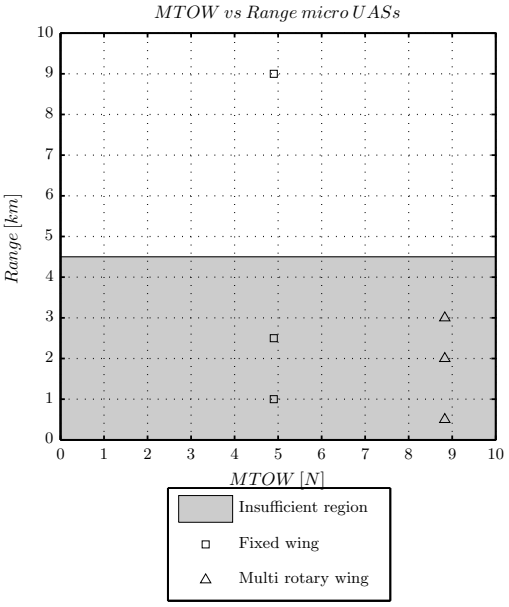

d: MTOW vs Range micro UAS

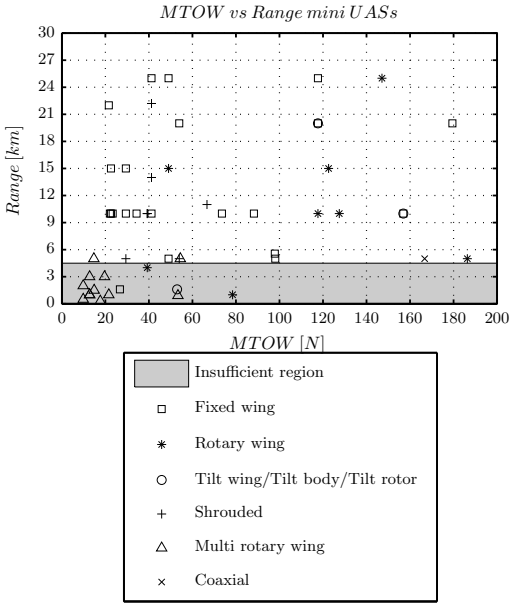

e: MTOW vs Range mini UAS

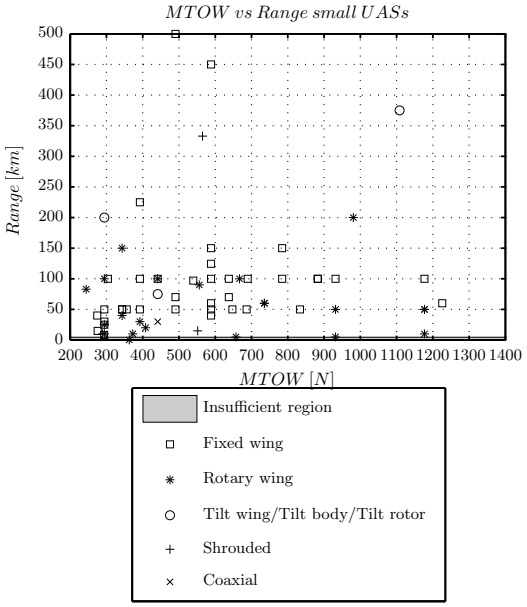

f: MTOW vs Range small UAS

Figure 4.2: MTOW vs Range micro, mini and small UAS

4.2.3 MTOW versus maximum speed

Subsequently, the maximum speed had to be considered in the analysis. Section 3.4 stated that a maximum speed of at least 130 [km/h] is required. Figure 4.3a through Figure 4.3c, represent the MTOW versus maximum speed for each UAS class. Micro UASs were not well represented again (see Figure 4.3a). From the data that was available can be concluded that micro UASs are not able to reach the required maximum speed. The mini UAS class is presented in Figure 4.3b. In contrast to the previously discussed parameters, not all UAS types of this class have a sufficient maximum speed. Only fixed wing UASs are able to fly 130 [km/h] or faster. Analyzing the small UAS class in Figure 4.3c, one can notice that all UAS types, except for coaxial UASs, are able to comply with the maximum speed requirement.

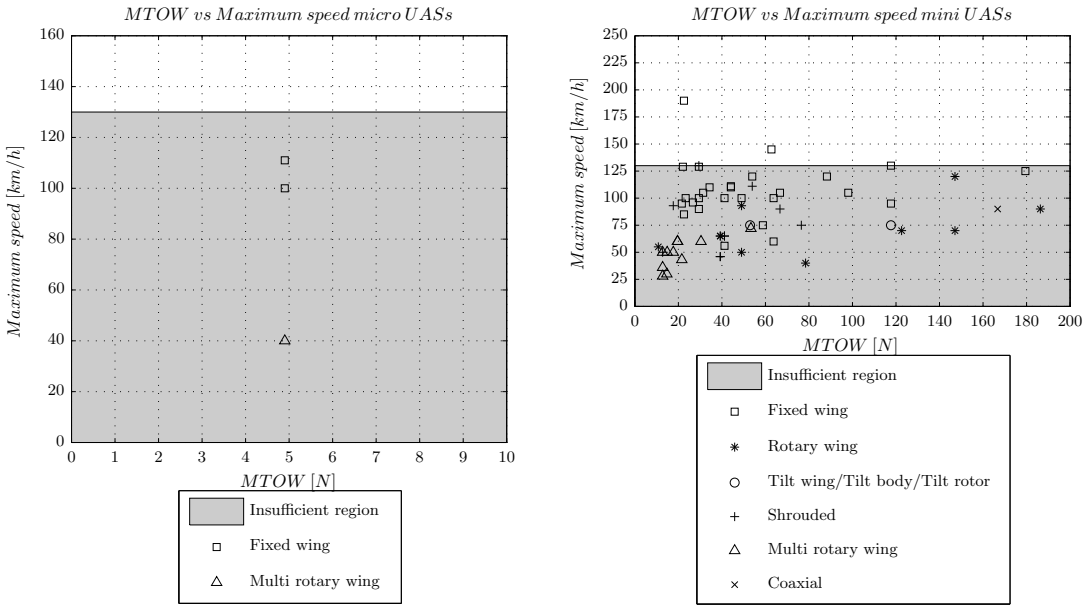

a: MTOW vs Max speed micro UAS

b: MTOW vs Max speed mini UAS

Figure 4.3: MTOW vs Max speed micro, mini and small UAS

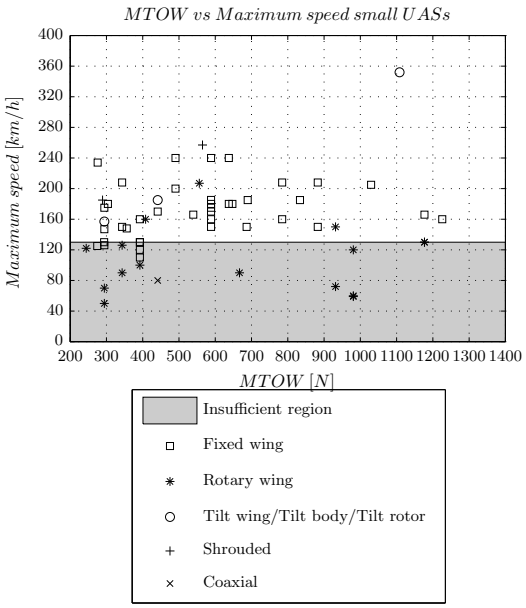

c: MTOW vs Max speed small UAS

Figure 4.3: MTOW vs Max speed micro, mini and small UAS (cont'd)

4.2.4 MTOW versus stall speed

Next, the minimum speed for the different classes had to be analyzed. In Section 3.4 was stated that a minimum speed of 30 [km/h] is required. For all UAS types, except for the fixed wing type, the minimum speed is not an issue. These UAS types have the ability to hover. For the fixed wing UAS type, the minimum speed of 30 [km/h] can be a problem. This minimum speed can approach the stall speed of the vehicle. In order to check if this is the case, the stall speed of the fixed wing UAS classes needed to be investigated. Figure 4.4d through Figure 4.4f represent the MTOW versus stall speed for all fixed wing UAS classes. From Figure 4.4d and Figure 4.4e can be seen that this minimum speed can be achieved by some micro and mini UASs. Looking at Figure 4.4f, one can conclude that most fixed wing UAS of the small UAS class are not able to comply with the minimum speed requirement.

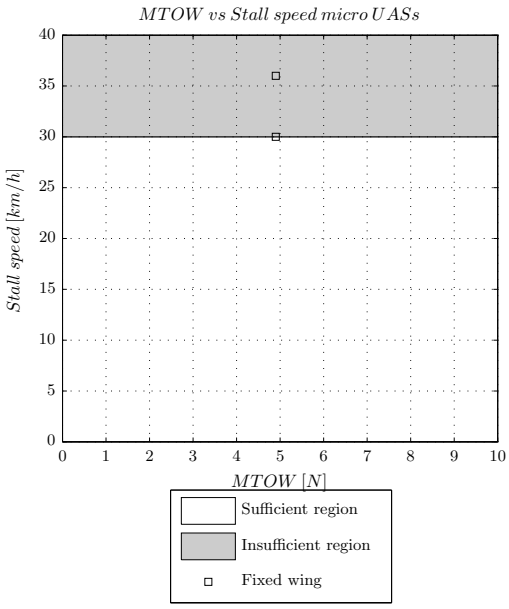

d: MTOW vs Stall speed micro UAS

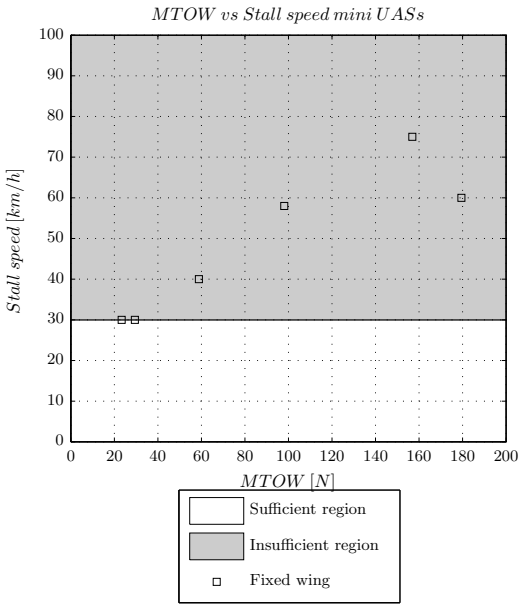

e: MTOW vs Stall speed mini UAS

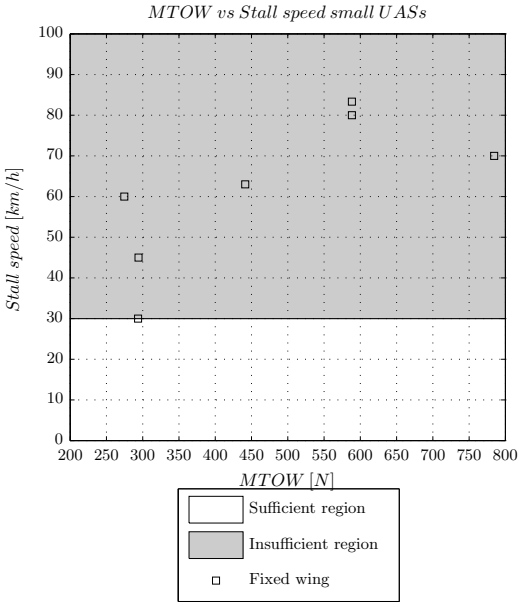

f: MTOW vs Stall speed small UAS

Figure 4.4: MTOW vs Stall speed micro, mini and small UAS

Maximum speed versus minimum speed

From Figure 4.3 and Figure 4.4 can be seen that fixed wing UASs are able to comply with the maximum and minimum speed requirements. However, from this can not be concluded that a UAS is able to satisfy both requirements at the same time. For this, the capabilities of the UASs with respect to both maximum speed and minimum speed had to be addressed. Figure 4.5 shows the maximum speed versus the minimum speed of all UAS classes. Note that in this case the stall speed was not used. Maximum speed in combination with stall speed resulted in to few data points. Therefore, it was chosen to use the minimum flight speed.

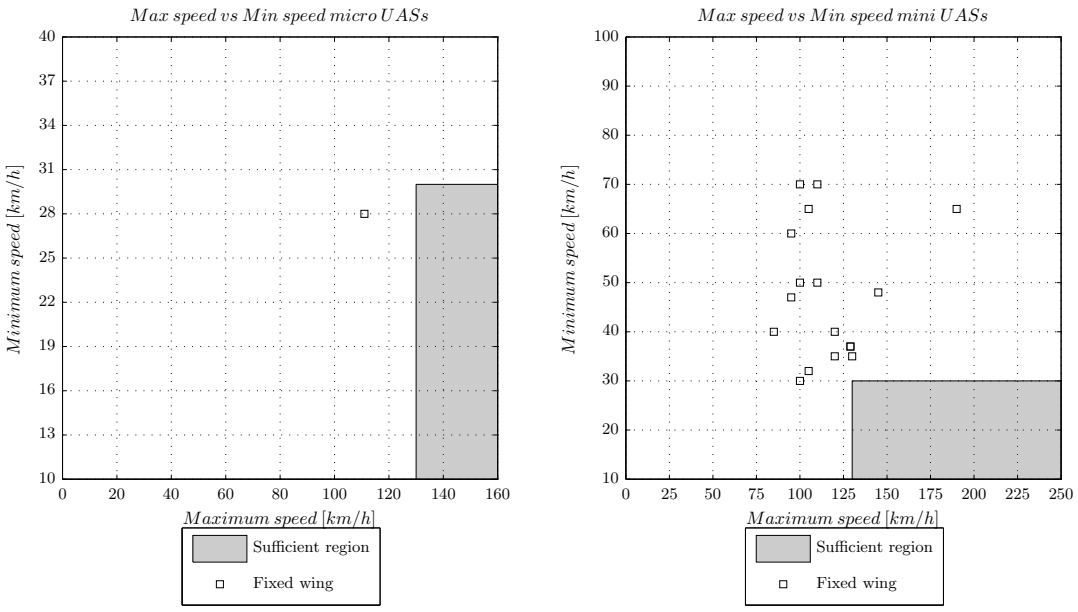

a: Max speed vs Min speed micro UAS

b: Max speed vs Min speed mini UAS

Figure 4.5: Maximum speed vs Minimum speed micro, mini and small UAS

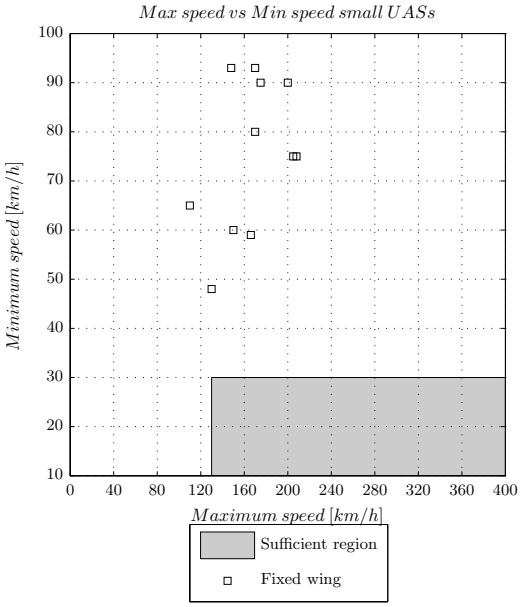

c: Maximum speed vs Minimum speed small UAS

Figure 4.5: Maximum speed vs Minimum speed micro, mini and small UAS (con't)

From Figure 4.5 can be seen that none of the UASs is able to comply with both maximum- and minimum speed requirements. The minimum flight range of mini UASs is between 30 and 70 [km/h]. Small UASs have a minimum flight range between 50 and 95 [km/h]. UASs from the mini class approach the requirements closest.

4.2.5 MTOW versus ceiling

Finally, the ceiling of the different classes had to be analyzed. Section 3.4 stated that the desired flight altitude is between 300 [m] and 490 [m]. Figure 4.6a through Figure 4.6c represent the MTOW versus ceiling for all UAS classes. For this case, the micro class data was scarce again. From Figure 4.6a can be seen that only one fixed wing UAS of this class has a sufficient ceiling. Looking at the mini and small UASs, as presented in Figure 4.6b and Figure 4.6c, one can conclude that the UASs of these classes are also able to comply with the ceiling requirement.

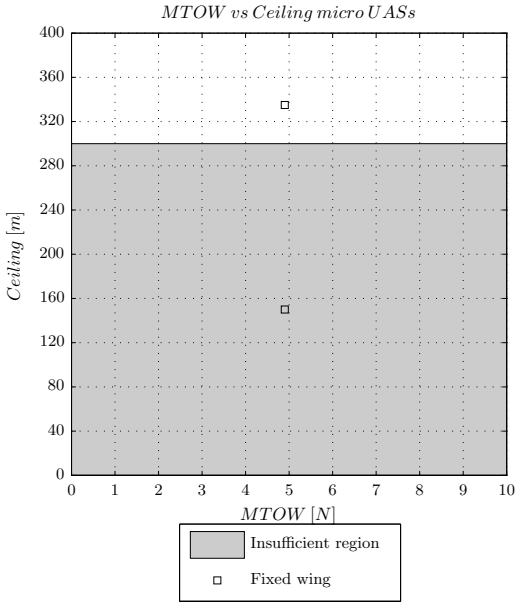

a: MTOW vs Ceiling micro UAS

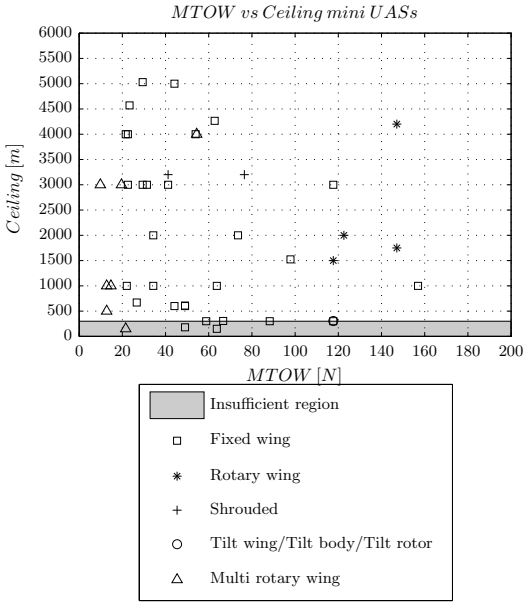

b: MTOW vs Ceiling mini UAS

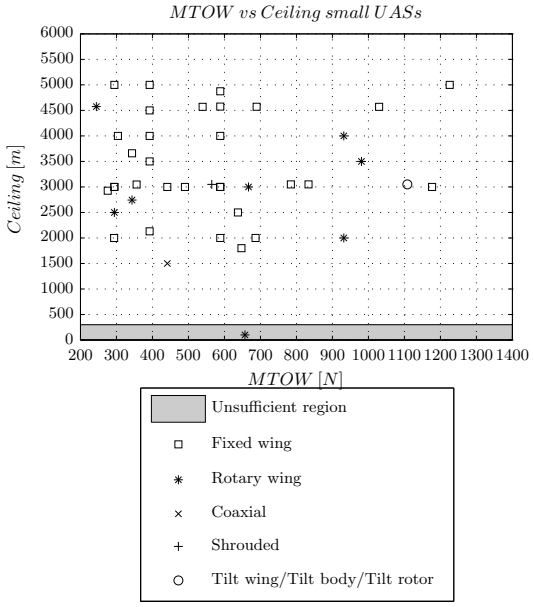

c: MTOW vs Ceiling small UAS

Figure 4.6: MTOW vs Ceiling micro, mini and small UAS

4.2.6 Conclusion

We arrived at the point that all important parameters have been discussed. Next, an overview of the results can be presented. Table 4.4a through Table 4.4c gives an overview of all results.

Table 4.4: Compliance with requirements micro, mini and small UAS

(a) Compliance with requirements micro UASs

Micro	FW[a]	RW[b]	TW/TB/TR[c]	S[d]	MR[e]	C[f]
MTOW vs Endurance	✓					
MTOW vs Range	✓					
MTOW vs Max. speed						
MTOW vs Stall speed	✓	N.A.[g]	N.A.	N.A.	N.A.	N.A.
MTOW vs Ceiling	✓					

(b) Compliance with requirements mini UASs

Mini	FW	RW	TW/TB/TR	S	MR	C
MTOW vs Endurance	✓	✓	✓	✓	✓	
MTOW vs Range	✓	✓	✓	✓	✓	
MTOW vs Max. speed	✓					
MTOW vs Stall speed	✓	N.A.	N.A.	N.A.	N.A.	N.A.
MTOW vs Ceiling	✓	✓	✓	✓	✓	

(c) Compliance with requirements small UASs

Small	FW	RW	TW/TB/TR	S	MR	C
MTOW vs Endurance	✓	✓	✓	✓		✓
MTOW vs Range	✓	✓	✓	✓		✓
MTOW vs Max. speed	✓	✓	✓	✓		✓
MTOW vs Stall speed		N.A.	N.A.	N.A.	N.A.	N.A.
MTOW vs Ceiling	✓	✓	✓	✓		✓

[a] Fixed wing
[b] Rotary wing
[c] Tilt wing/Tilt body/Tilt rotor
[d] Shrouded
[e] Multi rotary wing
[f] Coaxial
[g] Not applicable

From Table 4.4 can be seen that the rotary wing, tilt wing/tilt body/tilt rotor, shrouded and coaxial UASs of the small UASs class in most cases easily meet the requirements. The fixed wing UASs of this class have problems with the required minimum speed and are therefore not able to comply with all requirements.

Most UASs from the mini class do not satisfy the requirements. The fixed wing UASs on the other hand, are able to comply with all individual requirements. Combining requirements, e.g. maximum and minimum speed, results in none of the fixed wing mini UASs to comply with this requirement. UASs from the mini class closely approach the requirements. In order to decide which UAS class and configuration to choose, it was decided to use MTOW as the decisive factor. At the beginning of this section was discussed why MTOW is such an important parameter. Despite the fact that fixed wing mini UASs are not yet able to comply with both maximum and minimum speed requirements, this class was chosen for the UAS design. It is expected that a new UAS design will be able to satisfy all requirements. An overview of the most important parameters of current mini UASs is shown in Table C.1 of Appendix C.

Besides the reference parameters mentioned in Table C.1, some additional notes can be made. Most reference UASs are powered with an electrical engine, except for the Desert Hawk (7), A-3 Remez(16), A-4 Albatros(17), Swift-Eye(21), Puma AE(23) and Javelin(28). These five mini UASs are equipped with a piston engine. Other engine types do not occur within the mini UAS class. Also can be noted that almost all UASs are equipped with a single engine. The Evolution (27) is the only UAS that is equipped with two electrical engines. Besides that can be noted that most UASs are hand-launch-able. According to Gundlach[75], UASs with low wing loading, low weight (below 10 [kg]), low span (below 3 [m]) and high static thrust-to-weight ratio are hand-launch-able. One final remark can be made. All reference UASs are constructed out of composites (carbon fibre, Kevlar and epoxy).

This concludes the section on UAS configuration analysis. The next section initiates the UAS design by means of a weight buildup description.

4.3 UAS take-off weight buildup

The take-off weight buildup of the UAS design is discussed in this section. First, the typical mission profiles were described. Finally, the maximum take-off weight buildup is discussed. This subsection includes the description of each component that is included in the maximum take-off weight buildup.

4.3.1 Mission profiles

Based on Section 3.2, two main mission profiles were derived. Both profiles are presented in Figure 4.7. Figure 4.7a describes the first mission profile. This mission profile is split up into the following five sections:

- Take-off.
- Climb to loiter altitude.
- Loiter for at least 30 minutes in order to observe a certain area of interest.
- Descent.
- Land.

The second mission profile that is shown in Figure 4.7b is split up into the following six sections:

- Take-off.
- Climb to loiter altitude.
- Loiter until an object of interest is identified.
- Follow the object of interest for at least two minutes then cruise back to initial loiter location.
- Complete the remaining loiter time.
- Descent.
- Land.

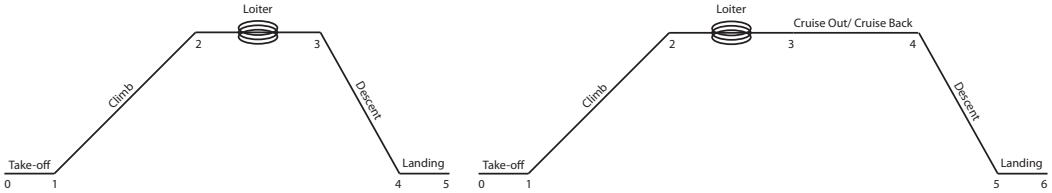

a: Mission profile 1: Observe certain area of interest

b: Mission profile 2: Observe certain area and follow object of interest

Figure 4.7: Mission profiles

The required amount of time for following the object of interest at least two minutes and cruising back to the initial loiter location, is deducted from the amount of available loiter time. This causes the loiter time to reduce in case of the second mission profile. The total amount of required power is based on the most energy intensive mission. Based on these mission profiles, the maximum take-off weight buildup was derived.

4.3.2 Maximum take-off weight buildup

The weight estimation technique of Roskam[1] is often used in preliminary aircraft design. Weight Estimating Relationships (WERs) commonly described in literature, such as Roskam[1], are applicable for UASs classes such as general aviation, transport aircraft and fighters. Extrapolating WERs is generally inappropriate and can lead to erroneous results because the methods were developed against a data set of aircraft that do not represent the UASs of interest. In order to use the weight estimation technique of Roskam[1], new WERs needed to be derived. Based on the available data in the database, these relationships were derived.

The MTOW was broken up into the following elements: empty weight, payload weight and fuel weight. The empty weight includes the structural weight, propulsion system weight, and fixed equipment weight. The structural weight is defined as the weight of the fuselage, wing and tail. The fixed equipment weight is build up from the avionic instrumentation weight, communication system weight and the flight control system weight. Equation (4.1) shows the maximum take-off weight buildup for a UAS in equational form. Figure 4.8 shows a graphical overview off all MTOW elements.

$$W_{TO} = W_{empty} + W_{payload} + W_{fuel} \tag{4.1}$$

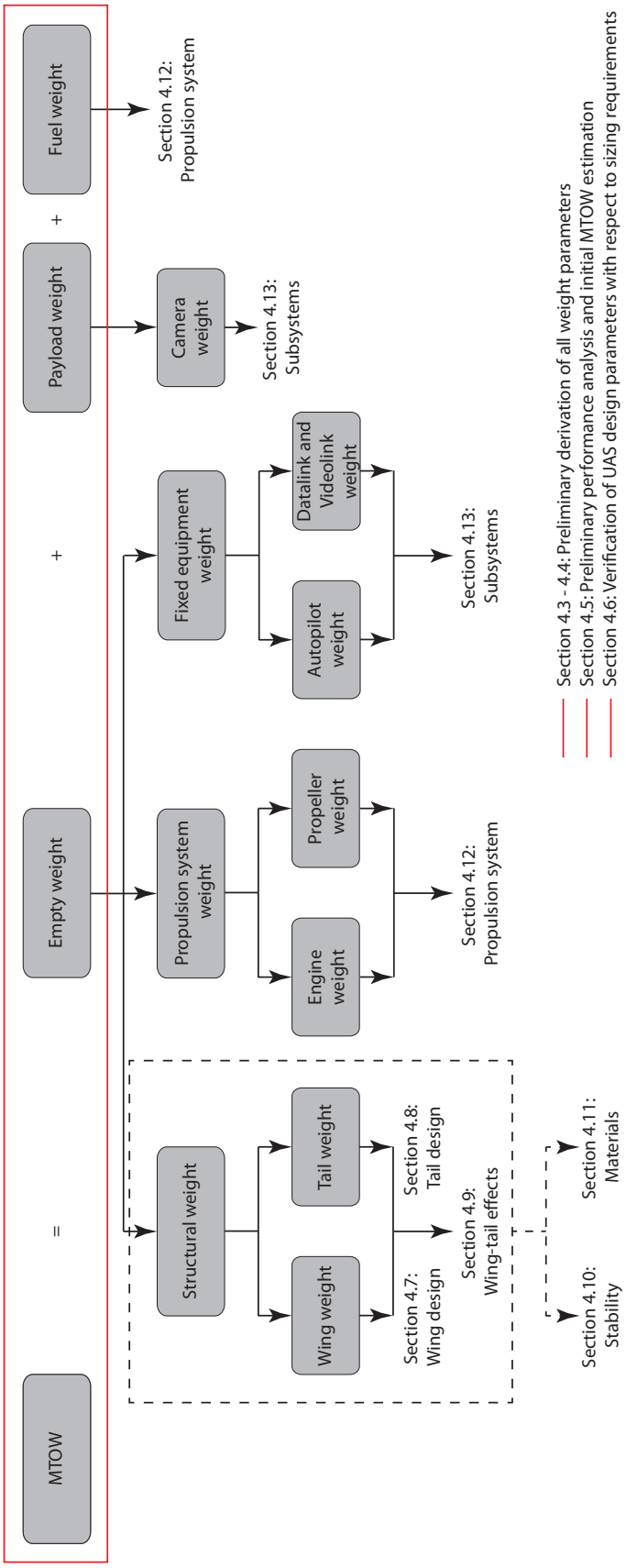

Figure 4.8: Overview MTOW buildup

As shown in Figure 4.8, every parameter of Equation (4.1) is discussed in a several subsections. In order to initiate the preliminary UAS design, the WERs were used in the derivation of all weight parameters. These WERs show a relationship with the MTOW, W_{TO}, of the UAS. From this can be concluded that an iterative process had to be used during the initial estimation of the weight parameters. This process is presented in Figure 4.9. The processes of the diagram are addressed in Section 4.3 through Section 4.5. First, the empty weight is estimated.

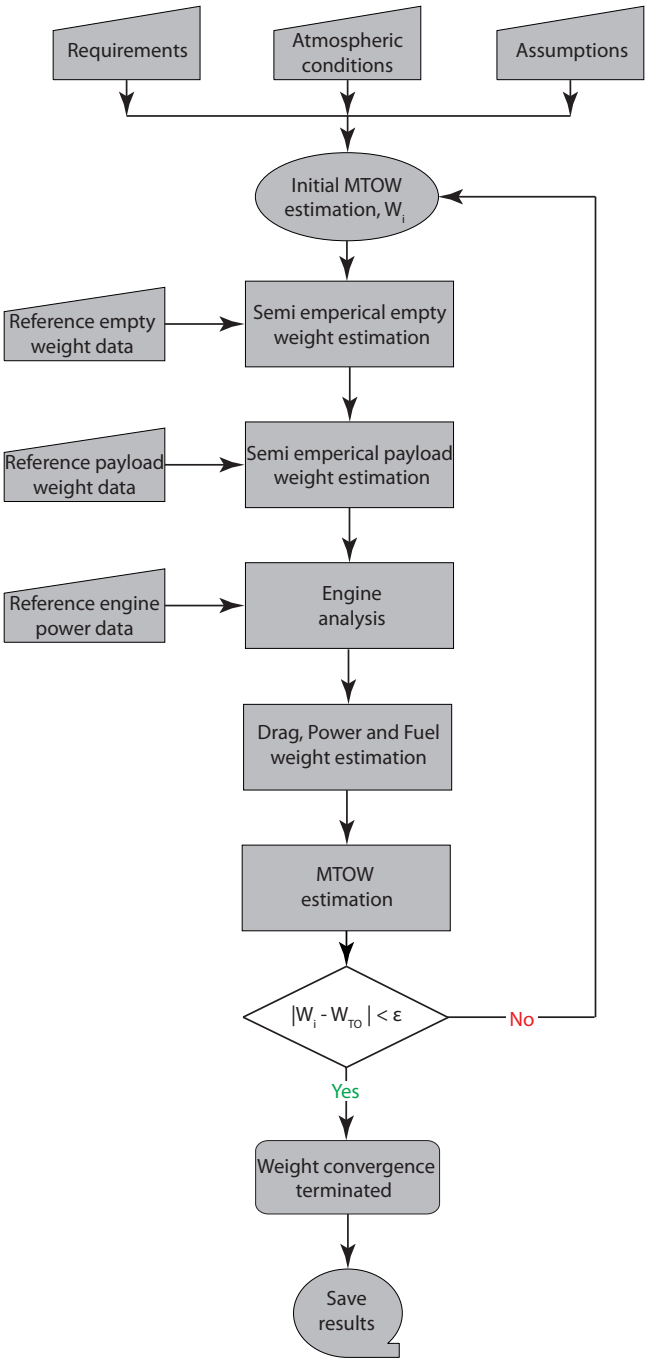

Figure 4.9: Weight convergence process

Empty weight estimation

The empty weight can be seen as the MTOW of the UAS without payload and fuel. The empty weight can be written as a function of the MTOW. Based on the reference data present in the UAS database, Figure 4.10 was created. This figure shows the relationship between the empty weight and MTOW for fixed wing mini UASs containing a piston or electrical engine. Unfortunately, UASs with other engine types were not present in the database. This can be explained by the fact that UASs of type mini are not equipped with other power sources (see the last part of Section 4.2). Later on, in Subsection 4.3.2 it becomes clear that UASs equipped with piston or electrical engines are in fact most efficient.

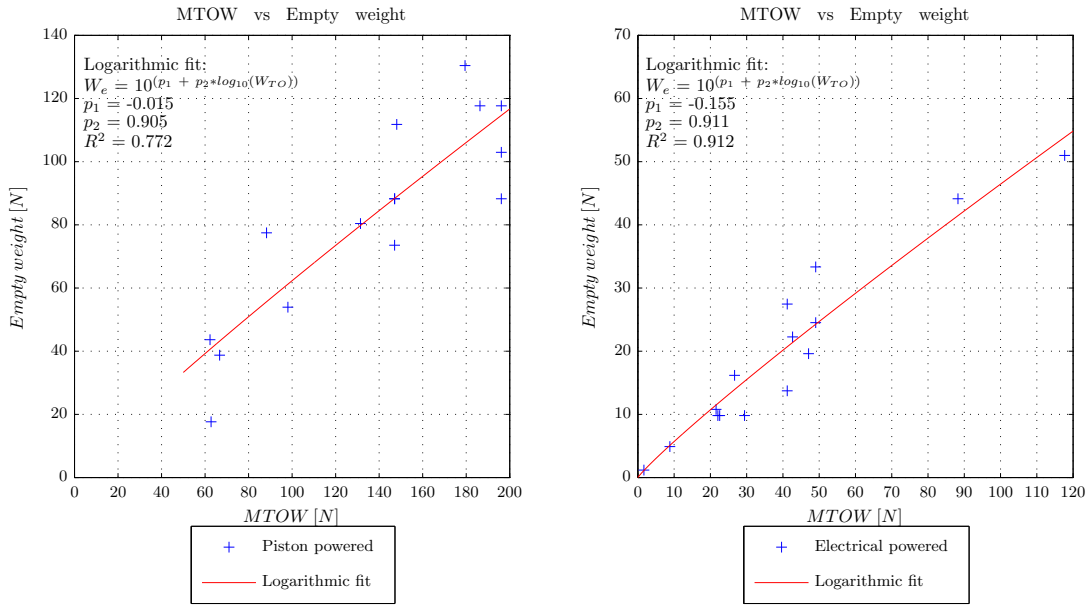

a: MTOW vs Empty weight fixed wing mini UAS with piston engine

b: MTOW vs Empty weight fixed wing mini UAS with electrical engine

Figure 4.10: MTOW vs Empty weight fixed wing mini UAS

From Figure 4.10a can be seen that there are no mini UASs with a MTOW less than 50 [N] having a piston engine. Mini UASs having a MTOW below 50 [N] are generally equipped with one electrical engines (see Figure 4.10b). A logarithmic fit was used to show the relationship between the empty weight and MTOW. In literature, logarithmic fits are often used to correlate statistical data of aircraft (Roskam[1]). The following equations represent the obtained relationships:

For a UAS with a piston engine the following relationship holds:

$$W_{e_{piston}} = 10^{-0.015+0.905\, log_{10}(W_{TO})} \tag{4.2}$$

The logarithmic relation for an electrical engine can be written as:

$$W_{e_{electrical}} = 10^{-0.155+0.911\,log_{10}(W_{TO})} \tag{4.3}$$

Note that Equation (4.2) is not a good representation of the actual relationship between empty weight and MTOW for piston powered UASs with a MTOW below 50 [N] ($\approx$ 5 [kg]). There is too little data available to get a good estimation for this regime. Since there was not more data available, this was the best approximation. The next step was to determine the payload weight.

Payload weight estimation

The payload weight can be seen as the MTOW minus the empty weight and the fuel weight. A payload can for example be a camera. Normally the payload weight is set by the requirements. Since no payload requirements were stated yet, the payload weight was also estimated based on historical data that was found from the created database. Figure 4.11 shows the relationship between the payload weight and MTOW, based on this data. Again this relationship is shown for both piston powered UASs and electrical powered UASs.

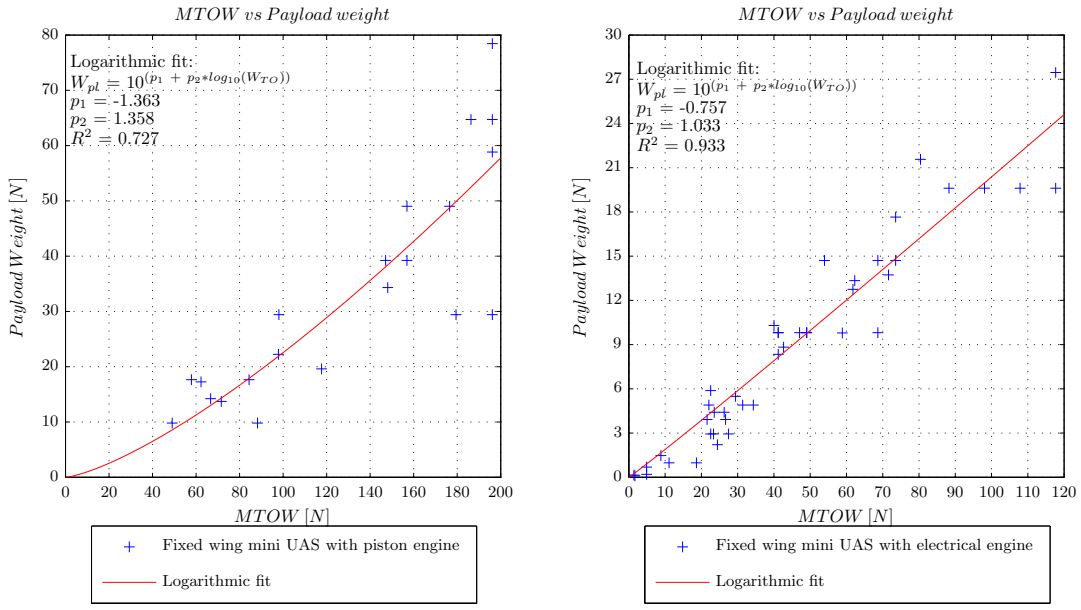

a: MTOW vs Payload weight fixed wing mini UAS with piston engine

b: MTOW vs Payload weight fixed wing mini UAS with electrical engine

Figure 4.11: MTOW vs Payload weight fixed wing mini UAS

From Figure 4.11 can be seen that for electrical powered UASs the logarithmic fit gives a good representation of the relation between the payload weight and the

MTOW. For piston powered UASs the fit is less accurate. In equational form this relationship can be be written as:

$$W_{pl_{piston}} = 10^{-1.363+1.358\,log_{10}(W_{TO})} \tag{4.4}$$

The logarithmic relation for an electrical engine can be written as:

$$W_{pl_{electrical}} = 10^{-0.757+1.033\,log_{10}(W_{TO})} \tag{4.5}$$

Equation (4.4) and Equation (4.5) were used to get an idea about the common amount of payload weight for a certain MTOW. From these relations can be concluded that electrical powered UASs have a higher payload to MTOW ratio. This is important for the trade-off between piston- or electrical powered UAS. For the calculations further on, the payload weight was set to a fixed value. This was done in order to ensure a fair assessment of both engine options. For this UAS, a camera is the main payload of the UAS. The specifications of the Prosilica GC 2450 showed that it is able to meet the requirements (shown in Subsection 3.2.2). The weight of this camera was used to get an indication of the payload weight. It weighs 186 gram without lens[60]. A Tamron C-mount lens[76] that can be used on this camera weighs approximately 50 [grams]. In order to be on the safe side, a payload weight of 500 [grams] was assumed. Later on in the section on payload selection, it becomes clear if this initial payload weight estimation is sufficient. If not, it has to be revised. Next, the fuel weight was estimated.

Fuel weight derivation

The final unknown parameter of Equation (4.1) was the fuel weight. At this stage of the design it was still unknown what kind of engine was going to be used in the design. Therefore, first the engine had to be selected. In order to get an idea about the required engine power, the engine power of similar UASs was analyzed. Based on historical data from the database, Figure 4.12 was created.

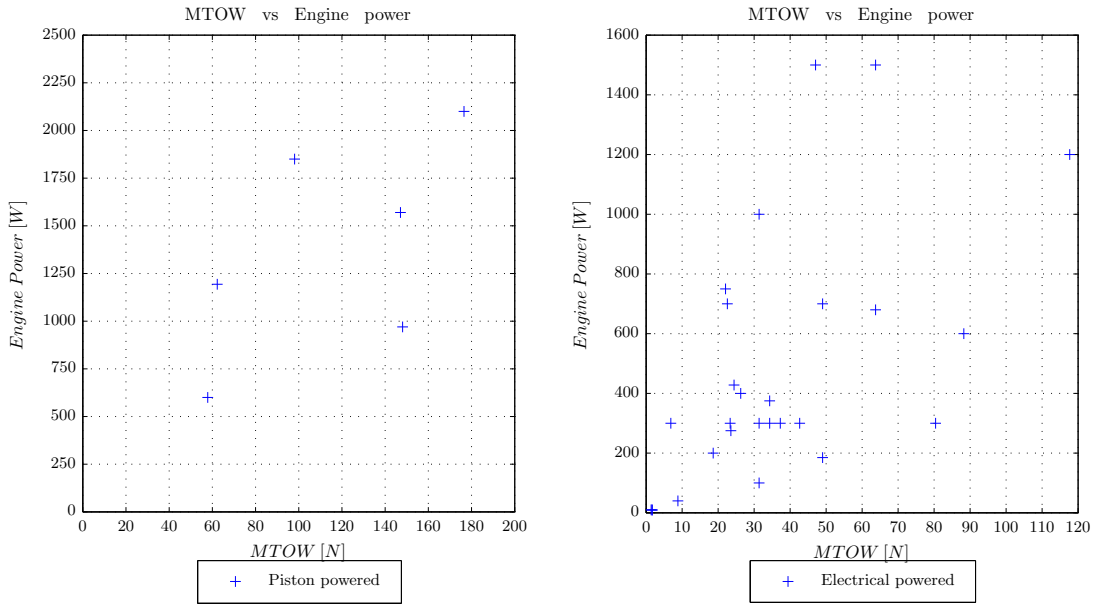

a: MTOW vs Engine power fixed wing mini UAS with piston engine

b: MTOW vs Engine power fixed wing mini UAS with electrical engine

Figure 4.12: MTOW vs Engine power fixed wing mini UAS

By comparing Figure 4.12a to Figure 4.12b the following can be concluded. Most UASs are equipped with an electrical engine. Generally piston powered UASs are equipped with a more powerful engine. Electrical engines can deliver smaller amounts of power and are therefore interesting for UASs that require a low amount of power. Overall can be seen that mini UASs have engines with power up to approximately 2500 [W]. Therefore this value was set as a maximum for the engine analysis. This analysis is performed in the next paragraph.

Engine analysis In Subsection 2.3.1 propulsion systems were already discussed. In Table 2.2 was already stated which engine type is most suited for what UAS type. In order to support the observations made in Subsection 2.3.1, various propulsion systems were included in a separate database. This data was used to create Figure D.1a through Figure D.3e that can be found in Appendix D.

From these figures can be seen that turbine engines were included and turboprop engines were not included. Turbine engines were included in order to get a complete overview of the available propulsion types, even though this propulsion type is not commonly used for mini UASs. Turboprop engines were not included in the database because this engine type is rare and therefore not enough data was available. Using Figure D.1a through Figure D.1e, it is possible to estimate the weight of an engine with a certain power. For now, the data presented in these figures is used to create an average power to weight ratio. This overview is shown in Table 4.5.

Table 4.5: Overview power to weight ratio mini UAS engines

Engine type:	**Power to weight ratio**, [W/N]:
2-stroke engine	225.31
4-stroke engine	157.10
Wankel engine	169.01
Electrical engine	527.74
Turbine engine	264.82

From Table 4.5 can be seen that the highest power to weight ratio can be produced by an electrical engine. In order to weigh all different options, not only the power to weight ratio was taken into account. Also (purchase) price and fuel consumption were taken into account. Therefore power versus price and power versus Fuel Consumption (FC) diagrams were created. In Figure D.2a through Figure D.2e the power to price diagrams are shown. Again an overview of the average ratios was created. These ratios are presented in Table 4.6.

Table 4.6: Overview power to price ratio mini UAS engines

Engine type:	**Power to price ratio**, [W/Euro]:
2-stroke engine	9.175
4-stroke engine	3.588
Wankel engine	1.689
Electrical engine	9.313
Turbine engine	1.383

From Table 4.6 can be seen that both 2-stroke and electrical engines have a high power to price ratio. Turbine engines on the other hand, are quite expensive. The cheapest turbine available costs about €2000,-[77]. Next, FC versus engine power plots were created. For all engines the FC is known in terms of [g/s], except for the electrical engines. Electrical engines are generally powered by batteries. Those batteries have a certain capacity and weight. Each electrical engine can produce a certain maximum power. From these parameters, the FC for electrical engines can be derived in terms of amount of battery weight that is required per second of flight, [g/s]. Equation (4.6) shows this derivation.

$$C_{p_{electrical\ engine}} = \frac{W_{battery}}{C_{battery}\,0.8}\,\frac{P_{e_{motor}}}{3600} \tag{4.6}$$

The FC in Equation (4.6) was calculated by using the battery parameters of the recommended electrical engine and battery combination which was provided by the manufacturer of the electrical engine. Taking into account that fully discharging the batteries is not desirable was also incorporated in Equation (4.6) (factor 0.8). Finally, FC versus engine power diagrams were created. These are shown in Figure D.3a through Figure D.3e. In order to compare the efficiency of the different

sized engines, the Brake Specific Fuel Consumption (BSFC) for every engine type was derived. The BSFC describes the fuel efficiency of an engine with respect to its power output. The resulting ratios are presented in Table 4.7.

Table 4.7: Overview brake specific fuel consumtion mini UAS engines

Engine type:	BSFC, [g/J]:
2-stroke engine	6.1157e-4
4-stroke engine	6.0445e-4
Wankel engine	4.1858e-4
Electrical engine	2.3166e-3
Turbine engine	1.6186e-3

From Table 4.7 can be seen that Wankel engines have the lowest SFC. The SFC of a 2-stroke and 4-stroke engines is approximately equal. Electrical engines have a much higher SFC. In calculating the battery SFC, the weight of the battery casing was already included in the total weight of the fuel. The other calculations were conducted without including the weight of a fuel tank and other additional systems.

From this paragraph can be concluded that 2-stroke engines and electrical engines are most favorable for the UAS design. From the last part of Section 4.2 was already observed that most UASs of the mini UAS class are equipped with these engine types. In order to get an idea about the impact of a piston engine and electrical engine on the total weight of the UAS, the fuel weight for both engines was estimated. Using these fuel weights in combination with Equation (4.2) and Equation (4.3), an engine choice was derived. First, the required amount of fuel for an electrical- and piston powered UAS was determined.

Fuel weight derivation electrical powered propeller aircraft based on range In this paragraph the Brequet range equation[4] was derived for an electrical powered propeller aircraft in steady symmetric flight. For the electrical powered UAS a range of at least 4500 [m] is required (see Section 3.4). Using Brequet's range equation with electrical current as fuel flow and battery capacity as fuel weight ultimately the fuel weight could be determined. Brequet's range equation was derived using the method of Dennis Trips[78]. The derivation of the fuel weight, based on the range requirement is presented in Section E.1 of Appendix E. The result is shown in Equation (4.7).

$$(C_1 - C_2) = \frac{R\left(\frac{C_D}{C_L}\frac{W_{TO}}{\eta_{tot}\,U_{e_{motor}}} + \frac{I_{e_{subsystems}}}{V_\infty}\right)}{3600} \tag{4.7}$$

In order to get a low fuel weight, C_L/C_D must be maximized. The second term of Equation (4.7) can be minimized by maximizing V_∞. V_∞ is limited by the required maximum velocity and therefore C_L/C_D must be maximized.

$(C_L/C_D)_{max}$ can be found by using the following derivation:

$$0 = \frac{d\left(\frac{C_L}{C_D}\right)}{d\,C_L} \tag{4.8}$$

with:

$$C_D = C_{D_0} + \frac{C_L^2}{\pi\,A\,e} \tag{4.9}$$

becomes:

$$\frac{d\left(\frac{C_L}{C_{D_0}+\frac{C_L^2}{\pi\,A\,e}}\right)}{d\,C_L} = \frac{\pi\,A\,e\,(C_{D_0}\,\pi\,A\,e + C_L^2) - (C_L\,\pi\,A\,e)\,2\,C_L}{(C_{D_0}\,\pi\,A\,e + C_L^2)^2} = 0 \tag{4.10}$$

Rewriting Equation (4.10):

$$0 = \frac{C_{D_0} - \frac{C_L^2}{\pi\,A\,e}}{\left(C_{D_0} - \frac{C_L^2}{\pi\,A\,e}\right)^2} \tag{4.11}$$

becomes:

$$0 = C_{D_0} - \frac{C_L^2}{\pi\,A\,e} \tag{4.12}$$

Combining Equation (4.9) and Equation (4.12):

$$C_D = 2\,C_{D_0} \tag{4.13}$$

Rewriting Equation (4.12) results in:

$$C_L = \sqrt{C_{D_0}\,\pi\,A\,e} \tag{4.14}$$

Combining Equation (4.13) and Equation (4.14) leads to:

$$\left(\frac{C_L}{C_D}\right)_{max} = \frac{\sqrt{C_{D_0}\,\pi\,A\,e}}{2\,C_{D_0}} \tag{4.15}$$

In order to be able to determine $(C_L/C_D)_{max}$, the parasite drag (zero lift drag), C_{D_0}, and the power consumption of the other subsystems needed to be determined. The drag derivation is presented in Section 4.4. In Section 4.5 the resulting fuel weight is presented.

Fuel weight derivation electrical powered propeller aircraft based on endurance
In order to determine the required amount of loiter fuel for a loiter period of at least 30 minutes (as stated in Section 3.4), Brequet's endurance equation[4] was derived for an electrical powered propeller aircraft in steady symmetric flight. Using Brequet's equation with electrical current as fuel flow and battery capacity as fuel weight again, the fuel weight was determined. Brequet's endurance equation was derived using the method of Dennis Trips[78] again. In Section E.2 of Appendix E the derivation of this equation is presented. The result is shown in Equation (4.16).

$$(C_1 - C_2) = E \frac{\sqrt{\frac{C_D^2}{C_L^3} \frac{2\,W_{TO}^3}{\rho\,S_{ref}}} + I_{e_{subsystems}}\,\eta_{tot}\,U_{e_{motor}}}{3600\,\eta_{tot}\,U_{e_{motor}}} \tag{4.16}$$

In order to get a low fuel weight, C_L^3/C_D^2 must be maximized. The second term of Equation (4.16) can be minimized by ensuring a low electrical current of the subsystems.

$(C_L^3/C_D^2)_{max}$ was found by using the same procedure that was applied in Equation (4.8). This resulted in:

$$C_{D_i} = 3\,C_{D_0} \tag{4.17}$$

and therefore:

$$C_D = 4\,C_{D_0} \tag{4.18}$$

The following lift coefficient was obtained:

$$C_L = \sqrt{3\,C_{D_0}\,\pi\,A\,e} \tag{4.19}$$

Combining Equation (4.18) and Equation (4.19) leads to:

$$\left(\frac{C_L^3}{C_D^2}\right)_{max} = \frac{(3\,C_{D_0}\,\pi\,A\,e)^3}{4\,C_{D_0}^2} \tag{4.20}$$

In order to be able to determine $(C_L^3/C_D^2)_{max}$, the parasite drag (zero lift drag), C_{D_0}, and the power consumption of the other subsystems needed to be determined. The drag derivation is presented in Section 4.4. In Section 4.5 the resulting fuel weight is presented.

Fuel weight derivation piston engine powered propeller aircraft based on range This paragraph describes the required amount of fuel that is needed to meet the range requirements. A range of at least 4500 [m] is required. The Brequet range equation[4] was used in determining the fuel weight. It is presented in Equation (4.21).

$$R = \left(\frac{\eta_p}{g\, c_p}\right)_{cruise} \left(\frac{L}{D}\right)_{cruise} ln\left(\frac{W_{before\,cruise}}{W_{after\,cruise}}\right) \tag{4.21}$$

Equation (4.21) assumes that the UAS is in leveled cruise flight (not accalerating). η_p was assumed to be 0.7 in cruise. This value was obtained from the aircraft design slides of Melkert[79]. c_p was found from Table 4.7 to be equal to $6.1157e^{-7}$ [kg/J]. As was stated in the paragraph about the required fuel weight for an electrical powered propeller aircraft based on range, the lowest fuel weight is achieved by maximizing C_L/C_D. Maximizing C_L/C_D is discussed in Section 4.5. The remaining unknown parameters of Equation (4.21) are derived in Section 4.4. In Section 4.5 the resulting fuel weight is presented.

Fuel weight derivation piston engine powered propeller aircraft based on endurance Besides the required cruise period of the UAS, also a loiter period of at least 30 minutes is required. The Brequet endurance equation[4] was used in determining the fuel weight. It is presented in Equation (4.22). This equation uses the same assumptions as in Subsection 4.3.2 ($L = W$ and $P_A = P_R = DV_\infty$).

$$E = \left(\frac{\eta_p}{V\, g\, c_p}\right)_{loiter} \left(\frac{L}{D}\right)_{loiter} ln\left(\frac{W_{before\,loiter}}{W_{after\,loiter}}\right) \tag{4.22}$$

η_p was assumed to be 0.6 in loiter. This value was again obtained from the aircraft design slides of Melkert[79]. c_p was assumed to be equal to $6.1157e^{-7}$ [kg/J]. In this case again fuel weight was optimized by maximizing (C_L^3/C_D^2). The method that was used in maximizing (C_L^3/C_D^2) is discussed in Section 4.5. The final unknown parameter of Equation (4.21), the lift over drag ratio, is derived in Section 4.4. In Section 4.5 the resulting fuel weight is presented.

This concludes the section on UAS take-off weight buildup. The next section discusses the drag components that were required for the fuel weight estimation.

4.4 Drag components

At subsonic speeds drag is build up from zero-lift/parasite drag, C_{D_0}, induced drag, C_{D_i} and wave drag, C_{D_w}. Since the maximum speed of the UAS will be far below Mach 1, the wave drag can be neglected since no shockwaves will occur at low subsonic speeds. The remaining drag coefficients are discussed in the upcoming subsections[1]. An overview of all drag components is presented in Figure 4.13.

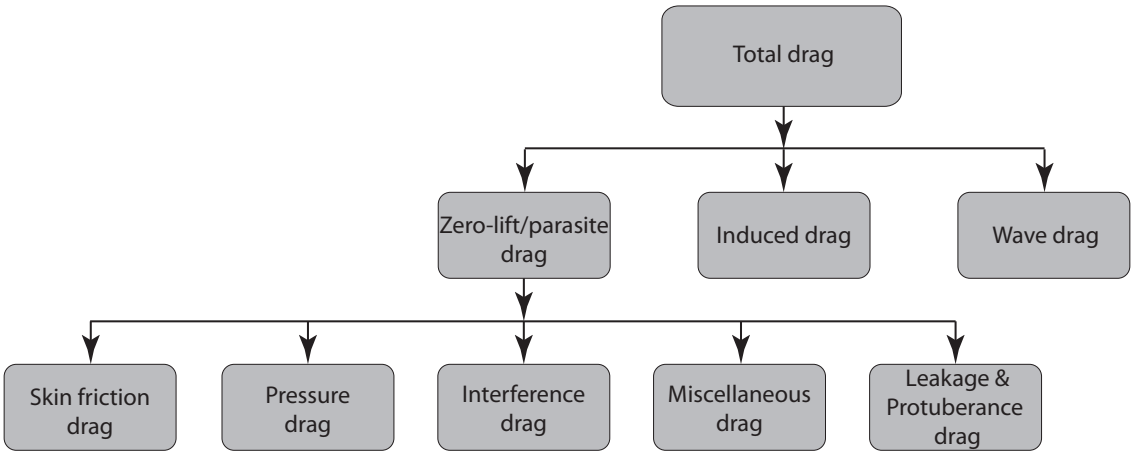

Figure 4.13: Overview drag components

4.4.1 Parasite drag

Components of drag due to viscosity do not contribute to lift. This type of drag is therefore considered to by parasitic in nature, parasite drag. The main components of parasite drag are:

- Drag due to skin friction, skin friction drag. It arises from the shearing stresses at the surface of a body due to viscosity.
- Drag due to pressure difference between the front and rear of an object, pressure drag. It is also produced by viscous effects, but not directly. The pressure distribution is modified by the presence of a boundary layer. In 2-D inviscid flow, the pressure on the forward and aft surfaces balance so that nog drag is produced. The effect of the boundary layers leads to an imperfect canceling of these pressures. This creates additional drag.
- Drag due to the interference of multiple bodies (horizontal and vertical tail e.g.), interference drag. Ideally, the pressure distributions on the intersecting bodies should complement each other's pressure distribution. In reality this is not always possible. This can result an increase in super-velocities increasing the drag.

[1] These subsections are mainly based on reference the aircraft design book of Kundu [2] and Raymer [3]

The minimum parasite drag occurs when shock waves and boundary-layer separation are at a minimum. Parasite drag can be calculated by using the component buildup method. This method estimates the parasite drag of each component of the aircraft. In equational representation the parasite drag is expressed as:

$$C_{D_0} = \frac{\sum_{i=1}^{n} C_{f_i} FF_i Q_i S_{wet_i}}{S_{ref_i}} + C_{d_{misc}} + C_{d_{L\&P}} \tag{4.23}$$

In the first part of Equation (4.23) all components are assumed to be a flat plate. In reality the components are never completely flat. Therefore a skin friction coefficient, C_f, is used to represent skin friction. In order to compensate for the actual form of a component, a component form factor, FF, is used. This factor accounts for super-velocities and pressure drag that occurs on the components due to their shape. Besides accounting for the actual form, also component interference factors, Q, need to be taken into account. These factors represent the interference between components. Finally, the actual area that is exposed to the flow needs to be determined. This area is also called the wetted area, S_{wet}.

Next to the above mentioned drag components there is also miscellaneous drag and leakage & protuberance drag. Miscellaneous drag is drag due to flaps, un-retracted landing gear or unfeathered props. Leakage drag is caused by the leakage through holes and gaps. Protuberance drag is created by antennas, lights, hinges e.g.

In the following paragraphs each component is worked out in detail.

Skin friction coefficient The flat-plate skin friction coefficient, C_f, depends upon the Reynolds number, R_e, Mach number and skin roughness. Assuming a linear flow, this coefficient can be expressed as:

$$C_f = \frac{1.328}{\sqrt{R_e}} \tag{4.24}$$

with:

$$R_e = \frac{V_{eff}\, l_c}{\nu} \tag{4.25}$$

In Equation (4.25), V_{eff} is the effective speeds over the object. For a wing e.g. this can be different to the flight speed when sweep is applied to the wing. l_c represents the length of the component (mean aerodynamic chord length, nose to tail length and engine length e.g.). Finally ν represents the kinematic viscosity of the flow.

Component form factor Form factors for subsonic-drag estimation are presented in Equation (4.26) through Equation (4.28).

$$FF_{wing\,and\,tail} = \left[1 + \frac{0.6}{(x/c)_m}\left(\frac{t}{c}\right) + 100\left(\frac{t}{c}\right)^4\right]\left[1.34M^{0.18}\left(cos\Lambda_m\right)^{0.28}\right] \tag{4.26}$$

$$FF_{fuselage} = \left(1 + \frac{60}{f_{ratio}^3} + \frac{f_{ratio}}{400}\right) \tag{4.27}$$

$$FF_{engine} = 1 + \left(\frac{0.35}{f_{ratio}}\right) \tag{4.28}$$

with:

$$f_{ratio} = \frac{l_c}{d} = \frac{l_c}{\sqrt{(4/\pi)A_{max}}} \tag{4.29}$$

Equation (4.26) can be used in order to determine the form factor for the wings and vertical tail. In this equation x/c is the chord wise location of the airfoil maximum thickness point. For most low speed airfoils, this equals 0.3. Λ_m refers to the sweep of the maximum thickness line in radians. The thickness over chord ratio is represented as t/c and is depending on the airfoil. f_{ratio} shows the fineness ratio which accounts for the increase in local velocities and pressure drag.

The form factor for the fuselage can be determined from Equation (4.27). In order to determine the form factor of the engine Equation (4.28) will be used.

Component interference factor The parasite drag is increased due to the mutual interference between components. The following factors are generally used for various components:

$$\begin{aligned} Q_{wing} &= 1.0 \\ Q_{tail_{clean\,vtail}} &= 1.03 \\ Q_{tail_{conventional}} &= 1.05 \\ Q_{fuselage} &= 1.0 \\ Q_{engine} &= 1.5 \end{aligned} \tag{4.30}$$

Wetted area The wetted area of an object is the area that is exposed to the flow. This area must be used in the drag calculations. For a wing and tail this area can be approximated by:

$$S_{wet_{wing\,and\,tail}} \approx 2\,(1 + 0.2\,\frac{t}{c})\,S_{ref} \tag{4.31}$$

The wetted area of the engine can be approximated by:

$$S_{wet_{engine}} \approx \pi R^2_{engine} + R_{engine}\,l_{engine} \tag{4.32}$$

In Equation (4.32) R_{engine} represents the radius of the engine and l_{engine} the length of the engine.

A reasonable approximation for the fuselage wetted area is:

$$S_{wet_{fuselage}} \approx 3.4 \left(\frac{S_{fuselage_{top}} + S_{fuselage_{side}}}{2} \right) \tag{4.33}$$

Miscellaneous drag coefficient

As mentioned previously, miscellaneous drag is drag due to for example flaps, un-retracted landing gear or unfeathered props. The miscellaneous drag due to flaps, $\Delta C_{D_{0_{flap}}}$, can be determined by:

$$\Delta C_{D_{0_{flap}}} = F_{flap}\,\frac{c_{flap}}{c}\,\frac{S_{flap}}{S_{ref}}\,(\delta_{flap} - 10) \tag{4.34}$$

In Equation (4.34), F_{flap} represents a coefficient equal to 0.0144 [-] for plain flaps and 0.0074 [-] for slotted flaps. c_{flap}/c, represents the flap chord over wing chord fraction. The flap area over wing area is expressed as S_{flap}/S_{ref}. δ_{flap} gives the flap angle in degrees.

The miscellaneous drag due to an un-retracted landing gear can be split up in the drag due to the wheel, tire and strut. This type of drag is often expressed in the drag to dynamic pressure ratio over frontal area ($(D/q)\,/A_{frontal}$). In equational form miscellaneous drag can be expressed as:

$$\Delta C_{D_{0_{lg\,and\,aft\,fus}}} = \frac{\sum_{i=1}^{n} \left(1.2\,\frac{(D/q)_i}{A_{frontal_i}}\,A_{frontal_i} \right) + \frac{(D/q)}{A_{max}}\,A_{max}}{S_{ref}} \tag{4.35}$$

The factor 1.2 in Equation (4.35) represents the interference factor between the landing gear components. The coefficient $(D/q)/A_{frontal}$ for the wheel, tire and strut were found from Raymer[3]. The $(D/q)/A_{frontal}$ coefficient for the upsweep of the aft fuselage is found from Equation (4.36).

$$\begin{aligned}\left(\frac{D/q}{A_{frontal}}\right)_{regular\,wheel\,and\,tire} &= 0.25\\ \left(\frac{D/q}{A_{frontal}}\right)_{round\,strut} &= 0.3\\ \left(\frac{D/q}{A_{max}}\right)_{upsweep\,aft\,fuselage} &= 3.83\,u^{2.5}\end{aligned} \tag{4.36}$$

In Equation (4.36), u represents the upsweep angle of the aft fuselage in radians.

During landing the propeller is stopped, creating extra miscellaneous drag. This drag can be estimated by:

$$\Delta C_{D_{0_{unfeathered\,props}}} = \frac{0.8\,\sigma\,A_{propeller\,disk}}{S_{ref}} \tag{4.37}$$

In Equation (4.37), σ displays the propeller solidity (ratio between the total blade area and the propeller disk area). The ratio 0.8 reflects the drag coefficient for a fixed pitch propeller.

Adding all the miscellaneous drag coefficients together becomes:

$$C_{D_{misc}} = \Delta C_{D_{0_{flap}}} + \Delta C_{D_{0_{landing\,gear}}} + \Delta C_{D_{0_{unfeathered\,props}}} \tag{4.38}$$

Leakage and protuberance drag coefficient

This drag type is difficult to predict by any method. Typically these drag increments are estimated as a percentage of the total parasite drag coefficient. For propeller aircraft generally 5% is used.

All coefficients of the parasite drag are known. In total the zero-lift/parasite drag coefficient becomes:

$$C_{D_0} = 1.05\left(\frac{\sum_{i=1}^{n} C_{f_i}\,FF_i\,Q_i\,S_{wet_i}}{S_{ref}} + C_{D_{misc}}\right) \tag{4.39}$$

4.4.2 Induced drag

The induced drag coefficient at small angles of attack (in cruise e.g.) is proportional to the square of the lift coefficient with a proportionality factor, K. This factor represents the drag that is caused by the lift that is produced. In classical wing theory the lift is assumed to be elliptical. In reality this is not the case. The extra drag due to the non-elliptical lift distribution and flow separation can be accounted for using, e, the Oswald span efficiency factor. Typically this factor is between 0.7 and 0.85. The lifting line theory gives an approximation of the induced drag using the Oswald span efficiency factor. Equation (4.40) shows this approximation.

$$C_{D_i} = K\, C_L^2 \tag{4.40}$$

with:

$$K = \frac{1}{\pi\, A\, e} \tag{4.41}$$

This theory assumes that the flow is incompressible, inviscid and steady. Low aspect ratio wings are also assumed in this theory. In Equation (4.40), C_L represents the lift coefficient of the wing. A, is the aspect ratio of the wing. The Oswald span efficiency factor can be estimated by using:

For a straight wing:

$$e_{straight\,wing} = 1.78\left(1 - 0.045\, A^{0.68}\right) - 0.64 \tag{4.42}$$

For a swept wing:

$$e_{swept\,wing} = 4.61\left(1 - 0.045\, A^{0.68}\right)(cos\Lambda_{LE})^{0.15} - 3.1 \tag{4.43}$$

with $\Lambda_{LE} > 30$ deg

In Equation (4.43), Λ_{LE} is the sweep angle of the wing leading edge.

Ground effect

When a wing is near the ground, the drag due to lift, K, can be reduced. This can be explained as a reduction in the induced downwash angle. Equation (4.44) calculates the factor that takes this effect into account. K must be multiplied with the following factor:

$$\frac{K_{effective}}{K} = \frac{33\,(h_g/b)^{1.5}}{1 + 33\,(h_g/b)^{1.5}} \tag{4.44}$$

in which h_g represents the height above the ground.

Flap effect

The effect of flaps on the parasite drag was already determined in Subsection 4.4.1. When flaps are applied, during landing for example, the lift is increased and therefore also additional lift induced drag is created. The additional lift induced drag can be calculated with:

$$\Delta C_{D_i} = k_f^2 \left(\Delta C_{L_{flap}}\right)^2 cos\Lambda_{\bar{c}/4} \tag{4.45}$$

In Equation (4.45), k_f is equal to 0.14 for full-span slaps and 0.28 for half-span flaps. Also in this equation $\Delta C_{L_{flap}}$ represents the incremental lift coefficient due to the flap. This increment can be calculated from the difference between maximum clean lift coefficient, $C_{L_{max\,clean}}$, and the maximum landing lift coefficient, $C_{L_{max\,landing}}$ since the platform is changing from a clean configuration to a landing configuration. $\Lambda_{\bar{c}/4}$ displays the sweep at a quarter of the mean aerodynamic chord.

All coefficients of the induced drag are known. In total the induced drag coefficient becomes:

$$C_{D_i} = K\,\frac{K_{effective}}{K}\,C_L^2 + \Delta C_{D_i} \tag{4.46}$$

4.4.3 Total drag coefficient

The total drag coefficient, C_D can be written as:

$$C_D = C_{D_0} + C_{D_i} \tag{4.47}$$

Implementing Equation (4.39) and Equation (4.46) results in:

$$C_D = 1.05\left(\frac{\sum_{i=1}^{n} C_{f_i}\,FF_i\,Q_i\,S_{wet_i}}{S_{ref_i}} + C_{D_{misc}}\right) + K\,\frac{K_{effective}}{K}\,C_L^2 + \Delta C_{D_i} \tag{4.48}$$

4.4.4 Drag estimation for preliminary design

In the early stages of the design, some assumptions are made in order to be able to estimate the drag. Usually statistics are used for these estimations. This was done because the dimensions of the platform were not known yet. Equation (4.48) was used as a starting point. First, the zero-lift/parasite drag of the wing were estimated. After that the induced drag estimation is discussed.

Zero-lift/parasite drag estimation In estimating the zero-lift/parasite drag; miscellaneous drag, leakage drag and protuberance drag were estimated to be a fraction of the total amount of zero-lift/parasite drag. This was done because at this point it is still unknown if a landing gear, flaps etc. are used. The zero-lift/parasite drag is estimated as follows:

$$C_{D_0} = \frac{f}{S_{ref}} = \frac{f}{W_{TO}} \frac{W_{TO}}{S_{ref}} \tag{4.49}$$

with:

$$f = C_f \, FF \, Q \, S_{wet} \tag{4.50}$$

In Equation (4.50), f, represents the equivalent parasite drag area. Using empirical data, f can be related to the wetted area of the aircraft. This is done by using a logarithmic relation. The form of this equation depends on the smoothness and streamlining of the design, represented by C_f. From Equation (4.24) and Equation (4.25) this factor was determined. The required flight speed was derived from Section 3.4. The mean aerodynamic chord, which is also used in Equation (4.25), of the wing is not yet known. Therefore C_f had to be assumed. In a later stage of the design this factor is verified. C_f was assumed to be equal to 0.002 [-]. The following expressions are used to determine the equivalent drag area and were based on the aircraft design book of Roskam[1].

$$log_{10} \, f_{sqft} = a + b \, log_{10} \, S_{wet_{sqft}} \tag{4.51}$$

with $a = -2.6990$ and $b = 1$. And:

$$log_{10} \, S_{wet_{sqft}} = c + d \, log_{10} \, W_{TO_{lb}} \tag{4.52}$$

with $c = 1.2362$ and $d = 0.4319$.

Rewriting Equation (4.52) becomes:

$$S_{wet_{sqft}} = 10^{1.2362+0.4319\, log_{10}\, W_{TO_{lb}}} \tag{4.53}$$

Implementing $S_{wet_{sqft}}$ in Equation (4.51) gives the following relation:

$$f_{sqft} = 10^{-2.6990+log_{10}\, S_{wet_{sqft}}} \tag{4.54}$$

Equation (4.54) was used to solve Equation (4.49). Besides the equivalent drag area that was presented in Equation (4.54), also the MTOW, W_{TO} was required. The maximum take-off weight was obtained from the wing loading, W_{TO}/S_{ref}. Rewriting the lift equation, the wing loading for take-off and landing could be derived:

$$\frac{W_{TO}}{S_{ref}} = \frac{1}{2}\, C_{L_{max}}\, \rho\, V_{stall}^2 \tag{4.55}$$

According to Melkert[79] an appropriate $C_{L_{max}}$ for home-build aircraft is 1.5 [-]. This maximum lift coefficient is rather high for a UAS therefore a $C_{L_{max}}$ of 1.2 [-] was chosen. Using this lift coefficient it was possible to derive a wing loading of approximately 36.77 $[N/m^2]$. At stall speed, the wing loading has the lowest value. The lowest wing loading value is the limiting value for the design (this is shown in Section 4.6).

Next, the obtained wing loading was used to derive the MTOW, W_{TO}. In order to derive this parameter, S_{ref} must be known. This value was based on reference aircraft. Using the created database, the reference area and MTOW of piston and electrical powered UASs was derived. An overview of those values is presented in Table 4.8.

Table 4.8: Overview derived reference area and MTOW piston and electrical powered UASs

Parameter	Symbol	Piston powered	Electrical powered	Unit
Reference area	S_{ref}	0.5867	0.4567	$[m^2]$
MTOW	W_{TO}	21.5772	16.7961	[N]

At stall, take-off and landing it is assumed that C_L will have the highest value. At those phases of the flight the highest parasite drag is expected. Using the obtained values from Equation (4.53) and Equation (4.54) in combination with Equation (4.49) results in a parasite drag estimated for both piston powered and electrical powered UASs. The results are presented in Table 4.9.

Table 4.9: Overview derived parasite/zero-lift drag coefficient piston and electrical powered UASs

Parameter	Symbol	Piston powered	Electrical powered	Unit
Parasite/zero-lift drag	C_{D_0}	0.0108	0.0124	[-]
Parasite/zero-lift drag with 10% increase	C_{D_0}	0.0119	0.0137	[-]

From Table 4.9 can be noticed that the parasite/zero-lift drag with a 10% increase was also presented. An increase of parasite/zero-lift drag with a factor of 10% was included in order to incorporate the miscellaneous drag, leakage drag and protuberance drag that was not yet included in the drag estimation. Next, the induced drag had to be estimated.

Induced drag estimation The induced drag was estimated by using Equation (4.40), without including the ground effect and flap effect. This results in the following expression:

$$C_{D_i} = \frac{C_L^2}{\pi\, A\, e} \tag{4.56}$$

From Equation (4.56) can be seen that the aspect ratio, A, was required to determine the induced drag. This aspect ratio was in first instance assumed according to the reference aircraft. From the database was derived that an aspect ratio of 7.5 is most suitable for this UAS type. The Oswald span efficiency factor was estimated to be equal to $e = 0.8$ in this phase of the design. All required parameters of Equation (4.56) were known at this point. Next, the total drag was estimated.

Total drag estimation Combing the parasite/zero-lift, Equation (4.49), and induced drag, Equation (4.56), the total drag equation becomes:

$$C_D = \frac{f}{W_{TO}} \frac{W_{TO}}{S_{ref}} + \frac{C_L^2}{\pi\, A\, e} \tag{4.57}$$

Varying C_L in Equation (4.57) from 0 to 2 resulted in the so called lift-drag polar. This polar is presented in Figure 4.14. The polar for both piston powered and electrical powered UASs is shown.

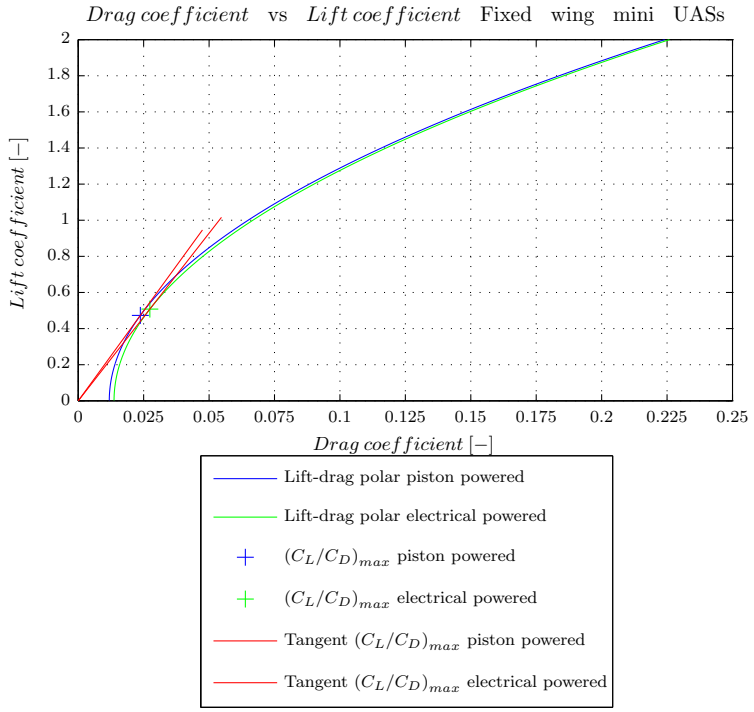

Figure 4.14: Initial *Lift-Drag* polar fixed wing mini UAS

In the next section is explained how the results of this subsection were used in determining the performance and initial take-off weight of the UAS.

4.5 Rough performance analysis and initial weight estimation

In Section 4.3 all components adding up to the maximum take-off weight of the UAS were discussed. Section 4.4 described the drag estimation for the UAS. In this section, the results and derived equations, that were discussed in those sections, were used to determine the initial MTOW. First, the performance of the UAS was analyzed. From this analysis the required amount of fuel was determined. From that moment on all weight fractions are known and an initial MTOW estimation was performed.

4.5.1 UAS performance analysis

For low subsonic propeller driven aircraft in steady symmetric flight the velocity, drag and required power were derived according to Ruijgrok[4] as follows:

$$V(i) = \sqrt{\frac{W_{TO}}{S_{ref}} \frac{2}{\rho} \frac{1}{C_L(i)}} \tag{4.58}$$

From the lift and drag equations the drag was estimated as follows:

$$D(i) = \frac{C_D(i)}{C_L(i)} W_{TO} \tag{4.59}$$

The required power is derived by combining Equation (4.58) and Equation (4.59). This results in:

$$P_r(i) = D\,V = W_{TO}\sqrt{\frac{W_{TO}}{S_{ref}} \frac{2}{\rho} \frac{C_D^2(i)}{C_L^3(i)}} \tag{4.60}$$

From Equation (4.58) through Equation (4.60) can be seen that C_D and C_L are changing. The varying C_D can be obtained by varying C_L in Equation (4.57) from 0 to 2. This was also done in Subsection 4.4.4 in order to obtain the drag polar (see Figure 4.14). In this section it was used to determine the drag and required power at varying velocities. The resulting diagrams are presented in Figure 4.16 and Figure 4.15.

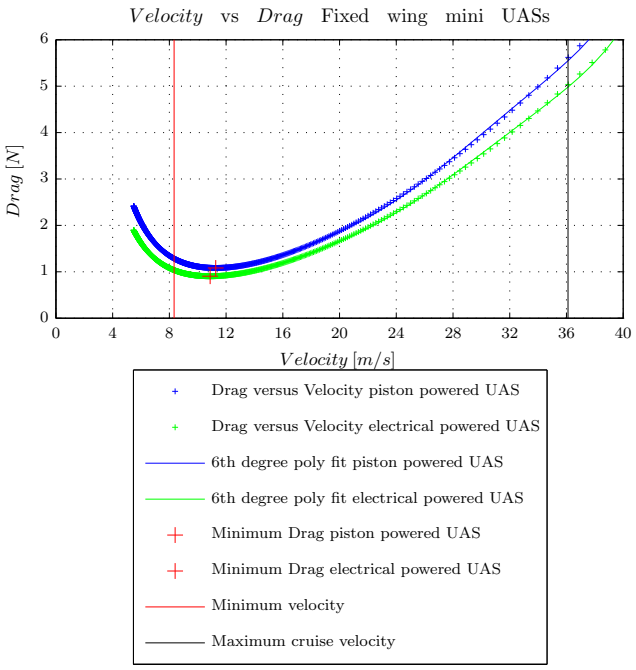

Figure 4.15: Initial Velocity vs Drag diagram fixed wing mini UAS

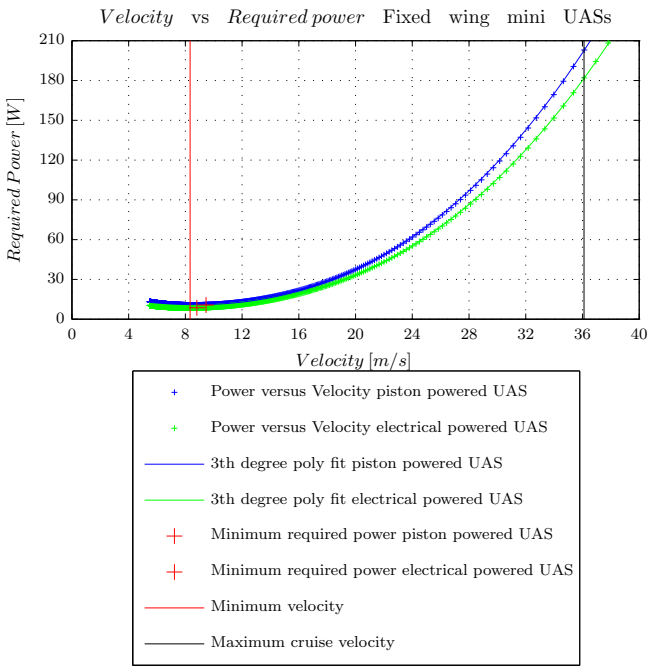

Figure 4.16: Initial Velocity vs Power diagram fixed wing mini UAS

From Figure 4.15 and Figure 4.16 can be seen that minimum drag and minimum required power are shown for both piston- and electrical powered UASs. Minimum drag occurs at an angle of attack for which C_L/C_D is maximum. The point of minimum drag is achieved during cruise at a certain velocity. The velocity corresponding with minimum drag corresponds to the condition $\frac{d\,D}{d\,V} = 0$. This becomes:

$$V = \sqrt{\frac{W_{TO}}{S_{ref}} \frac{2}{\rho} \frac{1}{C_L}} \tag{4.61}$$

From Equation (4.14) was found that for the range equation $C_L = \sqrt{C_{D_0}\,\pi\,A\,e}$. Implementing this in Equation (4.61) represents the velocity at which the drag is minimal. This can be presented as follows:

$$V_{D_{min}} = \sqrt{\frac{W_{TO}}{S_{ref}} \frac{2}{\rho} \frac{1}{\sqrt{C_{D_0}\,\pi\,A\,e}}} \tag{4.62}$$

The drag at $V_{D_{min}}$ was derived from the equation for drag in the following way:

$$D = \frac{1}{2}\,\rho\,S_{ref}\,C_D\,V^2 \tag{4.63}$$

From Equation (4.14) was found that for the range equation $C_D = 2\,C_{D_0}$. Using this and Equation (4.62) results in:

$$D_{min} = 2\,W_{TO}\,\sqrt{\frac{C_{D_0}}{\pi\,A\,e}} \tag{4.64}$$

Minimum required power occurs at an angle of attack for the maximum climb factor C_L^3/C_D^2. The point of minimum required power is achieved during loiter at a certain velocity. The velocity for which the required power is minimum corresponds to the condition $\frac{d\,P_r}{d\,V} = 0$. This was again derived from the lift equation (see Equation (4.61)). From Equation (4.19) was found that for the endurance equation $C_L = \sqrt{3\,C_{D_0}\,\pi\,A\,e}$. Implementing this in Equation (4.61) represents the velocity at which the required power is minimal. This becomes:

$$V_{P_{r_{min}}} = \sqrt{\frac{W_{TO}}{S_{ref}}\,\frac{2}{\rho}\,\frac{1}{\sqrt{3\,C_{D_0}\,\pi\,A\,e}}} \tag{4.65}$$

The required power at $V_{P_{r_{min}}}$ can be derived in the following way:

$$P_r = D\,V \tag{4.66}$$

Using the drag equation this becomes:

$$P_r = \frac{1}{2}\,\rho\,S_{ref}\,C_D\,V^3 \tag{4.67}$$

From Equation (4.18) was found that for the endurance equation $C_D = 4\,C_{D_0}$. Using this and Equation (4.65) leads to:

$$P_{r_{min}} = \frac{4}{3}\,W_{TO}\,\sqrt{\frac{W_{TO}}{S_{ref}}\,\frac{2}{\rho}\,\sqrt{\frac{3\,C_{D_0}}{(\pi\,A\,e)^3}}} \tag{4.68}$$

Using Equation (4.62), Equation (4.64), Equation (4.65) and Equation (4.68) it was possible to determine the velocity at which the drag is minimal, the minimum drag, the velocity at which the required power is minimal and the minimum required power. The results are presented in Table 4.10.

Table 4.10: Overview calculated minimum drag and required power for piston and electrical powered UASs

Parameter	Symbol	Piston powered	Electrical powered	Unit
Min drag velocity	$V_{D_{min}}$	11.27	10.87	[m/s]
Min drag	D_{min}	1.13	0.97	[N]
Min required power velocity	$V_{P_{r_{min}}}$	9.46	8.81	[m/s]
Min required power	$P_{r_{min}}$	11.09	8.906	[W]

From Table 4.10 can be seen that the cruise velocity at which the drag is minimal is not near the required cruise speed of 36.11 [m/s] (130 [km/h]). In order to determine the resulting drag for both piston- and electrical powered UAS, a sixth order degree fit was used to estimate the relation between the velocity and drag. Figure 4.15 shows this fit. Using this fit, the drag at cruise speed was estimated to be 5.55 [N] for piston powered UAS and 4.98 [N] for electrical powered UAS. The required power was estimated by using a third order degree fit on the relation between velocity and power. Figure 4.16 shows this fit. Using this fit, the required power at cruise was estimated to be 202.63 [W] for a piston powered UAS and 181.64 [W] for an electrical powered UAS. The optimum cruise velocity is attained while cruising back to the original loiter location after the high speed cruise (130 [km/h]) has been completed (see second mission profile in Subsection 4.3.1). The next step was to determine the required amount of fuel for both piston- and electrical powered UASs in order to complete the initial weight estimation.

Fuel weight electrical powered UAS In order to compare piston powered UASs with electrical powered UASs, the power drained by the subsystems must be excluded when comparing both UASs. It is expected that both UASs use the same subsystems and therefore an equal amount of power is drained by those systems. Therefore this has no impact on the fuel weight when comparing both UASs. The capacity based on the range equation, Equation (E.20), becomes:

$$C_{req\,cruise} = \frac{(R\,D)_{cruise}}{3600\,\eta_{tot}} \tag{4.69}$$

For loiter conditions also holds that power drained by the subsystems should not be incorporated in the calculations when comparing both UASs. The required capacity was derived from the endurance equation, Equation (E.41), and becomes:

$$C_{req\,loit} = \frac{(E\,D\,V)_{loit}}{3600\,\eta_{tot}} \tag{4.70}$$

For both equations η_{tot} was determined by using the following assumptions:

- Propeller efficiency = 85%.
- Engine speed controller efficiency = 97%.
- Engine efficiency = 90%.

This resulted in a η_{tot} of 74%. Combining Equation (4.69) and Equation (4.70) with the SFC found from Table 4.7, the battery weight could be derived as follows:

$$W_{fuel\,electrical} = 3600\, g\, C_{req}\, SFC \tag{4.71}$$

Equation (4.71) was used in determining the fuel weight for cruise, cruise back and loiter. Next the fuel weight for piston powered UASs was determined.

Fuel weight piston powered UAS For the piston powered UASs, the cruise fuel weight was derived from Equation (4.21). The result is as follows:

$$\frac{W_{before\,cruise}}{W_{after\,cruise}} = e^{\left(\frac{R_{cruise}}{\left(\frac{\eta_p}{g\,c_p}\right)_{cruise}\left(\frac{L}{D}\right)_{cruise}}\right)} \tag{4.72}$$

During loiter a different relation holds. The fuel weight was derived from Equation (4.22). The fuel weight based on this equation resulted in:

$$\frac{W_{before\,loiter}}{W_{after\,loit}} = e^{\left(\frac{E_{loit}}{\left(\frac{\eta_p}{V\,g\,c_p}\right)_{loiter}\left(\frac{L}{D}\right)_{loiter}}\right)} \tag{4.73}$$

For Equation (4.72) and Equation (4.73) the worst c_p (SFC) value for piston engines from Table 4.7 was selected. η_p was determined from the lecture series of Aircraft Design[79]. During cruise η_p was assumed to be 0.7 and during loiter 0.6. Combining all known parameters, the fuel weight for cruise, cruise back and loiter were determined.

Initial fuel weight Using Equation (4.71), Equation (4.72) and Equation (4.73); the fuel weight of both piston- and electrical powered UASs was determined. An overview of the results is shown in Table 4.11.

Table 4.11: Overview initial calculated fuel weight and (L/D) values for piston and electrical powered UASs

Parameter	Symbol	Piston powered	Electrical powered	Unit
Fuel weight cruise	$W_{cruise\ fuel}$	0.15	0.69	[N]
Fuel weight cruise back	$W_{cruise\ back\ fuel}$	0.03	0.12	[N]
Fuel weight loiter	$W_{loiter\ fuel}$	0.12	0.51	[N]
Lift over drag cruise	$(L/D)_{cruise}$	3.89	3.37	[-]
Lift over drag cruise back	$(L/D)_{cruise\ back}$	20.10	18.78	[-]
Lift over drag loiter	$(L/D)_{loiter}$	19.10	17.24	[-]

From Table 4.11 can be noticed that the fuel weight for piston powered UASs is significantly smaller than the fuel weight for electrical powered UASs. This can be explained by the fact that the fuel weight also includes the weight of the battery casing as well. This was also discussed in Subsection 4.3.2. Finally, it was possible to determine the initial MTOW. This is presented in the next paragraph.

Initial MTOW weight In Subsection 4.3.2 the MTOW buildup was discussed. In Equation (4.1) all MTOW components were presented. The empty weight was estimated by using Equation (4.2) and Equation (4.3) in combination with the initially determined MTOW for both UASs. The MTOW, W_{TO}, was found from Table 4.8. The second parameter of Equation (4.1) is the payload weight, W_{pl}. The payload weight was assumed to be 4.90 [N] ($\approx$ 0.5 [kg]). The last unknown parameter of Equation (4.1), the fuel weight, was derived in Subsection 4.5.1. The resulting fuel weights are presented in Table 4.11. Combining all parameters, it was possible to determine the initial MTOW weight. An overview of all parameters is presented in Table 4.12.

Table 4.12: Overview initial calculated MTOW parameters piston and electrical powered UASs

Parameter	Symbol	Piston powered	Electrical powered	Unit
Empty weight	W_e	15.57	7.71	[N]
Payload weight	W_{pl}	4.90	4.90	[N]
Total fuel weight	W_f	0.29	1.32	[N]
Total MTOW	W_{TO}	20.76	13.93	[N]
Initial MTOW	$W_{TO_{initial}}$	21.58	16.80	[N]

From Table 4.12 can be seen that the initial MTOW guess is not equal to the resulting total MTOW. The difference between these values had to be minimized in order to get an accurate MTOW approximation. Besides that, from Table 4.11 can also be seen that the L/D values are rather high for UASs of this size (above 15). Therefore it is decided to assume a $(L/D)_{max}$ of approximately 15 during loiter conditions. In the next subsection the MTOW convergence is discussed.

4.5.2 MTOW convergence

In order to minimize the difference between the initial MTOW guess and the resulting total MTOW, a Matlab optimization toolbox[80] is used. The convergence process was already presented in Figure 4.9 of Subsection 4.3.2. This optimization toolbox, fmincon, approximates at each major iteration the Hessian of the Lagrangian function using a quasi-Newton updating method. This is then used to generate a quadratic programming subproblem whose solution is used to form a search direction for a line search procedure. This subproblem can be solved using any quadratic programming algorithm. The solution is used to form a new iterate. During the optimization the upper bound of the MTOW has been constraint to 196 [N] (20 [kg]). This is the MTOW of UASs of the mini class.

As stated in the previous subsection, the $(L/D)_{max}$ was set to approximately 15 during loiter conditions. In order to accomplish this, the parasite/zero-lift drag for the piston powered UASs needed to be increased by 78%. For electrical powered UASs the parasite/zero-lift drag had to be increased by 60%. In a later stage of the design more detailed drag estimation will tell if this first estimate was right.

Next, the MTOW convergence procedure was performed. This resulted in a new approximation of the lift-drag polar and a revision of the performance analysis. The lift-drag polar is presented in Figure 4.17 and the revised performance analysis diagrams in Figure 4.18 and Figure 4.19.

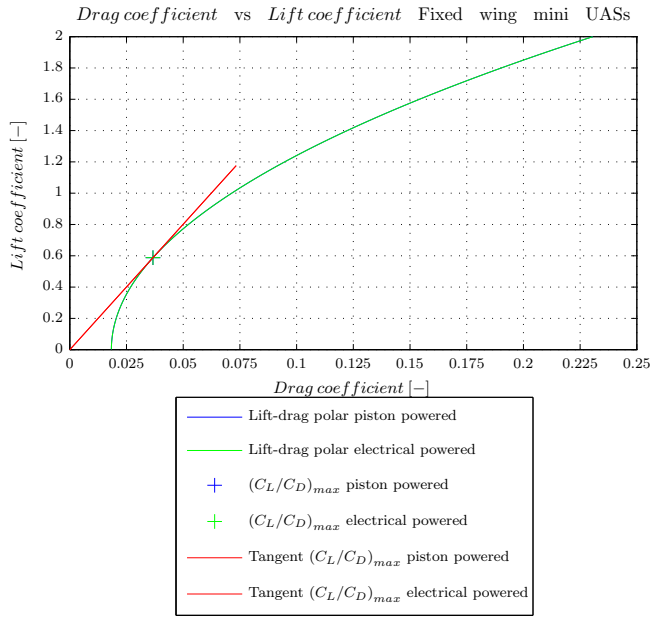

Figure 4.17: Lift-Drag polar for loiter $\frac{L}{D}$ of 15 for fixed wing mini UAS

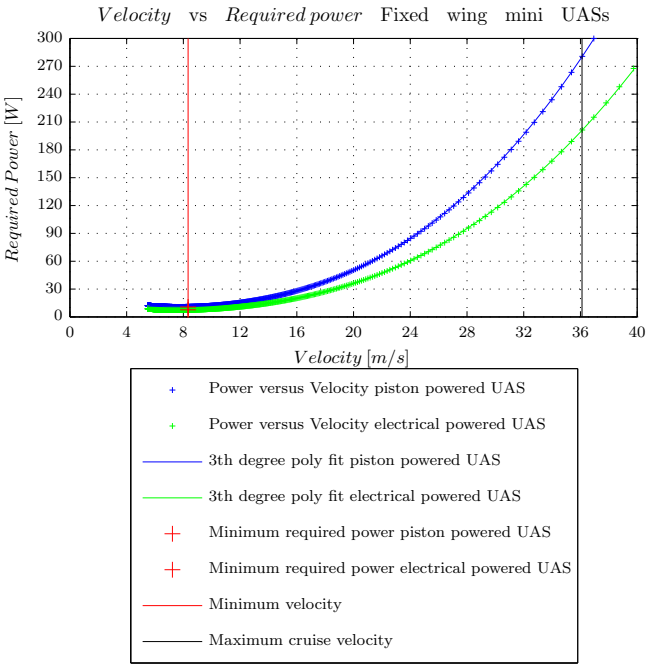

Figure 4.18: Velocity vs Power diagram for loiter $\frac{L}{D}$ of for 15 fixed wing mini UAS

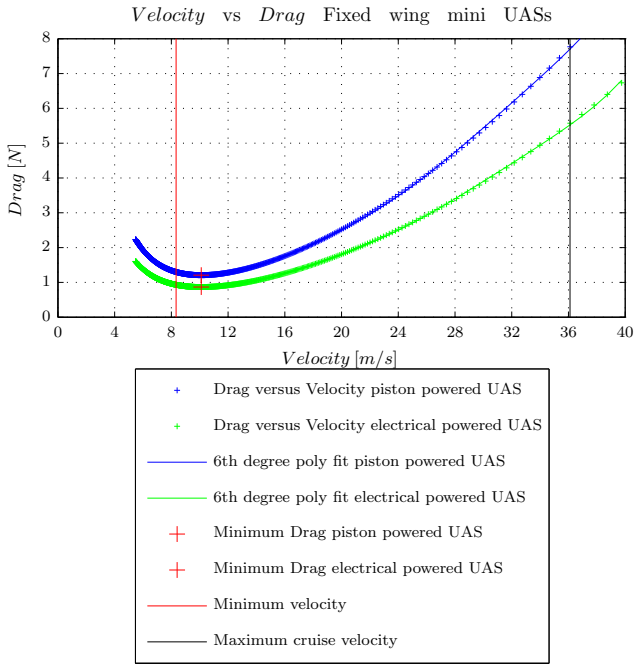

Figure 4.19: Velocity vs Drag diagram for loiter $\frac{L}{D}$ of 15 fixed wing mini UAS

The convergence procedure obviously resulted in new results for the MTOW buildup parameters. An overview of the results is presented in Table 4.13 and Table 4.14.

Table 4.13: Overview matched MTOW parameters piston and electrical powered UASs

Parameter	Symbol	Piston powered	Electrical powered	Unit
Empty weight	W_e	14.13	7.69	[N]
Payload weight	W_{pl}	4.90	4.90	[N]
Total fuel weight	W_f	0.35	1.30	[N]
Total MTOW	W_{TO}	19.38	13.90	[N]
Initial MTOW	$W_{TO_{initial}}$	19.38	13.90	[N]
Increased parasite/zero-lift drag	C_{D_0}	0.0183	0.0183	[-]
Reference area	S_{ref}	0.5269	0.3778	$[m^2]$

Table 4.14: Overview matched minimum drag and required power for piston and electrical powered UASs

Parameter	Symbol	Piston powered	Electrical powered	Unit
Cruise velocity	V_{cruise}	36.11	36.11	[m/s]
Cruise back velocity	$V_{D_{min}}$	10.11	10.11	[m/s]
Loiter velocity	$V_{P_{r_{min}}}$	8.33	8.33	[m/s]
Cruise drag	D_{cruise}	7.70	5.53	[N]
Cruise back drag	D_{min}	1.19	0.85	[N]
Loiter drag	D_{loit}	1.29	0.93	[N]
Required cruise power	$P_{r_{cruise}}$	280.22	201.00	[W]
Required cruise back power	$P_{r_{cruise\,back}}$	12.33	8.84	[W]
Required loiter power	$P_{r_{min}}$	11.10	7.96	[W]

From Table 4.13 can be seen that an electrical powered UAS design is significantly lighter than a piston powered UAS. Table 4.14 also shows that an electrical powered UAS experiences less drag and requires less power than a piston powered UAS. Electrical engines also have a much higher power to weight ratio (see Table 4.5). Also their power to price ratio is higher than piston engines (see Table 4.6). Another advantage of an electrical powered UAS is the higher payload to MTOW ratio. An electrical powered UAS can carry up to 50% more payload than a piston powered UAS (see Equation (4.4) and Equation (4.5)). From the reference UASs, mentioned in Section 4.2, was already concluded that most UASs are equipped with a single electrical engine. Therefore, it is not strange that the analysis performed in this section results in an electrical engine to be most favorable.

This concludes the subsection on initial MTOW convergence. In the next section, preliminary sizing is performed. This includes investigation of the results up until now. Note that this analysis proceeds with the electrical powered UAS design parameters.

4.6 Preliminary sizing

In this section, matching of all sizing requirements is performed. In order to match the requirements, a so called power loading (W/P) versus wing loading (W/S) diagram is constructed. Several values are required to produce this diagram. Ranges of appropriate values for the aspect ratio, A, and lift coefficient, C_L, are assumed. This is based on reference data and typical values. Although a range of lift coefficients is assumed, it is not yet clear whether the UAS will be fitted with high-lift devices. The W/P versus W/S diagram is constructed for five different cases; stall speed, landing, cruise back speed, loiter speed and climb. For climb, the aircraft can be sized for the climb rate as well as the climb gradient. The resulting graphs shows the design point and the limits of the UAS for the assumed values of A and C_L. Using this graph, an indication of the power loading can be obtained. Also can be checked if the wing loading, that was selected in Subsection 4.4.4, was chosen appropriate.

As the aircraft can be sized for many different requirements and situations, many different parameters have to be known or estimated. Every sizing method, like Torenbeek[81], Roskam[1] or Raymer[3] require different parameters. Based on the known parameters, it has been decided to use the sizing method as described in the lecture series of Aircraft Design[79]. This method is based on empirical data but it requires less parameters to be known (when comparing this method to the other methods). At this stage in the design process, the number of assumptions should be kept as low as possible, to keep every design option open for consideration.

4.6.1 Sizing for stall speed

First, the stall speed is considered. From the required minimum flight speed of 30 [km/h], the stall speed was derived. This minimum speed must be 15% higher than the stall speed (safety requirement). The stall speed, V_{st}, therefore needs to be 7.25 [m/s] (26.1 [km/h]). This case is simply evaluated by rewriting the formula for the lift force (see Equation (4.74)).

$$\left(\frac{W}{S}\right)_{Stall} = \frac{1}{2}\,\rho_{cruise\ altitude}\,C_{L_{max}}\,V_{st}^2 \tag{4.74}$$

From Equation (4.74) can be seen that the wing loading is a function of the lift coefficient. As this value is unknown at this point, a range of appropriate values is assumed ($1.2 < C_L < 1.8$)[79]. The obtained W/S values will form the first limits.

4.6.2 Sizing for landing

The W/S-value representing the landing-limit is also a function of the lift coefficient. Again a range of appropriate values is assumed ($1.2 < C_L < 1.8$)[79]. Furthermore, several constants have been assumed at this point. The landing distance, s_{land}, and the weight-ratio between landing and take-off, W_f, are required. The landing distance has assumed to be equal to $s_{land} = 50$ [m]. Since the UAS will be electrical powered it is assumed that the weight-ratio remains constant and therefore $W_f = 1$. Using equation 4.75 derived from Aircraft Design slides of Melkert[79], the second set of limits is obtained. Note that this equation is based on reference aircraft that have a much higher MTOW in comparison to the current UAS design. Later on in this section is shown that this landing-limit is not the overall limiting factor in the design. If, in another case, this limit is critical than it needs to be revised.

$$\left(\frac{W}{S}\right)_{Landing} = \frac{C_{L_{max}}\,\rho\,\frac{s_{land}}{0.5915}}{2W_f} \tag{4.75}$$

4.6.3 Sizing for cruise back

The third set of limits is based on the cruise back speed. From Subsection 4.3.2 was derived that in order to maximize the range during cruise back, C_L/C_D must be maximized. At $(C_L/C_D)_{max}$ the zero-lift/parasite drag equals the induced drag (see Equation (4.12)). This resulted in $C_L = \sqrt{C_{D_0}\,\pi\,A\,e}$ (see Equation (4.14)). This in combination with the lift equation results in an expression for wing loading that maximizes the range of a propeller aircraft. It also provides an estimation of the wing loading for minimum drag. It can be defined as:

$$\left(\frac{W}{S}\right)_{Cruise\,back} = \frac{1}{2}\,\rho_{cruise\,altitude}\,V^2_{cruise\,back}\,\sqrt{\pi\,A\,e\,C_{D_0}} \tag{4.76}$$

4.6.4 Sizing for loiter

In Subsection 4.3.2 was also derived that in order to optimize the loiter time, C_L^3/C_D^2 must be maximized. At $(C_L^3/C_D^2)_{max}$ the zero-lift/parasite drag equals three times the induced drag (see Equation (4.17)). This resulted in $C_L = \sqrt{3\,C_{D_0}\,\pi\,A\,e}$ (see Equation (4.19)). Again combining this with the lift equation results in an expression for wing loading that maximizes the loiter time. This formed the basis of the fourth set of limits. It can be defined as:

$$\left(\frac{W}{S}\right)_{Loit} = \frac{1}{2}\,\rho_{cruise\,altitude}\,V^2_{loit}\,\sqrt{3\,\pi\,A\,e\,C_{D_0}} \tag{4.77}$$

Equation (4.77) also represents the wing loading for minimum required power.

4.6.5 Sizing for climb rate

Although no climb requirements are given, by determining a reasonable climb rate, the required performance of the UAS can be determined more accurately. By taking into account the required operational altitude and mission, a climb rate of $RC = 5$ [m/s] was set as a minimum. Using the estimated zero-lift/parasite drag coefficient (see Table 4.9), the Oswald span efficiency factor (see Subsection 4.4.4) and propeller efficiency (see Subsection 4.5.1), the required power loading was derived. The power loading, W/P, can be expressed as a function of wing loading, W/S, in the following way:

$$\frac{P_r}{W} = \frac{C_D \, \frac{1}{2} \, \rho_{cruise\ altitude} \, V^3 \, S}{C_L \, \frac{1}{2} \, \rho_{cruise\ altitude} \, V^2 \, S} \tag{4.78}$$

This can be rewritten as:

$$\frac{P_r}{W} = \frac{C_D \, V}{C_L} \tag{4.79}$$

Using $V = \sqrt{\frac{W}{S} \frac{2}{\rho_{cruise\ altitude}} \frac{1}{C_L}}$ in combination with Equation (4.79) leads to:

$$\frac{P_r}{W} = \sqrt{\frac{W}{S} \frac{2}{\rho_{cruise\ altitude}} \frac{C_D^2}{C_L^3}} \tag{4.80}$$

From Equation (4.80) can be seen that maximum climb performance for a propeller driven aircraft can be achieved when C_L^3/C_D^2 is maximized. From Subsection 4.3.2 was found that at $(C_L^3/C_D^2)_{max}$, $C_L = \sqrt{3 \, C_{D_0} \, \pi \, A \, e}$ and $C_D = 4 \, C_{D_0}$. $(C_L^3/C_D^2)_{max}$ can be elaborated resulting in:

$$\left(C_L^3/C_D^2\right)_{max} = 1.8084 \, \frac{(A \, e)^{\frac{3}{2}}}{\sqrt{C_{D_0}}} \tag{4.81}$$

At normal climb angles, the climb rate is equal to:

$$RC = \frac{\eta_p \, P_{br}}{W} - \frac{P_r}{W} \tag{4.82}$$

Rewriting Equation (4.82) and using Equation (4.81) and Equation (4.80) leads to:

$$\left(\frac{W}{P}\right)_{Climb\,rate} = \frac{\eta_p}{RC + \sqrt{\frac{W}{S} \frac{2}{\rho_{cruise\ altitude}} \frac{1}{1.8084 \, \frac{(A \, e)^{\frac{3}{2}}}{\sqrt{C_{D_0}}}}}} \tag{4.83}$$

Equation (4.83) shows the fifth limit for the power loading versus wing loading diagram.

4.6.6 Sizing for climb gradient

Finally, the sizing for the climb gradient was performed. The climb gradient is the ratio between vertical and horizontal distance traveled. At normal climb angles the climb gradient is equal to the excess thrust divided by the weight of the UAS. The derivation of W/P as a function of W/S is shown in Equation (4.84).

$$\frac{RC}{V} = \frac{P_a - P_r}{W\,V} = \frac{\eta_p\,P_{br}}{W\,V} - \frac{D\,V}{W\,V} = \frac{\eta_p\,P_{br}}{W\,V} - \frac{C_D}{C_L} \tag{4.84}$$

Using $V = \sqrt{\frac{W}{S}\,\frac{2}{\rho_{cruise\ altitude}}\,\frac{1}{C_L}}$ in combination with Equation (4.84) results in:

$$\frac{RC}{V} = \frac{\eta_p\,P_{br}}{W\sqrt{\frac{W}{S}\,\frac{2}{\rho_{cruise\ altitude}}\,\frac{1}{C_L}}} - \frac{C_D}{C_L} \tag{4.85}$$

From Equation (4.85) can be seen that the climb gradient can be optimized by maximizing C_L/C_D. From Subsection 4.3.2 was found that at $(C_L/C_D)_{max}$, $C_L = \sqrt{C_{D_0}\,\pi\,A\,e}$ and $C_D = 2\,C_{D_0}$. $(C_L/C_D)_{max}$ can be elaborated resulting in:

$$\left(\frac{C_L}{C_D}\right)_{max} = 0.8862\sqrt{\frac{A\,e}{C_{D_0}}} \tag{4.86}$$

Rewriting Equation (4.85) and using Equation (4.86) leads to:

$$\left(\frac{W}{P}\right)_{Climb\ gradient} = \frac{\eta_p}{\left(\frac{RC}{V_{cruise\ back}} + \frac{1}{0.8862\sqrt{\frac{A\,e}{C_{D_0}}}}\right)\sqrt{\frac{W}{S}\,\frac{2}{\rho_{cruise\ altitude}}\,\frac{1}{\sqrt{C_{D_0}\,\pi\,A\,e}}}} \tag{4.87}$$

Equation (4.87) is function of the aspect ratio, A and the wing loading, W/S. The power loading, W/P, can also be derived as a function of $C_{L_{max}}$ and W/S. In order to get this relationship, Equation (4.85) is rewritten into:

$$\left(\frac{W}{P}\right)_{Climb\ gradient} = \frac{\eta_p}{\sqrt{\frac{W}{S}\,\frac{2}{\rho_{cruise\ altitude}}\,\frac{1}{C_{L_{max}}}}\left(\frac{RC}{V_{cruise\ back}} + \frac{2\,C_{D_0}}{C_{L_{max}}}\right)} \tag{4.88}$$

Both Equation (4.87) and Equation (4.88) represent the climb gradient limits for the power loading.

4.6.7 W/P vs W/S diagram

At this point all wing loading and power loading limits are known. The next step is to present the limits in a diagram. Equation (4.76), Equation (4.77), Equation (4.83), Equation (4.87), and Equation (4.88) are all combined in this diagram. From these equations can be seen that the aspect ratio, A, Oswald efficiency factor, e, the cruise speed, V_{cruise}, cruise back speed, $V_{cruise\,back}$, the loiter speed, V_{loit}, and the parasite/zero-lift drag, C_{D_0}, are also required in order to solve the equations. In Paragraph 4.4.4, A and e were discussed. The cruise, cruise back and loiter speed were determined in Subsection 4.5.1. Table 4.13 shows the estimated parasite/zero-lift drag.

Finally, it was possible to create a W/P versus W/S diagram. This diagram is presented in Figure 4.20.

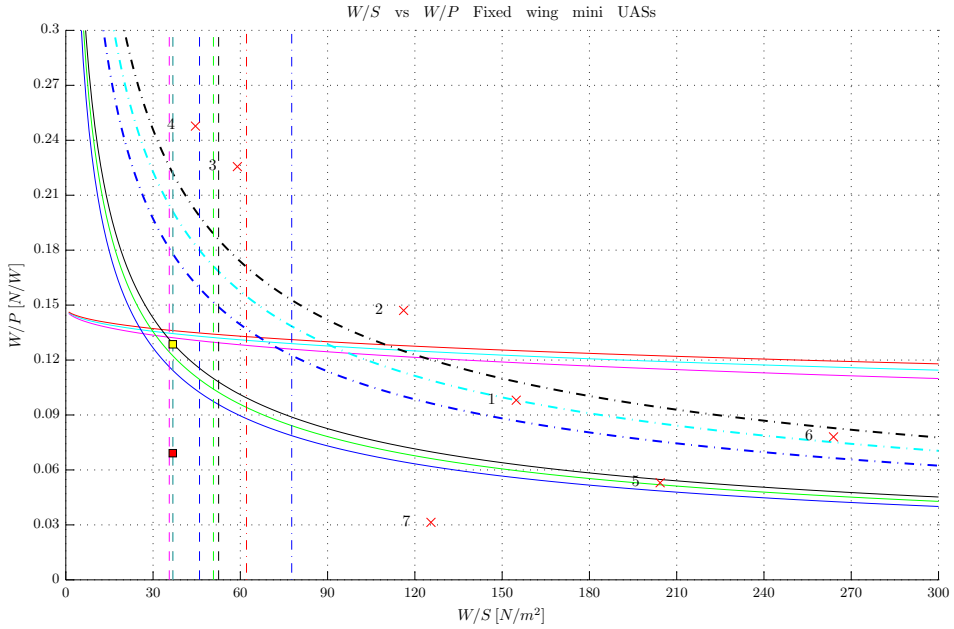

Figure 4.20: Initial W/S vs W/P fixed wing mini UAS

In Figure 4.20 the design point is already presented ($C_L = 1.2$ [-] and $A = 7.5$ [-]). For propeller driven aircraft holds that the power loading must be maximized in order to have the most efficient engine[79]. Also the wing loading must be maximized such that the wing is most effective[79]. From Figure 4.20 can be seen that the power loading is limited by the climb gradient at $A = 7.5$ [-]. The wing loading is limited by the stall speed at $C_L = 1.2$ [-]. At this design point the W/S value was estimated to be $36.77\,N/m^2$ and the W/P value to be 0.1286 [N/W]. Using the weight estimation from Table 4.13, leads to an area estimation of $0.38\,m^2$ and a power estimation of approximately 110 [W]. Subsequently, from Table 4.14 can be seen that this power estimation is not sufficient for the high speed cruise requirement. At high speed cruise, the required amount of power is at least 201 [W]. When this power

requirement is used, the W/P value becomes 0.0692 [N/W]. This is the design point for this UAS design. This point is also shown in Figure 4.20.

Table 4.15: Overview parameters reference UASs

(a) Overview parameters reference UASs

N	UAS name	MTOW [N]	Endurance [h]	Max. speed [km/h]	Min. speed [km/h]
1	Biodrone	117.68	1	130	35
2	Azimut 2	88.26	1	120	35
3	ZALA 421-08	22.56	1.67	190	65
4	ZALA 421-04M	47.07	2	160	65
5	A-3 Remez	98.07	2	105	-
6	A-4 Albatros	179.46	2	125	-
7	Desert Hawk I+	31.38	1	93	-

(b) Overview parameters reference UASs (cont'd)

N	UAS name	Stall speed [km/h]	$\frac{W}{S}$ $[N/m^2]$	$\frac{W}{P}$ [N/W]	S $[m^2]$	P [W]	A [-]
1	Biodrone	-	154.84	0.0981	0.76	1200	15.21
2	Azimut 2	-	116.13	0.1471	0.76	600	11.07
3	ZALA 421-08	-	58.98	0.2256	0.38	100	1.72
4	ZALA 421-04M	-	44.57	0.2477	1.056	190	2.42
5	A-3 Remez	58	204.31	0.0530	0.48	1850	8.3
6	A-4 Albatros	60	263.91	0.0780	0.68	2300	9
7	Desert Hawk I+	56	125.53	0.0314	0.25	1000	6.97

Besides the design point of the UAS design, also reference UASs are shown in Figure 4.20. In Table 4.15 an overview of the specifications of the, in Figure 4.20 presented, reference aircraft are shown. From this table can be seen that the current W/P value of the UAS design is plausible. The W/S value is lower in comparison to the other UASs. From this can be concluded that most reference aircraft are designed for higher speeds. The Biodrone and Azimut 2 on the other hand, have minimum and maximum speed specifications that almost suit the required values (30 [km/h] and 130 [km/h]). Using Equation (4.74) in combination with the air density, obtained minimum speed and W/S value from Table 4.15 leads to a lift coefficient, for those UASs, of more than 3. These UASs are not equipped with high lift devices and therefore it is not likely that they are able to fly at a minimum speed of 30 [km/h] with MTOW. Therefore the minimum speed values of those UASs are not realistic. The UAS design W/S value is much more likely. This concludes the evaluation of the W/P and W/S diagrams. In the following section, the obtained results will be used in designing the wing.

4.7 Wing design

After obtaining the design point, these results were used for the design of the wing. The UAS is optimized for loiter conditions because this part of the flight occurs in both mission profiles (see Figure 4.7). Besides that, it is also expected that the UAS will be used in most cases for observing a certain area of interest (loitering around this point of interest). In order to optimize for loiter, the design lift coefficient of the wings needs to be related to the design lift coefficient of the airfoils. Before this was done, a decision with respect to the number of wings and wing type had to be made (see Subsection 4.7.1). The derivation of the design lift coefficient is presented afterwards in Subsection 4.7.2. This is followed by Subsection 4.7.3 on airfoil selection. Next, the complete wing design optimization is presented and discussed (see Subsection 4.7.4). Finally, in Subsection 4.7.5 the impact of the new wing design on the UAS design is discussed.

4.7.1 Wing design options

There are numerous possibilities in designing a wing. Some of the most common design options are discussed in this subsection. During the first part of the design, the number of wings needed to be determined. The options are using a mono-plane, bi-plane or multi-plane. Nowadays, most planes have a mono-plane. There are a few aircraft that have a bi-plane. Applying multiple planes is not commonly used on modern aircraft. Because of practical reasons (ease of manufacturability e.g.) it has been decided to use a mono-plane for this UAS design. An overview of other design options, that are taken into account in this subsection, is presented in Figure 4.21.

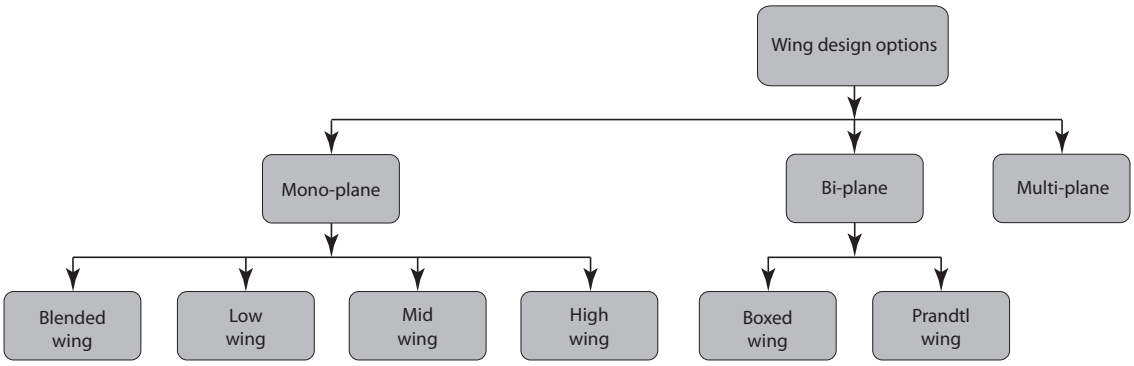

Figure 4.21: Wing design options

From Figure 4.21 can be seen that there are again quite a number of options when a mono-plane is considered. Most common used design options are the low wing, mid wing and high wing. In recent years, a lot of research is conducted into blended wing body design. Again, in order to keep the design as simple as possible, it was chosen to discard the blended wing body design option and to evaluate the remaining design options. In the following three paragraphs both advantages and disadvantages of the remaining design options are presented.

Low wing An example of a low wing UAS is shown in Figure 4.22.

Figure 4.22: Low wing UAS (Sperwer[82])

The advantages of a UAS with a low wing configuration are:

- When a landing gear is used and attached to the wing, it can be shorter and therefore be lighter. This will also reduce the structural weight of the wing.
- The frontal area of the aircraft is less in comparison to a UAS with a high wing configuration.
- Because of the ground effect, the take-off performance is better.
- The UAS has higher lateral control compared to a high wing configuration.
- The tail of a low wing configuration is more effective due to less downwash. The tail can be smaller and is therefore lighter as well.

The disadvantages of a UAS with a low wing configuration are:

- The wing is separated into two sections reducing the amount of generated lift (a high wing configuration produces more lift over the same span). Due to this, the stall speed is also higher. This increases the take-off run and reduces the landing performance (requires more landing run).
- There is a minimum ground clearance making the wing more sensitive to foreign object damage. The chance of striking the ground with the wing tips during landing is also higher.
- The fuselage needs to stiffened in order to pass through the wing box. This increases the structural weight of the UAS.
- A low wing configuration can block the view of a side looking camera when the UAS is loitering e.g.

High wing An example of a high wing UAS is shown in Figure 4.23.

Figure 4.23: High wing UAS (Raven[20])

The advantages of a UAS with a high wing configuration are presented in the following list:

- Better ground clearance than a low wing configuration. This lowers the chance of striking the ground with the wing tips during landing. The wing is also less sensitive to foreign object damage.
- High wing configurations feature a dihedral effect. During roll, the flow that escapes from below the downward wing passes around the fuselage and creates a local increase of angle of attack. This causes the UAS to roll more easily. Also the lateral stability is higher in comparison with a low wing configuration.
- External struts can be used to support the wing. This reduces the wing weight but increases the wing drag. Since most lift is created by the top part of the wing, the drag impact of using struts in a high wing configuration is less than low wing configuration with struts.
- Another structural benefit occurs if the wing box is carried over the top of the fuselage rather than passing through it. The fuselage does not need to stiffened in order to pass through the wing box.

The disadvantages of a UAS with a high wing configuration are:

- When the wing box is carried over the top of the fuselage this will increase the drag due to the increase in frontal area.
- The tail can be less effective due to the downwash of the wing. This requires the tail to bigger (and heavier).

Mid wing The mid wing configuration is a compromise between the low wing and high wing configuration. Therefore, both advantages and disadvantages of the high wing and low wing configuration apply for a mid wing configuration. An example of a mid wing UAS is shown in Figure 4.24.

Figure 4.24: Mid wing UAS (Reaper[23])

Wing configuration selection After evaluating the different wing configurations, it was decided to go for a high wing configuration. It is desired to hand or catapult launch the UAS and therefore no landing gear is required. In order to prevent damage to the wing during landing, it is desired to have a high wing configuration. Besides that, it is also desired to have the various payloads located in the fuselage facing down and/or sidewards. When a low wing is used, intrusion of the flow, by means of payloads sticking out of the fuselage, is not desired. The flow around the wing will be influenced significantly, reducing the amount of created lift. Also, when a side looking camera is used, the wing can block the view. Choosing a high wing configuration prevents this.

Next, the design lift coefficient for the wing had to be determined. This is discussed in the following subsection.

4.7.2 Design lift coefficient

The required lift coefficient during loiter is the design lift coefficient. This coefficient can be calculated by using Equation (4.89). This equation was obtained from the aircraft design slides of Melkert[79].

$$C_{L_{design}} = \frac{L}{0.5\,\rho\,V_{effective}^2\,S_{ref}} \tag{4.89}$$

with:

$$V_{effective} = V_{inf}\,cos(\Lambda_{LE}) \tag{4.90}$$

In Equation (4.89), the lift is assumed to be equal to the weight of the UAS (see Table 4.13). From this table the reference area was also derived. Furthermore, in this stadium of the design a sweep angle, Λ_{LE}, had to be assumed. Introducing a leading edge sweep angle is normally done to increase the critical Mach number (Mach number at which Mach 1 is reached on the wing). The structure can also be lighter (thicker airfoils can be used). In this UAS design $M<<1$. A sweep angle will therefore not be used to increase the critical Mach number but to create aeroelastic stability and gust tolerance. When a sudden lift is generated by a gust, the torsion of the wing, with consequent lowering of the angle of attack, is such that the amount of extra lift is lowered. Also the lateral controllability of the aircraft is increased because the effective wing span is lower reducing the wing mass moment of inertia. Hence, a higher sweep angle allows for better maneuverability. The downside of introducing a leading edge sweep is the increase of tip loading. This causes the boundary to thicken towards the tip. The wing will become more prone to tip stall. Wash-out can be applied to suppress the tip stall. Wash-out is applying negative twist consisting of decreasing airfoil incidence angles outboard along the span. This significant increases the complexity of the wing. In a later stage of the design is decided if sweep and wash-out are applied on the wing of the UAs.

A leading edge sweep angle of 20° was assumed initially. Later on in the design this sweep angle is evaluated. From Equation (4.90) can be seen that this sweep angle has an effect on the effective velocity (since the airflow is not perpendicular to the leading edge). Figure 4.25 gives a graphical overview of this effect.

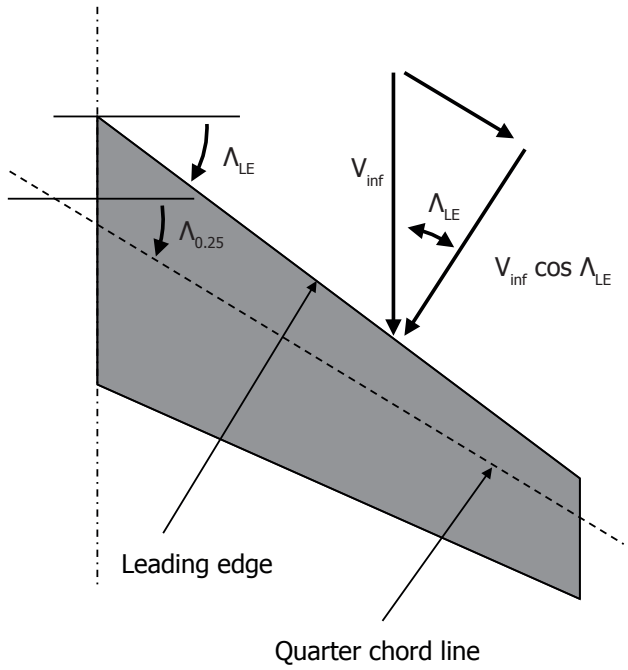

Figure 4.25: Effect of sweep on effective velocity

In order to select an appropriate airfoil that is able to deliver $C_{l_{design}}$, it is assumed that the lift can be generated by an airfoil operating at minimum drag conditions. An airfoil operating at an angle (sweep angle) with respect to the free stream, needs a higher $C_{l_{design}}$ value in order to match the required $C_{L_{design}}$ for the wing. $C_{l_{design}}$ was calculated while taking into account the sweep angle in the following way:

$$C_{l_{design}} = \frac{C_{L_{design}}}{cos(\Lambda_{LE})^2} \tag{4.91}$$

Using Equation (4.91) a design lift coefficient of 1.0276 [-] was determined. In the next subsection, the airfoil selection procedure is discussed.

4.7.3 Airfoil selection

In order to find a suitable airfoil for the wing of the UAS, an online database containing over 1500 airfoils, provided by the UIUC Applied Aerodynamics Group[83], was obtained. Subsequently, XFOIL[84] was used to analyze these airfoils for an angle of attack sweep.

XFOIL is an interactive program for the design and analysis of subsonic (low Reynolds number) isolated airfoils. Given the coordinates specifying the shape of a 2D airfoil, the Reynolds number and Mach number, XFOIL can calculate the pressure distribution on the airfoil and hence lift, drag and moment coefficients. Before XFOIL calculations were performed, first the required input parameters for XFOIL needed to be determined. As stated before, these input parameters are the Reynolds number and the Mach number. The Reynolds number is calculated by using Equation (4.92).

$$Re = \frac{\rho \, V_{effective} \, l}{\nu} \tag{4.92}$$

The Mach number was determined with Equation (4.93).

$$M = \frac{V_{effective}}{a} \tag{4.93}$$

In Equation (4.92), ν, represents the kinematic viscosity of the flow. The Mean Aerodynamic Chord (MAC) of the wing is displayed as l. The MAC is the chord-weighted average chord length of the wing. A graphical display of the MAC is shown in Figure 4.26. The MAC was calculated in the following way:

$$MAC = \frac{\left(\frac{2}{3} \, c_{root}\right)\left(1 + \lambda + \lambda^2\right)}{1 + \lambda} \tag{4.94}$$

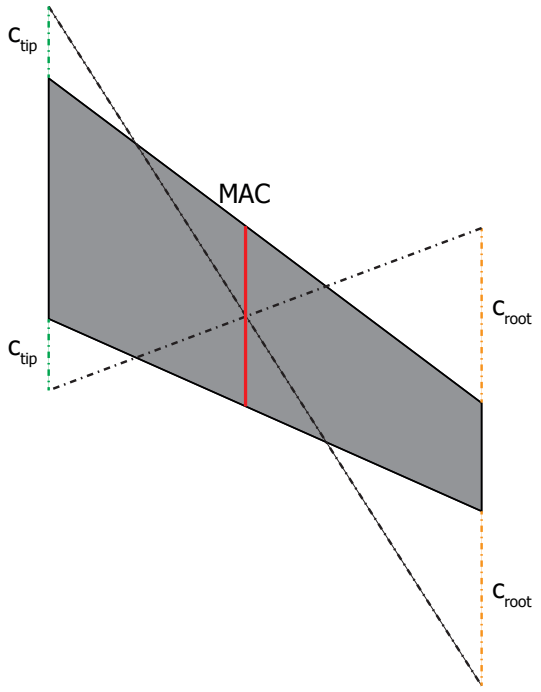

Figure 4.26: Graphical display MAC

λ in Equation (4.94) represents the taper ratio of the wing. The taper ratio is the ratio between the wing root chord length and the wing tip chord length. Wings with a high taper ratio are easier to manufacture. A high taper ratio causes an increase of tip chord and therefore also the amount of generated lift at the tip. As a result the resultant lift shifts towards the tip increasing the wing bending. In order to compensate for the wing bending the structure needs to be strengthened, increasing its weight. Due to the increase in lift generated at the tip the induced drag also increases (non-elliptical lift distribution). In order to initiate the design, again a value was assumed at this stage of the design (0.25 [-]). This value is also evaluated later on in the design.

All unknown parameters of Equation (4.92) and Equation (4.93) are known at this stage. Next, these parameters were used to calculate the Reynolds number and Mach number. A Mach number of 0.0246 [-] and a Reynolds number of $1.0962 \cdot 10^5$ [-] were calculated for loiter conditions. Subsequently, the XFOIL settings had to be determined.

In order to keep the calculation time to a minimum, the number of panels was set to 100 and the maximum number of iterations to 400. The airfoils were analyzed by varying the angle of attack, starting at $-4°$ and finishing at $12°$ with steps of $0.5°$.

The flow settings together with the XFOIL settings were implemented in a Matlab[85] code in order to automatically run XFOIL with the right settings for all airfoils in the database. A graphical overview of the XFOIL analysis can be seen in Figure 4.27.

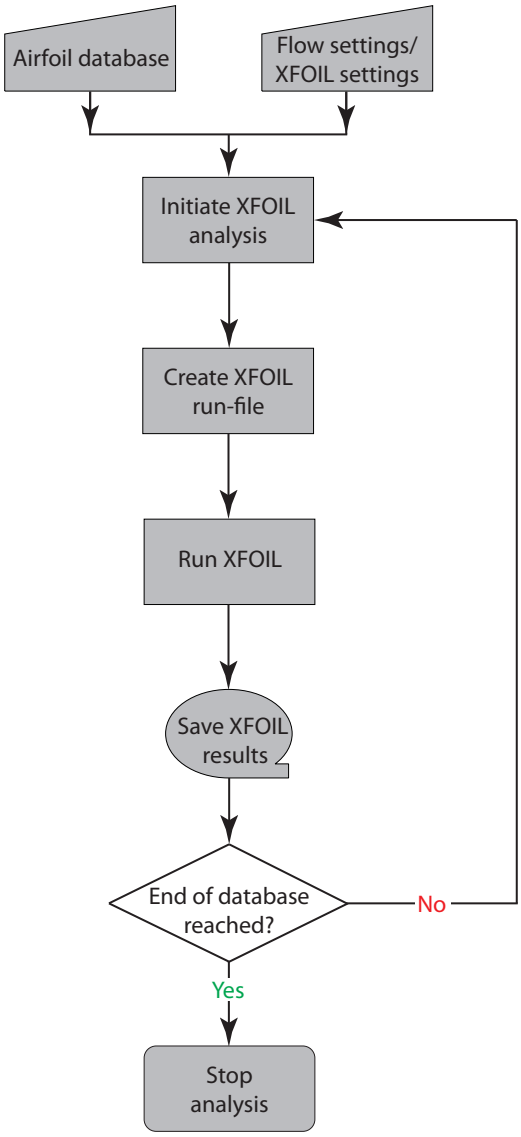

Figure 4.27: XFOIL airfoil analysis overview

Currently calculating the results for all airfoils required approximately one hour. It should be noted that not all airfoil analyses were completed successfully. Some airfoil calculations failed to converge and were therefore removed from the routine. This resulted in approximately 1500 airfoils left to analyze.

After analyzing the airfoils with XFOIL, an optimal airfoil had to be chosen such that the UAS design is optimized for loiter conditions. From Subsection 4.3.2 was found that at loiter conditions (C_l^3/C_d^2) must be maximized. Therefore, $(C_l^3/C_d^2)_{max}$ of each airfoil had to be determined. Next, the C_l value at $(C_l^3/C_d^2)_{max}$ was determined. This value was set to be equal to the required $C_l +/- 0.01$ value at loiter. This resulted in a selection of airfoils that have the largest amount of lift and the lowest amount of drag during loiter conditions. Next, the capabilities of the remaining airfoils were checked. The airfoils must also be able to produce the required lift coefficient at stall, landing, cruise back and cruise conditions. From this can be concluded that the airfoil analysis had to be performed four more times in order to cover all conditions. Using Equation (4.89) through Equation (4.91) again it was possible to obtain the required lift coefficients. In Table 4.16, all required lift coefficients are presented. The associated Reynolds numbers and Mach numbers at all conditions are also shown in Table 4.16.

Table 4.16: Overview required lift coefficients and input parameters for all conditions

Condition:	$C_{l_{required}}$ [-]	Re [-]	M [-]
Stall	1.2949	9.4466^4	0.0213
Loiter	1.0276	1.0962^5	0.0246
Landing	0.9791	1.0864^5	0.0245
Cruise back	0.6988	1.3293^5	0.0299
Cruise	0.0547	4.7502^5	0.1067

The remaining airfoils together with the associated Reynolds numbers and Mach numbers at all conditions that are shown in Table 4.16 were put into the airfoil analysis again. After obtaining the required data, the data analysis was continued. At this point, the airfoils that are able to produce the required $C_l +/- 0.01$ value at $(C_l^3/C_d^2)_{max}$ are left. The next step was to filter out all airfoils that are not able to produce the required $C_l +/- 0.1$ value during the other flight conditions. This resulted in three potential airfoils. These airfoils are the goe617, mh201 and naca23012 and are shown in Figure 4.29.

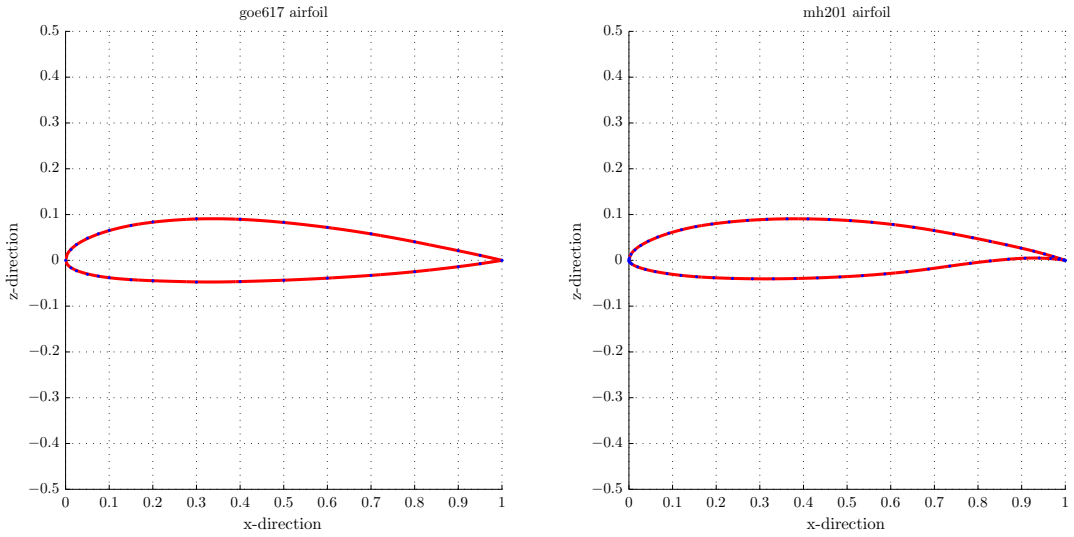

a: goe617 airfoil

b: mh201 airfoil

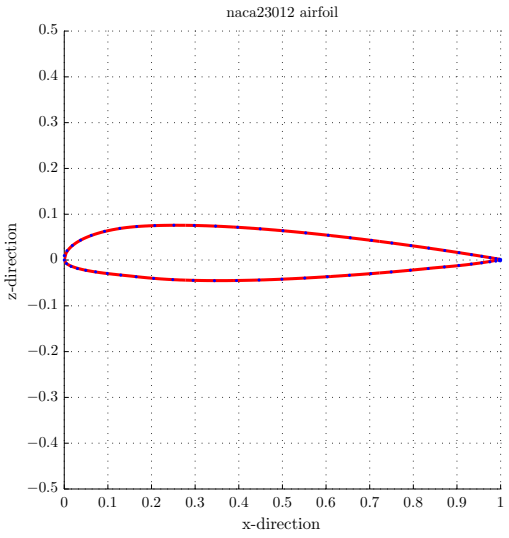

c: naca23012 airfoil

Figure 4.28: Selected airfoils

After selection was completed, the XFOIL calculations for the remaining airfoils were executed in more detail. An angle of attack sweep starting at 0° and finishing at 12° with steps of 0.1° was performed. The results from these detailed XFOIL calculations for loiter conditions can be found in Figure 4.29. Additional results are presented in Appendix F.

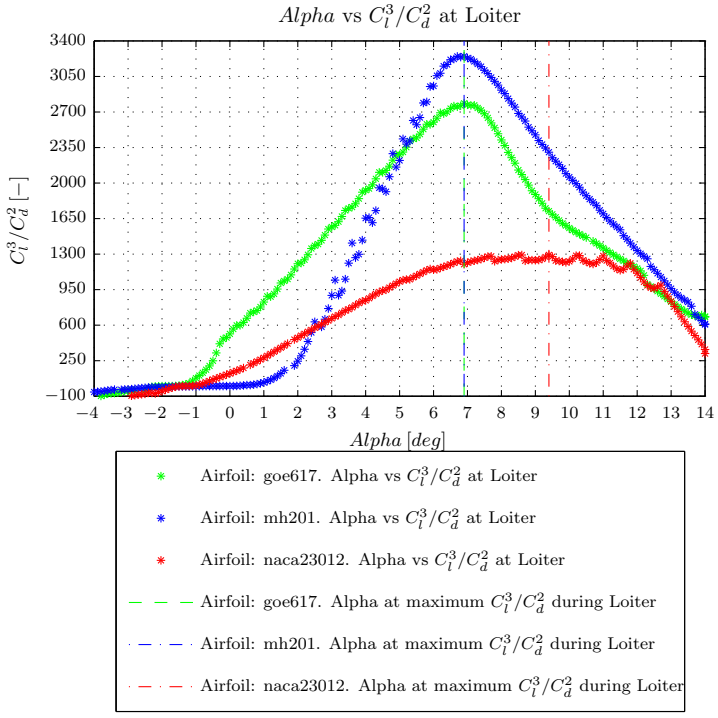

a: Alpha versus C_l^3/C_d^2

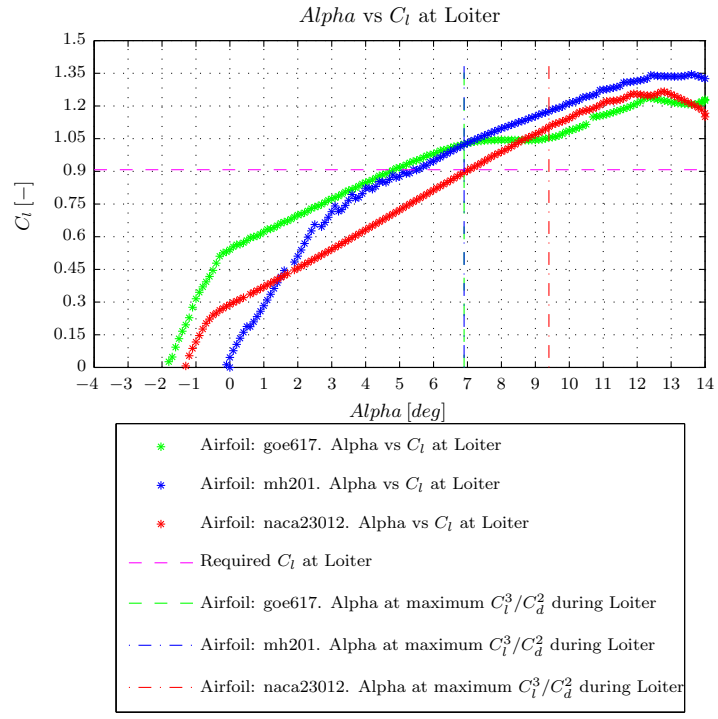

b: Alpha versus C_l

Figure 4.29: XFOIL results selected airfoils during loiter

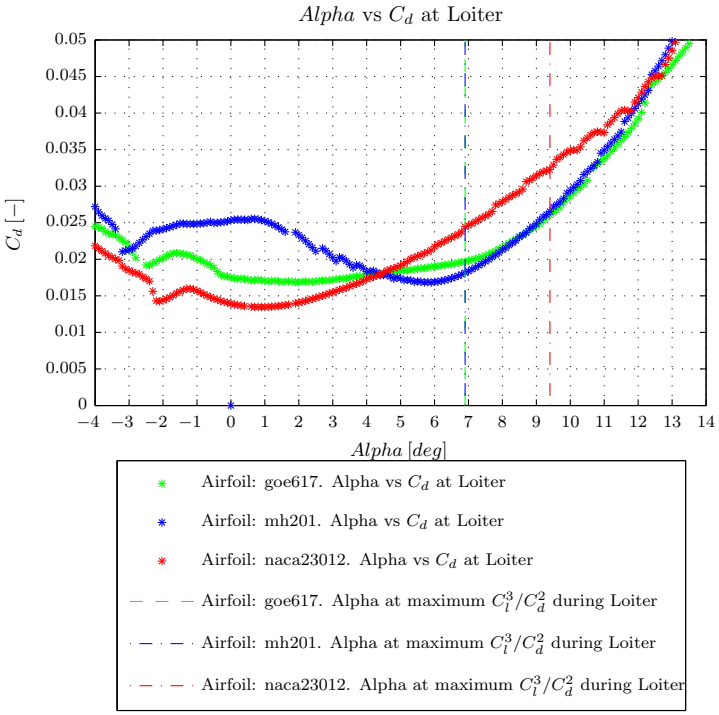

c: Alpha versus C_d

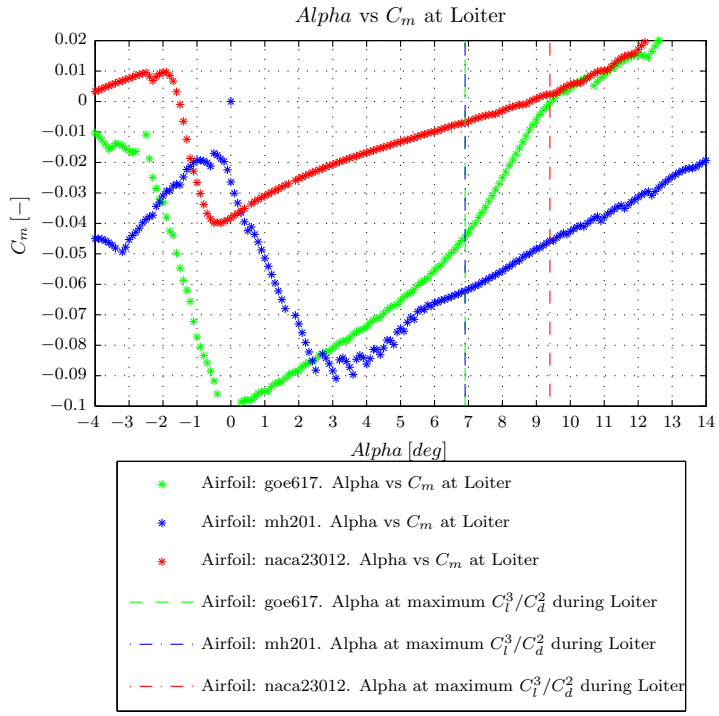

d: Alpha versus C_m

Figure 4.29: XFOIL results selected airfoils during loiter (cont'd)

From Figure 4.29a can be seen that the mh201 airfoil delivers the highest $(C_l/C_d)_{max}$ value. Figure 4.29b shows that the goe617 and mh201 are both able to generate the required C_l at their $(C_l^3/C_d^2)_{max}$ value. The naca23012 airfoil produces a slightly higher C_l value at $(C_l^3/C_d^2)_{max}$. The required angle of attack to generate the required C_l value for this airfoil is also much higher. One of the results of this can be seen in Figure 4.29c. The drag coefficient, C_d, of the naca23012 airfoil is much higher compared to the other two airfoils. The final set of results is presented in Figure 4.29d. This figure represents the moment coefficient, C_m, that is created by the airfoil during that certain flight condition. The moment that is created needs to be compensated by a moment created by the horizontal tail surface. From this can be concluded that a small moment coefficient is desired. From Figure 4.29d can be seen that the mh201 creates the largest negative moment coefficient while the naca23012 produces the smallest moment coefficient. When a closer look is taken at the moment coefficient of this airfoil, one can see that a positive moment coefficient is produced by this airfoil. This means that a horizontal tail producing positive lift can be used when using this airfoil for the wing. This can result in a significant decrease of drag for the wing and horizontal tail combination. Besides that also the longitudinal stability of the UAS benefits from selecting an airfoil that has a small moment coefficient. The effects of the three resulting airfoils is investigated at a later stage of the wing design. For now, an overview of the most important results is presented in Table 4.17.

Table 4.17: Overview result airfoil selection

Parameter	Symbol	goe617	mh201	naca23012	Unit
$(C_l^3/C_d^2)_{max}$	$(C_l^3/C_d^2)_{max}$	2785.4	3249.0	1292.4	[-]
Angle of attack at $(C_l^3/C_d^2)_{max}$	α	6.9	6.9	9.4	[deg]
Lift coefficient at $(C_l^3/C_d^2)_{max}$	C_l	1.0263	1.0229	1.1043	[-]
Drag coefficient at $(C_l^3/C_d^2)_{max}$	C_d	0.0197	0.0182	0.0323	[-]
Moment coefficient at $(C_l^3/C_d^2)_{max}$	C_m	-0.0445	-0.0605	0.0024	[-]
$(C_l/C_d)_{max}$	$(C_l/C_d)_{max}$	52.10	56.36	34.21	[-]

The results for the flight conditions, besides loiter, also needed to be investigated. From Appendix F can be seen that all airfoils can provide the required C_l values during all flight conditions except for the stall condition. Figure F.0 shows that the goe617 and naca23012 airfoil are not able to achieve the required C_l value at stall. These airfoils passed the filter because the lower limit for the required lift coefficient at stall was set at $C_l - 0.1$. Despite the fact that these airfoils do not comply with the stall requirements, they were still seen as potential airfoils for the wing. After analyzing the wing as a whole, the results give a more clear view on the performance of the airfoils when they are used for a wing.

This concludes the subsection on airfoil selection. The next subsection will describe the wing geometry based on the airfoil selection performed in this subsection.

4.7.4 Wing geometry

The next step in the design process was to design a wing based on the airfoils that were selected in the previous subsection (Subsection 4.7.3). A quasi-3D wing optimizer, created by Dennis Trips[78], has been used to optimize the wing for $(C_L^3/C_D^2)_{max}$.

The quasi-3D method of Trips combines a vortex lattice method (AVL) with viscous airfoil data (XFOIL). Athena Vortex Lattice (AVL)[86] employs an extended vortex lattice model for the lifting surfaces. In order to evaluate the aerodynamics of the wing in a fast manner, viscous airfoil data was combined with inviscid three dimensional wing calculations. The optimization part of the program is accomplished by a sequential quadratic programming algorithm. The results of the quasi-3D method were compared to windtunnel results. The method was found to be valid for low Reynolds numbers ($<2.5 \cdot 10^5$).

The viscous airfoil data was found from Xfoil viscous calculations. As stated in the previous subsection, Xfoil is an airfoil analysis and design tool developed specifically for low Reynolds number airfoils[84]. It calculates the viscous aerodynamics using a higher order panel method coupled with a viscous/inviscid interaction method. The three dimensional inviscid calculations were performed by using the vortex lattice method AVL.

One of the most important settings for the vortex lattice method is the grid layout.The grid is defined for half the wing and AVL is notified of the fact that it is symmetric. Trips investigated the optimal grid layout. The wing, independently of the number of sections, should have 40 elements in span-wise and 20 in chord-wise direction. This results in a total of 800 elements for half the wing. The distribution of these panels is such that they are more concentrated towards the edges and the root, as the pressure gradients are higher at these locations. However, the density for the tip and the leading edge are the highest. A typical grid layout for the vortex lattice method can be seen in Figure 4.30.

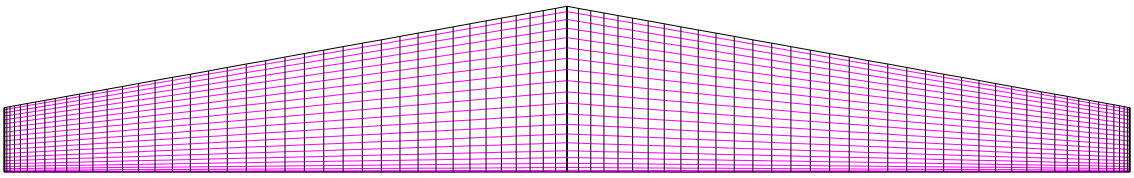

Figure 4.30: Typical AVL grid layout

Trips quasi-3D method optimizes the wing by making use of five variables. In order to keep the optimization within the desired space, some bounds were introduced. The variables together with the upper and lower bounds for these variables are presented in Table 4.18.

Table 4.18: Overview optimization variables and constraints

Parameter	Symbol	Lower bound	Upper bound	Unit
Half the wing span	$\frac{b}{2}$	0.5	1	[m]
Wing root chord	c_{root}	0.05	0.6	[m]
Wing sweep angle	Λ	0	20	[deg]
Taper ratio	λ	0.1	1	[-]
Effective velocity	V_{eff}	7.25	36.11	[m/s]

The bounds were obtained by experimenting with the optimization routine. An upper bound for half the wing span lower than 1 [m] resulted in a non-converging routine. The wing root chord bound was set to a value which was never reached. If, due to manufacturing purposes e.g., the wing root chord length has a maximum allowed value lower than the current value, this bound needs to be revised. The wing sweep angle has been set to a maximum value of 20° in order to avoid highly swept wings. Later on in the stability evaluation is discussed if this bound results in a wing that creates sufficient stability. The taper ratio has not been bound in this phase of the design. If, due to structural reasons e.g., the wing cannot be made strong enough, also this bound needs to be revised. Finally, the effective velocity has been bound by the minimum speed as stated in Subsection 4.6.1 and the maximum required cruise speed.

The next step was to use the optimization method in order to optimize for three different wings. Each wing consisting of one of the optimal airfoils that was derived in Subsection 4.7.3. All wings were required to have a stability margin of at least 2.5%. This stability margin ensures the wing to be stable. This means that the wing will have a natural pitch down moment. After a simulation time varying between 15 and 20 hours per wing, the results were analyzed. Figure 4.31 shows a graphical representation of the resulting wings.

From Figure 4.31 can be seen that there are similarities between the wing constructed out of goe617 airfoils and the wing constructed out of mh201 airfoils. The wing with naca23012 airfoils on the other hand, is quite different. The performance of the wings is presented in Figure 4.32.

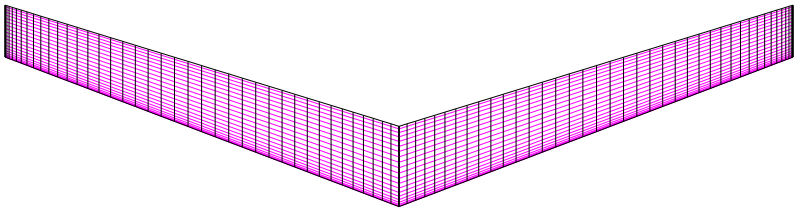

a: Optimized wing with goe617 airfoil

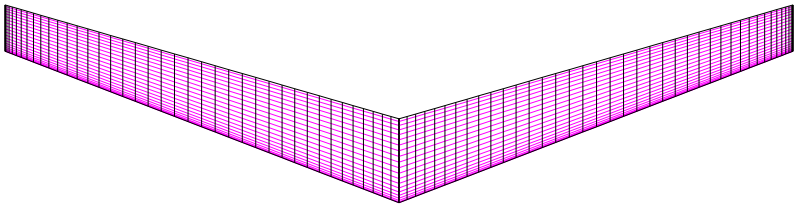

b: Optimized wing with mh201 airfoil

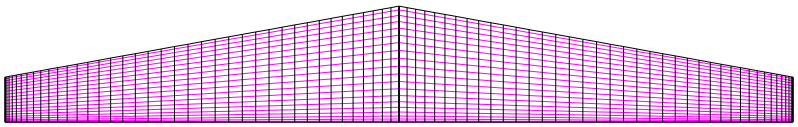

c: Optimized wing with naca23012 airfoil

Figure 4.31: Optimized wings

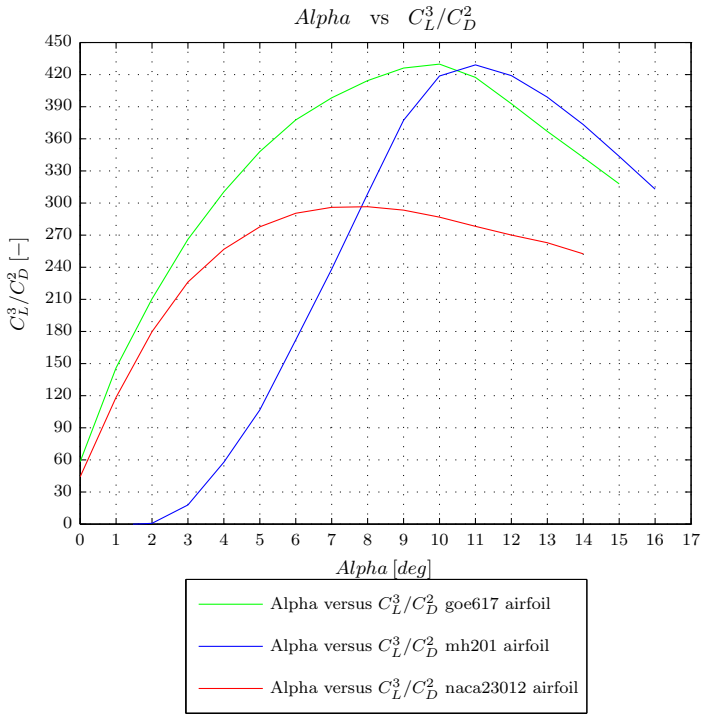

a: Alpha versus C_L^3/C_D^2

Figure 4.32: Results optimized wings

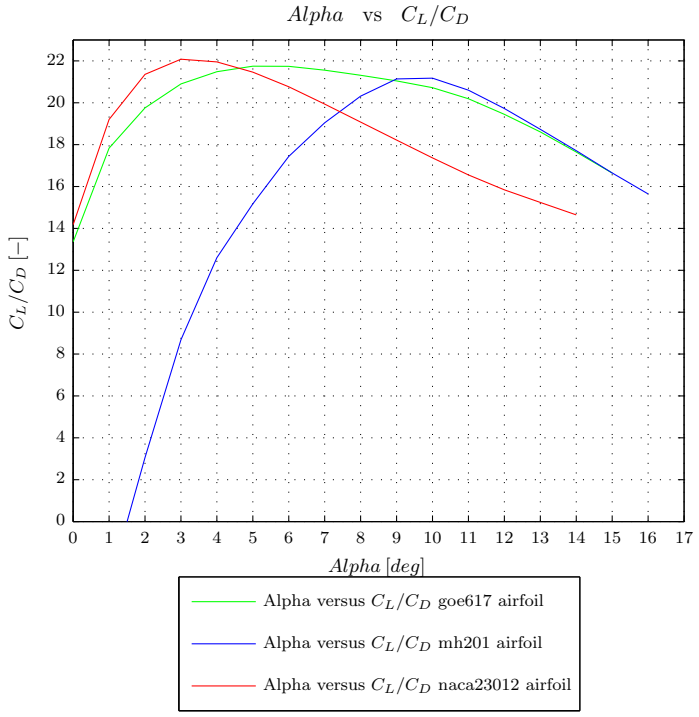

b: Alpha versus C_L/C_D

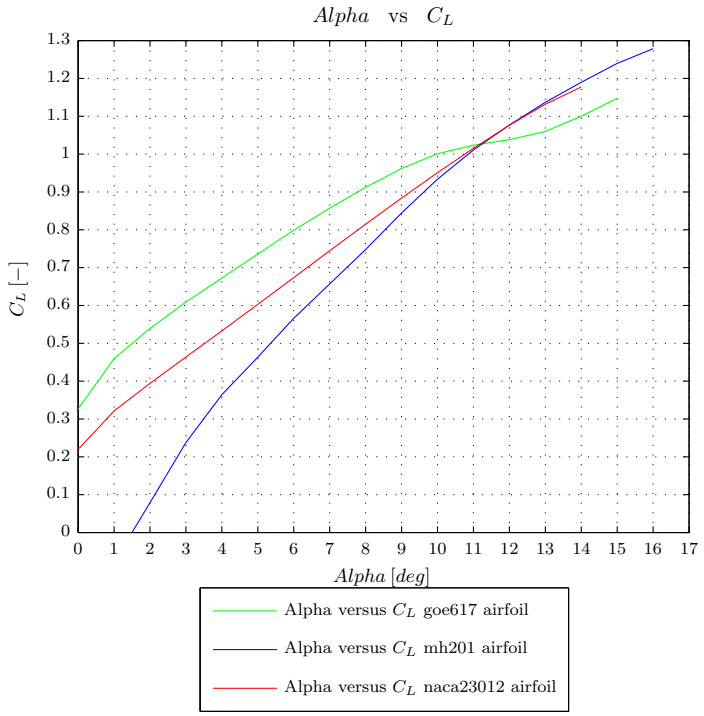

c: Alpha versus C_L

Figure 4.32: Results optimized wings (cont'd)

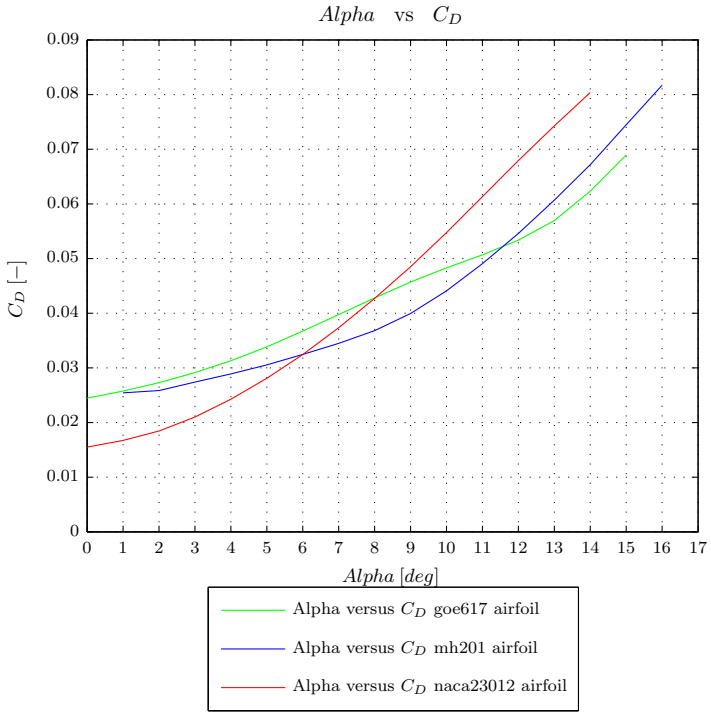

d: Alpha veruss C_D

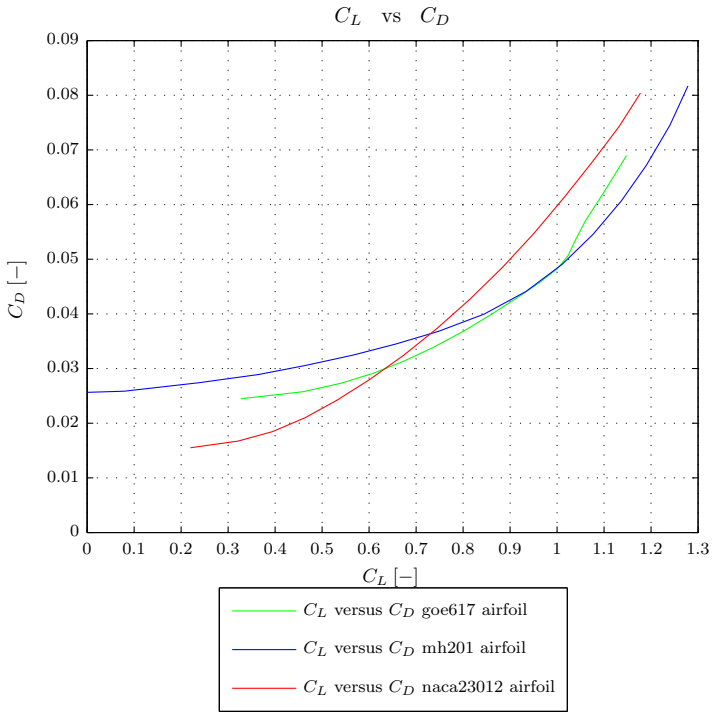

e: C_L versus C_D

Figure 4.32: Results optimized wings (cont'd)

From Figure 4.32a can be seen that a wing with goe617 airfoils or mh201 airfoils has a higher maximum C_L^3/C_D^2 value compared to a wing with naca23012 airfoils. The downside of these wings is the high angle of attack at which this maximum C_L^3/C_D^2 value is achieved. This leaves a smaller room for variation of angle of attack. A large increase of angle of attack (due to a gust e.g.) may cause the wing to stall. Figure 4.32d shows that the drag at loiter is smallest for the wing with the naca23012 airfoils. This wing requires a relatively small lift coefficient in order to produce the required amount of lift. Table 4.19 shows that a larger wing surface area compensates for this smaller lift coefficient. From Figure 4.32b can be seen that the maximum C_L/C_D value is also highest for the wing with the naca23012 airfoils. In case of a cruise situation this wing is therefore most favorable. Note that this must be verified by analyzing the wing performance at cruise speed. An overview of the most important properties of the three optimized wings is shown in Table 4.19.

Table 4.19: Overview results wing optimization

Parameter	Symbol	goe617	mh201	naca23012	Unit
$(C_l^3/C_d^2)_{max}$	$(C_l^3/C_d^2)_{max}$	429.8	429.1	296.5	[-]
Angle of attack at $(C_l^3/C_d^2)_{max}$	α	10	11	8	[deg]
Lift coefficient at $(C_l^3/C_d^2)_{max}$	C_l	1.001	1.011	0.8148	[-]
Drag coefficient at $(C_l^3/C_d^2)_{max}$	C_d	0.04831	0.04907	0.04271	[-]
Moment coefficient around the AC	$C_{m_{ac}}$	-0.0218	-0.0533	-0.0126	[-]
Wing surface area	S_{ref}	0.3356	0.3304	0.4089	$[m^2]$
Span	b	2	2	2	[m]
Sweep	Λ	19.8770	19.8397	0	[deg]
Wing tip twist	ϵ_{wing}	-1.9536	-6.0572	0	[deg]
Taper	λ	0.6467	0.5519	0.3885	[-]
Root chord	c_{root}	0.2038	0.2129	0.2945	[m]
Tip chord	c_{tip}	0.1318	0.1175	0.1144	[m]
MAC	c_{mac}	0.1704	0.1698	0.2176	[m]

From Table 4.19 some additional conclusions could be drawn. A common result for all wings is the wing span. The upper bound is reached in all cases. From Equation (4.41) can be seen that in order to reduce the induced drag, the aspect ratio needs to be as high as possible. The highest aspect ratio is achieved by maximizing the wing span. Next, from Table 4.19 can be noted that the wing moment coefficient around the aerodynamic center is smallest for a wing with naca23012 airfoils (factor four compared to the other two wings). This wing will therefore require the smallest counteracting moment which has to be created by the tail. The lift that has to be created by the tail is also smallest resulting in the least amount of lift induced drag. Also should be noted that this optimized wing does not have any sweep or twist. From a manufactural point of view this is very advantageous. As mentioned previously, all wings were required to have a stability margin of at least 2.5%. In order to comply with this, the wing with the goe617 and mh201 airfoils required to have sweep and twist.

After evaluating the wings, the next step in the process was to choose a suitable wing for the UAS design. Based on the discussion, the wing with the naca23012 airfoils was chosen. This wing was chosen despite the fact that this wing does not have the highest C_L^3/C_D^2 value.

This concludes the subsection on wing geometry decision based on the optimum airfoils. The next subsection presents more detailed graphs of the naca23012 wing in both loiter and cruise conditions. Also the impact off the wing on the overall UAS design will be discussed.

4.7.5 Wing design impact

In the previous subsection the optimum wing geometry was derived for loiter conditions. Besides loiter conditions the wing must also be able to provide lift during cruise conditions. The wing parameters that resulted from the previous subsection were used together with the wing optimizer in order to analyze the wing performance at cruise speed conditions in detail. The results of this analysis together with a detailed analysis of the wing at loiter conditions are presented in Figure 4.33.

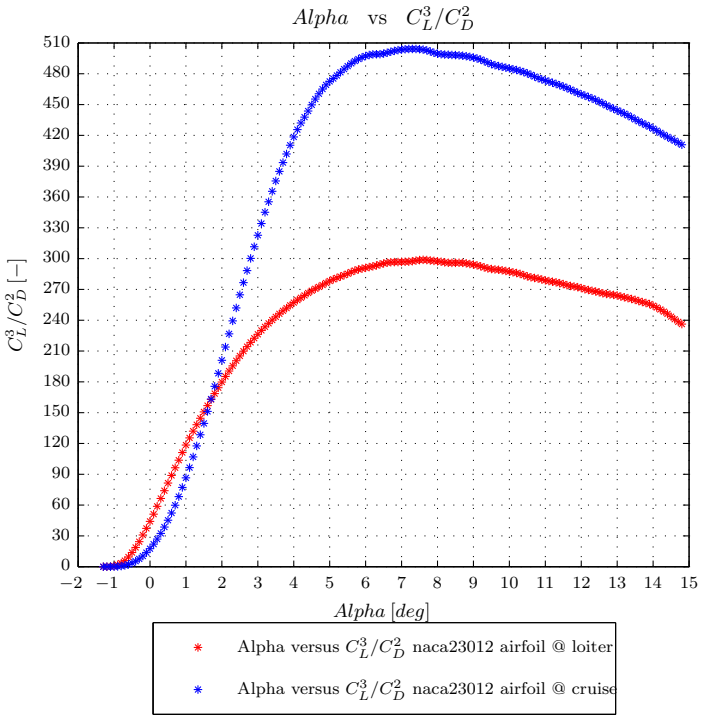

f: Alpha versus C_L^3/C_D^2

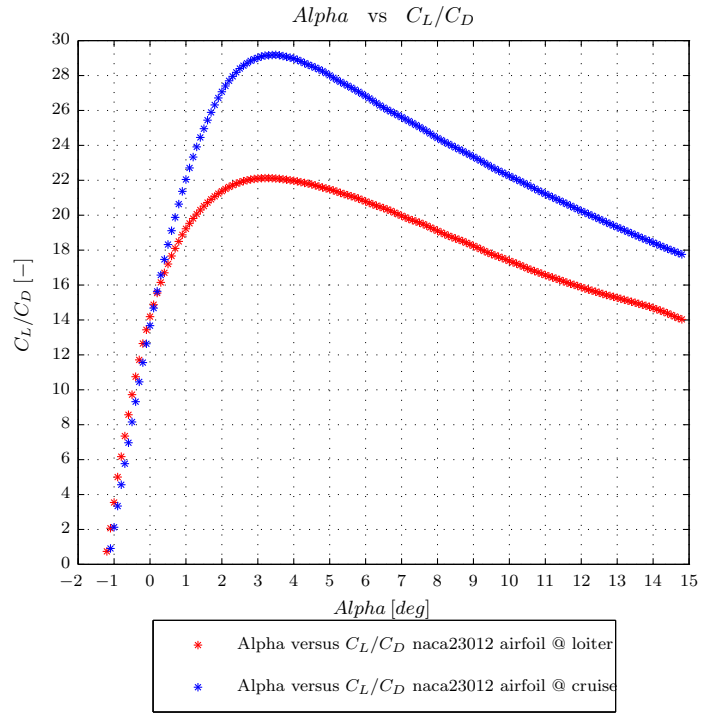

g: Alpha versus C_L/C_D

Figure 4.33: Detailed results optimized wings

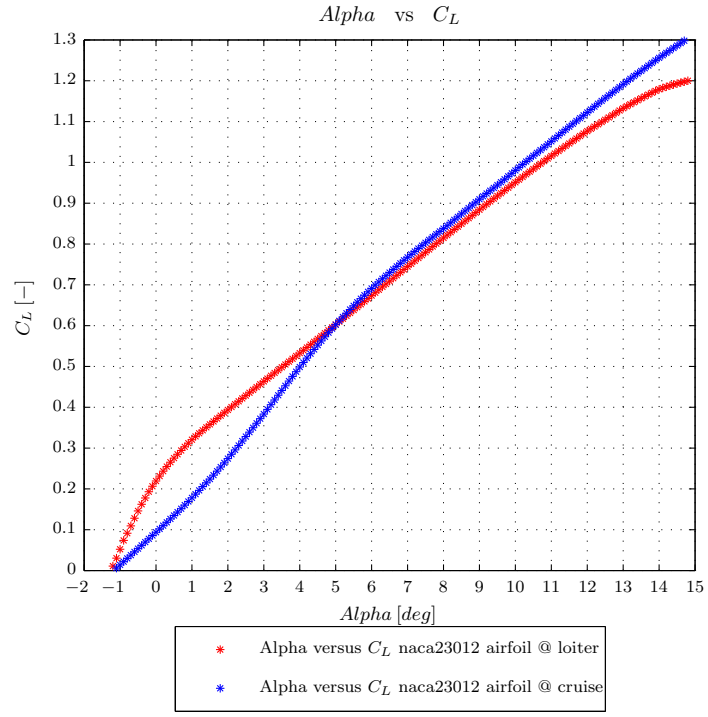

h: Alpha versus C_L

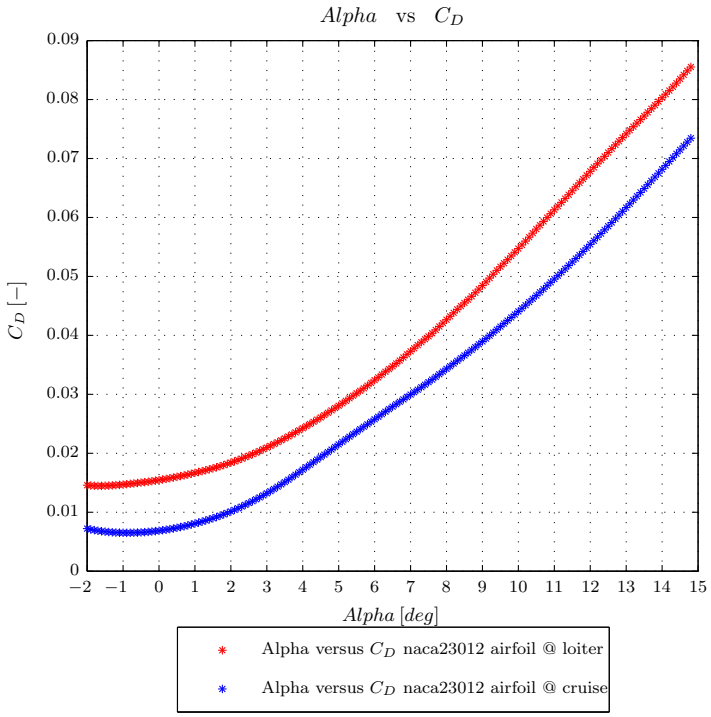

i: Alpha veruss C_D

Figure 4.33: Detailed results optimized wings (cont'd)

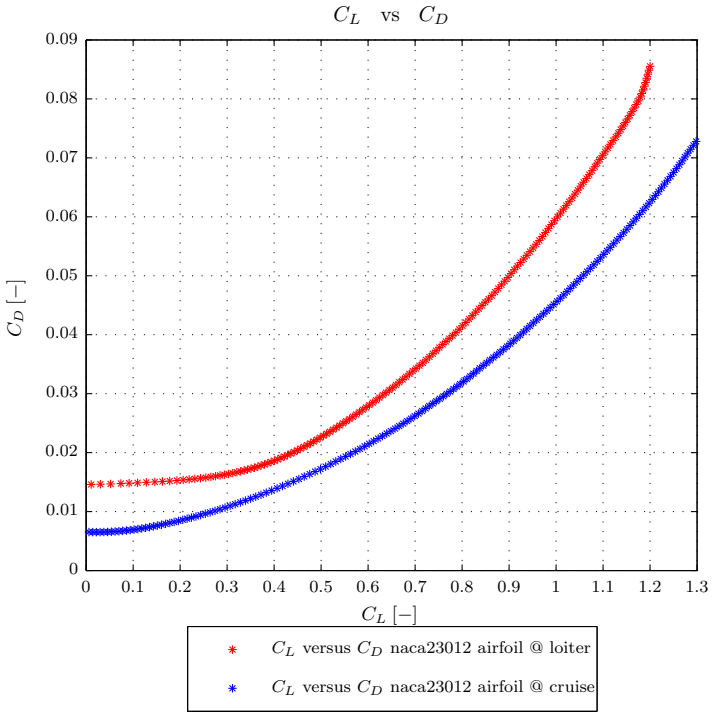

j: C_L versus C_D

Figure 4.33: Detailed results optimized wings (cont'd)

From Figure 4.33 can be seen that the wing is more efficient in cruise conditions. This is expected because at cruise the lift coefficient coefficient is much lower than at loiter conditions reducing the amount of drag of the wing. The lift coefficient required for the UAS to remain airborne was determined to be 0.0425. Figure 4.33h was used to obtain the required angle of attack at cruise. An angle of attack of $-0.6°$ was found to be sufficient. The most efficient cruise angle of attack was determined from Figure 4.33g. $(C_L/C_D)_{max}$ was calculated to be approximately 29 [-] at an angle of attack of 3.4°. An overview of the all loiter- and cruise parameters is shown in Table 4.20.

Table 4.20: Overview detailed results wing optimization

	Symbol	Results	Unit
naca23012 wing at loiter:			
$(C_l^3/C_d^2)_{max}$	$(C_l^3/C_d^2)_{max}$	296.5	[-]
Angle of attack at $(C_l^3/C_d^2)_{max}$	α	8	[deg]
Lift coefficient at $(C_l^3/C_d^2)_{max}$	C_l	0.8148	[-]
Drag coefficient at $(C_l^3/C_d^2)_{max}$	C_d	0.04271	[-]
Moment coefficient around the aerodynamic center	$C_{m_{ac}}$	-0.0126	[-]
naca23012 wing at cruise:			
$(C_l/C_d)_{max}$	$(C_l/C_d)_{max}$	29.17	[-]
Angle of attack at $(C_l/C_d)_{max}$	α	3.4	[deg]
Lift coefficient at $(C_l/C_d)_{max}$	C_l	0.4295	[-]
Drag coefficient at $(C_l/C_d)_{max}$	C_d	0.01472	[-]
Moment coefficient around the aerodynamic center	$C_{m_{ac}}$	-0.0098	[-]

After processing the new wing parameters, the effect of the optimized wing on the whole UAS design was analyzed. In Table 4.13 and Table 4.14 the old UAS parameters were presented. Table 4.21 shows both the old UAS parameters and the new UAS parameters.

Table 4.21: Overview old and new UAS parameters

	Symbol	Old UAS parameters	New UAS parameters	Unit
Empty weight	W_e	7.69	7.70	[N]
Payload weight	W_{pl}	4.90	5.02	[N]
Total fuel weight	W_f	1.30	1.19	[N]
Total MTOW	W_{TO}	13.90	13.90	[N]
Cruise velocity	V_{cruise}	36.11	36.11	[m/s]
Cruise back velocity	$V_{D_{min}}$	10.11	9.18	[m/s]
Loiter velocity	$V_{P_{r_{min}}}$	8.33	8.33	[m/s]
Cruise drag	D_{cruise}	5.53	5.54	[N]
Cruise back drag	D_{min}	0.85	0.71	[N]
Loiter drag	D_{loit}	0.93	0.73	[N]
Cruise power	$P_{r_{cruise}}$	201.00	200.89	[W]
Cruise back power	$P_{r_{cruise\,back}}$	8.84	6.68	[W]
Loiter power	$P_{r_{min}}$	7.96	6.22	[W]

From Table 4.21 can be seen that the payload weight has increased. In order to prevent having to go through the whole wing design process again, the payload weight was increased to keep the total weight of the UAS equal to its initial weight. Later on when the design is complete, a review of the drag prediction is carried out.

This concludes the section on wing design. In the following subsection the tail design will be presented.

4.8 Tail design

In the previous section the wing design was discussed. In this section, the tail design is presented. The tail of a conventional aircraft consists out of two components, a horizontal tail and vertical tail. The primary function of the tail is to trim the aircraft, provide stability and controllability. The primary function of the horizontal tail is longitudinal trim. The vertical tails' primary function is to provide directional stability. Figure 4.34 gives a graphical representation of the axis of ration for the UAS.

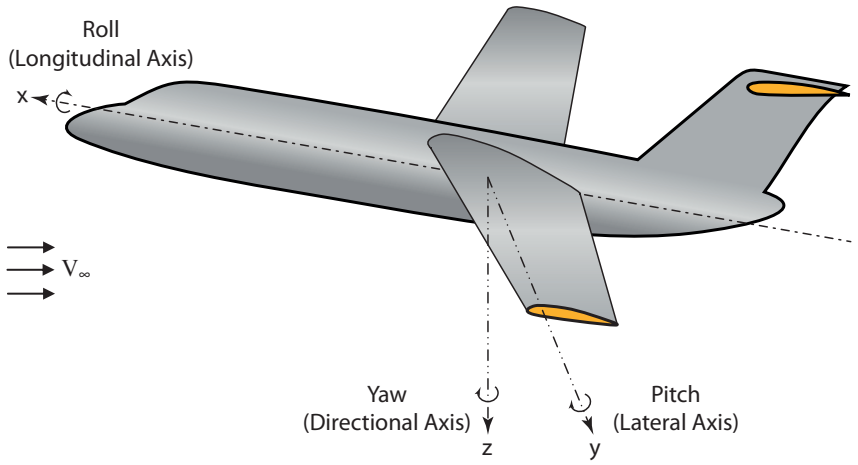

Figure 4.34: Axis of rotation

Longitudinal trim in a conventional aircraft configuration is applied through the horizontal tail. Several pitching moments about the aircraft center of gravity of the aircraft need to be trimmed about the lateral axis. The summation of these moments about the aircraft center of gravity is often negative. This moment needs to be counteracted by means of a negative horizontal tail lift. For this reason, the horizontal tail angle is often negative when compared to the angle of attack of the wing. To support trimming the aircraft, an elevator is used. Note that the elevator design is not included in this report. The horizontal tail design is presented (see Subsection 4.8.2).

Directional trim is applied through the vertical tail. When an aircraft has multiple engines, the vertical tail has great responsibility during one engine inoperative situation in order to maintain directional trim. A yawing moment needs to be

generated in order to balance the aircraft for the moment that is generated by the active engine(s). The vertical tail design is described in Subsection 4.8.3.

The second function of the tail is to providing stability. Again the horizontal tail is responsible for the longitudinal stability, while the vertical tail is responsible for the directional stability. Aircraft stability is defined as the tendency of an aircraft to return to the original trim conditions when the aircraft is diverted by a disturbance. One of the most common disturbances are gusts.

The third function of the tail is to provide control of the aircraft. The elevator is designed for longitudinal control, while the rudder is responsible for directional control. The tail must be able to control the aircraft such that the aircraft can change from one flight condition, e.g. cruise, to another flight conditions, e.g. loiter. In general, the tail is designed based on the trim requirements. In a later stage of the design the tail design is revised and will be based on stability and control requirements.

Before the tail design was initiated, first the type and location of the tail had to be determined. This is discussed in Subsection 4.8.1.

4.8.1 Tail design options

First, the tail type was selected. Numerous types can be thought of. The most common types are presented in Figure 4.35. In order to keep the design simple, it was decided to select a single boom conventional tail.

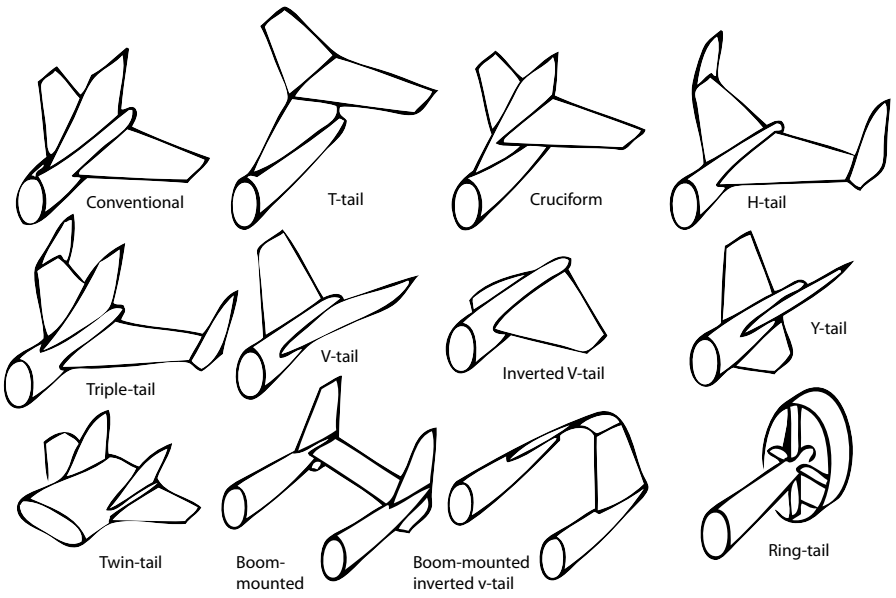

Figure 4.35: Tail design options[3]

From Figure 4.35 can be seen that within the group of single boom conventional tails there is also a variation in horizontal tail location. Figure 4.36 displays the

different horizontal tail options. From this figure can be seen that at higher angles of attack the horizontal tail has a significant effect on the flow over the vertical tail. Mid and low horizontal tails create a wake that effects the efficiency of the vertical tail. In order to prevent the horizontal tail effecting the vertical tail, a high horizontal tail was selected for this design. Besides the positive effect on the flow of the vertical tail, a high horizontal tail has also more ground clearance. This reduces the risk of striking the ground during landing.

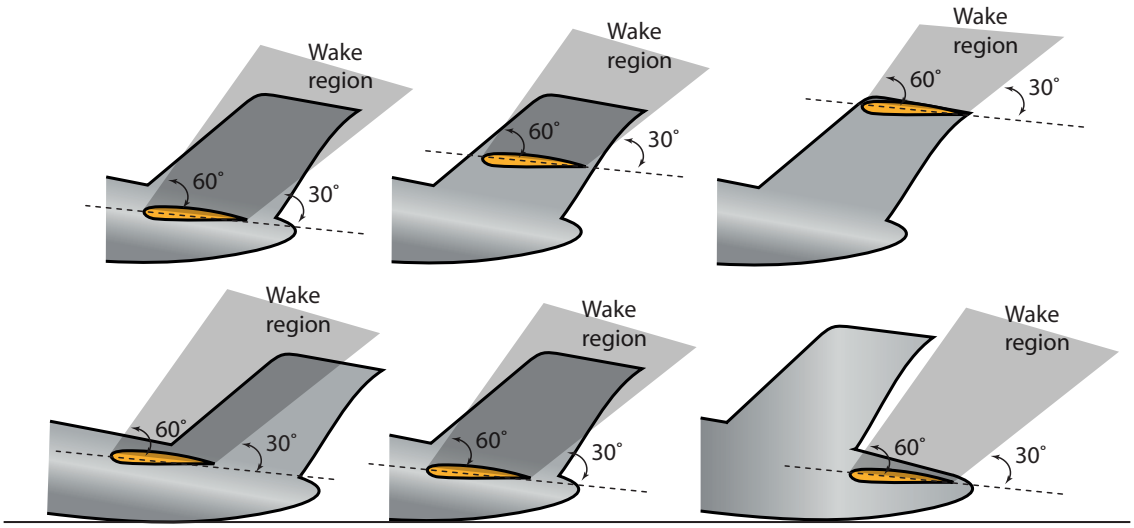

Figure 4.36: Horizontal tail location options

Besides the effect of the horizontal tail on the vertical tail, the wing has also an effect on the tail as a whole. Figure 4.37 shows the effect of the wing wake on the total tail configuration. It is desired to have a horizontal tail that is located above the wake that is created when the wing of the UAS is stalling. Assuming that the horizontal tail is also not in a stalling condition, this would allow the horizontal tail to maneuver the UAS back into normal flight conditions. To ensure this, a high horizontal wing (T-tail) configuration was selected. The next step in the process was to initiate the horizontal tail design.

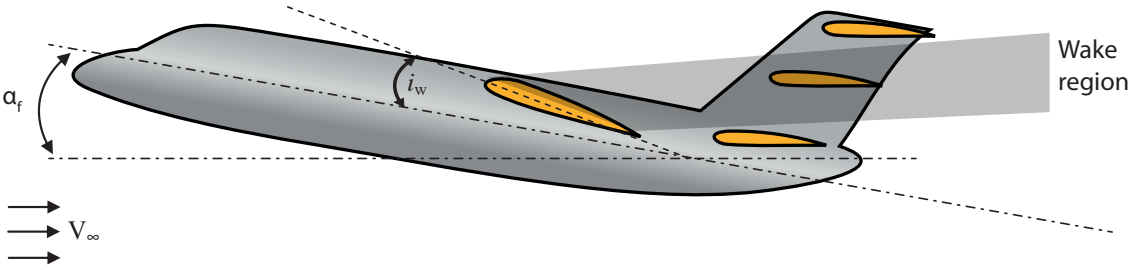

Figure 4.37: Effect of wing on tail

4.8.2 Horizontal tail design

The primary function of the horizontal tail is to provide longitudinal trim. During the horizontal tail design process the side view of the UAS is considered. Figure 4.38 shows this side view.

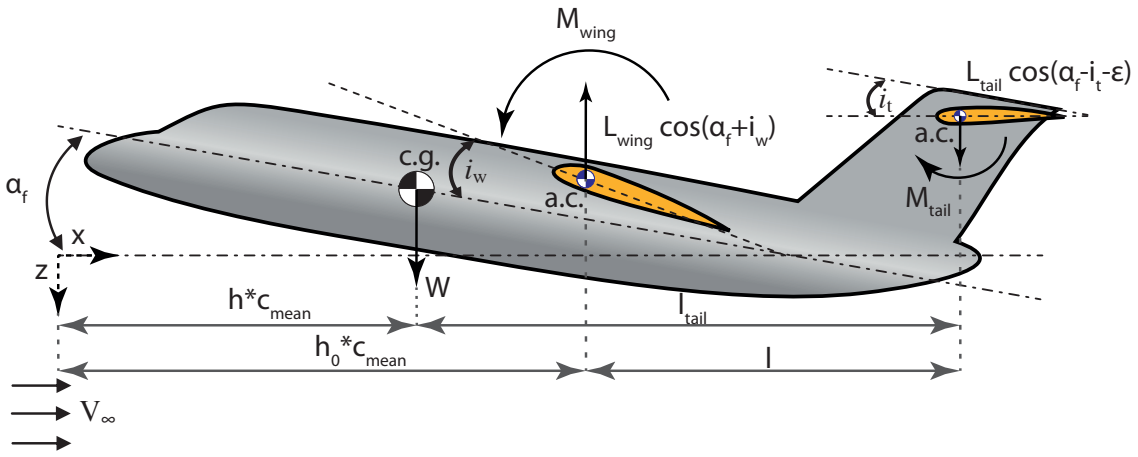

Figure 4.38: Longitudinal trim

From Figure 4.38 can be seen that the center of gravity of the UAS is forward of the aerodynamic center. In order to trim the UAS, the several moments about the y-axis need to be balanced. The aerodynamic pitching moment that is created by the wing is one of these moments. The moment about the center of gravity that is created by the wing lift is another one. Other moments are the caused by the fuselage, the engine thrust and wing drag e.g. These latter moments will not be incorporated in this preliminary design yet. Later on in the detailed design phase, its contribution has to be evaluated. For now this is considered to be out of the scope of the project. The pitching moment of the tail is also ignored.

From Figure 4.38 can be seen that the fuselage angle of attack, the wing incidence angle, the tail incidence angle and the downwash of the wing have an effect on the lift. The required angle of attack during loiter was determined to be 8° (see Table 4.19). From Table 4.20 was found that the optimum angle of attack during cruise is 3.4°. In order to have a fuselage angle of attack of zero degrees, the wing incidence angle, i_w, was set to 3.4°. In order to get the required wing angle of attack during loiter, the angle of attack of the fuselage must be increased to 4.6°. The tail incidence angle, i_t, depends on the required angle of attack of the horizontal tail and the downwash angle, ϵ, that occurs due to the presence of the wing. The required angle of attack of the horizontal tail is estimated in this subsection. After the tail design is complete, the downwash angle can be determined resulting in the required tail incidence angle. The wing and horizontal tail incidence angle can be optimized, such that minimum required power is achieved. This is out of the scope of this thesis. In future research this optimization can be worked out in detail.

Next, the horizontal tail design was initiated. Using Figure 4.38, the following equations were setup:

$$L = W = L'_{wing} - L'_{tail} \tag{4.95}$$

with:

$$L'_{wing} = L_{wing}\, cos(\alpha_f + i_{wing}) \tag{4.96}$$
$$L'_{tail} = L_{tail}\, cos(\alpha_f - i_{tail}) \tag{4.97}$$
$$\tag{4.98}$$

Elaborating Equation (4.95) becomes:

$$0.5\,\rho\,V^2\,S\,C_L = 0.5\,\rho\,V^2\,S_{wing}\,C_{L'_{wing}} - 0.5\,\rho\,V^2\,S_{H-tail}\,C_{L'_{tail}} \tag{4.99}$$

with:

$$C_{L'_{wing}} = C_{L_{wing}}\, cos(\alpha_f + i_{wing}) \tag{4.100}$$
$$C_{L'_{tail}} = C_{L_{tail}}\, cos(\alpha_f - i_{tail}) \tag{4.101}$$

Rewriting Equation (4.99):

$$C_L = C_{L'_{wing}} - \frac{S_{H-tail}}{S_{wing}} C'_{L_{tail}} \tag{4.102}$$

The moment about the center of gravity can be written as:

$$0 = M_{wing} - L'_{wing}(h_0\, c_{mean} - h\, c_{mean}) + L'_{tail}\, l_{tail} \tag{4.103}$$

with:

$$M_{wing} = 0.5\,\rho\,V^2\,S\,C_{m_{wing}}\,c_{mean} \tag{4.104}$$

Combining Equation (4.99) through Equation (4.104) becomes:

$$0 = C_{m_{wing}} - C_{L'_{wing}}(h_0 - h) + C_{L'_{tail}} \frac{l_{tail}}{c_{mean}} \frac{S_{H-tail}}{S_{wing}} \tag{4.105}$$

From Figure 4.38 the following can be derived:

$$l + h_0\, c_{mean} = l_{tail} + h\, c_{mean} \tag{4.106}$$

This leads to:

$$\frac{l_{tail}}{c_{mean}} = \frac{l}{c_{mean}} + (h_0 - h) \tag{4.107}$$

Combining Equation (4.105) and Equation (4.107) becomes:

$$0 = C_{m_{wing}} + (h_0 - h)\left(C_{L'_{tail}} \frac{S_{H-tail}}{S_{wing}} - C_{L'_{wing}}\right) + C_{L'_{tail}} \frac{l}{c_{mean}} \frac{S_{H-tail}}{S_{wing}} \tag{4.108}$$

Combining Equation (4.102) with Equation (4.108) leads to:

$$0 = C_{m_{wing}} - (h_0 - h)\, C_L + C_{L'_{tail}} \frac{l}{c_{mean}} \frac{S_{H-tail}}{S_{wing}} \tag{4.109}$$

From Equation (4.109) can be seen that the tail effectiveness is proportional to the tail area, the moment arm of the tail, the mean aerodynamic chord of the wing and the wing area. This factor is known as the horizontal tail volume coefficient[3] and is often used for initial estimation of the tail size. It can be written as:

$$c_{HT} = \frac{l}{c_{mean}} \frac{S_{H-tail}}{S_{wing}} \tag{4.110}$$

For the length between the wing aerodynamic center and the horizontal tail aerodynamic center a value is estimated. At this stage of the design this can be approximated by means of a percentage of the fuselage length. For now it is assumed that the propulsion system of the UAS is located above the wing. Using this together with the fact that the UAS has an aft tail leads to a 55% percentage (according to Raymer[3]). UASs were not yet included in determining this percentage. Later on, when the stability of the UAS is evaluated, the results must justify the chosen percentage. The next step in the process was to determine the average fuselage length of similar UASs. The average fuselage length of the UASs, that are listed in Table C.1, was determined to be 1.17 [m]. The mean aerodynamic chord and the surface area of the wing were found from Table 4.19. Before Equation (4.110) was used to determine the horizontal tail area, the horizontal tail volume coefficient had to be determined. Generally this value varies between 0.4 and 1.0 [-] (Raymer[3]). In order to have a relatively stable UAS, a value of 0.75 [-]was chosen. Combining all know values at this point together with Equation (4.110) a horizontal tail surface area of 0.1037 $[m^2]$ was determined.

Next, the wing pitching moment coefficient, $C_{m_{wing}}$, had to be determined. Raymer[3] provides an empirical formula for estimating the moment coefficient of a wing. Equation (4.111) represents this formula.

$$C_{m_{wing}} = C_{m_0}\left(\frac{A\, cos(\Lambda)^2}{A + 2\, cos(\Lambda)}\right) + 0.01\alpha_{twist} \tag{4.111}$$

At this stage of the design the aspect ratio, the sweep angle and the twist angle of the wing are known. The only unknown parameter of Equation (4.111) is the airfoil zero lift moment coefficient, C_{m_0}. By making use of XFOIL, it was possible to determine the moment coefficient of the naca23012 airfoil at loiter with a C_l-value of zero. Together with Equation (4.111) this resulted in a wing pitching moment coefficient of -0.0094 [-]. The wing pitching moment coefficient was also determined for the cruise flight condition. The resulting value turned out to be smaller than the wing pitching moment coefficient at loiter conditions. Therefore, the wing pitching moment coefficient at loiter conditions was used for the horizontal tail design.

The next step in the process was to determine the required lift coefficient of the horizontal tail, $C_{L_{tail}}$, in order to balance the UAS. For this, Equation (4.109) was used. Before this equation was solved, first $(h_0 - h)$ needed to be determined. This value was assumed to be equal to 0.1 [m]. Later on when the complete layout of the UAS is know this value is verified. The last value that had to be determined before the required horizontal tail lift coefficient was calculated, is the sweep angle of the horizontal tail. According to Raymer[3] the sweep angle is usually set to 5° more than the wing sweep. For this UAS design this would mean a sweep angle of 5°. Finally, by using this assumption together with the known wing lift coefficient, it was possible to determine the required lift coefficient. The result was a required horizontal tail lift coefficient of 0.0909 [-].

Subsequently, a horizontal tail airfoil had to be selected. Symmetrical airfoils are often employed for the horizontal and vertical tail. These airfoil types have a design lift coefficient and zero lift angle of attack of zero. This results in a low zero-lift/parasite drag, which is desired. An existing NACA-type airfoil was used for the tail design. In deciding which airfoil is most suitable for the horizontal tail, thickness of the airfoil is important. On one side it is preferable to have an airfoil as thin as possible (from an aerodynamic point of view), on the other hand the airfoil is preferred to be as thick as possible (from a structural point of view). A compromise should be reached. The naca0010 and naca0012 symmetrical airfoils are often used in tail design and were analyzed in order to see which one is most suitable for the horizontal tail.

In order to produce the required horizontal tail lift coefficient of 0.0909, XFOIL was used to find the associated angle of attack for both airfoils. An angle of attack of 1.10° was found for the naca0010 and an angle of attack of 0.39° was found for the naca0012 airfoil. From this analysis was also found that, as expected, the naca0012 airfoil has a larger drag coefficient than the naca0010 airfoil (0.0169 [-] versus 0.0142 [-]). Also the moment coefficient of the naca0012 airfoil was much larger than the moment coefficient of the naca0010 airfoil (-0.0115 [-] versus -0.0003 [-]).

At this point, the basis for the horizontal tail design is created. Next, the horizontal tail span, taper, root and tip chord length had to be determined. Generally, the horizontal tail aspect ratio is smaller than the aspect ratio of the wing. As a result, the horizontal tail will stall at a higher angle of attack. This allows the horizontal tail to maneuver the UAS back into normal flight conditions when the wing is stalling. Another reason why the aspect ratio of the horizontal tail is smaller is to reduce the bending moment that is created when the elevators are deflected. The horizontal tail aspect ratio was estimated to be $A_{H-tail} = \frac{2}{3}A_{wing}$(Raymer[3]). This

resulted in an aspect ratio of 6.54 [-]. Subsequently, Equation (4.112) in combination with the known required horizontal tail surface could be used to determine the horizontal tail span.

$$b_{H-tail} = \sqrt{A_{H-tail}\, S_{H-tail}} \tag{4.112}$$

This resulted in a horizontal tail span of 0.75 [m]. The taper ratio for a horizontal tail is generally between 0.3 and 0.5 (Raymer[3]). For this design a value of 0.5 was chosen. Later on this value is evaluated. For now this value was used to determine the horizontal tail root chord (see Equation (4.113)).

$$c_{root_{H-tail}} = \frac{2\, S_{H-tail}}{b_{H-tail}\,(1+\lambda_{H-tail})} \tag{4.113}$$

This resulted in a horizontal tail root chord value of 0.184 [m]. Using the taper ratio, the horizontal tail tip chord was determined to be 0.092 [m]. The final parameter that had to be determined was the mean aerodynamic chord of the horizontal tail. Equation (4.114) was used in determining this value. This resulted in a mean aerodynamic chord of 0.138 [m].

$$c_{mean_{H-tail}} = \frac{2}{3}\, c_{root_{H-tail}} \left(\frac{1+\lambda_{H-tail}+\lambda_{H-tail}^2}{1+\lambda_{H-tail}} \right) \tag{4.114}$$

This concludes the subsection on horizontal tail design. Table 4.22 represents an overview of the derived parameters in this subsection. From this overview can be seen that the naca0010 airfoil has a better performance than the naca0012 airfoil. It's drag and moment coefficient are both lower and therefore this airfoil is preferred. The next subsection describes the vertical tail design.

Table 4.22: Overview horizontal tail parameters

Parameter	Symbol	Value	Unit
Wing ac to horizontal tail ac distance	l	0.6435	[m]
Horizontal tail volume coefficient	c_{HT}	0.75	[-]
Horizontal tail area	S_{H-tail}	0.1037	[m^2]
Wing pitching moment coefficient	$C_{m_{wing}}$	-0.0094	[-]
Required tail lift coefficient	$C_{L_{tail}}$	0.0091	[-]
Required naca0010 airfoil loiter angle of attack	$\alpha_{naca0010}$	1.10	[deg]
Required naca0012 airfoil loiter angle of attack	$\alpha_{naca0012}$	0.39	[deg]
Drag coefficient naca0010 at loiter	$C_{d_{naca0010}}$	0.0142	[-]
Drag coefficient naca0012 at loiter	$C_{d_{naca0012}}$	0.0169	[-]
Moment coefficient naca0010 at loiter	$C_{m_{naca0010}}$	-0.0003	[-]
Moment coefficient naca0012 at loiter	$C_{m_{naca0012}}$	-0.0115	[-]
Aspect ratio horizontal tail	A_{H-tail}	6.54	[-]
Horizontal tail sweep angle	Λ_{H-tail}	5	[deg]
Horizontal tail span	b_{H-tail}	0.75	[m]
Taper ratio horizontal tail	λ_{H-tail}	0.5	[-]
Root length chord horizontal tail	$c_{root_{H-tail}}$	0.184	[m]
Tip length chord horizontal tail	$c_{tip_{H-tail}}$	0.092	[m]
Mean aerodynamic chord length horizontal tail	$c_{mean_{H-tail}}$	0.138	[m]

4.8.3 Vertical tail design

The primary function of the vertical tail is to provide directional stability. During the vertical tail design process again the side view of the UAS is considered. Figure 4.39 shows this side view.

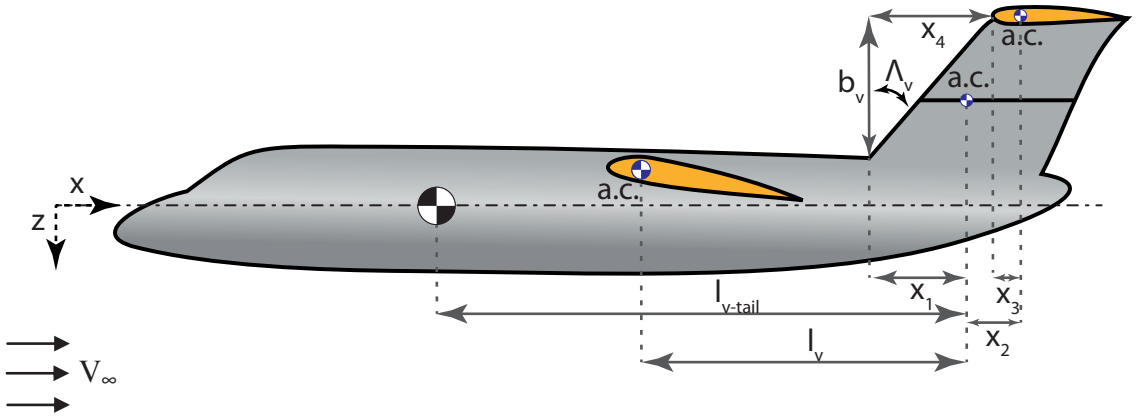

Figure 4.39: Directional trim

As in the previous subsection, also for the vertical tail design a tail volume coefficient is used to estimate the size of the tail (see Equation (4.110)). For the vertical tail this coefficient can be written as:

$$c_{VT} = \frac{l_v}{b}\frac{S_{V-tail}}{S_{wing}} \tag{4.115}$$

The vertical tail volume coefficient, c_{VT}, was assumed to be equal to 0.06 [-] (Raymer[3]). Subsequently, Figure 4.39 was used to determine the distance between the aerodynamic center of the wing and the vertical tail. First, the span, root chord length, tip chord length and the sweep angle of the vertical tail had to be determined. A value of 0.3 [m] was assumed for the vertical tail span. The tip chord length of the vertical tail was assumed to be equal to the horizontal tail root length, 0.184 [m]. The taper ratio was again obtained from Raymer[3] and estimated to be equal to 0.6 [-]. Using this taper ratio it was possible to determine the root chord length of the vertical tail. This resulted in a root chord length of 0.307 [m]. Using Equation (4.114) it was possible to determine the mean aerodynamic chord of the vertical tail. This resulted in $c_{mean_{V-tail}} = 0.251$ [m].

For low speed aircraft, there is little reason for having a vertical tail sweep beyond 20° (Raymer[3]). Therefore this sweep angle was assumed for the vertical tail sweep. Later on when the stability of the UAS is addressed, the resulting values are evaluated. Next, Equation (4.116) together with Figure 4.39 was used to obtain the distance between the horizontal tail aerodynamic center and the vertical tail aerodynamic center.

$$x_2 = x_4 + x_3 - x_1 \tag{4.116}$$

In case the aerodynamic center of the horizontal tail lies in front of the aerodynamic center of the vertical tail the following relation must be used:

$$x_2 = x_1 - x_4 - x_3 \tag{4.117}$$

with:

$$x_4 = tan(\Lambda_{V-tail})\, b_{V-tail} \tag{4.118}$$

$$x_3 = 0.25\, c_{mean_{H-tail}} \tag{4.119}$$

$$x_1 = \frac{x_4 \left(c_{root_{V-tail}} + 2\, c_{tip_{V-tail}}\right)}{3 \left(c_{root_{V-tail}} + c_{tip_{V-tail}}\right)} + 0.25\, c_{mean_{V-tail}} \tag{4.120}$$

The mean aerodynamic chord length of the vertical tail was determined as follows:

$$c_{mean_{V-tail}} = \frac{2}{3}\, c_{root_{V-tail}} \left(\frac{1 + \lambda_{V-tail} + \lambda_{V-tail}^2}{1 + \lambda_{V-tail}}\right) \tag{4.121}$$

Combining Equation (4.116) through Equation (4.121), x_2 was calculated to be 0.0310 [m]. Next, the distance between the aerodynamic center of the wing and the vertical tail was determined. From the previous subsection on horizontal tail design the, l was obtained (see Figure 4.38 and Table 4.22). Combining this value with x_2 results in $l_v = 0.6745$ [m]. Combining all know values together with Equation (4.115), a tail vertical surface area of 0.0495 $[m^2]$ was determined. Subsequently, the vertical tail aspect ratio was calculated. It was determined to be equal to 1.82 [-]. The vertical tail aspect ratio is generally between 1.5 and 2.0 [-] (Raymer[3]). A typical vertical tail surface area value is between 0.1 and 0.15 times the wing surface area (Raymer[3]). In this vertical tail design the ratio between the vertical tail surface area and the wing surface area was determined to be 0.1210 [-].

Subsequently, a vertical tail airfoil had to be selected. From the previous subsection was concluded that the naca0010 airfoil performs best for the horizontal tail design. The properties and performance of both airfoils also apply to the vertical tail design and therefore also a naca0010 airfoil is chosen for this part of the tail design. This concludes the subsection on vertical tail design. Table 4.23 represents an overview of the derived parameters in this subsection.

Table 4.23: Overview vertical tail parameters

Parameter	Symbol	Value	Unit
Wing ac to vertical tail ac distance	l_v	0.6745	[m]
Vertical tail volume coefficient	c_{VT}	0.06	[-]
Vertical tail area	S_{V-tail}	0.0495	$[m^2]$
Aspect ratio vertical tail	A_{V-tail}	1.82	[-]
Vertical tail sweep angle	Λ_{V-tail}	20	[deg]
Vertical tail span	b_{V-tail}	0.3	[m]
Taper ratio vertical tail	λ_{V-tail}	0.6	[-]
Root length chord vertical tail	$c_{root_{V-tail}}$	0.307	[m]
Tip length chord vertical tail	$c_{tip_{V-tail}}$	0.184	[m]
Mean aerodynamic chord length vertical tail	$c_{mean_{V-tail}}$	0.251	[m]

In the upcoming section, the wing-tail effects are addressed. In this section also the tail incidence angle is calculated.

4.9 Wing-tail effects

The previous section, Section 4.8, described the design of the tail. As discussed, it is desired to have a horizontal tail that is not in the wake of the wing when stall occurs. This allows the horizontal tail to maneuver the UAS back into normal flight conditions. This section shows the effects of the wing on the tail. The tail incidence angle is also derived in this section.

4.9.1 Wing wake

First, the effect of the wing on the tail is presented. In order to visualize the effect of the wing on the tail, XFLR5[87] is used. XFLR5 is an analysis tool for planes operating at low Reynolds numbers. It includes XFOIL's direct and inverse analysis capabilities. Wing design and analysis capabilities based on Lifting Line Theory, Vortex Lattice Method (Horseshoe vortex and ring vortex) and 3D Panel Method (Dirichlet and Neumann) are also included in XFLR5. The preliminary UAS design was implemented in this program. Figure 4.40a through Figure 4.40d show the UAS at loiter conditions. Figure 4.40e shows the UAS at stall conditions.

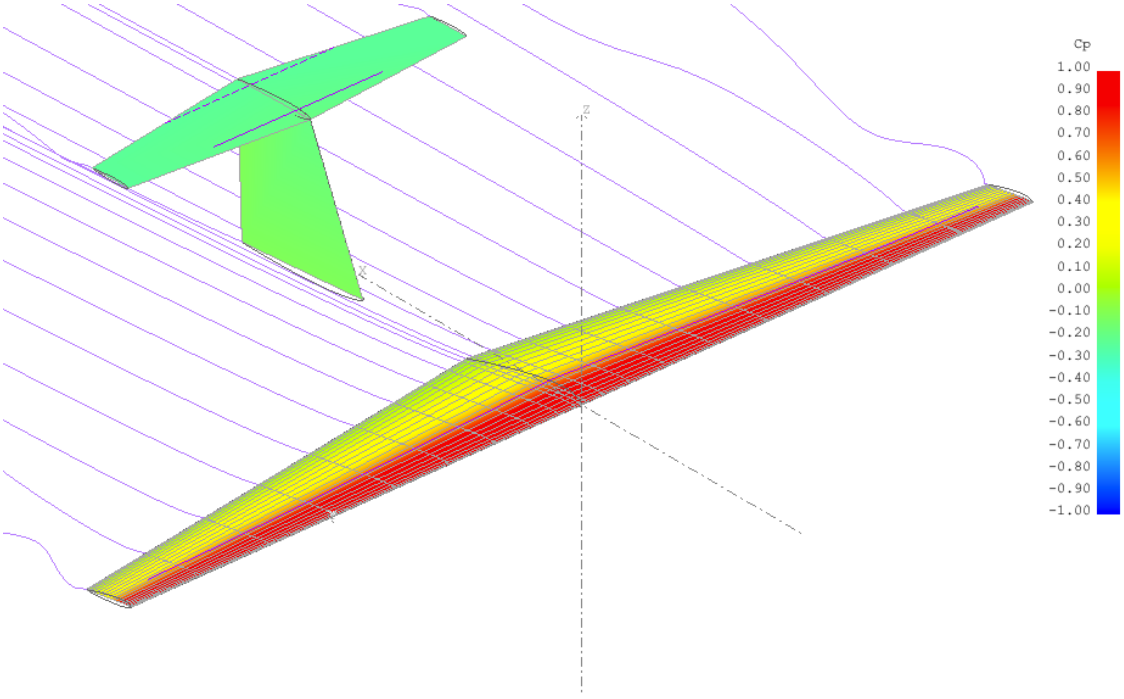

a: XFLR5 isometric view UAS at loiter

Figure 4.40: XFLR5 results

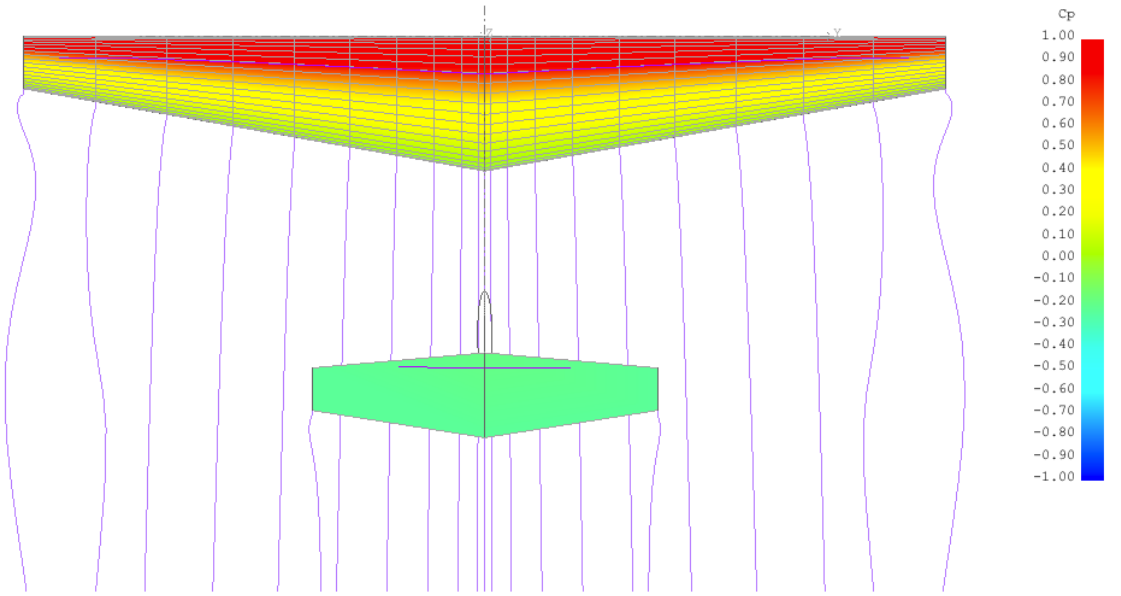

b: XFLR5 xy-view UAS at loiter

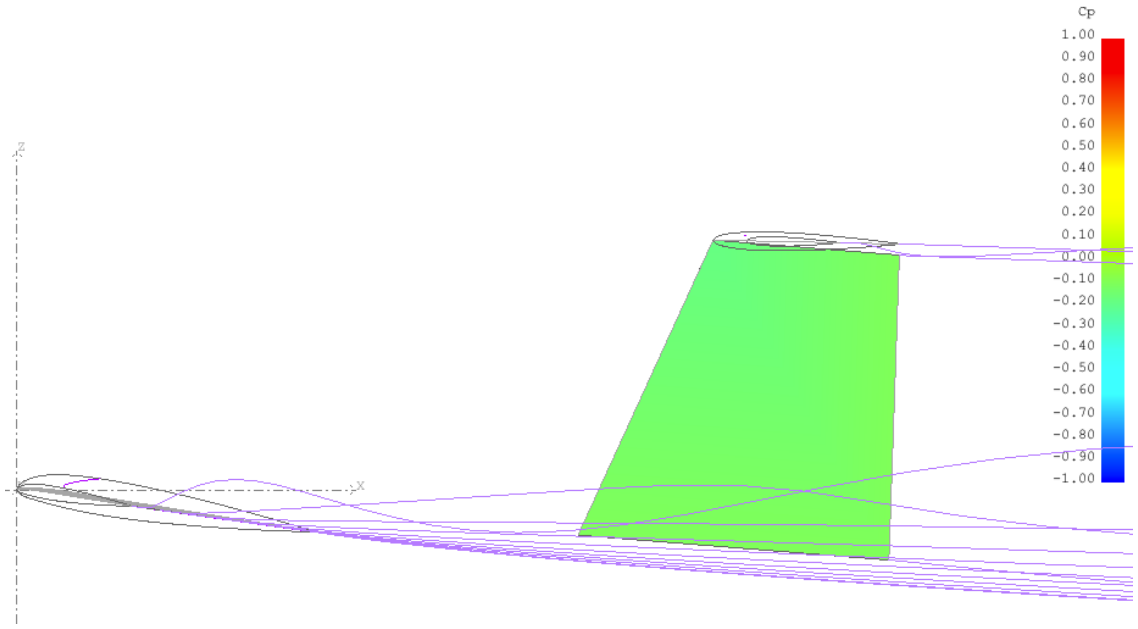

c: XFLR5 xz-view UAS at loiter

Figure 4.40: XFLR5 results (cont'd)

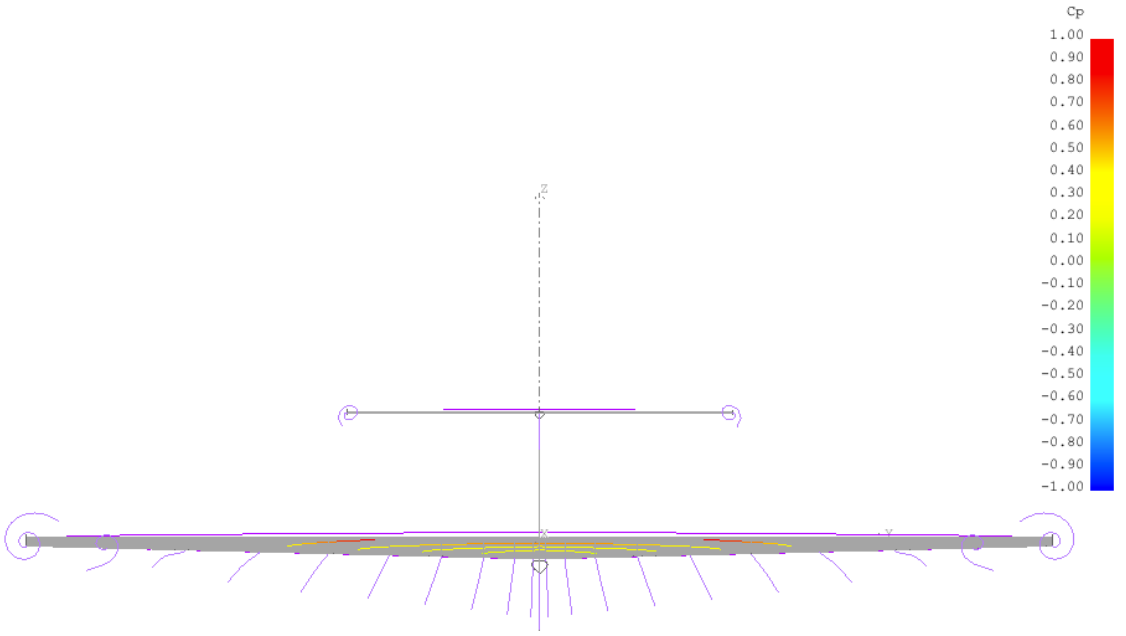

d: XFLR5 yz-view UAS at loiter

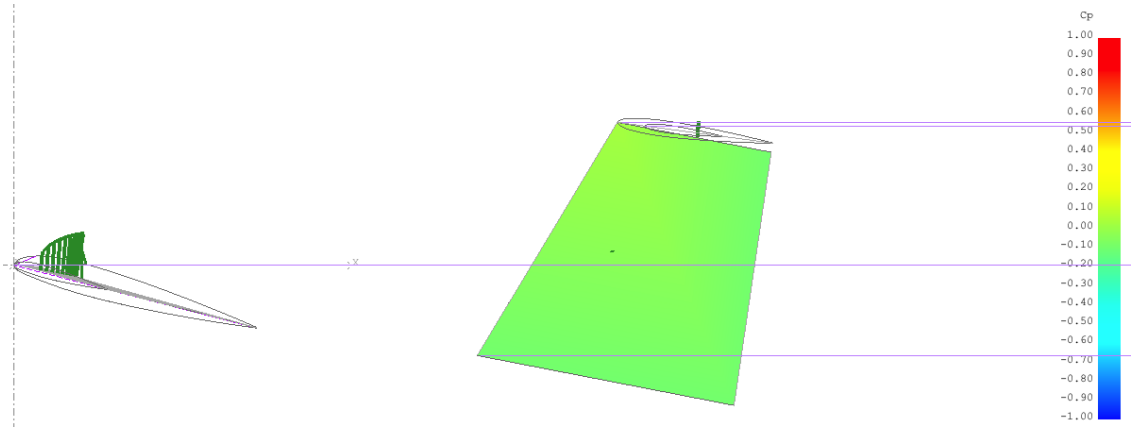

e: XFLR5 xz-view UAS at stall

Figure 4.40: XFLR5 results (cont'd)

From Figure 4.40c can be seen that during loiter the horizontal tail is not in the wake of the wing. From this can be concluded that for this flight conditions the wake of the wing does not significantly affect the performance of the horizontal tail. Figure 4.40e represents the UAS during loiter at an angle of attack of 11°, which means an effective angle of attack of approximately 15°. From Figure 4.33 can be seen that stall occurs at this angle of attack. XFLR5 also found that this angle of attack was out of the flight envelope. Therefore no circulation structure was created by XFLR5. In order to check if the horizontal tail is in the wake of the wing, the worst case scenario was used. The separation was assumed to start at the leading edge of the wing and the streamlines were assumed to be parallel to the incoming flow. When this scenario is considered, Figure 4.40e shows that the horizontal tail is still not in the wake of the flow. The horizontal tail therefore has the ability

to maneuver the UAS back into normal flight conditions. The horizontal tail size may even be reduced (after the stability has been addressed). This concludes the subsection on wing wake. In the following subsection the tail incidence angle is calculated.

4.9.2 Tail incidence angle

In order to determine the tail incidence angle, the wake downwash angle had to be determined. This angle was determined by using AVL again. AVL allows one to create a so called Trefftz plane. The Trefftz plane is a plane located at an infinite distance downstream of the UAS which is perpendicular to the wake. This plane is presented in Figure 4.41. By utilizing the Trefftz plane, the average downwash angle was estimated to be $-0.058°$.

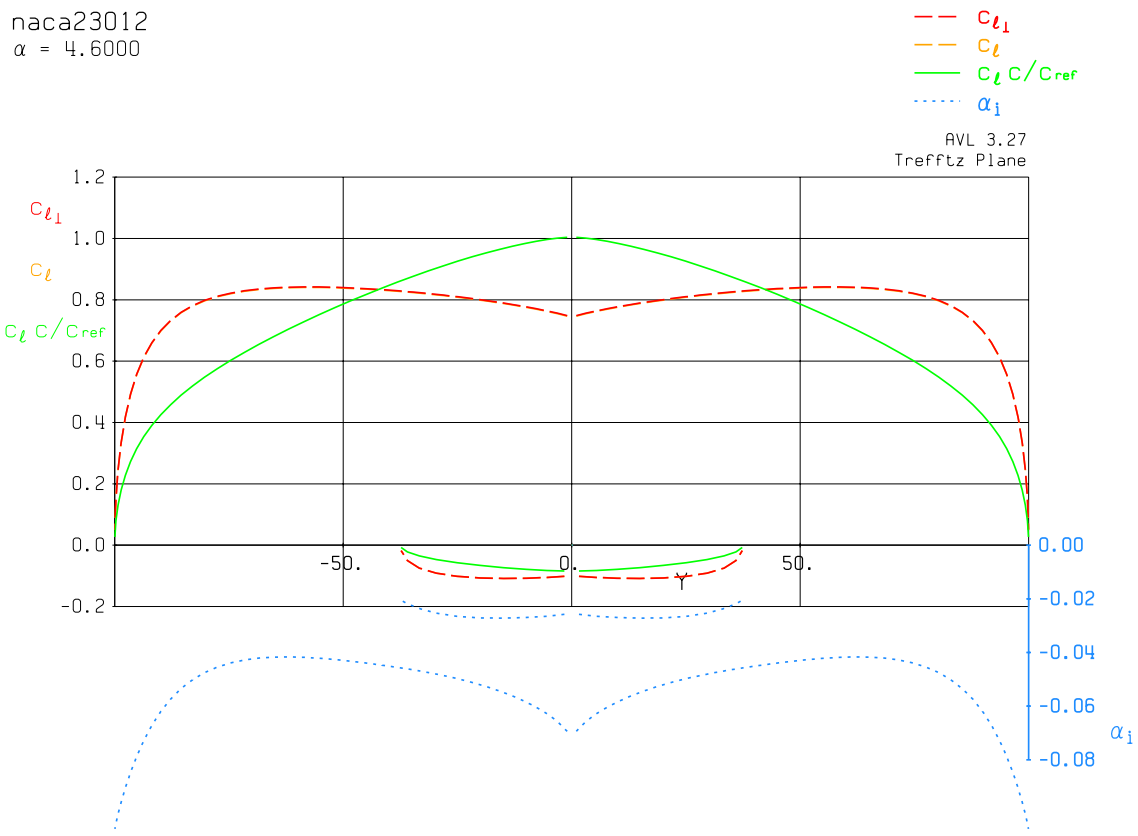

Figure 4.41: Trefftz Plane at 4.6 degrees angle of attack

Knowing the angle of attack requirements for the tail and the downwash angle of the wing at loiter, the tail incidence angle was determined. The angle of attack during loiter was determined to be 4.6°. The required angle of attack for the tail is 1.1°. These values in combination with the approximated downwash angle of $-0.058°$, resulted in a tail incidence angle of 3.4412°.

This concludes the section on wing-tail effects. Next, the stability of the UAS is evaluated. The results of this evaluation determine if the horizontal and/or vertical tail design must be revised.

4.10 Stability parameters

The previous two sections described the horizontal & vertical tail design and the effect of the wing on the tail. For now, the tail design has to satisfy stability requirements only. In a later stage of the design (detailed design), control requirements for the UAS design must also be satisfied. This requires a revision of the current tail design. This section presents the stability derivatives based on the current preliminary UAS design. Note that the stability of the UAS will not be addressed extensively.

Stability of an aircraft is defined as the tendency of an aircraft to oppose a disturbance and return to its initial condition. Stability is often divided into two groups, static and dynamic stability.

Static stability is defined as the initial response of an aircraft to a disturbance. Positive static stability means that the the aircraft has the tendency to return to its steady state flight condition without assistance (of the elevator e.g.). Dynamic stability is defined as the ability of the aircraft to damp out oscillations caused by the response of the aircraft to a disturbance.

The stability of the aircraft can be expressed in terms of stability derivatives. These derivatives can be computed by using relations. For this UAS design it was decided to not use these relations but to use the capabilities of AVL[86]. As stated in Subsection 4.7.4, AVL is a program that uses a vortex lattice method that is able to perform three dimensional inviscid calculations. This program was used to determine the stability derivatives for the UAS in loiter conditions. The wing parameters that were determined in Section 4.7 and the tail parameters that followed from Section 4.8 formed the input for AVL. The UAS geometry, as implemented in AVL, is shown in Figure 4.42 while the AVL input file can be found in Appendix I. Note that the fuselage is not included.

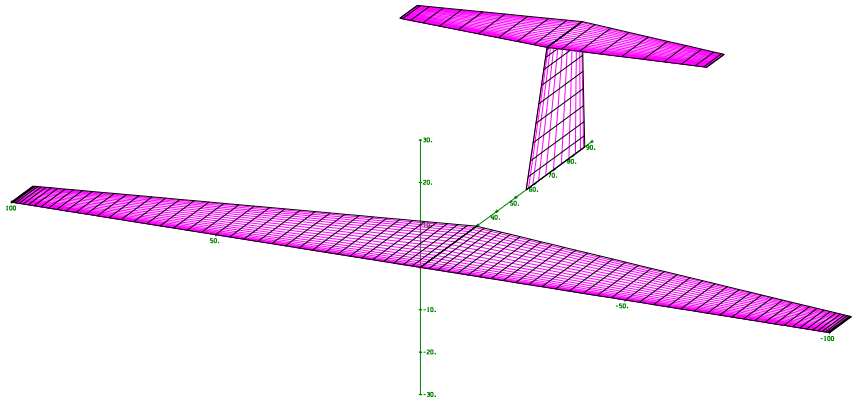

Figure 4.42: AVL UAS geometry

The results of the AVL stability analysis are presented in the upcoming two subsections. First the static stability is addressed. After that the dynamics stability is discussed.

4.10.1 Static stability

For an aircraft to be stable in all directions it must have longitudinal, lateral and directional stability (see Figure 4.34). The longitudinal stability is defined as the stability of any rotation about the y-axis (pitch e.g.). The lateral stability corresponds to the stability of any rotational motion about the x-axis (roll e.g.) and any linear motion along the xz-axis (sidewards motion e.g.). Finally the directional stability can be defined as the stability of any rotation about the z-axis (yaw e.g.) and any linear motion along the xy plane (sideslip e.g.). This requires the following:

- $C_{m_\alpha} < 0$
- $C_{l_\beta} < 0$
- $C_{n_\beta} > 0$

Every direction of stability is discussed in a separate part.

Longitudinal stability

The longitudinal stability is mainly influenced by the horizontal tail. The primary derivative that determines the static longitudinal stability is C_{m_α}. C_{m_α} represents the rate of change in pitching moment due to a change in angle of attack. In a stable, conventional aircraft, the center of gravity is forward of the neutral point of the airplane. An increase in angle of attack from trim increases the amount of lift generated by the wing and results in an increasing (negative) pitch-down moment. This drives the airplane back toward its original angle of attack. Besides the effect of the wing on the longitudinal stability also the fuselage has an influence. The thrust produced by the engine can also contribute to the longitudinal stability. Both effects are considered to be insignificantly small.

AVL calculated a C_{m_α}-value of $-3.748\,[1/rad]$. This value is rather high. This means that the UAS is very stable, maybe even to stable. This can be verified by checking the stability margin of the UAS. The stability margin is expressed as:

$$\frac{x_{n_{fix}} - x_{cg}}{c_{mean}} = -\frac{C_{m_\alpha}}{C_{L_\alpha}} \tag{4.122}$$

In order to solve for the stability margin, Equation (4.122) requires the lift curve slope denoted as C_{L_α}. From the AVL stability analysis, a value of $5.690\,[1/rad]$ was found. Using Equation (4.122) resulted in a stability margin of 0.66 [-]. A high stability margin results in an aircraft that may be hard to maneuver. Generally this value ranges between 0.1 and 0.3 [-][88]. When, after detailed analysis, is concluded that the aircraft is too stable in longitudinal direction, the horizontal tail design needs to be revised.

Lateral/directional stability

There is a coupling between the lateral and directional motion. Therefore the stability in those directions is combined. The primary lateral stability derivative is C_{l_β}. C_{l_β} is also called the dihedral effect, and is one of the important parameters for lateral/directional stability and handling qualities. A stable dihedral effect causes the vehicle to roll away from the sideslip. C_{l_β} is denoted as the rate of change in rolling moment coefficient due to a change in sideslip angle, β. For this UAS design, C_{l_β} was estimated to be $-0.043\,[1/rad]$. The requirement for this stability parameter is to be larger than zero.

The directional stability is mainly concerned with motion in yaw. The directional stability is mainly provided by the vertical tail. The fuselage also has a contribution to the stability. Again note that the effect of the fuselage is not included in the stability calculations for this UAS design. The primary derivative that determines the static directional stability is C_{n_β}. C_{n_β} represents the rate of change in yawing moment coefficient due to a change in sideslip angle, β. For the UAS to be stable, this parameter must be larger than zero. C_{n_β} was estimated to be $0.118\,[1/rad]$.

This concludes the static stability. Next, the dynamic stability is addressed.

4.10.2 Dynamic stability

Dynamic stability is hard to determine as the values for the stability derivatives are badly estimated using the vortex lattice method, AVL. A better way to approach this problem is to optimize the design and determine these values in a wind tunnel or with advanced CFD-methods and then make small changes to the design to ensure dynamic stability. For now, the AVL derivatives is all we have.

For the aircraft to have sufficient dynamic stability, it is required that all eigenmotions of the aircraft are stable, except for the spiral which is allowed to be unstable as long as the divergence of the aircraft happens slowly. In order to asses the dynamic stability often use is made of the linearized equations of motion. These equations were not used in assessing the dynamic stability. The following stability derivatives were addressed in stead:

- $C_{m_q} < 0$
- $C_{l_p} < 0$
- $C_{n_r} < 0$

Longitudinal stability

The primary longitudinal stability derivative is C_{m_q} (also pitch damping derivative). C_{m_q} is the rate of change of pitching moment coefficient with respect to change in pitch rate, q. A negative value for this stability derivative means a stable UAS. AVL showed a result of $-27.317\,[1/rad]$ for C_{m_q}. This value is rather high meaning that the UAS has high longitudinal stability.

Lateral/directional stability

Again the lateral and directional stability derivatives are combined in the same paragraph. One of the primary derivatives that determines the dynamic lateral stability is C_{l_p} (roll damping derivative). C_{l_p} is the effect of rolling moment due to roll rate derivative. At low speeds near stall, an increase in angle of attack on the down going wing may cause the wing to stall. A negative value for C_{l_p} ensures that the wing will autorotate back. For this UAS design, C_{l_p} was estimated to be $-0.516\,[1/rad]$.

As stated in the subsection on static stability, the directional stability is mainly provided by the vertical tail. The primary derivative that determines the dynamic directional stability is C_{n_r} (yaw-damping derivative). C_{n_r} is the rate of change of yawing moment coefficient with respect to change in yaw rate, r. A dynamically directionally stable aircraft requires the real parts of the roots of the lateral-directional characteristic equation to be negative. One of the major contributor to this requirement is C_{n_r}. This stability derivative needs to be negative in order to provide stability. For this UAS design, C_{n_r} was estimated to be $-0.100\,[1/rad]$.

This concludes the subsection on dynamic stability. Next, a short conclusion is drawn.

4.10.3 Conclusion

In this section the primary stability derivatives were determined. All parameters showed that the aircraft is both statically and dynamically stable (dynamic stability was only asses for loiter conditions). Note that the dynamic stability was not assessed by analyzing the eigenmotions. During the detailed design phase all stability parameters need to be fine tuned through CFD analysis and wind-tunnel testing. Even after that, actual flight testing must show that further tweaking is not required. Unfortunately, time to perform these advanced analysis was not available. Therefore this is a recommendation for further detailed design of the UAS.

An overview of all stability parameters that were obtained is shown in Table 4.24.

Table 4.24: Overview stability parameters

Parameter	Value
Static stability parameters:	
C_{m_α}, [-]	-3.748
C_{l_β}, [-]	-0.043
C_{n_β}, [-]	0.118
Dynamic stability parameters:	
C_{m_q}, [-]	-27.317
C_{l_p}, [-]	-0.516
C_{n_r}, [-]	-0.100

This concludes the section on static and dynamic stability parameters. In the next section, UAS material options are presented and discussed.

4.11 Materials

This section describes the material options for the UAS design. Note that structural analysis is not performed. For this thesis the structural analysis is out of the scope.

Numerous materials can be used for the construction of the UAS. It ranges from foam to titanium, all heaving different strengths and weaknesses. The structure needs to be strong and light-weight in order to give the UAS the best structural characteristics. Besides that, the structure also needs to be resistant to impacts (during landing e.g.). Different material options can be considered in a UAS design.

Foam is often used as a material for model aircraft. Off course there are different types of foam. Expanded PolyStyrene (EPS) and (EPP) are very popular. EPS has a density range of about 15 to 640 $[kg/m^3]$[89], is stiff, easy to moderate but brittle. EPS easily breaks on impact. EPP on the other hand, has good impact characteristics due to its low stiffness. This allows EPP to resume its shape after impacts. Due to the softness of EPP it is recommended to strengthen the material with (carbon) fiber reinforcements or to add carbon rods in critical areas. EPP has a density ranging between 20 and 200 $[kg/m^3]$[90]. EPP is harder to moderate and more expensive than EPS. Based on the impact performance and the low density of EPP, can be concluded that EPP is the most interesting foam option for this UAS design.

Besides foam, composites are also often used. At the end of Section 4.2 was already noted that currently all mentioned UASs of the mini UAS class are constructed out of composite materials. Carbon fiber, kevlar or glass fibers can be used together with a resin to form the composite. The density of, for example, carbon fibers is about 1750 $[kg/m^3]$[91]. Carbon has a very high stiffness and therefore light structures can be created. On the other hand, carbon fibers are relatively expensive and creating a composite structure is very labour intensive and time consuming. First, a mould should be created in which the layers of fibre need to be directed. Subsequently, the resin is added after which curing must take place.

The last material option that is considered is ABS plastics. This plastic is rigid, hard, easy to mould, has a high quality surface finish but is also brittle. The density of ABS is about 1000 $[kg/m^3]$[92]. If we compare this to the other options one can see that its density is much higher. This material is considered because so called 3D printers use this material. This allows a user to work out a design with 3D design software (Autodesk[93], Catia[94] or SolidWorks[95] e.g.). The resulting design can be send to a 3D printer (HP Designjet Color 3D Printer[96] e.g.) that is able to print three dimensional products from ABS plastic. Printing products is a relatively new technique and therefore large improvements are expected in the near future. Note that alternative 3D printers exist that use other materials to print their products. These materials may have the similar properties with a lower density, making it more interesting. This particular type of 3D printer is considered because the NLR owns such a 3D printer and allowed for rapid printing of 3D models. This enabled me to experiment with this new technique. An overview of alternative 3D printers is presented at a later stage of this subsection.

The most relevant material options that were considered during this UAS design are listed in Table 4.25. The advantages and disadvantages of each option are also listed in this table.

Table 4.25: Overview material design options

Design options:	Advantages:	Disadvantages:
EPP in combination with carbon fiber reinforcements.	Relatively easy to manufacture (easier than option 3). Strong, stiff and low skin roughness (less drag).	Heavier than option 2.
EPP with carbon rods	Easy to manufacture (easier than option 1 and 3). Light weight and cheap.	Relatively high skin roughness. Sensitive to breaking.
Composite	Strong, stiff and low skin roughness (less drag). Complex structures can be created.	Difficult to manufacture (labour intensive and time consuming). Heavier than option 1 and 2. Rather expensive.
ABS plastic	Very easy to manufacture (3D printer). High plasticity. High quality surface finish. Allows complex designs.	Brittle and heavy (heavier than all options).

Besides the 3D printer of the NLR that uses ABS plastic, the KLPD also owns four different 3D printers. In the following list an overview of the specifications of those printers is presented.

Table 4.26: Overview KLPD 3D printer options

Parameter	Dimension[97]	Zcorp[98]	Objet[99]	Solido[100]
Material	ABS	High performance composite material	Range of 107 different materials with up to 14 different materials in a single part	PVC material in combination with an in-house developed adhesive
Dimensions	250x250x300 (WxLxH) in [mm]	508x381x229 (WxLxH) in [mm]	500x400x200 (WxLxH) in [mm]	160x210x135 (WxLxH) in [mm]
Price	Starting at €25.900,-	On request	On request	Starting at €10.000,-
Advantages		No support material is required. Supports printing of logos, labels and images on the product. Fast printing abilities.	Solid products. Range of many different materials.	Relatively low cost printer.
Disadvantages	Prints a coarse structure. Support material is required (needs to be resolved after printing).	grain-like structure which results in a relative weak structure. In order to strengthen the product it can be immersed in wax.	The price is on request but the printer is expected to be expensive due to its abilities.	Print dimensions are small (compared to the other printers). The resulting products are laborious (support material must be removed by the user).

From this overview can be concluded that there is a wide variety in 3D printing. The dimensions that can be printed today are still limited but it is expected that future innovations will increase the abilities of 3D printing. As mentioned in the introduction of this section, structural analysis of the UAS design was out of the scope of this thesis. The ability of the UAS to withstand maneuver and gust loads must therefore be investigated in the follow up of this project. For now, option four of Table 4.25 was considered for this UAS design. This was done in order to get a feeling for the 3D printing technique.

The HP Designjet Color 3D Printer[96] of the NLR has the ability to print the following dimensions: 203x203x152 (WxLxH) in [mm]. With this in mind and looking at the dimensions of the UAS, one can conclude that the UAS needs to be printed in parts. The wing, for example, has to be printed in 10 parts. A 3D model of the UAS was created with a combination of Autodesk[93] and SolidWorks[95]. The resulting model can be seen in Figure 4.43a.

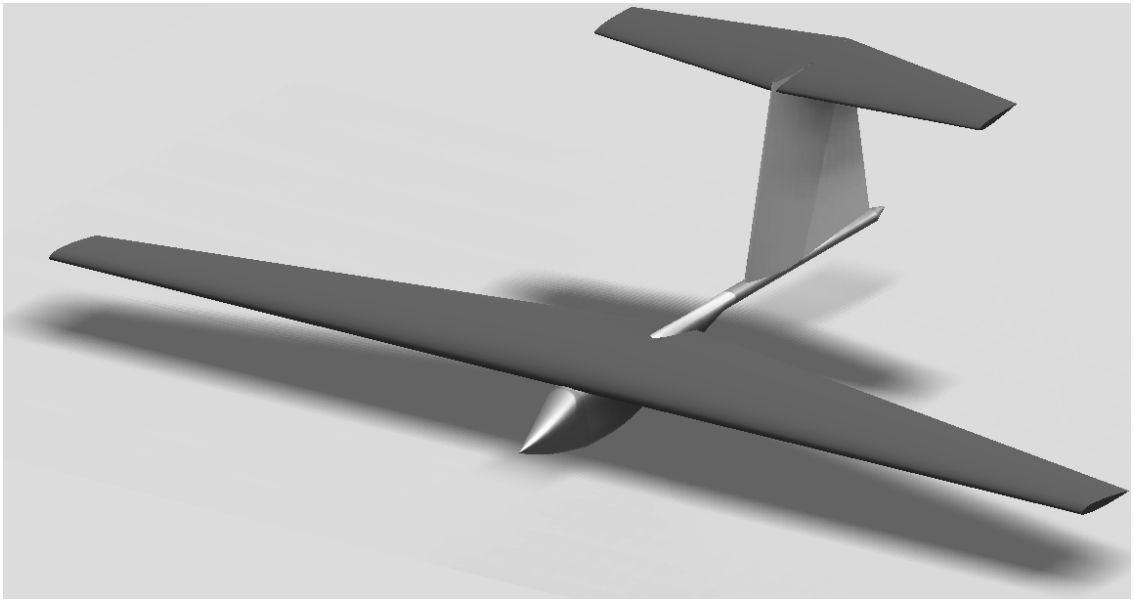

a: 3D UAS model

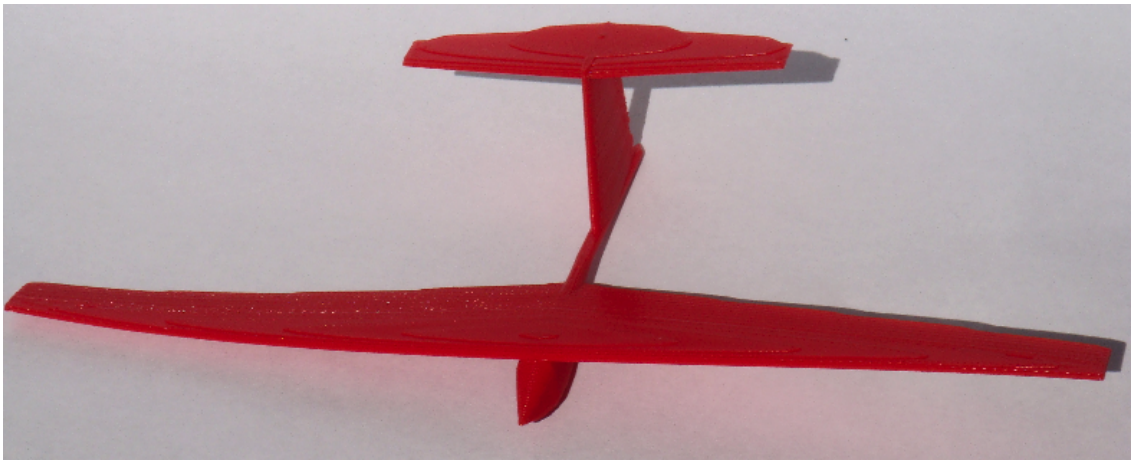

b: 3D-printed UAS model

Figure 4.43: UAS 3D model and UAS 3D-printed model

Experience with 3D printing resulted in the following experiences. Heat produced by the machine during printing caused the product to deform. In Figure 4.43b can be seen that the right wing (left wing for the viewer) of the UAS scale model is bended upwards. Looking at the edges of the printed scale model, one can see that the printer has difficulties in printing. From Figure 4.44 can be seen that some edges are not straight or have a 'saw-tooth-like' profile. The edge finishing is dependent

on the print direction. Edges in the horizontal plane are not straight because of the build-up of layer platforms. This can be seen from Figure 4.44b. In the vertical plane, the edges are faced with support material that is created by the printer to support the next layer. After washing out the support material a 'saw-tooth-like' edge profile remains (see Figure 4.44a). The edges can be smoothened by using sand paper but obviously this is not desirable.

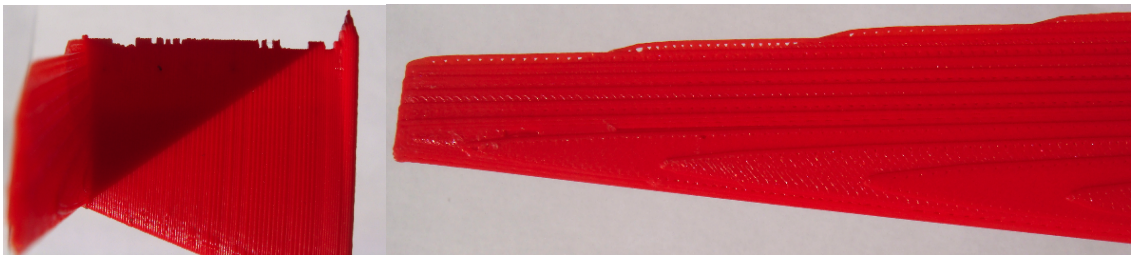

a: Side view 3D-printed UAS model

b: Top view 3D-printed UAS model

Figure 4.44: Side and top view 3D-printed UAS model

Some conclusions with respect to the material itself can also be stated. The material is very brittle and therefore may break on impact (if the thickness of the material is too low). Besides that, the density of the material is relatively high resulting in a heavy UAS design (in comparison with for example a composite structure). For now can be concluded that this manufacturing method is not yet suitable for creating UAS designs. The technique of 3D printing has much potential for future purposes but a lot of work is still to be done before this technique can be applicable for UAS designs. For now it is recommended to create the UAS structure out of EPP in combination with carbon fiber reinforcements/carbon rods. If, in a later stage of the design, it appears that this structure is not strong enough, a composite structure can be considered. For now an EPP in combination with carbon fiber reinforcements/carbon rods is considered to be sufficient.

Finally, the weight of the UAS material was estimated by using the volumes that were obtained from the Autodesk[93] 3D software. The volumes in combination with the density of EPP resulted in a weight of 288 [g] for the EPP parts. Three carbon fiber rods of 1 [m] long with a diameter of 1 [cm] were assumed to give enough strength to the wings and fuselage. The weight of these rods was also estimated with Autodesk[93]. A weight of 236 [g] was found for the carbon rods. This resulted in a total weight of 524 [g].

This concludes the section on materials. In the next section, the propulsion system design is elaborated.

4.12 Propulsion system

In this section the propulsion system of the UAS is discussed. First, the propulsion system design is discussed. After that, the propeller and engine combination selection is presented. Finally, the battery selection is shown.

4.12.1 Propulsion system design

Generally, the propulsion system consist out of a propeller, electrical engine and an Electrical Speed Controller (ESC). The ESC is connected to the electrical engine and the autopilot. In this way the autopilot can regulate the voltage of the engine.

The propulsion system needs to provide sufficient thrust to attain horizontal flight during loiter and high speed cruise. From Subsection 4.5.2 was concluded that electrical propulsion is most favorable for this UAS design. Electrical propulsion is not uncommon these days. As a result, a lot of electric engines are available. This makes the choice of electrical engine and propeller combination very difficult. In order to select the best electrical engine and propeller combination, different analysis programs were considered. Propcalc[101] is often used to estimate the performance of propellers for model aircraft. This program allows you to analyze a single propeller. In order to find the best suited propeller, it is not desired to manually compare the results of all propeller performance estimations. Therefore this program is not considered to be an option. A program that is also often used for electrically powered model aircraft is Drivecalc[102]. This program computes the performance of electrical engines. Unfortunately, this program does not have the ability to compare and analyze results of more than one engine at a time. This is not desired and therefore this program is discarded. The best option would be to have a program that is able to estimate the performance of multiple propellers and engines. QPROP[103] is such a program.

QPROP is an analysis program for predicting the performance of engine-propeller combinations. It is intended for large-scale parametric sweeps, driven manually or via batch execution. QPROP has a relatively sophisticated and accurate propeller aerodynamic model, and a general engine model which can be implemented via a user-supplied subroutine if necessary.

The propeller is modeled with an advanced blade-element/vortex method. The enhancement is primarily in the correct accounting of the prop's self-induction, which makes QPROP accurate for very high disk loadings, all the way to the static-thrust case. The blade airfoil lift characteristic is assumed to be a simple linear $C_{L,\alpha}$ line with $C_{L_{max}}$ and $C_{L_{min}}$ stall limiting. The profile drag characteristic is a quadratic $C_D(C_L)$ function, with an approximate stall drag increase, and power scaling with Reynolds number.

QPROP requires a fairly detailed description of the propeller geometry and blade airfoil characteristics. Although it would be nice to just specify the propeller's diameter and pitch, this is in general insufficient to accurately capture the propeller's performance.

The engine analysis uses basic engine parameters including the engine speed constant, K_v , the electrical resistance, R , and a no-load current, i_0. Matching the propeller and engine is initiated by determining the required electrical power by means of calculating the circulation. Subsequently, the circulation is be used to determine the torque and thrust. After QPROP has found the optimal values, the program will be terminated.

QPROP is based on brushed direct current electrical engines, therefore it is limited. Brushed direct current electrical engines have rotating coils which act as an electromagnet with two poles. The direction of the electrical current is reversed twice every cycle in order to create a push-pull effect against the permanent magnets on the outside of the engine. BrushLess Direct Current (BLDC) electrical engines are used more often nowadays. A BLDC engine uses an external rotor that contains permanent magnets. The three phase driving coils are activated, one phase after the other.

There are some advantages of choosing a BLDC electrical engine over a brushed direct current electrical engine. BLDC engines generate higher torque to weight ratios and torque to power ratios due to the absence of brushes. This results in a relatively high efficiency. Because of the absence of brushes, minimum maintenance is required. Also, the speed range is not limited when using a BLDC engine (also due to the absence of brushes). The windings of the engine are connected to the stator, which is connected to the case, giving it good heat dissipation properties. The downside of BLDC engines is the higher purchasing costs because a speed controller is required.

The advantages of the BLDC engine exceed the downside in purchasing costs. Therefore, a BLDC engine will be used in this UAS design. Because QPROP does not have the ability to model BLDC engines and the fact that the engine database is outdated, an alternative program had to be addressed. It happened to be that a fellow student was working on a program similar to QPROP. This program is called the UAV Propulsion Development Kit (UPDK) and is developed by Sander Hulsman[104].

The UPDK is a numerical simulation program that has the ability to examine a propeller and engine combination. It combines the theory of propeller performance with the theory of electrical engines and relates the resulting data to the flight characteristics of the proposed UAS. The simulation program is developed in Matlab[85]. In the next subsection the setup of the UPDK is presented.

4.12.2 UPDK setup

The UPDK consists out of different modules. Each module represents a part of the calculation process. A modular design has been chosen to create the possibility of easily adding modules. The modules implemented at the start of the thesis project are the propeller modeling module, an engine modeling module and a module modeling the behavior of the airframe. An overview of the interaction between the modules is shown in Figure 4.45.

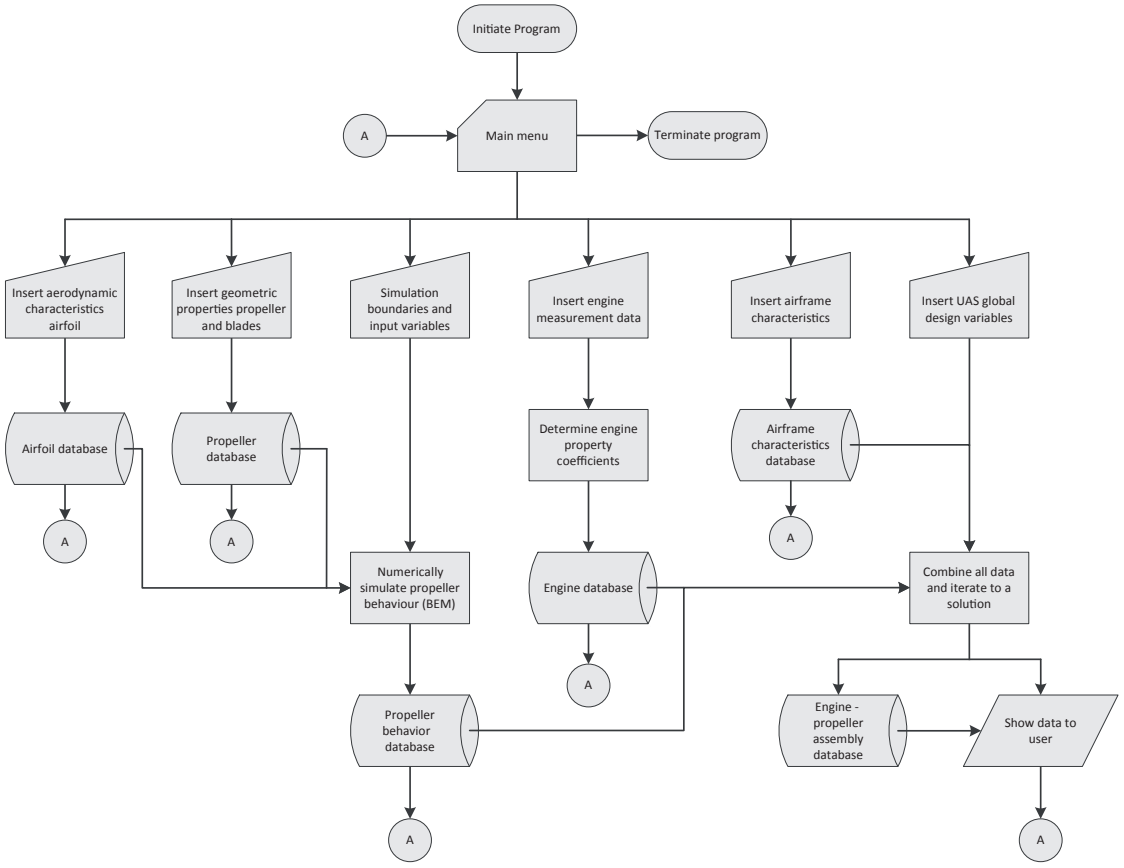

Figure 4.45: Flow chart UPDK[105]

After initiating the program an overview with four possibilities is shown to the user. The user can, for example, choose to simulate the performance and behavior of a propeller. Before the simulation can be initiated, the user must supply the program with data about the propeller. After completing the propeller simulation, the user must provide the program with engine and airframe data. Subsequently, the program can use the obtained data to analyze the assembly in flight. Each step in the process is described in a separate subsection.

Propeller modeling module

In order to simulate the propeller, Blade Element Momentum (BEM)[106] theory is used. This theory describes the steady state flow properties behind the rotating propellers. The propeller blade is broken down into several small part. The forces on each small blade element need to be determined. In order to find these forces, the induced angle of attack created by the rotating propeller blades needs to be calculated. This is where momentum theory comes into play. This theory assumes incompressible, inviscid and irrotational flow everywhere in the system. The propeller is modeled as an infinitely thin disk. By using Bernoulli's equations the pressure difference created by the propeller can determined. From this, the induced

velocity can be determined. Subsequently, the forces are integrated over the span of the blade in order to obtain the thrust and torque produced by the entire rotor at a certain flight velocity and rotational speed. Finally, the required shaft power that is needed to maintain the propeller's rotational motion can be computed.

The performance and behavior of the propeller is simulated for the required RPM- and velocity range that is set by the user of the program. Some corrections had to be applied for using BEM theory. BEM theory is able to investigate the 2D aerodynamics of a propeller blade. However, 3D effects play a role in the performance of a propeller. Vortices are created at the tip of the blade. Therefore, a correction factor was applied. Also, the behavior of the blade beyond the stall angle of the blade had to estimated. From the report of Hulsman et all[105] was obtained that the lift coefficient of the blade beyond the stall angle of attack was approximated by $C_l = 0.9\,C_{l_{max}}$. This assumption also accounts for tip losses. The drag coefficient must also be corrected at higher angles of attack. Viterna's method[107] was applied to correct the drag coefficient.

This describes in short the theory that is used for the propeller modeling module. The module was verified by comparing the results to the results that were obtained from Propcalc. More details about this module can be found in the report of Hulsman et all[105].

Engine modeling module

The behavior of the electrical engines was modeled by using analytical equations[108]. An electrical engine is able to rotate and exercise torque due to the constantly changing magnetic flux induced in the coils of the engine. The data required to model the behavior of the electrical engines was derived from DriveCalc[102]. This program includes static measurement data of the engines. The engine modeling module uses this data to iteratively estimate the performance and coefficients of the engine. During this loop, the estimated engine coefficients and performance data are compared to the available test data. To ensure that the module was working properly, the results were compared to calculations that were performed with DriveCalc. More details on the theory behind this module can also be in the report of Hulsman et all[105].

Airframe modeling module

This module describes the performance of the UAS in short. The lift and drag of the UAS at a certain angle of attack over a typical velocity range are required in this module. This performance data is used in the last module. Other values like wingspan, wing area, weight and height of the UAS can also be provided to this module. These values are used to analytically estimate the UAS performance when the user has not supplied the module with lift and drag data. This module is a bit then, but will be extended in the near future.

Engine-propeller assembly module

This last module combines the previously described modules. The propeller simulations and calculated engine performances in combination with the airframe performance are used to determine the performance of the complete propulsion system. There are two modes that can be addressed in this module, hover mode and forward flight mode. For this UAS design, hover mode is not applicable. Within the horizontal flight mode, the amount of props, the design velocity and the battery voltage need to be provided before the module can be initiated.

In determining the horizontal flight performance of the propulsion system, multiple iterations are performed. First, the RPM at which the propeller delivers the required amount of thrust was found. This calculation was performed for the entire speed range that was provided in the airframe module. Once the right propeller RPM and thrust is found, the required shaft power can be determined. The next step was to find the operation point of the engine. The engine must be able to deliver the required amount of shaft power at the RPM that is required by the propeller. In this way, the propulsion system characteristics were determined for the entire flight envelope of the UAS. From this data the optimum flight speed was derived based on the lowest amount of required shaft power. This information together with the efficiency and electrical power consumption at the design speed is presented to the user by means of a table. Note that a more detailed airframe file also results in a more detailed analysis of the complete propulsion system. From this can be concluded that the airframe file forms a key element in whole process.

In order to verify that the module works properly, the results of various engine-propeller assemblies were compared to results from the same assembly in Drivecalc.

This concludes the description of the four UPDK modules. Next, the extensions of the UPDK are discussed.

UPDK extensions

At the start of this thesis project, the program was able to determine the performance of a single engine-propeller combination. Together with the developer of the UPDK, Sander Hulsman, and a fellow graduation student, Stefan Otting, it was decided to expand the abilities of the UPDK. Extending the engine and propeller database was the first priority.

The latest electrical engines were incorporated in the UPDK. DriveCalc[102] was used to derive the required parameters of the engines. Test data of the engines was also obtained from DriveCalc[102]. 1700+ engines with more that 7000 test data records were derived from the databases of DriveCalc[102]. This database was filtered based on the available test data. Engines that did not have any test data were discarded. This resulted in a database containing about 1500 engines. Subsequently, a script was created, writing the data to a readable format for the UPDK. The format of such an engine file is shown in Appendix H.1.

Next, additional propellers were obtained from PropCalc[101]. This resulted in a total of 40 propellers. Again, a script was written in order to write the data into

a readable format for the UPDK. The format of the propeller file is presented in Appendix H.2.

Subsequently, a batch mode had to be added to the UPDK in order to be able to analyze all the available engine-propeller combinations. Hulsman took this task upon himself. After refining the engine-propeller assembly module it was possible to run all engine-propeller combinations. Before the batch run was initiated, first all 40 propellers were simulated for a flight speed range between 0 and 40 m/s with steps of 1 m/s. The RPM was also varied ranging from 1000 [RPM] to 30000 [RPM] with steps of 1000 [RPM]. Next, a test batch of 100 combinations was performed. After this batch it became clear that more work was required. The test took over 20 minutes to complete. Analyzing the all engine-propeller combinations ($1500 \cdot 40 = 60000$ combinations) would require more than eight days of computational time. In order to reduce the computation time, preselection of the engines and propellers had to be performed.

The preselection of the propellers was based on the propeller simulations that were executed. After setting the required thrust and flight speed, it was possible to check which propellers were able to deliver the required thrust at that flight speed. The required thrust at loiter and cruise speed were obtained from the equations derived in Subsection 4.5.1. The maximum RPM at which the propellers deliver that thrust force was also limited (to keep the noise level to a minimum). Finally, a certain minimum efficiency was required at the operating point of the propeller. These filters are used for the propeller preselection. It is possible to add more filters. The diameter of the propeller and the number of blades can also be used in order to filter out undesired propellers.

The preselection of the engines was based on the required engine power, the amount of available test data sets and the engine weight. From the calculations in Subsection 4.5.1, the required engine power was estimated for both loiter and cruise flight condition. In order to get a reliable performance estimation it was decided to discard engines that have less than four test datasets available. From the engine file, that is shown in Appendix H.1, can be seen that for all datasets the power can be estimated by multiplying the voltage with the current. This gives an indication of the amount of power that can be delivered by the engine. Note that this is a static amount of power. There is a chance that engines, with the ability to produce the required amount of power, will drop out. For now this is taken for granted but in future research this effect must be examined. Finally, the engine database was also filtered based upon engine weight. Besides executing preselection based upon these variables, it is also possible to include other additional filters. Price, maximum current or engine speed constant (amount of RPM/Voltage) can be used to filter out more electrical engines.

Besides preselection of the engines and propellers, also the propeller modeling module was revised. Circulation/swirl (Helmoltz's theorem) was implemented by Hulsman in order to account for 3D effects. The engine modeling module was also revised. A second order electric engine model was included. The main difference between this model and the previous model is the included heat dissipation. The assembly module of the UPDK was also revised. Newton's method was included.

This method is specialized in finding the minima of differentiable functions. Implementing this method significantly reduced the matching time of the engine-propeller combinations. Previously up to 500 iterations, or more, were required to match the engine-propeller combination. After implementing Newton's method, the amount of iterations were reduced by approximately 98%. This increased the chance of obtaining a good match without reaching the maximum allowed number of iterations that was set to 500.

Finally, multi-core functionality was added to the program. This resulted in a significant decrease of computational time. This concludes the extensions that were included in the UPDK. Before the UPDK was used to determine the optimum engine-propeller combination, first the propulsion system location had to be determined.

4.12.3 Propulsion system location

There are a number of possible locations for the propulsion system. The locations that were considered during this UAS design are presented in Figure 4.46. Each location has its pro's and con's.

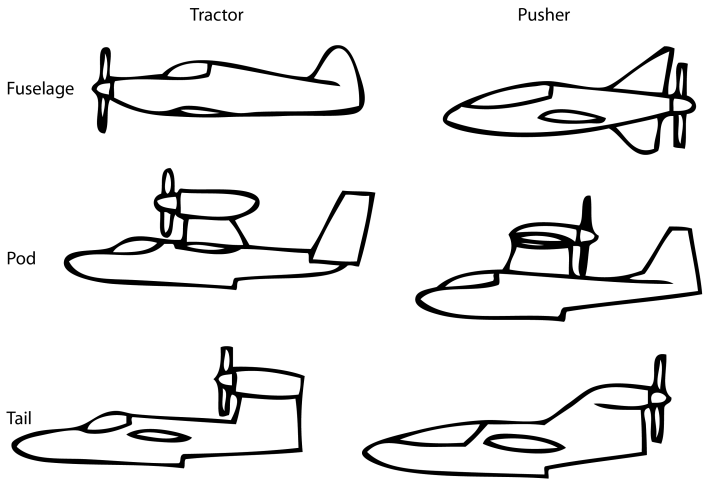

Figure 4.46: Propulsion system location options[3]

A tractor installation has the propeller in front of its attachment point. A pusher location on the other hand, has the propeller behind the attachment point. The tractor location provides a source of cooling air and places the propeller in undisturbed air. On the other hand, having a tractor installation creates a noticeable amount of extra skin friction drag (due to the turbulence from the propeller wake). Having a pusher installation allows the wing of the UAS to fly in undisturbed air.

Upper fuselage pods and tail-mounted pods are generally used for UASs that need a large amount of propeller clearance. The high thrust line can cause negative control effects (nose down pitching moment).

For this UAS design it is decided to use a tail mounted tractor installation. This allows the engine to be cooled by the ram air. Also, ground clearance during take-off and landing is important for this UAS design. This location not only provides sufficient clearance, it also provides noise shielding. This is beneficial when the UAS is used for a reconnaissance mission. The effect of extra friction drag is not expected to be very large. Obviously extra friction drag is created on the tail. This effect and the effect of the relatively high thrust line of the system must be investigated in future research on this UAS design. When control issues are identified during this analysis, the installation location needs to be revised. For now this is considered to be out of the scope of this thesis.

Next, the engine and propeller selection based on the UPDK with extensions are discussed.

4.12.4 Engine and propeller selection

The next step in the process was to analyze the results from the UPDK. As stated previously, approximately 1500 engines and 40 propellers were implemented in the UPDK. In order to keep the computational time to a minimal preselection was applied. Table 4.27 gives an overview of the preselection parameters that were used for the preselection of both the engine and the propeller.

Table 4.27: Overview UAS engine and propeller preselection parameters

Preselection parameters	Symbol	Value	Unit
Preselection parameters engine:			
Min. available max. power	P	200	[W]
Number of available data sets	N	4	[-]
Max. weight	W_{engine}	200	[g]
Preselection parameters propeller:			
Cruise speed	V_{cruise}	35	[m/s]
Thrust at cruise speed	T_{cruise}	5.5	[N]
Max. RPM at cruise speed	RPM_{max}	30000	[rev/min]
Min. efficiency at cruise speed	$\eta_{p_{cruise}}$	0.8	[-]

From Table 4.27 can be seen that an engine must at least be able to produce 200 [W] of power. This is based on the estimated cruise power stated in Table 4.21. In order to increase the accuracy of the engine performance estimation, at least four sets of test data had to be available for the engines. The final preselection parameter for the engines was weight. This was set to a maximum of 200 [g].

The preselection of the propellers was based on the ability of the propeller to produce the required amount of thrust at cruise speed. A maximum RPM and minimum efficiency at cruise speed were also used in the preselection of the propellers.

Next, the preselection parameters were implemented in a Matlab[85] code in order to automatically analyze the engines and propellers available in the UPDK database. A graphical overview of the propulsion system analysis is shown in Figure 4.47.

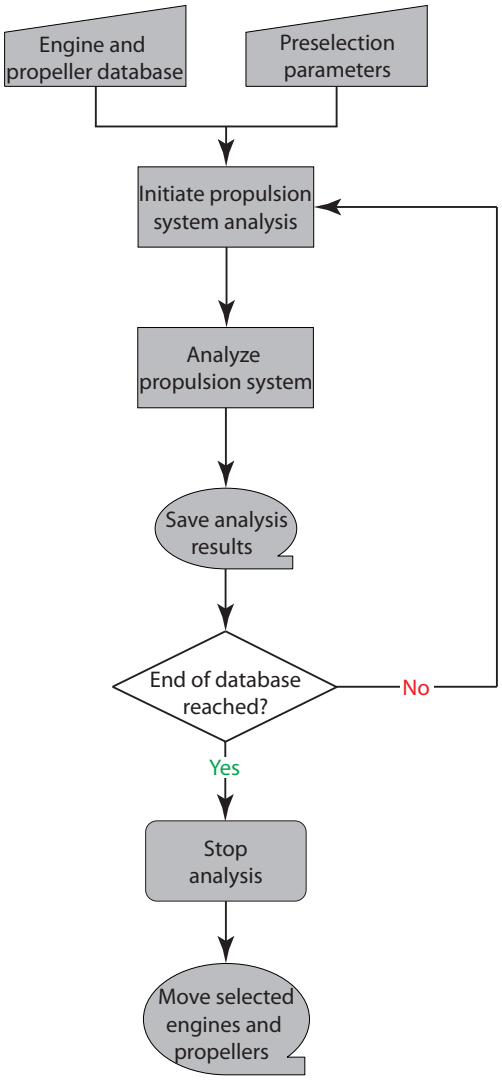

Figure 4.47: Propulsion system analysis overview

After performing the preselection of the engines and propellers, 346 engines and 8 propellers remained. Subsequently, these engines and propellers were analyzed by using the UPDK. Analyzing the combinations required a computational time of approximately 7 hours. The analysis resulted in 1572 healthy combinations. This means that 1572 engine-propeller combinations are able to provide propulsion to the UAS up to the cruise flight velocity.

The next step in the process was to find the best engine-propeller combination for this preliminary UAS design. Again a filter was applied. Based on the mission profiles described in Subsection 4.3.1, this filter was defined. Mission profile one requires the UAS to loiter for at least 30 minutes. In order to ensure the least amount of fuel to be carried by the UAS, the required amount of energy must be kept to a minimum. This was achieved by finding the point of minimum required power within the complete flight velocity range. This in combination with the loiter time results in the amount of required energy. From the results, a top five selection was created. In Figure 4.48, the results of the engine and propeller selection for mission profile one are presented.

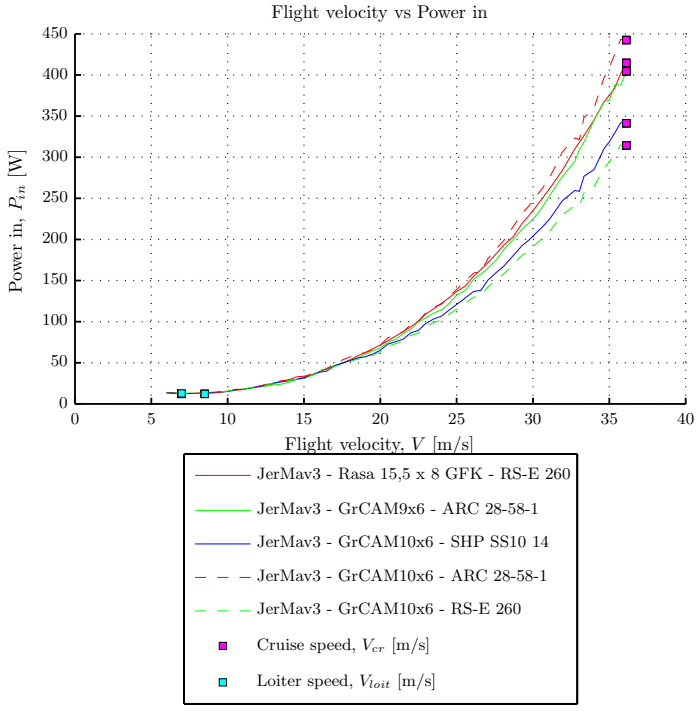

a: Flight velocity versus Power in

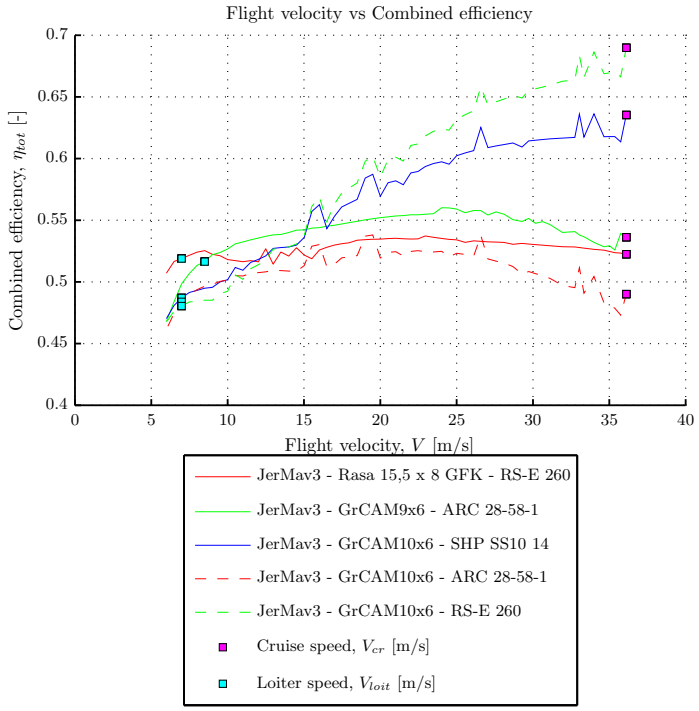

b: Flight velocity versus Combined efficiency

Figure 4.48: Results engine and propeller selection mission profile 1

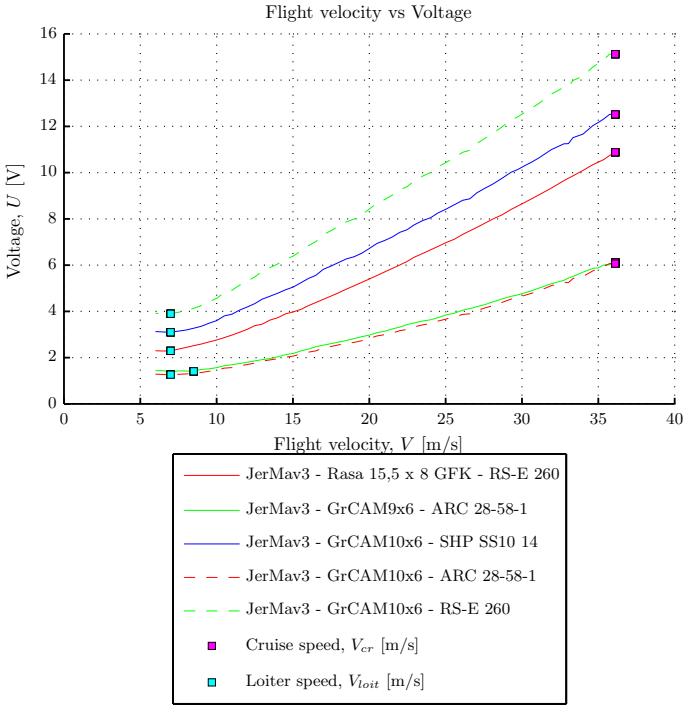

c: Flight velocity versus Voltage

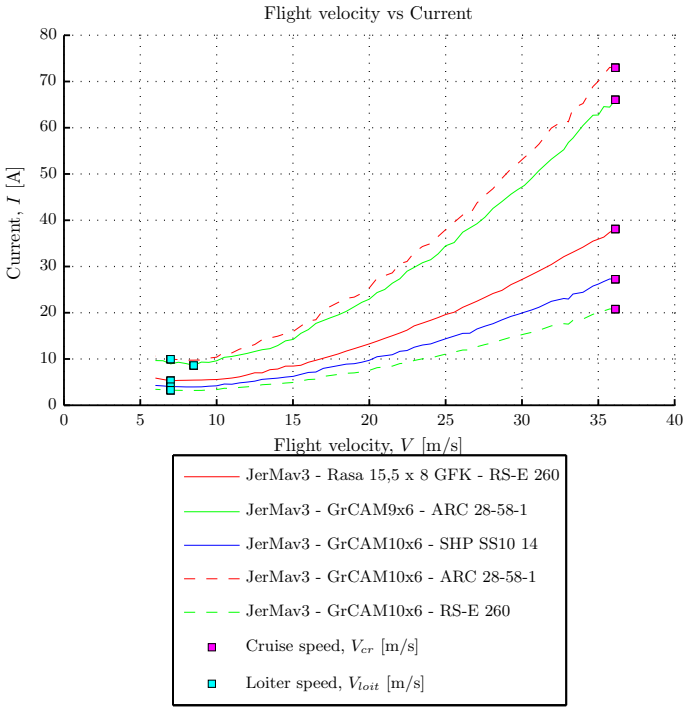

d: Flight velocity versus Current

Figure 4.48: Results engine and propeller selection mission profile 1 (cont'd)

Subsequently, the most important parameters derived from Figure 4.48 in combination with additional parameters are presented in Table 4.28.

Table 4.28: Overview selected UAS engine and propeller parameters mission profile 1

Parameters	Symbol	1[a]	2[b]	3[c]	4[d]	5[e]	Unit
Overall parameters:							
Optimum loiter speed	$V_{P_{r_{min}}}$	7.0	8.5	7.0	7.0	7.0	[m/s]
Actual loiter speed	V_{loit}	8.33	8.33	8.33	8.33	8.33	[m/s]
Cruise speed	V_{cruise}	36.11	36.11	36.11	36.11	36.11	[m/s]
Comb. efficiency at loiter	$\eta_{com_{loit}}$	0.519	0.516	0.487	0.484	0.481	[-]
Comb. efficiency at cruise	$\eta_{com_{cruise}}$	0.523	0.536	0.635	0.490	0.690	[-]
Total required energy	E_{total}	6.06	6.08	6.26	6.30	6.35	[Wh]
Engine parameters:							
Loiter power	P_{loit}	12.12	12.15	12.61	12.93	13.23	[W]
Cruise power	P_{cruise}	415	405	341	442	314	[W]
Efficiency at loiter	$\eta_{e_{loit}}$	0.722	0.708	0.694	0.698	0.682	[-]
Efficiency at cruise	$\eta_{e_{cruise}}$	0.739	0.655	0.783	0.604	0.850	[-]
Voltage at loiter	U_{loit}	2.29	1.41	3.15	1.27	3.90	[V]
Voltage at cruise	U_{cruise}	10.88	6.13	12.52	6.07	15.12	[V]
Current at loiter	I_{loit}	5.29	8.62	4.04	9.96	3.26	[A]
Current at cruise	I_{cruise}	38.11	66.03	27.27	72.96	20.79	[A]
Weight	W_{engine}	128	153	90	153	128	[g]
Price	-	-	78,-[109]	-	78,-[109]	-	[€]
Propeller parameters:							
Efficiency at loiter	$\eta_{p_{loit}}$	0.728	0.729	0.711	0.711	0.711	[-]
Efficiency at cruise	$\eta_{p_{cruise}}$	0.707	0.818	0.812	0.812	0.812	[-]
RPM at loiter	RPM_{loit}	1912	3800	3288	3288	3288	[rev/min]
RPM at cruise	RPM_{cruise}	7252	13041	11864	11864	11864	[rev/min]
Diameter	D_p	0.384	0.229	0.254	0.254	0.254	[m]

[a] Rasa 15.5x8 GFK + RS-E 260
[b] Graupner CAM9x6 + ARC 28-58-1
[c] Graupner CAM10x6 + SHP SS10 14
[d] Graupner CAM10x6 + ARC 28-58-1
[e] Graupner CAM10x6 + RS-E 260

From Table 4.28 can be seen that from an energy point of view the Rasa 15.5x8 GFK propeller with the RS-E 260 engine is the best solution for mission profile one. However, looking at the availability of the engine results in a problem. The engine is not available and therefore a different option needed to be considered. Options three and five were also not available and therefore option two was the best option for mission profile one.

Next, the top five selection based on mission profile two was determined. Mission profile two requires the UAS climb, cruise for at least 2 minutes, cruise back at optimum speed and loiter for the remainder of the 30 minutes. Again, minimization of the required amount energy was applied. For this case however, the combined amount of required energy is minimized. This was achieved by finding the point of minimum required power within the complete range of flight velocity. This in combination with the loiter time results in the amount of required energy for loiter. The required amount of energy for cruise was simply found from the amount of required power at cruise speed and the cruise time. From the results a top five selection was again obtained. In Figure 4.49, the results of the engine and propeller selection for mission profile two are presented.

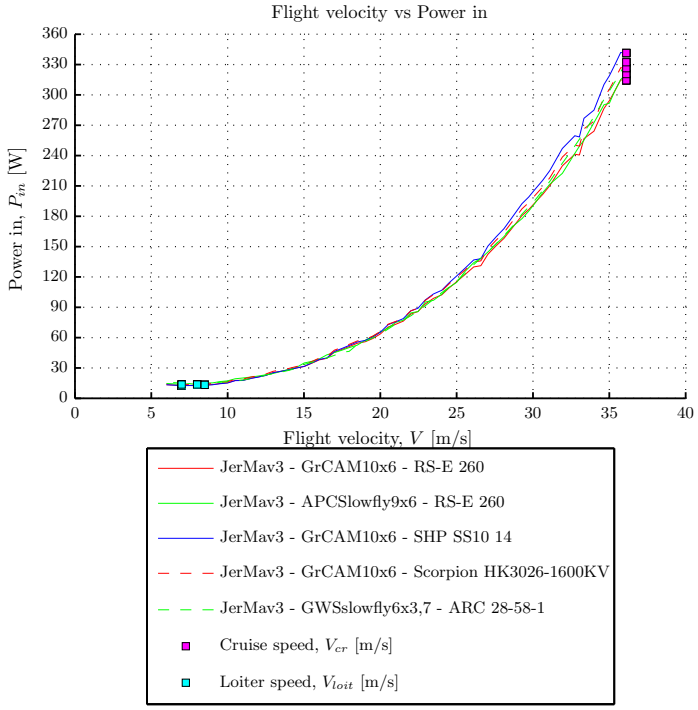

a: Flight velocity versus Power in

Figure 4.49: Results engine and propeller selection mission profile 2

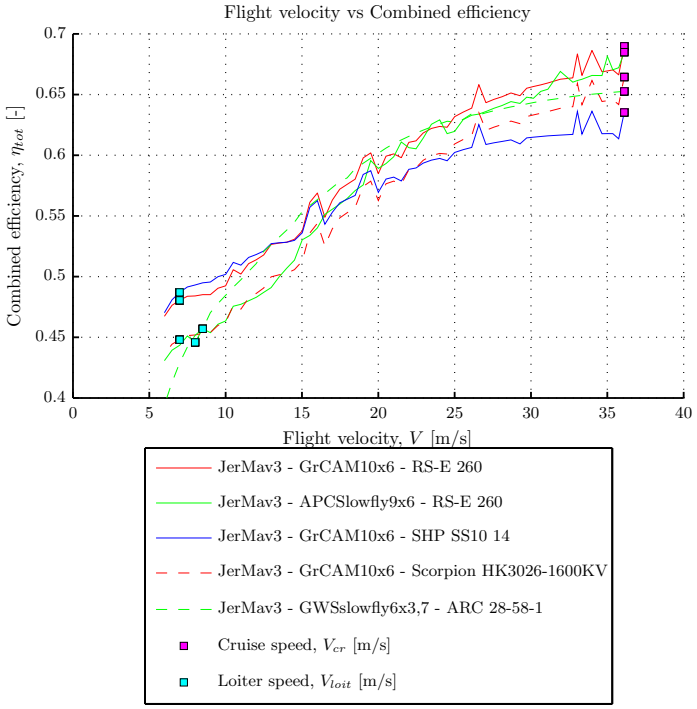

b: Flight velocity versus Combined efficiency

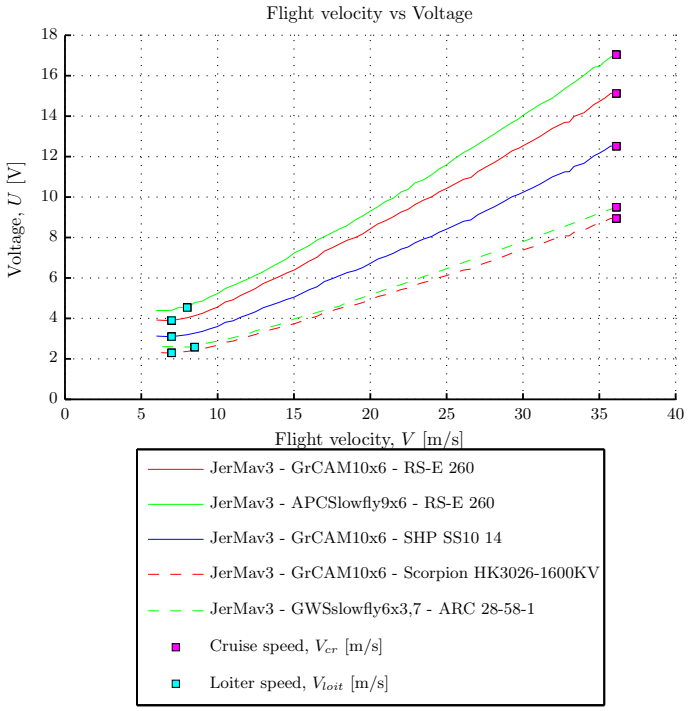

c: Flight velocity versus Voltage

Figure 4.49: Results engine and propeller selection mission profile 2 (cont'd)

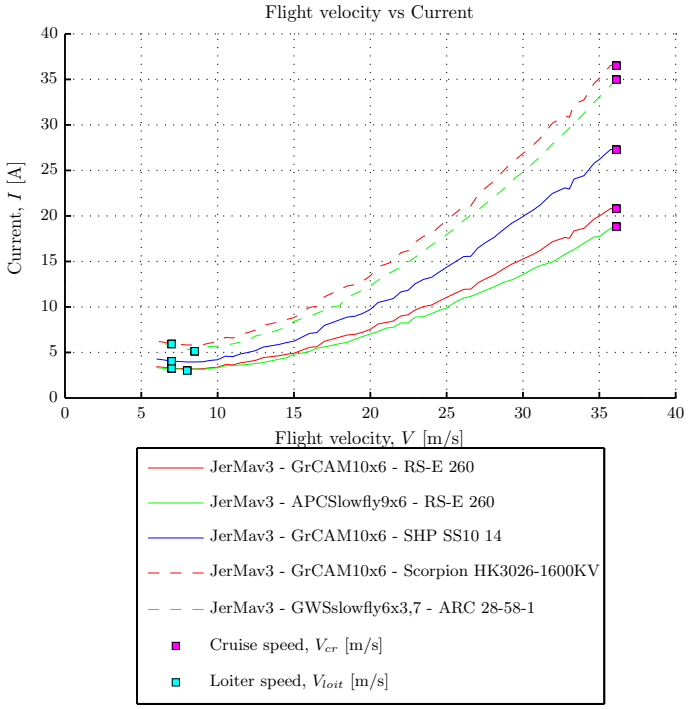

d: Flight velocity versus Current

Figure 4.49: Results engine and propeller selection mission profile 2 (cont'd)

Again, the most important parameters derived from Figure 4.49 in combination with additional parameters are presented in a table. Table 4.29 shows all parameters.

Table 4.29: Overview selected UAS engine and propeller parameters mission profile 2

Parameters	Symbol	1[a]	2[b]	3[c]	4[d]	5[e]	Unit
Overall parameters:							
Optimum loiter speed	$V_{P_{r_{min}}}$	7.0	8.0	7.0	7.0	8.5	[m/s]
Actual loiter speed	V_{loit}	8.33	8.33	8.33	8.33	8.33	[m/s]
Cruise speed	V_{cruise}	36.11	36.11	36.11	36.11	36.11	[m/s]
Comb. efficiency at loiter	$\eta_{com_{loit}}$	0.481	0.446	0.487	0.448	0.457	[-]
Comb. efficiency at cruise	$\eta_{com_{cruise}}$	0.690	0.685	0.635	0.665	0.653	[-]
Total required energy	E_{total}	16.40	17.06	17.22	17.23	17.27	[Wh]
Engine parameters:							
Loiter power	P_{loit}	12.81	14.58	12.61	13.73	14.53	[W]
Cruise power	P_{cruise}	314	320	341	326	332	[W]
Efficiency at loiter	$\eta_{e_{loit}}$	0.683	0.685	0.694	0.638	0.706	[-]
Efficiency at cruise	$\eta_{e_{cruise}}$	0.850	0.857	0.783	0.818	0.865	[-]
Voltage at loiter	U_{loit}	3.96	4.55	3.15	2.33	2.59	[V]
Voltage at cruise	U_{cruise}	15.12	17.04	12.52	8.94	9.50	[V]
Current at loiter	I_{loit}	3.23	3.20	4.01	5.89	5.60	[A]
Current at cruise	I_{cruise}	20.79	18.82	27.27	36.51	34.97	[A]
Weight	W_{engine}	128	128	90	195	153	[g]
Price	-	-	-	-	90,-[110]	78,-[109]	[€]
Propeller parameters:							
Efficiency at loiter	$\eta_{p_{loit}}$	0.711	0.659	0.711	0.711	0.626	[-]
Efficiency at cruise	$\eta_{p_{cruise}}$	0.812	0.799	0.812	0.812	0.754	[-]
RPM at loiter	RPM_{loit}	3288	3800	3288	3288	7800	[rev/min]
RPM at cruise	RPM_{cruise}	11864	13579	11864	11864	27263	[rev/min]
Diameter	D_p	0.254	0.229	0.254	0.254	0.153	[m]

[a] Graupner CAM10x6 + RS-E 260
[b] APCSlowfly9x6 + RS-E 260
[c] Graupner CAM10x6 + SHP SS10 14
[d] Graupner CAM10x6 + Scorpion HK3026-1600KV
[e] GWSslowfly6x3.7 + ARC 28-58-1

From Table 4.29 can be seen that from an energy point of view the GrCAM10x6 propeller with the RS-E 260 engine is the best solution for mission profile two. Again the problem of availability arised and therefore a different option needed to be considered. Options two and three were also not available and therefore option four was the best option for mission profile two. However, looking at the weight of engines four and five, one can conclude that option five may be more suitable when it comes to total weight of the propulsion system. Therefore, this was further investigated.

The required amount of battery weight was derived from the total amount of required energy and the average energy density of Lithium polymer batteries (130 [Wh/kg][75]). The difference in battery weight between option four and five was estimated to be 0.3 [g]. This difference is negligible and therefore option five is the best option with respect to total weight op the propulsion system. One final

parameter had to be taken into consideration in choosing between option four and five, the RPM. In the UAS requirements was stated that the UAS should emit the least amount of noise (see Table 3.1). From Table 4.29 can be seen that the RPM of combination five is significantly higher than that of combination four. This is caused by the fact that combination five is equipped with a propeller that has a smaller diameter. This results in a much higher noise emission for combination five. Based on this aspect, can be concluded that option four is most interesting for mission profile two.

This concludes the evaluation of engine-propeller combination for mission profile one and two. Next, a combination had to be selected for this preliminary UAS design. From the engine-propeller assembly analysis for mission profile one was concluded that the ARC 28-58-1 electrical engine in combination with the Graupner CAM 9x6 propeller was the best option. For now this assembly is called assembly one. The engine-propeller assembly analysis for mission profile two resulted in the Scorpion HK3026-1600KV electrical engine and Graupner CAM 10x6 propeller combination. This assembly, is called assembly two.

The engine-propeller assembly decision is based on the difference in battery and engine-propeller weight between the two options considering both mission profiles. The required amount of energy for assembly one and mission profile one is 6.08 [Wh]. Again assuming a Lithium polymer battery with a density of 130 [Wh/kg] [75], results in a battery weight of 47 [g]. For assembly two this resulted in 7.20 [Wh] of required energy which is equal to a battery weight of approximately 55 [g]. Next, the required amount of energy for assembly one and mission profile two was determined. This resulted in 19.17 [Wh] of required amount of energy which is equal to a battery weight of approximately 147 [g]. For assembly two this resulted in 17.23 [Wh] which is equal to a battery weight of approximately 133 [g]. The difference in battery weight between the two assemblies for mission profile one is 8 [g]. For mission profile two, the difference in battery weight is higher, 14 [g]. From this can be concluded that cruise has a higher impact on the increase in required amount of energy for assembly one, than the impact of loiter has on the increase in required amount of energy for assembly two.

Subsequently, the total assembly weight was estimated for both mission profiles. The total weight of assembly one for mission profile one is approximately 200 [g]. For option two this was estimated to be 250 [g]. In case of mission profile two, the weight for assembly one was estimated to be 300 [g] while option two is approximately 328 [g]. From the previous observation was concluded that assembly one is most interesting for the defined mission profiles. When the cruise time of mission profile two is extended, option two becomes more interesting. With respect to noise emission, assembly two is also more interesting. The RPM in both loiter and cruise condition is lower than that of assembly one. Besides that, the Scorpion HK3026-1600KV electrical engine is able to produce a maximum power output of 1470 [W] while the ARC 28-58-1 can only deliver a maximum power output of 1000 [W]. In order to comply with the noise requirement and to have a larger tolerance in the power range, it was decided to select the Scorpion HK3026-1600KV electrical engine and Graupner CAM 10x6 propeller combination. This combination is presented in Figure 4.50.

a: Scorpion HK3026-1600KV electrical engine[110]

b: Graupner CAM 10x6 propeller[111]

Figure 4.50: Chosen electrical engine and propeller

Some final remarks can be stated about the chosen engine. One final detailed run of the engine-propeller combination was conducted. This was done in order to find the maximum flight speed of the combination. A maximum flight speed of approximately 40 [m/s] was determined (flying at a higher speed was limited by the performance of the propeller). This resulted in an associated required engine power of 433 [W]. Besides that, also some remarks with respect to the estimated engine power can be made. In Subsection 4.7.5, the required engine power was slightly underestimated. From Table 4.21 can be seen that a loiter power of 8 [W] was determined while the actual amount of loiter power is 14 [W] . The cruise power estimation was also underestimated in Subsection 4.7.5. In stead of an actual required cruise power of 326 [W], a cruise power of 201 [W] was calculated. This was caused by overestimating the efficiency of the engine and propeller combination. In Subsection 4.5.1 an engine efficiency of 90 [%] was estimated and a propeller efficiency of 85 [%] was estimated. From Table 4.29 was derived that in reality the engine efficiency varied between 63.8 [%] and 81.8 [%] and the propeller efficiency between 71.1 [%] and 81.2 [%]. Due to this, also the fuel weight (battery weight) was underestimated. The difference in actual battery weight is discussed in Subsection 4.12.5.

The next step was to determine the required amount of energy for the climb part of the mission. Based on the amount of power available and the power required at each flight velocity, the rate of climb was determined. The maximum rate of climb was found at a forward speed of 7.25 [m/s]. A further increase of the maximum climb rate was limited by the minimum speed as stated in Subsection 4.6.1. From the specifications of the engine was found that the engine is able to deliver 1470 [W] of continuous power. This is a static amount of power and therefore in calculating the maximum climb rate, the maximum power at cruise speed was used. The maximum climb rate achieved at this speed is approximately 24 [m/s]. In Subsection 4.6.5, a climb rate of 5 [m/s] was set as a minimum requirement. Note that this value is easily achieved. Next, the climb time was determined. In order to climb to the required 480 [m] altitude, 20 [s] are required. Subsequently, the required amount of energy was derived. When the UAS climbs with the maximum amount of power at minimum forward speed, the required amount of climb energy was estimated to be 1.81 [Wh]. Combining this with the required energy for mission profiles two, which is most fuel intensive, this results in a total amount of 19 [Wh] of required energy. Obviously one can choose for a lower rate of climb setting, resulting in a

lower amount of required energy. For now the worst case scenario was used.

Based on the maximum rate of climb, the flight path angle was estimated. For small angles this can be estimated by the ratio of rate of climb over forward flight speed. This results in a flight path angle of approximately 3.3° which is reasonable. The horizontal distance covered during this climb was estimated to be 145 [m].

This concludes the subsection on engine and propeller selection. In the next subsection, the battery weight is determined based on the required amount of energy.

4.12.5 Battery selection

Several battery chemistries have been used for UAS propulsion systems. Table 4.30 gives an overview of the properties of several battery types.

Table 4.30: Characteristics of battery characteristics[75]

Battery type	**Practical specific energy** [Wh/kg]	**Cell Voltage** [V]
Lead acid	30-50	1.2
Nickel Cadmium	60	1.2
Nickel Metal	23-85	0.94-1.2
Lithium Ion	100-135	3.6
Lithium Polymer	50.7-220	3.7
Lithium Sulfur	350	2.5

Nickel Cadmium batteries were dominant in the 1980's and 1990's. The Nickel Metal hydride batteries made a brief appearance in the late 1990's and the early 2000's. Today, Lithium Ion and Lithium Polymer batteries are the main battery types in use today. The most promising battery technology in development today is the Lithium Sulfur battery cell. During the development of this cell type an energy density of 350 [Wh/kg] was achieved in 2004[112]. The company that is developing the next generation Lithium Sulfur battery cells focusses on an energy density of 600 [Wh] in the near future. An overview of the Lithium Sulfur battery specifications is shown in Table 4.31.

Table 4.31: Lithium Sulfur battery specifications

Parameter	**Value**	**Unit**
Minimum Voltage on discharge	1.7	[V]
Maximum charge Voltage	2.5	[V]
Nominal Voltage	2.15	[V]
Nominal capacity	2.5 at C/5	[Ah]
Maximum continuous discharge rate	2C	[-]
Maximum charge rate	C/5	[-]
Specific energy	350	[Wh/kg]
Battery cell length	55	[mm]
Battery cell width	37	[mm]
Battery cell height	11.5	[mm]
Battery cell weight	16	[g]

The Lithium Sulfur battery specifications listed in Table 4.31 are very promising. However, charge and discharge cycles are currently limited for this battery type.

Therefore, it is decided to wait with implementing this type of batteries until development is completed. Off-the-shelf Lithium Polymer batteries are used in stead. In order to power the UAS, battery packs are often used. These packs consist of multiple cells that can be arranged in series, parallel or a combination of the two. The arrangement depends on the input voltage for the engine and the maximum current required. This is derived from the engine specifications of Table 4.29. For the climb- and cruise part of mission profile two 8.94 [V] and 36.51 [A] is required. The loiter part of mission profile two requires 2.33 [V] and 5.89 [A]. In order to provide the required amount of Voltage during climb and cruise, at least three Lithium Polymer cells need to be put in series resulting in a battery voltage of 11.1 [V] (see Table 4.30). In the previous subsection, the total amount of required energy was estimated to be 19 [Wh]. For safety reasons and the fact that the additional onboard UAS equipment also require energy, 20% extra energy capacity was implemented, resulting in 23 [Wh] of required energy. This in combination with the 11.1 [V] results in a minimum required capacity of at least 2.1 [Ah]. A battery had to be selected corresponding with all three values. Obviously there are numerous batteries that comply with those requirements. Two battery solutions were taken into consideration, the Graupner Lipo V-MAXX 35C 2/2200 11,1V G2[113] and the Thunder Power 11.1V 2100mAh 25C[114]. The differences between the two solutions are expressed in weight, size, maximum discharge rate and price. An overview of the differences is presented in Table 4.32.

Table 4.32: Differences in considered battery options

Parameters	Graupner Lipo V-MAXX 35C 2/2200 11,1V G2[113]	Thunder Power 11.1V 2100mAh 25C[114]
Weight, [g]	190	147
Size, [LxWxH in mm]	104x35x27	103x35x21
Max discharge rate, [C]	35	50
Price, [€]	35,20	32,50

From Table 4.32 can be seen that the Thunder Power battery has better properties than the Grauper battery. Therefore, for this preliminary UAS design, the Thunder Power battery was chosen. Note that the actual battery weight closely resembles the estimated weight as calculated in Subsection 4.12.5 (133 [g] versus 147 [g]). In an earlier stage of the design, the battery weight was slightly underestimated. From Table 4.21 of Subsection 4.7.5 can be seen that a battery weight of 121 [g] ($\approx$ 1.19 [N]) was determined. Again this was caused by overestimating the efficiency of the engine and propeller.

When Lithium Sulfur batteries become available in the hear future, this will have a significant impact on the battery weight of UASs. From the specific energy density stated in Table 4.30, can be derived that a Lithium Sulfur battery for this application will approximately weigh 65 [g]. This means that the UAS equipped with this battery type can carry more payload or have a tremendous increase in endurance while keeping the MTOW equal.

In order to check if the chosen battery is able to provide the required amount of power during cruise, the discharge rate at cruise is evaluated. From Table 4.29 was

found that during cruise 326 [W] of power needs to be delivered by the engine. The battery can deliver a current of 2.1 [A] at a 1 [C] discharge rate with a constant voltage of 11.1 [V]. In order to produce the required 326 [W], the battery needs to deliver at least 30 [A] of current. This results in a maximum discharge rate of approximately 14 [C] during cruise. From Table 4.32 can be seen that the battery is able to cope with this discharge rate. In order to charge the battery, a simple battery charger can be used. A Thunder Power TP1430C[115] is an example of such a charger and is chosen without any evaluation.

Finally, a so called called Electronic Speed Controller (ESC) had to be selected in order to control the speed of the engine. The ESC was selected based on the maximum required current input of the engine. Earlier in this subsection, was determined that at cruise the maximum current of approximately 30 [A] is required. Generally, an addition of 30% is added to the maximum input current which prevents burn-out of the ESC during peak load. This results in a maximum current of 38 [A]. Based on this number the ESC was selected. The manufacturer of the engine also produces ESCs. A Scorpion Commander[116] ESC with a maximum continuous current of 45 [A] was chosen for this UAS design. The weight of the ESC is approximately 46 [g]. An additional advantage of this ESC is the ability of cutting of the power to the engine when the voltage of the battery becomes lower than a set value. This allows the user to keep control over the UAS while the engine power is cut off.

This concludes the subsection on battery selection. In the next subsection, the conclusions are drawn.

4.12.6 Conclusion

In this section, the propulsion system design of the UAS was discussed. This was initiated by evaluating the different propulsion system design options. From this was concluded that the UAV Development kit was a very promising program. After describing the first version of the program, new implementations in the program were discussed. More than 1700 engines with more than 7000 test data records were implemented in the program together with 40 additional propellers. Besides that, the engine and propeller modeling module were revised and a batch mode in combination with a multi-core functionality was implemented as well. The next step in the process was to determine the propulsion system location. For this preliminary UAS design a tail mounted tractor installation was chosen. This allows the engine to be cooled by the ram air. Besides that, ground clearance during take-off and landing is also ensured by choosing this location. An additional advantage of this location is the noise shielding created by the structure of the UAS.

Next, the preselection of the engines and propellers was presented. This was followed by an analysis of the remaining combinations. After evaluation of the top five combinations, the Scorpion HK3026-1600KV electrical engine in combination with the Graupner CAM 10x6 propeller were chosen for this preliminary UAS design. Subsequently, the battery selection was presented. It was determined that off-the-shelf Lithium Polymer batteries are the best battery solution for now. Lithium Sulfur batteries were discarded because this battery type is still in development.

When this battery type becomes available in the near future, this will have a significant impact on the weight of batteries. The chosen battery was the Thunder Power 11.1V 2100mAh 25C[114].

This concludes the section on propulsion system design. The next section describes the UAS subsystems that are included in the UAS design.

4.13 Subsystems

This section describes the subsystems that are included in the UAS design. These systems include the autopilot, control station, camera(s) and datalink/videolink. Every system is addressed in a separate subsection. A general introduction of most systems was already presented in Section 2.3.

4.13.1 Autopilot

From the requirements, stated in Section 3.4, can be concluded that no direct requirements relating to the autopilot were stated. From these requirements however, the autopilot requirements were derived. It must be able to "fly" the UAS up to a range of 4500 [m] at a maximum altitude of 490 [m]. The UAS must be able to autonomously climb to loiter altitude, loiter for at least 30 minutes, descent to the landing site and land. During loiter it must be possible to track an object of interest for at least two minutes at a cruise speed up to 130 [km/h].

In recent years, numerous autopilots are developed. Not all autopilots could be taken into consideration. Autopilots with the largest potential for this UAS design are listed below:

- MicroPilot MP2128g[117]
- Paparazzi Lisa/L[118]
- ArduPilotMega[119]
- Pixhawk[120]

Details of every autopilot are presented in the following paragraphs:

MicroPilot MP2128g[117] An impression of the MicroPilot MP2128g is shown in Figure 4.51.

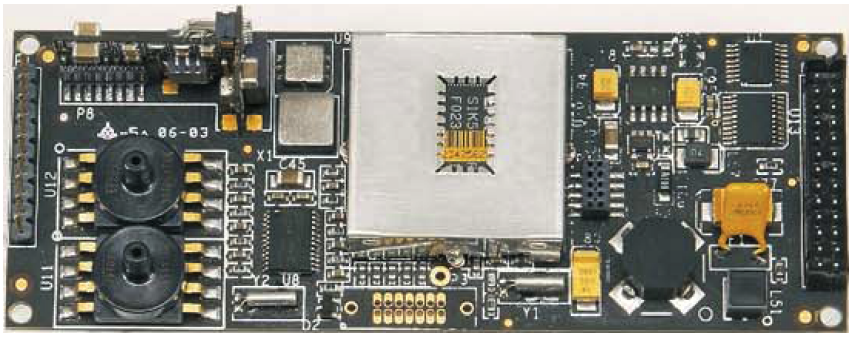

Figure 4.51: MicroPilot MP2128g[117]

This autopilot has a single core processor board with a capability of 150 Millions of Instructions Per Second (MIPS). It has the ability to save waypoints (which can be changed in-flight), data logging and telemetry capabilities (with video overlay). The autopilot also includes an airspeed sensor, an altimeter, a three-axis rate gyro & accelerometers, a digital compass and a GPS module. This allows a UAS to autonomously takeoff, bungee launch, hand launch and land. The dimensions of the board are as follows: length 10 [cm], width 4 [cm]. The complete assembly weighs 28 [grams], comes with Micropilot UAV Horizon ground control software, costs €1230,- and is not open source.

Paparazzi Lisa/L[118] An impression of the Paparazzi Lisa/L is shown in Figure 4.52a.

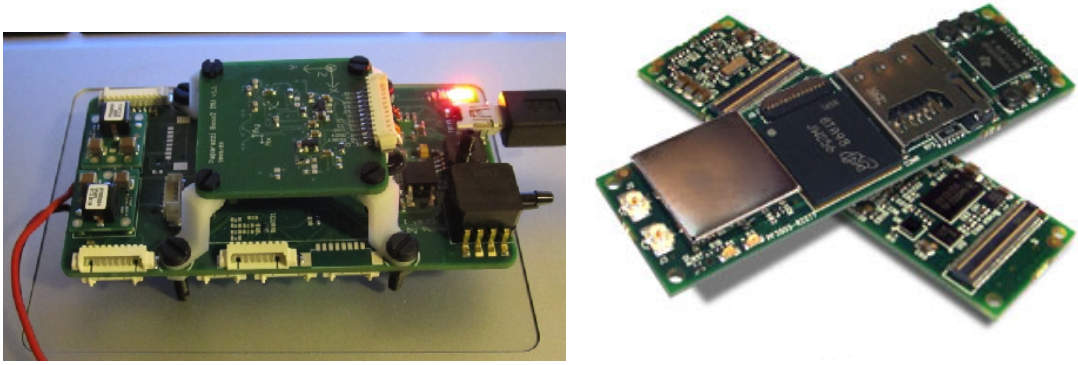

a: Paparazzi Liza/L autopilot[118] b: Gumstix Overo Fire COM[121]

Figure 4.52: Paparazzi Lisa/L[118] autopilot and Gumstix Overo Fire COM[121]

This autopilot has a dual core processor board with 150 MIPS of computing power. It has the ability to save waypoints (which can be changed in-flight), data logging and telemetry capabilities (with video overlay). The autopilot also includes an airspeed sensor, an altimeter, a three-axis rate gyro & accelerometers, a digital compass and a GPS module. This allows a UAS to autonomously takeoff, bungee launch, hand launch and land. The Lisa/L is designed to have a Gumstix Overo[121] mounted onboard (see Figure 4.52b). This increases the computing power of the autopilot with 1200 MIPS, allowing on-board video processing. A tiny, OMAP3530-based Computer-On-Module (COM) that delivers ARM Cortex-A8, Digital Signal Processor (DSP) and 3D graphics acceleration with 802.11b/g and Bluetooth communications on-board the COM and is built with components rated for extended temperatures. The dimensions of the autopilot board including the Gumstix Overo are as follows: length 9 [cm], width 6 [cm]. The complete assembly weighs approximately 25 [grams], comes with Paparazzi ground control software and costs approximately €700,- (including the Gumstix Overo) and is open source.

ArduPilotMega APM2[119] An impression of the ArduPilotMega APM2 is shown in Figure 4.53.

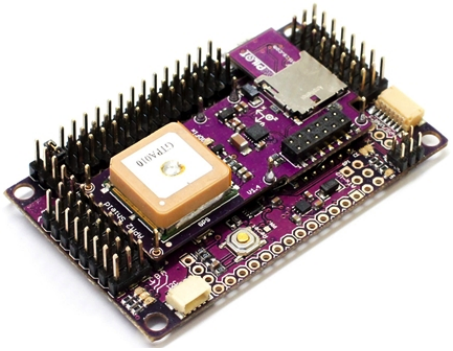

Figure 4.53: ArduPilotMega APM2[119]

This autopilot has a single core processor board with 32 MIPS of computing power. It has the ability to save waypoints (which can be changed in-flight), data logging and telemetry capabilities (with video overlay). The autopilot also includes an airspeed sensor, an altimeter, a three-axis rate gyro & accelerometers, a digital compass and a GPS module. This allows the UAS to autonomously takeoff and land. The ArduPilotMega APM2 is equipped with an additional processor. This is a safety processor which ensures a connection with the UAS when connection with the main processor is lost. The dimensions of the autopilot board are as follows: length 6.5 [cm] and width 4 [cm]. The complete assembly weighs approximately 45 [grams], comes with ArduPlane ground control software, costs approximately €165,- and is open source.

Pixhawk[120] An impression of the Pixhawk is shown in Figure 4.54a.

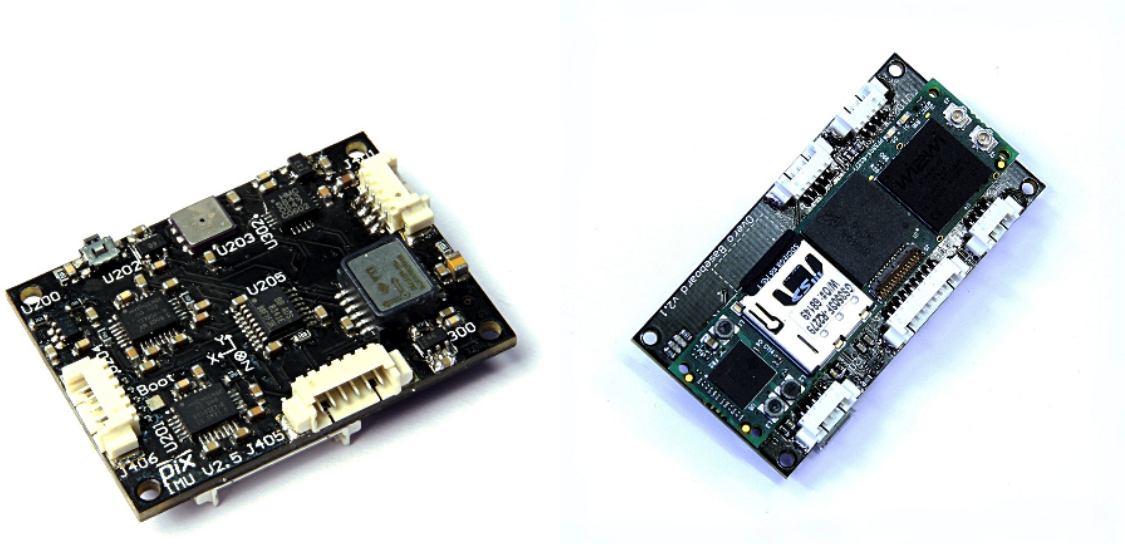

a: Pixhawk autopilot[120] b: Pixhawk-designed expansion board[120]

Figure 4.54: Pixhawk autopilot and expansion board[120]

This autopilot has a single core processor board with 120 MIPS of computing power. It has the ability to save waypoints (which can be changed in-flight), data logging and telemetry capabilities (with video overlay). The autopilot also includes an airspeed sensor, an altimeter, a three-axis rate gyro & accelerometers, a digital compass and a GPS module. This allows the UAS to autonomously takeoff and land. The Pixhawk can be connected to a Pixhawk-designed expansion board (see Figure 4.54b). This expansion board can, as with the Lisa/L autopilot board, be equipped with a Gumstix Overo COM[121] (see Figure 4.52b). In that way an increase of 1200 MIPS of computing power can be realized. This allows on-board video processing e.g. The dimensions of the boards are as follows. Autopilot: 3 [cm] width and 4 [cm] length. Extension board (including Overo COM): length 9.5 [cm], width 9.5 [cm]. The complete assembly weighs approximately 248 [grams] (235 [grams] for the expansion board), comes with QGroundControl software and is open source. The autopilot board, which is priced at €350,-, will only be made in batches of at least 30. Note that this is the price for the autopilot only.

Before an autopilot was selected, first the different ground control station software interfaces were analyzed. Based on those findings together with the specifications of the autopilot a selection is made.

4.13.2 Control station

The control station consist out of software(interface) and hardware. First the interface of the control station is addressed. After that the hardware options are discussed.

Control station interface

Based on the requirements, stated in Section 3.4, the control station interface must be simple, programmable and able to support different video streams. The interface of every autopilot is discussed separately.

Micropilot UAV Horizon ground control software[122] The MicroPilot MP2128g[117] autopilot comes with Micropilot UAV Horizon ground control software. An impression of the interface is shown in Figure 4.55.

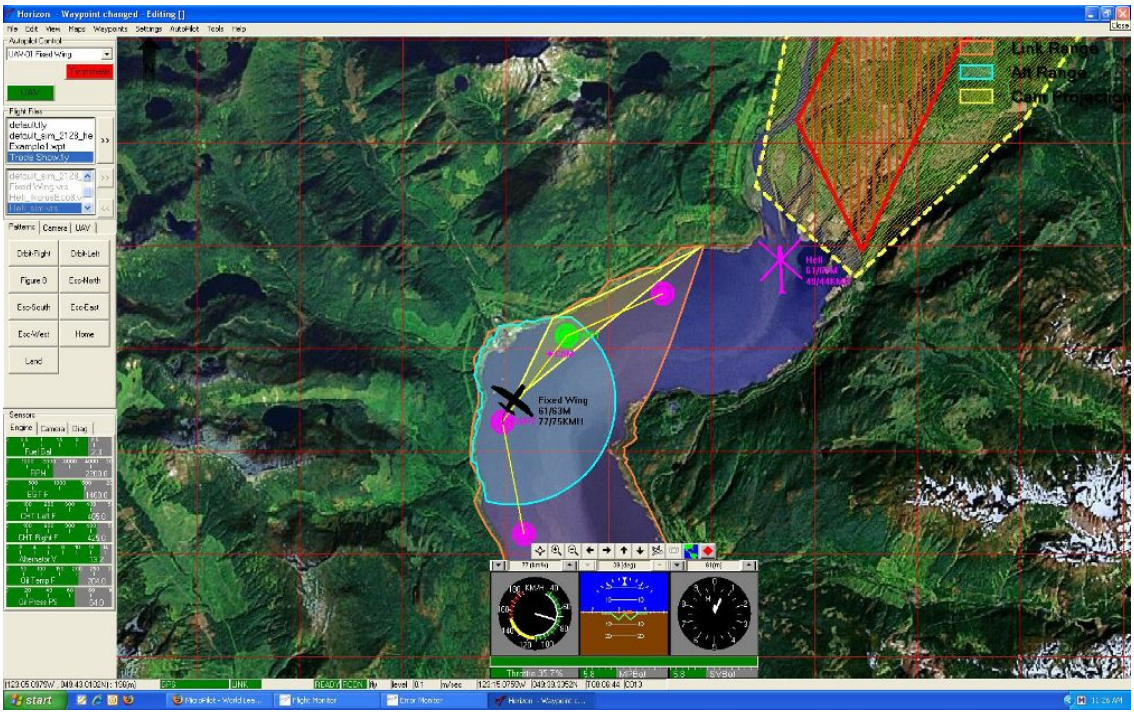

Figure 4.55: MicroPilot HORIZON ground control station interface[122]

The Micropilot UAV Horizon ground control software runs on a Windows operating system. It is able to display real-time sensor and payload data and a live video stream. The software offers antenna tracking as well as mission planning and real-time movable waypoints. Simultaneous control of multiple UASs is possible. The software also has a build-in mission simulator which supports multiple missions. Despite the fact that the software is not open source, it does allow the user to configure up to eight different sensors in three formats. There is no information available about which kind of maps are used in the interface.

Paparazzi ground control software[118] The Lisa/L[118] comes with Paparazzi ground control software. Figure 4.56a gives an overview of the Paparazzi software interface.

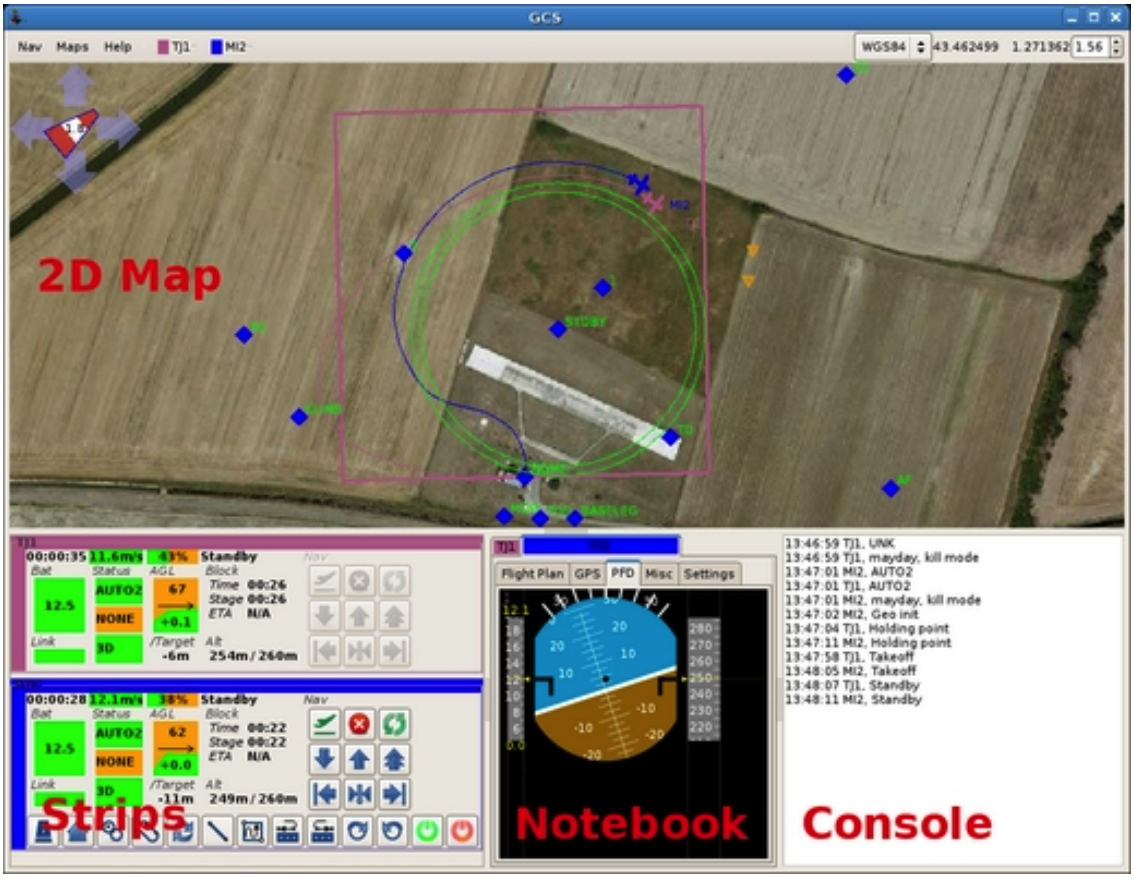

Figure 4.56: Paparazzi ground control station interface[123]

The Paparazzi ground control software runs on a Linux- and Max OS X operating system. It is able to display real-time sensor and payload data and a live video stream. The software allows mission planning and realtime movable waypoints. Simultaneous control of multiple UASs is possible. The software also has a build-in mission simulator in which complex flight plans can be tested. The software is free and open source. This allows the user to freely configure the GUI. 2D maps are available which consist of Google Satellite, OpenStreetMaps Images and Microsoft Satellite Maps.

ArduPlane ground control software[119] The ArduPilotMega APM2[119] comes with ArduPlane ground control software. An impression of the software interface is shown in Figure 4.57.

Figure 4.57: ArduPilot ground control station interface[124]

The ArduPlane ground control software runs on a Windows operating system. It is able to display real-time sensor and payload data and a live video stream. The software allows mission planning and realtime movable waypoints. Simultaneous control of multiple UASs is possible. The software also has a build-in mission simulator in which complex flight plans can be tested. The software is free and open source. Google Maps are available in the interface.

QGroundControl software[120] The Pixhawk[120] comes with QGroundControl software. Figure 4.58 gives an overview of this software interface.

Figure 4.58: QGroundControl ground control station interface[125]

The QGroundControl software runs on a Windows-, Linux- and Mac OS X operating system. It is able to display real-time sensor and payload data and two live video streams. The software allows mission planning and realtime movable waypoints. Simultaneous control of multiple UASs is possible. The software also has a build-in mission simulator in which complex flight plans can be tested. The software is free and open source. Only Google Earth Streaming is available in the interface.

Control station hardware options

Besides the interface part of the control station, also different hardware options were available. Based on the requirements, stated in Section 3.4, the control station hardware must be portable, have an IP resistance of at least 54 and have an endurance of at least 30 minutes. For this UAS, three hardware options were considered. These options are as follows:

- Motion computing J3500 tablet[65]
- Panasonic CF-53 laptop[126]
- Nook Simple Touch e-reader[127]

Motion computing J3500 tablet[65] Figure 4.59 gives an impression of the Motion computing J3500 tablet[65].

Figure 4.59: Motion computing J3500 tablet[65]

The Motion J3500 tablet is a rugged and powerful tablet computer. The tablet can be powered with a 1.46 GHz Intel Core i7 processor and has a hot-swappable dual battery capability with up to 7 hours of continuous use. It has a weight of approximately 1.6 [kg]. The tablet has a build-in wifi antenna and GPS module. It is equipped with a 12.1" 1280x800 resolution WXGA wide screen. The J3500 is shock proof, water, dust and splash resistant. The price of the J3500 tablet starts at €1250,-.

Panasonic CF-53 laptop[126] An impression of the Panasonic CF-53 laptop is shown in Figure 4.60.

Figure 4.60: Panasonic CF-53 laptop[126]

The Panasonic CF-53 delivers the power of a desktop in a semi-rugged design that provides the flexibility to work anywhere. It has a shock-mounted flex-connect hard drive, magnesium alloy casing, spill-resistant keyboard & touchpad and weighs approximately 3.0 [kg]. The toughbook has a 14" 1366x768 resolution LED display, can be powered by a 2.5 GHz Intel Core i5 processor and has a battery capability up to 10 hours. Besides a wifi antenna it has also an integrated mobile broadband module. The price of the Panasonic CF-53 starts at €1400,-.

Nook Simple Touch e-reader[127] Figure 4.61 gives an impression of the Nook Simple Touch e-reader.

Figure 4.61: Nook Simple Touch e-reader[127]

The Nook Simple Touch e-reader has a low performance CPU running on 800 MHz. This results in a battery life up to 30 hours. The e-reader can be equipped with a Linux operating system. It has a 6" 800x600 resolution gray scale screen. The screen allows good visibility in sunny conditions. Unfortunately the Nook is not rugged. The e-reader weighs approximately 0.2 [kg] and has a build-in wifi antenna. The price of the Nook Simple Touch e-reader is low compared to the other two solutions (€99,-). This concludes the subsection on control station options. Next, the camera options are presented.

4.13.3 Camera

The camera is one of the key elements of this UAS design and must therefore be chosen carefully. The requirements, as stated in Section 3.4, are rather strict. These requirements apply for the camera that is used for observing the area of interest. Requirement for an additional camera that can be used for low quality streaming

are not stated. The camera requirements for the observation camera are listed in short. The camera must at least have 1960 pixels in the direction parallel to the traffic stream in order to comply with the precision requirement at 490 [m]. The weight of the camera is restricted to 500 [grams]. It is desired to have a global shutter in order to prevent motion in a picture. A high resolution recording time and low resolution streaming time of 30 minutes is required. During this period the camera must deliver at least 10 frames per second with low image compression. Besides these requirements it is also desired to have optical and/or digital zoom with auto focus abilities.

Nowadays, numerous cameras are available. This ranges from simple webcams to high resolution digital reflex cameras. Finding a camera that is able to comply with all requirements proved to be hard. Especially off the shelf cameras with streaming abilities were hard to find. Cameras with the largest potential for this UAS design were considered. These cameras are listed below.

- Prosilica GB 2450[128]
- GoPro HD Hero2[129]
- Caspa FS[130]
- Sense IT panorama camera[131]

Every listed camera is discussed in a separate paragraph.

Prosilica GB 2450[128] In Subsection 3.2.2 was mentioned that the Prosilica GC 2450[128] was used for gathering traffic data. The manufacturer of this camera also produces the Proscillica GB 2450. This camera is a small form-factor, low weight camera with similar properties. This camera is shown in Figure 4.62.

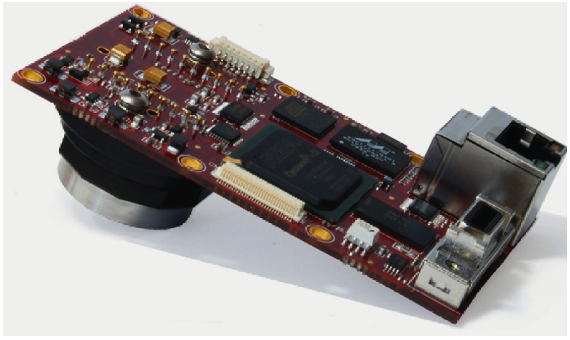

Figure 4.62: Prosilica GB 2450[128] camera

The Prosillica GB 2450 has a resolution of 2448x2050 pixels (WxH) with a maximum frame rate at full resolution of 15 frames per second. The camera includes auto exposure, gain and white balance features. The weight of the camera without lens is 54 [grams] and its size is 55x89 (WxL in [mm]). This camera is not quipped with a battery and needs to be powered by an external power source. Besides that, the camera is equipped with a global shutter and ethernet connection. The costs of the camera (without lens) is €2530,-.

This camera covers most requirements. Onboard recording and/or streaming abilities of the camera were discussed with the manufacturer of the camera. It became clear that off the shelf streaming abilities were not present. In order to stream the images, an embedded micro PC (PC104) must be used. Software capable of capturing the stream and providing it to a data link must be developed by the user of the camera.

GoPro HD Hero2[129] A very popular camera which is often used in model aircraft is the GoPro camera. GoPro has developed a new high-definition camera, the GoPro HD Hero2[129]. This camera is shown in Figure 4.63.

Figure 4.63: GoPro HD Hero2[129]

The GoPro HD Hero2 has a resolution of 1920x1080 pixels (WxH) with a maximum frame rate at full resolution of 30 frames per second. The camera produces non-interlaced (progressive) images. Besides its video capabilities, the camera has also the ability of shooting ten 11 mega pixel photos per second with a field of view up to 170°. This angle provides a wide field of view that exhibits some fisheye distortion around the edges of the frame (see Figure 4.64). The medium angle setting, 120°, is also pretty wide, with less pronounced distortion. The narrow setting provides a 90° field of view. The images can be saved on a memory card up to 32GB. The camera does not have a zoom function. However, by changing the field of view in 1080p mode one can shorten the focal distance, effectively zooming in the camera.

The camera is also equipped with a composite port through which an analog video output (NTSC/PAL) signal can be delivered. This signal can be used for a video stream on the control station. The camera has a battery life up to two hours. Unfortunately, the camera has a rolling shutter causing its images to be prone to motion. The weight of the camera without waterproof housing is approximately 90 [grams] and it size is 42x60 (WxL in [mm]). The waterproof housing is made out of clear polycarbonate and allows you to dive up to 60 [m]. The camera costs €245,-.

Figure 4.64: GoPro HD Hero2 11 MP image

Caspa FS[130] In Subsection 4.13.1, the capabilities of the Paparazzi Lisa/L[118] autopilot were listed. This autopilot is designed to have a Gumstix Overo[121] mounted onboard (see Figure 4.52b). The Caspa FS camera, as shown in Figure 4.65, can be connected to this Overo chip. Digital video streaming to the control station can be achieved using this combination.

Figure 4.65: Caspa FS camera[130]

The Caspa FS has a resolution of 360x960 pixels (WxH) with a maximum frame rate at full resolution of 60 frames per second. The resolution of the camera does not allow it to be used for observation (at least 1960 pixels in the direction parallel to the traffic stream at 490 [m] altitude). However, this camera can be used for delivering a video stream to the control station. This camera can receive the full-spectrum of light including the infra-red range, which can be useful in some applications. The

Caspa is powered by the Gumstix Overo board and has a global shutter. The weight of the camera is 23 [grams] and its size is 39x25.7 (WxL in [mm]). The camera costs approximately €60,-.

SenseIT panorama camera[131] SenseIT is currently developing a 180° panorama camera based on the VRmagic multi-sensor camera[132]. This camera is shown in Figure 4.66.

Figure 4.66: Sense IT panorama camera[131]

The panorama camera has a resolution of 4x754x480 pixels (number of sensors x WxH). This camera has build in real-time image stitching, image enhancement & stabilization and compression. The images are automatically stored on a usb stick. Parallel streaming of compressed panorama images and high resolution region of interest selection is also possible. An analog video output is also present. The camera is equipped with a global shutter. The VRmagic has a dual core processor and is freely programmable (Linux OS). The weight of the camera is approximately 200 [grams] (housing included) and its main board size is 42x38 (WxL in [mm]). Costs of the SenseIT panorama camera are unknown at this time since the camera is still in development.

4.13.4 Datalink and videolink

Besides the camera, the datalink and videolink are also an important part of the UAS design. From the requirements, as stated in Section 3.4, was derived that the only requirement for the datalink is a range of at least 4500 m. No requirements regarding the videolink were stated. Besides the range requirement it is also desired to have a secured link. The datalink and videolink may use different links. One link for the control & telemetry data and one link for the video data. A long range low data rate link is required for the control & telemetry data. This ensures a stable connection with the flying platform. A short range high data rate link is required for the videolink.

For the videolink, a digital or analog stream can be used. Research resulted in choosing an analog video stream. When the UAV is flying at the edge of its range

or in an area with bad reception, this results in a low data rate connection with the ground control station. Part(s) of the video stream will be lost, resulting in distorted images on the ground control station. In case of a digital video stream, the images will look blocky. From these images an operator is often not able to recognize objects. In case of an analog video stream, the images will be noisy but recognizable.

Any wireless device providing a serial link can be used for the telemetry and datalink, even audio-channel based telemetry has been used. The most common datalink device is the XBee series of radio modem. Other systems include powerful long range radios such as the Digi XTend module[133] or the digital datalink of Aerovironment[134] (which are not allowed without a permit), cellular network communications or satellite communications with Iridium satellite modems. In the Netherlands certain regulations apply for the use of a datalink[135] (without a license). In discussing the considered datalinks, these regulations are presented.

The telemetry part of the link is used to obtain status information about the UAS to aid an operator and monitor mission progress, as well as provide some payload data. The datalink part of the link is used to send commands to the aircraft and interact with a payload. For example, telemetry provides the current location of the aircraft which can be viewed on the map of the ground control station, while the datalink allows the user to move a waypoint in order to adjust the flight path of the UAS.

A traditional radio control transmitter and receiver pair is used to provide a manual control option for the UAS. The airborne hardware and software support the connection to a standard radio-control receiver. The autopilot reads the output from the R/C receiver onboard the aircraft and decides what control mode is desired. When in manual mode, a safety pilot on the ground may use the R/C transmitter to control the aircraft.

Datalinks/videolinks with the largest potential for this UAS design were taken into account. These links are listed below.

- Xbee-PRO 868[136]
- Xbee 868LP[137]

Every listed link is discussed in a separate paragraph.

Xbee-PRO 868[136] The Xbee-PRO 868 is a long-range 868 MHz radio frequency module. This link is shown in Figure 4.67.

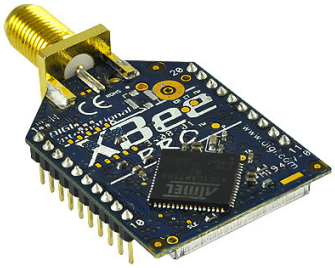

Figure 4.67: Xbee-PRO 868[136]

The Xbee-PRO 868 supports line of sight distances up to 80 [km] (40 [km] with dipole antennas and 80 [km] with high gain antennas). The data rate of the datalink is approximately 24 [kbps] and limited to 10% duty cycle. Its transmit power can be varied between 1 [mW] (0 [dBm]) and 315 [mW] (+25 [dBm]). In the Netherlands the 868 [MHz] frequency is limited to 25 [mW] effective radiated power[135]. The connection is secured by a 128-bit AES encryption. The dimensions of the Xbee are 24x33 (WxL in [mm]) and its weight is approximately 2 [grams]. The Xbee-PRO 868 development kit (including antennas) costs approximately €120,-.

Xbee 868LP[137] The Xbee 868LP is also a 868 MHz radio frequency module. This link is shown in Figure 4.68.

Figure 4.68: Xbee 868LP[137]

The XBee 868LP for Europe is the first radio frequency module using 868MHz and surrounding frequencies for LBT + AFA (Listen Before Talk and Adaptive Frequency Agility). This eliminates interference by listening to the radio environment before any transmission starts, and automatically shifting to a new channel when interference is detected (rfequency hopping). This frequency scan occurs automatically and in a matter of microseconds so as not to impact performance.

The range of the Xbee 868LP is much shorter than it's brother the XBee-PRO 868, but it can use the 868 G4 band which does not have restrictions on its duty cycle. Its transmit power is 16 [mW] (12 [dBm]). The connection is secured by a 128-bit AES encryption. As mentioned in the previous paragraph, the 868 MHz frequency is limited to 25 [mW] effective radiated power in the Netherlands[135]. Despite that, this module is able to attain a line of sight communication up to 4 [km] with a data rate of 80 [kbps]. The dimensions of the Xbee 868LP are 24x33 (WxL in [mm]) and its weight is approximately 2 [grams]. The Xbee 868LP development kit (including antennas) costs approximately €160,-.

This wraps up all system options. In the upcoming subsection, every chosen option is presented and discussed.

4.13.5 Conclusion

From the Subsection 4.13.1 can be concluded that all autopilots are able to comply with the requirements. Also can be concluded that the autopilots have many features in common. An overview of the autopilot features that differ are shown in Table 4.33.

Table 4.33: Overview autopilot specifications

	MP2128g	Lisa/L	APM2	Pixhawk
Processing power, [MIPS]	150	1350 (incl. Overo)	32	1320 (incl. Overo)
Weight, [grams]	28	25	45	248
Price, [€]	1230,-	700,- (incl. Overo)	165,-	30 x 350,-
Open source		✓	✓	✓

Based on Table 4.33 and their ground control software, the Lisa/L autopilot was chosen. This autopilot has lots of processing power, the ability to connect a Gumstix Overo mounted camera, is open source and low weight. It's price is moderate at €700,- (including the Gumstix Overo). The Paparazzi ground control software is supported on Linux and Mac OS X. The software is open source and therefore the interface is freely configurable. Besides that, the software also supports a large amount of maps including Google Satellite, OpenStreetMaps and Microsoft Satellite Maps and is able to handle different video streams.

In order to run the ground control software ground control hardware is required. An overview of the, in Subsection 4.13.2 listed, options is shown in Table 4.34.

Table 4.34: Overview ground control hardware specifications

	J3500	CF-53	Simple Touch
Processing power, [MHz]	5840	5000	800
Weight, [kg]	1.6	3	0.2
Endurance, [h]	7	10	30
Screen size [inch]	12.1	14	6
Screen resolution, [-]	1280 x 800	1366 x 768	800 x 600
Price, [€]	1250,-	1400,-	99,-
Rugged	✓	✓	

Based on the, in Subsection 4.13.2, listed specifications and the requirements stated in Section 3.4, the Motion J3500 tablet was chosen. This tablet provides an amazing amount of processing power, sufficient endurance (over 30 minutes) and moderate weight. Besides that, the tablet is also rugged and has good screen properties. The Nook Simple Touch does not have sufficient processing power and therefore it dropped out. The Panasonic CF-53 is very heavy, more expensive than the Motion J3500 and has less processing power than the Motion J3500.

Choosing the right camera proved to be a difficult task. First, an overview of the camera specifications are shown in Table 4.35

Table 4.35: Overview camera specifications

	GC 2450	GoPro Hero2	Caspa FS	SenseIT
Resolution, [-]	2448 x 2050	1920 x 1080	360 x 960	4 x 754 x 480
Weight, [g]	54	90	23	200
Frame rate, [fps]	15	30	60	69
Price, [€]	2530,-	245,-	60,-	?
Global shutter	✓		✓	✓
Onboard storage		✓		✓
Analog video		✓		✓

Based on the camera requirements, as stated in Section 3.4, and Table 4.35 the following was decided. The Prosilica GB 2450 was discarded based on the fact that software development is required in order to setup a video stream. Focussing on the resolution of the three remaining cameras one can conclude that the Caspa FS camera is not able to comply with the resolution requirement. The GoPro Hero2 is just not able to meet the required 1960 pixels in the direction parallel to the traffic stream. In order to comply with this requirement the UAS is limited to an altitude of 480 [m]. The effective resolution of the SenseIT panorama camera is not known at this point in time. With respect to the weight restriction can be said that both cameras (GoPro Hero2 and SenseIT) comply. Besides that, both cameras are able to produce wide field of view images (170° for the GoPro and 180° for the SenseIT). The SenseIT camera uses four image sensors to create this field of view while the GoPro camera uses a single image sensor. Due to the single image sensor, the GoPro camera exhibits some fisheye distortion around the edges of the frame. Software can be used to compensate for the distortion but this is not ideal. Besides that, the GoPro camera does not have a global shutter. Unfortunately, not

much is known about the image quality of the SenseIT panorama camera because the camera is still in development. It is known that the camera can store images onboard and is able to produce an analog video output. The GoPro camera has these properties in common.

As stated earlier, choosing the right camera proved to be a difficult task. For now the GoPro camera was chosen. This was simply based on the fact that the SenseIT camera is still in development. As a secondary camera the Caspa FS can be used. This camera can can be connected to the Gumstix Overo on the Lisa/L autopilot. The advantages of this camera are its light weight, low costs, global shutter and IR capabilities. The total payload combination weighs 113 [g]. Note that in Subsection 4.3.2 a payload weight of 500 [g] was anticipated. By using Equation (4.5) one can conclude that a payload weight of 270 [g] is actually more suitable for this UAS design. After all weight component have been evaluated, additional statements are given about this weight difference.

Last but not least, the datalink and videolink had to be chosen. An overview of the main specifications of these links are shown in Table 4.36.

Table 4.36: Overview datalink and videolink specifications

	Xbee-PRO 868	**Xbee 868LP**
Range, [km]	80	4
Data rate, [kbps]	24	80
Weight, [g]	2	2
Price, [€]	120,-	160,-
Encryption	✓	✓

From the requirements, as stated in Section 3.4, was derived that the only requirement for the datalink is a range of at least 4500 [m]. No requirements regarding the videolink were stated. It is desired to have a secured link. In Subsection 4.13.4 was stated that it is desired to use two separate links. One link for the control & telemetry data and one link for the video data. A long range low data rate link is required for the control & telemetry data. This ensures a stable connection with the flying platform. Most of the missions are short range. Therefore a short range high data rate link can be used for the videolink. From Table 4.36 can be seen that the Xbee 868LP can serve as a short range high data rate videolink while the Xbee-PRO 868 can be used for the long range datalink.

Besides the links mentioned in Subsection 4.13.4, other links are also possible. The 3G network may be such an alternative option. Tests are required in order to check if the data rate provided by the link is sufficient. Using a 2.4 GHz directional antenna in combination with the available wifi on the Gumstix Overo board that is connected to the Lisa/L autopilot board, it is possible to setup a high data rate link which can be used as a videolink. The TurboWifi v2[138] is an example of such a directional antenna. The GPS data that is send from the Xbee-PRO 868 to the ground station can be used to aim the antenna. The antenna costs €109,-.

This concludes the section on subsystems that are included in the UAS design. In the next chapter, the UAS design characteristics are presented.

Chapter 5

UAS design characteristics

This chapter describes the UAS preliminary design characteristics. First the overall characteristics are presented. This is followed by the power breakdown. Next, the total costs for the preliminary UAS design are listed. Finally, the design evaluation is presented.

5.1 Characteristics

In this section all UAS characteristics are presented.

The first overview represents the UAS dimensions and is shown in Table 5.1.

Table 5.1: Overview UAS dimensions

(a) Overall dimensions and wing dimensions UAS

	Symbol	Value	Unit
Overal dimensions:			
Span	b	2	[m]
Length (leading edge wing to trailing edge horizontal tail tip)	L_{wt}	0.788	[m]
Height (wing to horizontal tail)	h_{wt}	0.3	[m]
Wing:			
Airfoil	-	naca23012	[-]
Surface area	S_{ref}	0.4089	$[m^2]$
Mean aerodynamic chord	c_{mac}	0.2176	[m]
Aspect ratio	A	9.78	[-]
Taper ratio	λ	0.3885	[-]
Sweep	Λ	0	[deg]

Table 5.1: Overview UAS dimensions (con't)

(b) Horizontal tail dimensions and vertical tail dimensions

	Symbol	Value	Unit
Horizontal tail:			
Airfoil	-	naca0010	[-]
Span	b_{H-tail}	0.75	[m]
Surface area	S_{H-tail}	0.1037	$[m^2]$
Mean aerodynamic chord	$c_{mean_{H-tail}}$	0.1380	[m]
Aspect ratio	A_{H-tail}	6.54	[-]
Taper ratio	λ_{H-tail}	0.5	[-]
Sweep	Λ_{H-tail}	5	[deg]
Vertical tail:			
Airfoil	-	naca0010	[-]
Span	b_{V-tail}	0.3	[m]
Surface area	S_{V-tail}	0.0495	$[m^2]$
Mean aerodynamic chord	$c_{mean_{V-tail}}$	0.2510	[m]
Aspect ratio	A_{V-tail}	1.82	[-]
Taper ratio	λ_{V-tail}	0.6	[-]
Sweep	Λ_{V-tail}	20	[deg]

Next, the UAS weight characteristics are displayed in Table 5.2.

Table 5.2: Overview UAS weight characteristics

Weight components	Symbol	Value	Unit
MTOW	W_{TO}	13.90	[N]
Empty weight (excluding fixed equipment and propulsion system weight)	$W_{empty\,excl}$	5.14	[N]
Propulsion system weight	$W_{propulsion}$	2.38	[N]
Fixed equipment weight	W_{feq}	0.41	[N]
Payload weight (GoPro and Caspa)	$W_{payload}$	1.11	[N]
Fuel weight	W_{fuel}	1.44	[N]
Rest weight	W_{rest}	3.42	[N]

From Table 5.2 can be seen that there is a large rest weight. This is caused by the fact that the payload weight was lower than expected (113 [g] versus the anticipated 500 [g]). The payload weight was intentionally overestimated in order to have some freedom in the payload selection. In Subsection 4.13.5, it was already mentioned that a payload weight of 270 [g] is actually more suitable for this UAS design (based on the WERs). From this can be concluded that the reference UASs are equipped with heavier or more additional payloads.

The empty weight of the UAS was estimated by using the WER, Equation (4.3). This resulted in 785 [g] of empty weight. This weight also includes the weight of the propulsion system and fixed equipment. By subtracting the weight of those

components an estimation of the structural weight results. A value of 500 [g] was calculated. The structural weight calculated in Section 4.11 on materials was 524 [g]. From this can be concluded that the WER underestimates the structural weight. The large wing span, in comparison to the reference UASs, resulted in a higher structural weight causing it to differ from the result of the WER. Fortunately, the weight of the payload was overestimated. Part of the rest weight, introduced by the lower payload weight, could therefore be used by the battery weight and structural weight which were underestimated. Note that this still results in a large rest weight. This rest weight can be used for an increase in battery capacity or for additional payloads.

Subsequently, the UAS propulsion system characteristics are presented in Table 5.3.

Table 5.3: Overview UAS propulsion system characteristics

	Value	Unit
Engine:		
Type	Scorpion HK3026-1600KV	[-]
Max RPM	33600[110]	[rot/min]
Maximum power	1470	[W]
Weight	195	[g]
ESC:		
Type	Scorpion Commander[116]	[-]
Max continuous current	45	[A]
Weight	46	[g]
Propeller:		
Type	Graupner CAM 10x6	[-]
Max RPM	30000 (based on UDK results)	[rot/min]
Diameter	0.254	[m]
Battery:		
Type	Thunder Power 11.1V 2100mAh 25C	[-]
Size	103x35x21	[LxWxH in mm]
Capacity	23.3	[Wh]
Max discharge rate	50	[C]
Max current	70	[A]
Weight	147	[g]

Besides the propulsion system characteristics, also an overview of the payload characteristics is shown. This is presented in Table 5.4.

Table 5.4: Overview UAS payload characteristics

	Value	Unit
Autopilot:		
Type	Lisa/L with Gumstix Overo	[-]
Processing power	1350	[MIPS]
Weight	25	[g]
Ground control hardware:		
Type	J3500 tablet	[-]
Processing power	5.84	[GHz]
Endurance	7	[h]
Weight	1.6	[kg]
Observation camera:		
Type	GoPro HD Hero2	[-]
Resolution	1920x1080	[-]
Endurance	2	[h]
Frame rate	30	[fps]
Weight	90	[g]
Secondary camera:		
Type	Caspa FS	[-]
Resolution	360x960	[-]
Frame rate	60	[fps]
Weight	23	[g]
Datalink:		
Type	Xbee-PRO 868	[-]
Range	80	[km]
Data rate	24	[kbps]
Weight	2	[g]
Videolink:		
Type	Xbee 868LP	[-]
Range	4	[km]
Data rate	80	[kbps]
Weight	2	[g]

Finally, the UAS operating characteristics are presented in Table 5.5.

Table 5.5: Overview UAS operating characteristics

	Symbol	Value	Unit
Operating characteristics			
Loiter speed	V_{loit}	30	[km/h]
Cruise speed	V_{cruise}	130	[km/h]
Cruise back speed	$V_{cruise\,back}$	30	[km/h]
Maximum speed	V_{max}	145	[km/h]
Maximum rate of climb	RC_{max}	24	[m/s]
Range:			
Max range at maximum speed	$R_{max\ speed}$	7.8	[km]
Max range at cruise speed	R_{cruise}	9.3	[km]
Max range at cruise back speed	$R_{cruise\,back}$	50	[km]
Max range based on datalink (theoretical)	$R_{datalink}$	80	[km]
Max range based on videolink (theoretical)	$R_{videolink}$	4	[km]
Endurance:			
Max endurance at maximum speed	$E_{max\ speed}$	3.2	[min]
Max endurance at cruise speed	E_{cruise}	4.3	[min]
Max endurance at loiter speed	E_{loiter}	100	[min]
Operating altitude:	$H_{operating}$	480	[m]

From Table 5.5 can be seen that the videolink is limiting the range of the UAS. In order to increase the range of the videolink, a directional antenna can be used. This antenna can be directed by using the GPS data that is received by the datalink. Besides that, note that the operating altitude is reduced to 480 [m]. This is caused by the fact that the GoPro camera does not have the required resolution to be able to record images at 490 [m].

This concludes the section on UAS characteristics. In the next section, the power breakdown of the UAS is presented.

5.2 Power breakdown

In this section the power breakdown for both mission profiles is presented in tabular format. The mission profiles are shown in Figure 4.7 and discussed in Subsection 4.3.1.

The first overview represents the power breakdown for mission profile one and is shown in Table 5.6.

Table 5.6: Onboard power breakdown mission 1

Subsystems	Description	Power [W]	time [h]	Energy [Wh]
Electrical engine during climb	Scorpion HK3026-1600KV	326	0.0055	1.81
Electrical engine during loiter	Scorpion HK3026-1600KV	13.73	0.5	6.87
Autopilot	Lisa/L+IMU+GPS	0.66	0.5	0.33
Expansion board	Gumstix Overo	0.71	0.5	0.36
Extra camera	Caspa FS	0.32	0.5	0.16
Videolink	Xbee-PRO 868	2.88	0.5	1.44
Datalink	Xbee 868LP	0.17	0.5	0.09
Total:				**11.06**

Next, the power breakdown for mission profile two can be found in Table 5.7.

Table 5.7: Onboard power breakdown mission 2

Subsystems	Description	Power [W]	Time [h]	Energy [Wh]
Electrical engine during climb	Scorpion HK3026-1600KV	326	0.0055	1.81
Electrical engine during loiter	Scorpion HK3026-1600KV	13.73	0.322	4.42
Electrical engine during cruise	Scorpion HK3026-1600KV	326	0.033	10.86
Electrical engine during cruise back	Scorpion HK3026-1600KV	13.73	0.145	2.00
Autopilot	Lisa/L+IMU+GPS	0.66	0.5	0.33
Expansion board	Gumstix Overo	0.71	0.5	0.36
Extra camera	Caspa FS	0.32	0.5	0.16
Videolink	Xbee-PRO 868	2.88	0.5	1.44
Datalink	Xbee 868LP	0.17	0.5	0.09
Total:				**21.47**

By comparing Table 5.6 to Table 5.7, one can notice a large difference in required energy. In order to be able to perform both mission profiles, the battery selection was based on mission profile two.

This concludes the section on UAS power breakdown. In the upcoming section the UAS costs are estimated.

5.3 Costs

This section describes the costs of all UAS components.

An overview of all items and associated prices is presented in Table 5.8.

Table 5.8: Overview UAS hardware costs

Fixed equipment:	**Value [€]:**
Lisa/L + IMU + GPS	505,-
Xbee-PRO 868 (development kit)	120,-
Xbee 868LP (development kit)	160,-
Payload:	
Gumstix Overo	195,-
Caspa FS	60,-
GoPro Hero2	245,-
Power:	
Thunder Power 11.1V 2100mAh 25C battery	4 x 32,50 = 130,-[114]
Thunder Power TP1430C charger	200,-[115]
Propulsion system:	
Scorpion HK3026-1600KV electrical engine	90,-[110]
Scorpion Commander electronic speed controller	97,-[116]
Graupner CAM 10x6 propeller	5,-[111]
Control station:	
Motion Computing J3500	1250,-
Optional:	
SenseIT panorama camera	?
TurboWifi v2	109,-
Total (including TurboWifi option):	**3166,-**

From Table 5.8 can be seen that three additional batteries are included in the costs. This allows the user to charge the empty batteries while continuing UAS operations. Note that Table 5.8 does not include structural, manufacturing and operating costs. Also additional servos in order to control the elevator, ailerons and rudder were not included in the cost overview.

This concludes the section on UAS costs. The next section describes the preliminary UAS design evaluation.

5.4 Design evaluation

This section describes the design evaluation of the preliminary UAS design.

A compliance matrix is used in evaluation the design. The recommendations presented in Section 3.4 are also incorporated in the matrix. This matrix is presented in Table 5.9.

Table 5.9: Compliance matrix

(a) Compliance matrix

UAV requirements:	Fulfilled?	Comments
Flight regime between 30 [km/h] and 130 [km/h]	✓	Maximum speed is was determined to be 145 [km/h] .
Range of 4500 [m]	✓	The videolink has a theoretical range of only 4 [km]. In order to increase the range, a directional antenna in combination with the onboard wifi module can be used.
Endurance of 30 [min]	✓	For mission profile one a maximum endurance of 100 [min] was determined. For mission profile two an endurance of 30 [min] was estimated.
Operational altitude between 300 [m] and 490 [m]	✓	Due to the limited amount of pixels of the observation camera, the observation altitude was limited to 480 [m].
Operating costs below €20.000 per year with maximum purchasing costs between €10.000,- and €20.000,-.	✓	The purchasing costs were estimated to be 3166,- [€]. Note that this does not include structural, manufacturing and operating costs. Additional servos were also not included in the costs estimation.
Operable within 10 [min]		This requirements could not be tested/verified.
Withstand a wind force of 4 [Bft]	✗	3 [Bft] can be achieved (15 [m/s] wind force).
Resistant against 0.1 [mm] precipitation per hour		The proposed materials for the structure can create a waterproof UAS design. The engine is not water resistant. It can withstand low amounts of precipitation but tests must verify this.
Operate in dust and smoke with visibility below 100 [m]		The UAS has an onboard IR camera that allows it to navigate in poor visibility. Unfortunately, this was not verified/tested.
Emit the least amount of noise	✓	The engine-propeller combination selection was partly based on this requirement. Actual noise calculations were not performed.

Table 5.9: Compliance matrix (con't)

(b) Compliance matrix (con't)

Camera requirements:	Fulfilled?	Comments
EO and/or IR sensor(s)	✓	Two separate sensors were used. One EO- and one IR sensors
At least 1960 pixels in the direction parallel to the traffic stream at an operating altitude of 490 [m]	✗	The GoPro camera has only 1920 pixels in this direction. This reduces the max observation altitude to 480 [m].
Non-interlaced video	✓	The GoPro produces progressive images.
Global shutter	✗	The GoPro has a rolling shutter. The Caspa FS does have a global shutter but is not used for recording images.
$10 - 15$ frames per second	✓	The GoPro has a frame rate of 30 [fps]. The Caspa FS has a frame rate of 60 [fps].
$10 - 30$ minutes of high resolution recording time and an equal amount of simultaneous low resolution streaming time	✓	The GoPro has a recording time up to 2 [h]. The recording time of the Caspa FS was set to 30 [min]. Within the power breakdown there is room left for an increase of this value. Low resolution streaming is provided by either the Xbee 868LP module or a directional antenna in combination with the onboard wifi module.
Low image compression	✓	The GoPro has no image compression. The Caspa FS is connected to the Gumstix Overo board. Images can be compressed in order to be send to a ground station through a videolink.
Optical/digital zoom	✗	The GoPro does not have a zoom function. However, by changing the field of view in 1080p mode, one can shorten the focal distance, effectively zooming in the camera.
Auto focus	✓	The GoPro and the Caspa FS both have auto focus.
Ground station requirements:		
Portable	✓	A 1.6 [kg] tablet serves as a portable ground station
IP resistance of at least 54	✗	This tablet has an IP resistance of only 52 (less resistance against water and dust).
Simple and programmable interface	✓	The Lisa/L autopilot comes with Paparazzi ground control station software. This software is open source and has a programmable interface
Capability of supporting different video streams	✓	This tablet can cope with every desired video stream. The Paparazzi ground control station software is able to handle different types of video streams

From Table 5.9a can be seen that not all UAV requirements are fulfilled. One requirement was not met and three requirements could not be tested. Withstanding a wind force of 4 [Bft] was not achieved. A maximum speed of 145 [km/h] was estimated. This is equal to a wind force of 3 [Bft]. In the section on engine-propeller evaluation was stated that the UAS requires approximately 433 [W] to attain this maximum speed. Also was shown that the engine has a maximum power of 1470 [W]. From this can be concluded that the UAS may be able to fly even faster. The UPDK revealed that flying at a higher speed is limited by the performance of the propeller. Tests should reveal if this is in fact the case. Note that structural analysis was not performed during this thesis. Therefore nothing can be stated about the structural resistance against wind forces.

From Table 5.9b can be seen that the UAS is not able to operate at the upper bound of the flight regime. The GoPro camera does not have the required resolution, 1960 pixels, in the direction parallel to the traffic stream. Therefore the maximum operating altitude is limited to 480 [m]. This is still within the required operating regime. Besides that can also be seen from Table 5.9b that the camera does not have a global shutter and optical/digital zoom. This means that the images can suffer from motion artifacts. Although the GoPro does not have a zoom function, by changing the field of view in 1080p mode one can shorten the focal distance, effectively zooming in the camera. One final remark can be made about Table 5.9b. It can be seen that the IP resistance of the ground control station is not met. This means that it is less resistant to water and dust.

In Table 5.9, airworthiness requirements were not incorporated. When the UAS design is taken into production it must obviously comply with all airworthiness requirements. Therefore, these requirements must already be taken into account during the UAS design itself. Unfortunately, clear airworthiness requirements are not present yet and therefore these requirements could not be taken into account during this UAS design.

This concludes the chapter on UAS design characteristics. The next chapter finalizes this thesis report. It describes the conclusions and recommendations for this preliminary UAS design.

Chapter 6

Conclusions and recommendations

In this chapter an overview of all conclusions and recommendations is presented.

6.1 Conclusions

The goal of this thesis was to create a preliminary design of a multi-mission UAS by using off-the-shelf systems. This UAS must be able to perform both low and high speed missions. These missions are based on the requirements defined by the faculty of Civil Engineering at Technical University Delft, the Dutch National Aerospace Laboratory (NLR) and the Dutch National Police (KLPD). The mission objectives include providing support during fire and rescue operations, collecting aerial footage and conducting traffic monitoring, surveillance and reconnaissance.

To reach the stated goal several sub-goals were defined. A clear overview of all requirements had to be created first. The requirements were obtained by interviewing the above stated parties. This was followed by extensive market research in order to get an overview of the performance of current UAS designs. This market research was captured in a database containing over 400 entries. Based on the requirements in combination with the obtained database, all UAS classes and configurational options have been evaluated. The evaluation revealed that a new fixed wing electrical powered mini UAS design may be able to comply with the all UAS requirements.

The preliminary UAS design was initiated by estimating all Maximum Take-Off Weight (MTOW) components. In order to estimate these weight components, existing Weight Estimation Relationships (WERs) are often used in preliminary aircraft design. For this UAS design, however, the existing WERs could not be used. At present, there are no WERs available for mini UAS design. Therefore, new WERs have been derived for preliminary mini UAS design. These WERs were based on the available data in the database that was created. From this it was concluded concluded that most UASs are equipped with an electrical or piston powered propulsion system. The effect of the two different propulsion systems was investigated. It was concluded that an electric propulsion system is more suitable for this preliminary mini UAS design. Therefore, the remainder of the design was based on the obtained results for a UAS with an electric propulsion system.

After obtaining all weight parameters, the constraints of the preliminary UAS design were tested. This resulted in a new design point. Based on this new design point, the wing design was initiated. A quasi-3D optimizer was used to optimize the wing shape of the UAS. In order to initiate the wing optimizer, an airfoil had to be selected. After analyzing over 1500 airfoils, three suitable airfoils were chosen. Based on the performance and geometry of the three optimized wings, the wing with the naca23012 airfoils was chosen for this UAS wing design. This was followed by a revision of the MTOW parameters.

Subsequently, the horizontal and vertical tail designs were created by using volume coefficients. Based on the obtained wing parameters and reference UASs parameters in combinations with these volume coefficients, the tail design was defined. After that, the effect of the wing on the tail was investigated. From this analysis was concluded that the horizontal tail is not in the wake of the wing at stall conditions. This allows the horizontal tail to maneuver the UAS back into normal flight conditions while the wing is in stall conditions. In the next step of the preliminary design, the stability of the UAS was addressed. AVL was used in order to compute the primary static and dynamic stability derivatives of the UAS. From the obtained stability derivatives was concluded that the UAS is both statically and dynamically stable.

Next, the UAS material options for the structure were evaluated. During this evaluation a new manufacturing technique, 3D printing, was tested. Based on the results was concluded that this manufacturing method is not yet suitable for creating UAS designs. Therefore, it is recommended to create the UAS structure out of EPP in combination with carbon fiber reinforcements/carbon rods. After constructing the UAS by using 3D software, the structural weight of the UAS was estimated. The evaluation of this structural weight revealed that the initial structural weight was slightly underestimated.

After obtaining the structural weight of the UAS, the propulsion system of the UAS was designed. The UAV Propulsion Development Kit (UPDK) was used to estimate the performance of a propeller and electrical engine combination. The UPDK was extended with additional engines, propellers and data records. Besides that, the engine and propeller modeling module were revised and a batch mode in combination with a multi-core functionality was implemented. After preselection of the engines and propellers, the UPDK was used to analyze the remaining combinations. Based on the evaluation of the top five combinations, the Scorpion HK3026-1600KV electrical engine in combination with the Graupner CAM 10x6 propeller were chosen for this preliminary UAS design. From this selection was concluded that the required power for the UAS was underestimated in the preliminary UAS design. This was caused by overestimating the efficiency of the engine and propeller. Next, the Thunder Power 11.1V 2100mAh 25C battery Lithium Polymer battery was selected based on the total amount of required energy capacity. The required energy capacity was calculated for two mission profiles. Based on the most energy intensive mission profile, the battery capacity was selected. The weight of this battery was also underestimated because of overestimating the efficiency of the engine and propeller.

Subsequently, the UAS subsystems were selected. These subsystems included the autopilot, control station, camera(s), datalink and videolink. Based on the specifications of the hardware and software, the Lisa/L autopilot was chosen. A Motion computing J3500 tablet was selected for running the autopilot software. Selecting an off the shelf camera that respects all requirements proved to be difficult. The GoPro Hero 2 was selected as an observation camera. The composite video out connection of the camera is used for streaming purposes. An additional Caspa FS camera was selected to catch the infrared part of the light spectrum. This camera can easily be connected to the autopilot which allows onboard processing of the images. For the datalink, a long range low data rate Xbee-PRO 868 module was selected while for the videolink a short range high data rate Xbee 868LP module was selected. When the range and/or data rate of videolink is not sufficient an additional TurboWifi v2 directional antenna can be used to improve the link. From these results, the payload weight was derived. The assumed payload weight and estimated weight based on the WER was higher than the actual payload weight.

After all subsystems were selected, the UAS design characteristics were evaluated. From this it was concluded concluded that the fuel and structural weight were underestimation while the payload weight was overestimated. The large wing span, in comparison with the reference UASs, resulted in a higher structural weight causing it to differ from the result of the WER. The payload weight was intentionally overestimated in order to have some freedom in the payload selection. The WER however, did not accurately estimate the actual payload weight for the UAS. It was concluded that the reference UASs are equipped with heavier or additional payloads. Part of the overestimated payload weight was used to compensate the underestimated weights. After this compensation there was still a rest weight. This rest weight can be used for an increase in battery capacity or for additional payloads.

Finally, the UAS design was evaluated. The following conclusions were drawn. The UAS is able to fly at the required minimum speed of 30 [km/h] as well as the required cruise speed of 130 [km/h]. Despite the fact that the UAS is able to achieve a maximum speed of 145 [km/h], it is not able to fly with a head wind of 4 [Bft]. Note that the engine has enough access power to achieve a higher maximum speed. The UPDK revealed that flying at a higher speed is limited by the performance of the propeller. Note that structural analysis was not performed during this thesis. Therefore nothing can be stated about the structural resistance against wind forces. Furthermore, the videolink may not be capable of streaming images at the edge of the UAS range. In order to increase the range of the videolink, a directional antenna can be used on the ground. The resistance of the UAS against precipitation, the ability to operate within 10 [min] and in conditions with dust and smoke could not be tested. However, an additional infrared camera was selected in order to allow navigation in poor visibility. Also was concluded that the observation camera limits the maximum observation altitude to 480 [m]. This is caused by its “low” resolution. Note that the maximum field of view of this camera is 170°. Due to that, and the fact that the camera has a single image sensor, the GoPro camera exhibits some fisheye distortion around the edges of the frame. Besides that, the GoPro camera does not have the required global shutter, which can result in motion artifacts. The camera also does not have the ability to zoom. However, by changing the field of

view in 1080p mode, one can shorten the focal distance, effectively zooming in the camera. One final remark can be made about the ground station requirements. The J3500 tablet has an internal protection resistance of only 52 instead of 54. This means that the ground station is less resistance against water and dust.

Overall can be concluded that it is possible to create a preliminary mini UAS design based on the derived WERs. Together with off-the-shelf systems it was possible to create a design that is able to comply with most requirements. In future research should be kept in mind that predicting the efficiency of the propulsion system greatly affects the resulting weight estimation outcomes. Also finding a suitable camera proved to be difficult. Not one of the considered off-the-shelf cameras were able to comply with all requirements.

6.2 Recommendations

Throughout the preliminary design of this UAS, a couple of recommendations drew my attention as areas of improvement. These recommendations are presented in the following overview.

- Obtain more detailed information about the UASs. The created database is incomplete and must be elaborated in order to increase the precision of the weight estimation relationships that were derived from the data. The UASs must also be separated by means of applications. This can also lead to an increase in precision of the derived WERs.
- Revise the WER for the payload.
- Create a user friendly tool that allows preliminary mini UAS design.
- Redesign and expand the wing optimizer created by Trips[78]. First, the user-friendliness must be improved. A feedback loop, recalculating the required lift and associated drag of the UAS, can be implemented in the optimizer. Subsequently, the optimizer should be redesigned such that it creates a first estimate of the optimized wing. This first estimate can be used in further design calculations (tail design, drag estimation, power estimation, engine-propeller combination, new MTOW). The results can be fed back into the wing optimizer until convergence is achieved. After that, the obtained parameters can be used to perform a more detailed wing optimization. This should reduce the calculation time substantially.
- The flight characteristics and aerodynamics of the UAS must be estimated for the entire flight regime. The drag of the fuselage must also be included in the UAS design. Also, the effect of the propeller wake on the body and other surfaces should be taken into account.
- Incorporate the design of control surfaces and perform detailed stability & control analysis.
- Include structural analysis in the preliminary UAS design and experiment with more 3D printing techniques.
- Follow up on the work of Hulsman[104]. The engine and propeller database was already expanded. The UAV Propulsion Development Kit can be elaborated

by including even more engine and propeller data. In order to further verify the program, compare the results with QPROP.
- Test the performance of the selected subsystems.
- Try to obtain Lithium Sulfur batteries in order to test its capabilities.

References

[1] Roskam, J., *Airplane design. Pt. 1. Preliminary sizing of airplanes*, Airplane design, DARcorporation, 1997.

[2] Kundu, A., *Aircraft Design*, Cambridge University Press, The Edinburgh Building, Cambridge CB2 8RU, UK, 2010.

[3] Raymer, *Aircraft Design: A Conceptual Approach*, Fourth Edition, AIAA, 2006.

[4] Ruijgrok, G., *Elements of Airplane Performance*, Delft University Press, 2600 MG Delft, The Netherlands, 2004.

[5] Staff, R. T., "UAS Market Forecast to Reach $2.3 Billion Dollars Worldwide by 2017," http://www.researchandmarkets.com/reportinfo.asp?report_id=1553924&tracker=related, March 2011, Online; accessed: 28-07-2011.

[6] "UAS Roadmap 2005-2030," http://www.fas.org/irp/program/collect/uav_roadmap2005.pdf, July 2005, Online; accessed: 27-07-2011.

[7] Newcome, L. R., *Unmanned Aviation - A Brief History of Unmanned Aerial Vehicles*, AIAA, Reston, 1st edition ed., 2004.

[8] "21st Century Aerial Robotics," http://www.personal.psu.edu/lnl/001/uav1.pdf, 2001, Online; accessed: 28-07-2011.

[9] "Fritz X," http://upload.wikimedia.org/wikipedia/commons/3/3b/Fritz_X_side.jpg, Online; accessed: 28-07-2011.

[10] "MQM-57 Falconer," http://www.503rd-b-co-buddies.com/images/MQM-57-Falconer.jpg, Online; accessed: 28-07-2011.

[11] "Gyrodyne QH-50," http://www.gyrodynehelicopters.com/qh-50a_models1.htm, Online; accessed: 28-07-2011.

[12] "BQM-34 Firebee," http://upload.wikimedia.org/wikipedia/commons/8/88/DC-130_mounted_Firebees_DN-SC-85-06043.jpg, Online; accessed: 28-07-2011.

[13] "Scout," http://www.israeli-weapons.com/weapons/aircraft/uav/scout/scaut2.jpg, Online; accessed: 29-07-2011.

[14] "Laima," http://www.ctie.monash.edu.au/hargrave/images/as_ocean_320_x_240.jpg, Online; accessed: 29-07-2011.

[15] "Global Hawk," http://en.wikipedia.org/wiki/File:Globalhawk.750pix.jpg, Online; accessed: 29-07-2011.

[16] "Helios," http://upload.wikimedia.org/wikipedia/commons/c/c3/Pages_from_64317main_helios-1.jpg, Online; accessed: 01-08-2011.

[17] Austin, R., *Unmanned Aircraft Systems*, Aerospace Series, A John Wiley and Sons, Ltd., Publication, Chichester, 2010.

[18] "DelFly," http://www.delfly.nl, Online; accessed: 01-08-2011.

[19] "Wasp," http://www.designation-systems.net/dusrm/app4/wasp.html, Online; accessed: 01-08-2011.

[20] "Raven," http://www.designation-systems.net/dusrm/app2/q-11.html, Online; accessed: 02-08-2011.

[21] "Aerovision Fulmar," http://www4.janes.com, Online; accessed: 20-10-2011.

[22] "Predator," http://science.howstuffworks.com/predator.htm, Online; accessed: 02-08-2011.

[23] "Reaper," http://www.digitaljournal.com/img/7/4/6/4/4/7/i/5/3/0/o/800px-MQ-9_Reaper_in_flight__282007_29.jpg, Online; accessed: 02-08-2011.

[24] "TCOM 598 Independent Study of Telecommunications Unmanned Aerial Vehicles (UAVs) Enebled by Technology," https://telecom.gmu.edu/sites/default/files/publications/TCOM598-2006-Puels-UAVs.pdf, Online; accessed: 20-10-2011.

[25] "Raven UAV Draws Raves From The Field," http://www.defenseindustrydaily.com/raven-uav-draws-raves-from-the-field-067/, Online; accessed: 20-10-2011.

[26] "MQ-1B Predator," http://www.af.mil/information/factsheets.asp?id=122, Online; accessed: 20-10-2011.

[27] "Specifications Reaper," http://www.af.mil/information/factsheets/factsheet.asp?id=6405, Online; accessed: 02-08-2011.

[28] "MQ-9 Reaper," http://www.af.mil/information/factsheets.asp?fsID=6405, Online; accessed: 20-10-2011.

[29] "Specifications Global Hawk," http://www.af.mil/information/factsheets/factsheet.asp?id=13225, Online; accessed: 02-08-2011.

[30] "RQ-4 Global Hawk," http://www.af.mil/information/factsheets.asp?fsID=13225, Online; accessed: 20-10-2011.

[31] "Boeing X-45," http://www.boeing.com/companyoffices/gallery/images/military/x-45/dvd-782-1.html, Online; accessed: 16-08-2011.

[32] "Buster," http://www.designation-systems.net/dusrm/app4/buster.html, Online; accessed: 16-08-2011.

[33] "Camcopter S-100," http://thefutureofthings.com/pod/288/camcopter-s-100-uav.html, Online; accessed: 16-08-2011.

[34] "EADS Sharc," http://www.fsd.rwth-aachen.de/English/Research/Sharc.php, Online; accessed: 16-08-2011.

[35] "Dragonfly DP-6," http://www.flightglobal.com/articles/2007/09/17/216798/dragonfly-pictures-unveils-tandem-rotor-dp-6-uav.html, Online; accessed: 10-08-2011.

[36] "AscTec Pelican," http://www.asctec.de/asctec-pelican-3/, Online; accessed: 17-10-2011.

[37] "AscTec Falcon 8," https://picasaweb.google.com/asctec/AscTecFalcon8#5452262544589569794, Online; accessed: 16-08-2011.

[38] "Panther," http://www.iai.co.il/Templates/Gallery/GalleryPopup.aspx?docID=41360&lang=en&num=1, Online; accessed: 10-08-2011.

[39] "Festo SmartBird," http://www.festo.com/net/SupportPortal/Downloads/46270/Brosch_SmartBird_en_8s_RZ_300311_lo.pdf, Online; accessed: 16-08-2011.

[40] "t-BLIMP," http://www.v-tol.com/images/tblimp_l.jpg, Online; accessed: 17-08-2011.

[41] "Ascending Technology Atom Processor Board," http://www.asctec.de/assets/Downloads/Manuals/CoreExpressCarrierboardmanualv10.pdf, Online; accessed: 01-09-2011.

[42] "UAV Engines Plant," http://ae-www.technion.ac.il/~jetlab/6thsmp/hemi.pdf, Online; accessed: 08-08-2011.

[43] "AXI 4130/20 Goldline electrical engine," http://www.modelmotors.cz/download/katalog_2011_hr.pdf, Online; accessed: 15-08-2011.

[44] "BGX-1 3500 RN O.S. 2 Stroke Engine," http://www.osengines.com/engines/osmg0350.html, Online; accessed: 15-08-2011.

[45] "49-PI Type II .30 Wankel Engine," http://www.osengines.com/engines/osmg1401.html, Online; accessed: 15-08-2011.

[46] "FT-300 O.X. 4 Stroke Engine," http://www.osengines.com/engines/osmg1250.html, Online; accessed: 15-08-2011.

[47] "Wren 44 Turboprop," http://www.wrenturbines.co.uk/engines/turboprop/wren-44-turboprop, Online; accessed: 15-08-2011.

[48] "Wren 160 Pro Turbojet," http://www.wrenturbines.co.uk/engines/turbojet/wren-160, Online; accessed: 15-08-2011.

[49] "Ring laser gyroscopes," http://www.ringlaser.org.nz/content/about_us.php, Online; accessed: 24-08-2011.

[50] "Nanosar," http://www.aviationnews.eu/blog/wp-content/uploads/2008/03/scaneagle_nanosar3.jpg, Online; accessed: 09-08-2011.

[51] "Ultrasonic range finder," http://www.buildyourowndrone.co.uk/v/vspfiles/photos/SMB-1030-1.jpg, Online; accessed: 22-08-2011.

[52] "TASE 200," http://www.cloudcaptech.com/gimbal_tase200.shtm, Online; accessed: 09-08-2011.

[53] "Infrared Image," http://www.solarcrete.com/pictures/thermal-images/infrared-northern-illinois-mold-huntley-illinois.jpg, Online; accessed: 23-08-2011.

[54] "MMIST CQ-10 SnowGoose," http://www.designation-systems.net/dusrm/app2/q-10.html, Online; accessed: 23-08-2011.

[55] "Transportation box Raven," http://upload.wikimedia.org/wikipedia/commons/4/42/Raven_UAV.jpg, Online; accessed: 24-08-2011.

[56] "Transportation box Raven," http://en.wikipedia.org/wiki/Boeing_ScanEagle, Online; accessed: 24-08-2011.

[57] "Global Hawk ground station," http://www.happynews.com/news/4142010/nasa-global-hawk-completes-first-flight.htm, Online; accessed: 17-08-2011.

[58] Ladiges, R. and van Sijll, M., "OT&E scenario's for KLPD UAS," Document deriving UAS requirements by means of example scenario's.

[59] ten Buuren G. and F, M., "UAS survey," Tech. rep., KLPD.

[60] "Prosilica GC2450," http://www.alliedvisiontec.com/emea/products/cameras/gigabit-ethernet/prosilica-gc/gc2450.html, Online; accessed: 05-03-2012.

[61] "Progressive scanning," http://www.indiana.edu/~aainfo/DigitalVideo/Info/Adobe/prmr_interlace.pdf, Online; accessed: 09-09-2011.

[62] "DCF77 long-wave time signal radio station," http://en.wikipedia.org/wiki/DCF77, Online; accessed: 09-09-2011.

[63] "Multi-sensor camera," http://www.vrmagic.com/imaging/cameras-framegrabber/multi-sensor-cameras/, Online; accessed: 26-06-2012.

[64] "3D modeling," http://www.mantis-vision.com/page/products, Online; accessed: 26-06-2012.

[65] "Motion computing tablet," http://www.motioncomputing.com/products/tablet_pc_J35.asp, Online; accessed: 26-06-2012.

[66] "NLR ground station interface," .

[67] (ICAO), I. C. A. O., "Convention on International Civil Aviation (Doc 7300)," Tech. rep., International Civil Aviation Organization (ICAO), 2006.

[68] (ICAO), I. C. A. O., "Unmanned Aircraft Systems (UASs) Circular 328," Tech. rep., International Civil Aviation Organization (ICAO), 2011.

[69] "Regulations EC," http://www.easa.eu.int/language/nl/home.php, Online; accessed: 27-09-2011.

[70] "Regeling Modelvliegen," http://www.modelvliegsport.nl/index.php/algemeen/regeling-modelvliegen, Online; accessed: 27-09-2011.

[71] "Airspace Classes," http://www.centennialofflight.gov/essay/Dictionary/airspace/DI79G1_hi.jpg, Online; accessed: 30-09-2011.

[72] "GC-201 Class I certificate," http://www.geocopter.nl/, Online; accessed: 26-06-2012.

[73] "Raven Class II certificate," http://investor.avinc.com/releasedetail.cfm?ReleaseID=439771, Online; accessed: 26-06-2012.

[74] "Janes all the world UAVs," http://www4.janes.com, Online; accessed: 25-11-2011.

[75] Gundlach, J., *Designing Unmanned Aircraft Systems: A Comprehensive Approach*, AIAA Education Series, AIAA, 2012.

[76] "Tamron C-mount lens," http://www.tamron.eu/uploads/tx_kedownloads/M118FM50_01.pdf, Online; accessed: 05-03-2012.

[77] "Turbojet mini UAS engines," http://www.modelaircraftcompany.com/turbines/jet-cat/cat_150.html, Online; accessed: 01-02-2012.

[78] Dennis Trips, "Aerodynamic Design and Optimization of a Long Range Mini-UAV," 2010.

[79] Melkert, J. A., "Preliminary sizing of Aircraft," Course Notes: AE3021 Aircraft Design (2008-2009 Q1), 2009, Faculty Of Aerospace Engineering, TU Delft.

[80] "Matlab fmincon toolbox," http://www.mathworks.nl/help/toolbox/optim/ug/fmincon.html, Online; accessed: 21-03-2012.

[81] Torenbeek, E., *Synthesis of Subsonic Airplane Design*, Kluwer Academic Press, 1982.

[82] "Sperwer UAS," http://www.strategypage.com/military_photos/military_photos_20071010144016.aspx, Online; accessed: 17-05-2012.

[83] "Airfoil database," http://www.ae.illinois.edu/m-selig/ads/coord_database.html, Online; accessed: 05-04-2012.

[84] "Xfoil," http://web.mit.edu/drela/Public/web/xfoil/, Online; accessed: 06-04-2012.

[85] "Matlab," http://www.mathworks.nl/products/matlab/, Online; accessed: 01-05-2012.

[86] "AVL," http://web.mit.edu/drela/Public/web/avl/, Online; accessed: 01-05-2012.

[87] "XFLR5," http://www.xflr5.com/xflr5.htm, Online; accessed: 09-07-2012.

[88] J., R., *Airplane Flight Dynamics and Automatic Flight Control*, DAR Corp, 2007.

[89] Goodier K., "Making and using expanded plastic," *New Scientist*, , No. 240, 1961, pp. 706.

[90] "Specifications EPP," http://www.bpf.co.uk/Plastipedia/Polymers/Expanded_Polypropylene_EPP.aspx, Online; accessed: 18-06-2012.

[91] "Specifications carbon fibres," http://www.carlesso.net/inglese/carbonioecc.jsp, Online; accessed: 18-06-2012.

[92] "Specifications ABS," http://www.bpf.co.uk/Plastipedia/Polymers/ABS_and_Other_Specialist_Styrenics.aspx, Online; accessed: 18-06-2012.

[93] "Autodesk," http://www.autodesk.nl/adsk/servlet/home?siteID=431528&id=847010, Online; accessed: 17-06-2012.

[94] "Catia," http://www.3ds.com/products/catia, Online; accessed: 17-06-2012.

[95] "SolidWorks," http://www.solidworks.nl/, Online; accessed: 17-06-2012.

[96] "HP Designjet Color 3D Printer - Specifications," http://h10010.www1.hp.com/wwpc/uk/en/ga/WF06b/18972-18972-3328061-4154659-4154659-4154512-4154513.html?dnr=1, Online; accessed: 17-06-2012.

[97] "Dimension 3D printer," http://www.dimensionprinting.com/3d-printers/3d-printing-1200es.aspx, Online; accessed: 11-07-2012.

[98] "Zcorp 3D printer," http://www.zcorp.com/documents/1206_9394-ZPrinterBrochure.pdf, Online; accessed: 11-07-2012.

[99] "Objet 3D printer," http://www.objet.com/3D-Printer/Objet_Eden500V/, Online; accessed: 11-07-2012.

[100] "Solido 3D printer," http://www.solido3d.com/AdminLockedFiles/File115604.pdf, Online; accessed: 11-07-2012.

[101] "Propcalc," http://www.drivecalc.de/PropCalc/index.html, Online; accessed: 20-03-2012.

[102] "Drivecalc," http://www.drivecalc.de, Online; accessed: 20-03-2012.

[103] "QPROP," http://web.mit.edu/drela/Public/web/qprop/, Online; accessed: 25-03-2012.

[104] S., H., "UAV Propulsion Development Kit (UPDK)," http://www.updk.nl, 2012.

[105] et all, H. S., "UAVForge challenge," Tech. rep., Technical University Delft, 2012.

[106] Robert S. Merril, "Nonlinear aerodynamic corrections to blade element momentum module with validation experiments," .

[107] Kocurek, J. D. and Tangler, J. L., "Wind turbine post-stall airfoil performance characteristics guidelines for blade-element momentum methods," Tech. rep., National Renewable Energy Laboratorium.

[108] Bruss, H., "Solar Flug," Tech. rep., GMBH Munchen.

[109] "ARC 28-58-1 electrical engine," http://shop.rc-electric-jets.com/Arc-28-58-1-3180kv-70-mm-Brushless-Motor-ARC28-58-1.htm, Online; accessed: 31-07-2012.

[110] "Scorpion HK-3026-1600KV electrical engine," http://www.scorpionsystem.com/catalog/discontinued/motor/hk30_1/HK30-1600KV/, Online; accessed: 31-07-2012.

[111] "Graupner CAM 10x6 propeller," http://www.graupner.de/en/products/0e83a7f8-937c-4999-aa76-dda2618f2c65/1360.25.15/product.aspx, Online; accessed: 31-07-2012.

[112] "Sion Power Litium Sulfur batteries," http://sionpower.com/pdf/articles/LIS%20Spec%20Sheet%2010-3-08.pdf, Online; accessed: 01-08-2012.

[113] "Graupner Lipo TX3/2800 mAh battery," http://www.graupner.de/en/products/18f1457c-4971-481b-a510-512b72af385d/7649.3G2/product.aspx, Online; accessed: 01-08-2012.

[114] "Thunder Power 11.1V 2100mAh 25C," http://thunderpowerrc.com/html/G6ProLite25CSeriesBatteries.htm, Online; accessed: 01-08-2012.

[115] "Thunder Power TP1430 battery charger," http://www.aerobertics.be/productDetail.php?prod=6492&cat=9&brand=40, Online; accessed: 01-08-2012.

[116] "Scorpion Commander," http://www.scorpionsystem.com/catalog/discontinued/speed_controller/26v_esc/6S-Com45A-ESC//, Online; accessed: 01-08-2012.

[117] "MicroPilot MP2128g," http://www.micropilot.com/products-mp2128g-specs.htm, Online; accessed: 09-07-2012.

[118] "PaparazzI Lisa/L," http://paparazzi.enac.fr/wiki/Lisa/L, Online; accessed: 09-07-2012.

[119] "ArduPilotMega," http://www.diydrones.com/notes/ArduPilot, Online; accessed: 09-07-2012.

[120] "Pixhawk," https://pixhawk.ethz.ch/electronics/base_small, Online; accessed: 09-07-2012.

[121] "Overo Fire COM," https://www.gumstix.com/store/product_info.php?products_id=227, Online; accessed: 10-07-2012.

[122] "MicroPilot HORIZON ground control station," http://www.micropilot.com/products-horizonmp.htm, Online; accessed: 10-07-2012.

[123] "Paparazzi ground control station," http://paparazzi.enac.fr/wiki/GCS, Online; accessed: 10-07-2012.

[124] "ArduPilot mission planner," http://code.google.com/p/ardupilot-mega/wiki/Mission, Online; accessed: 10-07-2012.

[125] "QGroundControl ground control station," http://qgroundcontrol.org/screenshots, Online; accessed: 10-07-2012.

[126] "Panasonic CF-53 laptop," http://www.panasonic.com/business/toughbook/semi-rugged-laptop-toughbook-53.asp, Online; accessed: 10-07-2012.

[127] "Nook e-reader," http://www.barnesandnoble.com/u/nook/379003208/, Online; accessed: 10-07-2012.

[128] "Prosilica GB2450," http://www.alliedvisiontec.com/emea/products/cameras/gigabit-ethernet/prosilica-gb/gb2450.html, Online; accessed: 05-03-2012.

[129] "GoPro HD Hero2," http://gopro.com/hd-hero2-cameras/, Online; accessed: 12-07-2012.

[130] "Caspa FS," https://www.gumstix.com/store/product_info.php?products_id=254, Online; accessed: 12-07-2012.

[131] "SenseIT panorama camera," http://www.senseit.nl/, Online; accessed: 12-07-2012.

[132] "VRmagic multi-sensor camera," http://www.vrmagic.com/imaging/cameras-framegrabber/multi-sensor-cameras/, Online; accessed: 12-07-2012.

[133] "Digi Xtend module," http://www.digi.com/products/wireless-wired-embedded-solutions/zigbee-rf-modules/point-multipoint-rfmodules/xtend-module#overview, Online; accessed: 15-07-2012.

[134] "Aerovironment digital data link," http://www.avinc.com/downloads/DDLDataSheet2012.pdf, Online; accessed: 15-07-2012.

[135] "Regulations radio frequency use," http://wetten.overheid.nl/BWBR0023553/volledig/geldigheidsdatum_10-07-2012, Online; accessed: 15-07-2012.

[136] "Xbee-PRO 868," http://www.digi.com/products/wireless-wired-embedded-solutions/zigbee-rf-modules/point-multipoint-rfmodules/xbee-pro-868#overview, Online; accessed: 15-07-2012.

[137] "Xbee 868LP," http://www.digi.com/products/wireless-wired-embedded-solutions/zigbee-rf-modules/zigbee-mesh-module/xbee-868lp#overview, Online; accessed: 15-07-2012.

[138] "TurboWifi v2 USB directional antenna," http://www.wifiantennes.nl/index.php?action=article&aid=1078&group_id=48&lang=NL, Online; accessed: 18-07-2012.

Appendix A

Work Flow Diagram

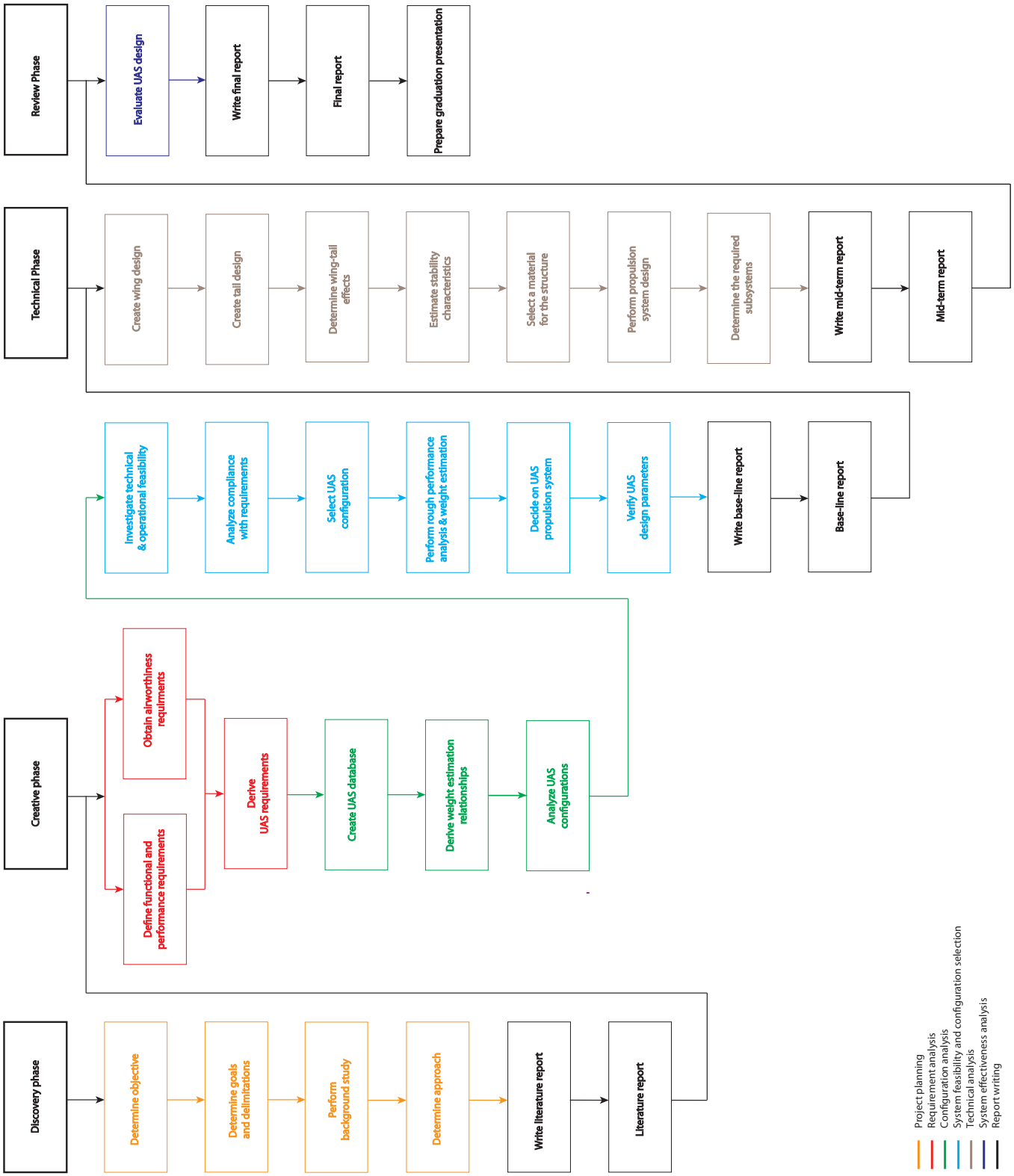

Figure A.1: Work Flow Diagram

Appendix B

Inventory of user specifications KLPD

This appendix contains classified information and is therefore not displayed in this version of the report.

Appendix C

Overview parameters reference UASs

For the sake of clarity, the tables are put side by side on the next two pages.

Table C.1: Overview parameters reference UASs

(a) Overview parameters reference UASs

N	UAS name	MTOW [N]	Endurance [h]	Range [km]	Max. speed [km/h]
1	**ASN-217**	53.94	1.5	20	120
2	**Biodrone**	117.68	1	20	130
3	**Azimut 2**	88.26	1	10	120
4	**Skybird**	23.34	1	10	100
5	**Trogon**	22.06	0.75	10	129
6	**Silent Eye**	34.32	1	10	110
7	**Desert Hawk**	66.69	2	10	105
8	**Rover**	49.03	1	5	100
9	**L Surveillance UAV**	44.13	0.67	5	110
10	**Nietoperz-3L**	63.74	1.5	15	100
11	**ZALA 421-08**	22.56	1.67	15	190
12	**ZALA 421-03**	117.68	1	25	95
13	**Eleron T25**	31.38	1	25	105
14	**RemoEye 006**	58.84	1.5	15	75
15	**Mantis**	29.42	1.25	10	100
16	**A-3 Remez**	98.07	2	5	105
17	**A-4 Albatros**	179.46	2	20	125
18	**E-Swift Eye**	21.57	1	22	95
19	**Midge**	22.56	0.83	10	85
20	**S.O.D. I**	29.42	1	10	129
21	**Swift-Eye**	62.76	0.67	3.2	145
22	**Hawkeye**	37.27	1	10	85
23	**Puma AE**	57.86	2	15	83
24	**RQ-11 Raven**	18.63	1.5	12	96
25	**Super Swiper**	40.01	2	16	112
26	**Swiper**	14.71	1	3.2	72
27	**Evolution**	28.93	0.75	10	80
28	**Javelin**	66.69	2	8	105
29	**Desert Hawk I+**	31.38	1	11.1	93
30	**Maveric**	11.08	0.83	5	102

Table C.1: Overview parameters reference UASs (cont'd)

(b) Overview parameters reference UASs (cont'd)

N	UAS name	Min. speed [km/h]	Stall speed [km/h]	Ceiling [m]	Payload [N]
1	**ASN-217**	40	-	4000	14.71
2	**Biodrone**	35	-	300	27.46
3	**Azimut 2**	35	-	300	19.61
4	**Skybird**	-	30	4570	2.94
5	**Trogon**	37	-	1000	4.90
6	**Silent Eye**	70	-	1000	4.90
7	**Desert Hawk**	32	-	305	-
8	**Rover**	30	-	610	9.81
9	**L Surveillance UAV**	50	-	600	-
10	**Nietoperz-3L**	50	-	1000	-
11	**ZALA 421-08**	65	-	4000	2.94
12	**ZALA 421-03**	60	-	3000	19.61
13	**Eleron T25**	65	-	3000	-
14	**RemoEye 006**	-	40	-	-
15	**Mantis**	70	30	-	-
16	**A-3 Remez**	-	58	-	29.42
17	**A-4 Albatros**	-	60	-	29.42
18	**E-Swift Eye**	47	-	4000	2.94
19	**Midge**	40	-	3000	5.88
20	**S.O.D. I**	37	-	5030	5.49
21	**Swift-Eye**	48	-	4265	-
22	**Hawkeye**	50	-	300	-
23	**Puma AE**	37	-	152	17.65
24	**RQ-11 Raven**	43	-	152	0.98
25	**Super Swiper**	48	-	-	10.3
26	**Swiper**	24	-	-	-
27	**Evolution**	-	40	-	4.41
28	**Javelin**	-	32	305	14.22
29	**Desert Hawk I+**	-	56	2285	4.9
30	**Maveric**	-	34	-	0.98

Appendix D

Additional figures engine trade-off

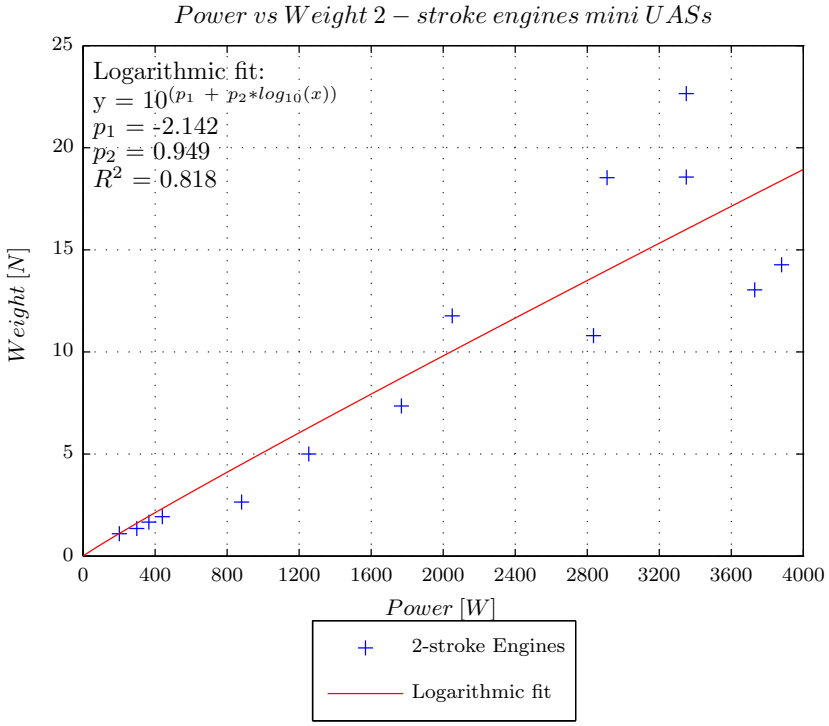

a: Engine weight vs Engine power 2-stroke engine mini UAS

Figure D.1: Engine weight vs Engine power engines mini UAS

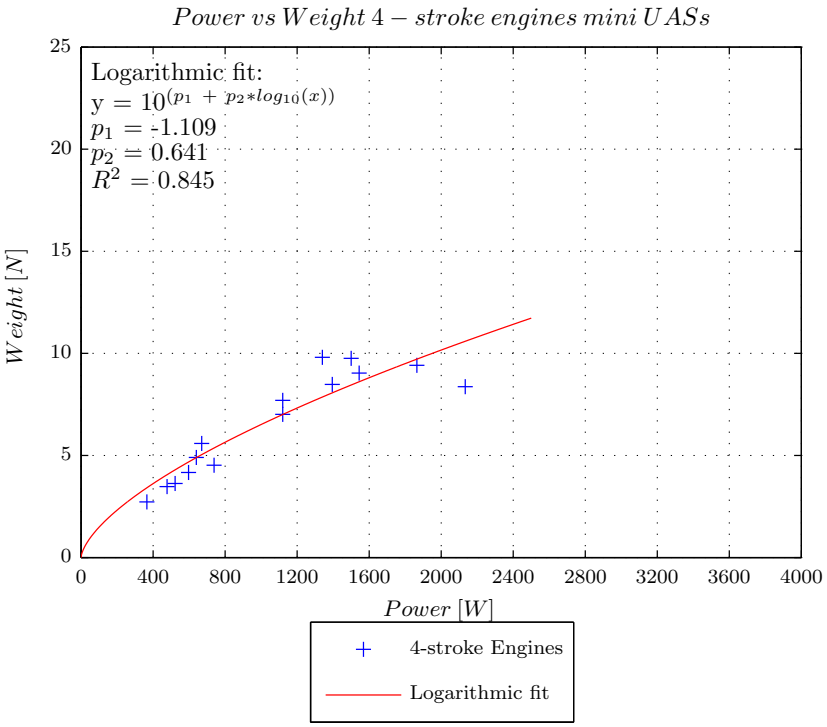

b: Engine weight vs Engine power 4-stroke engine mini UAS

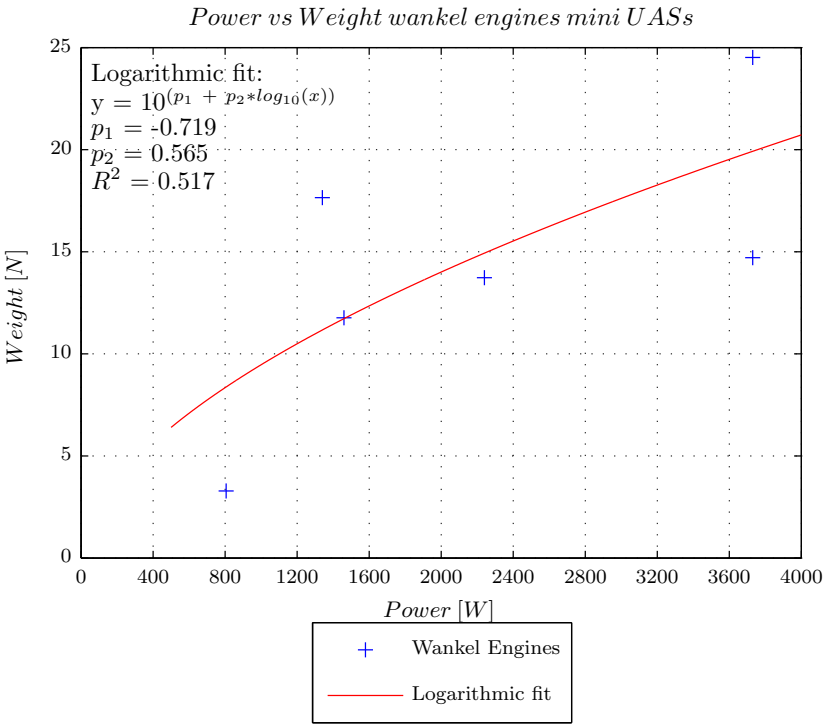

c: Engine weight vs Engine power wankel engine mini UAS

Figure D.1: Engine weight vs Engine power engines mini UAS (cont'd)

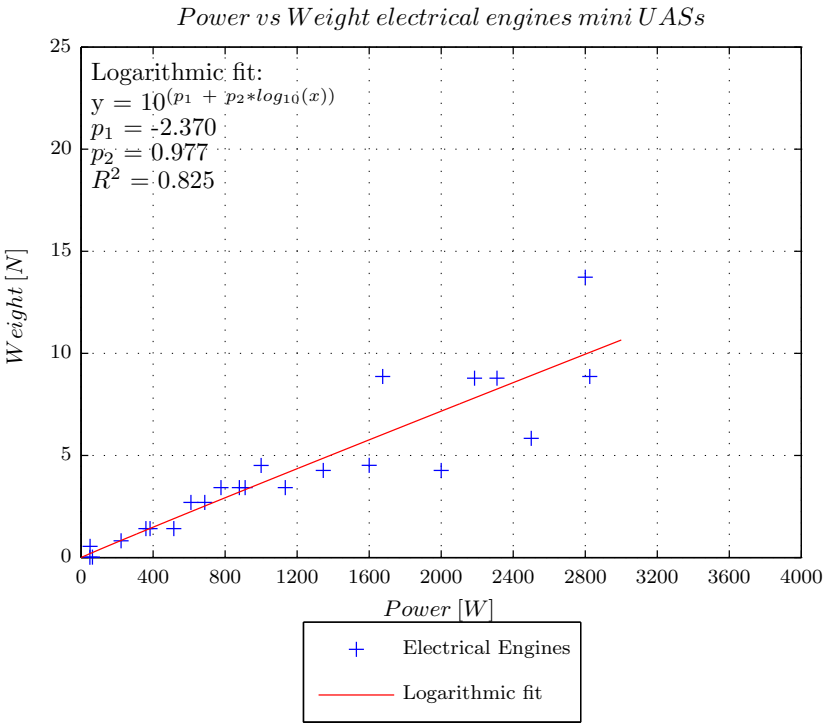

d: Engine weight vs Engine power electrical engine mini UAS

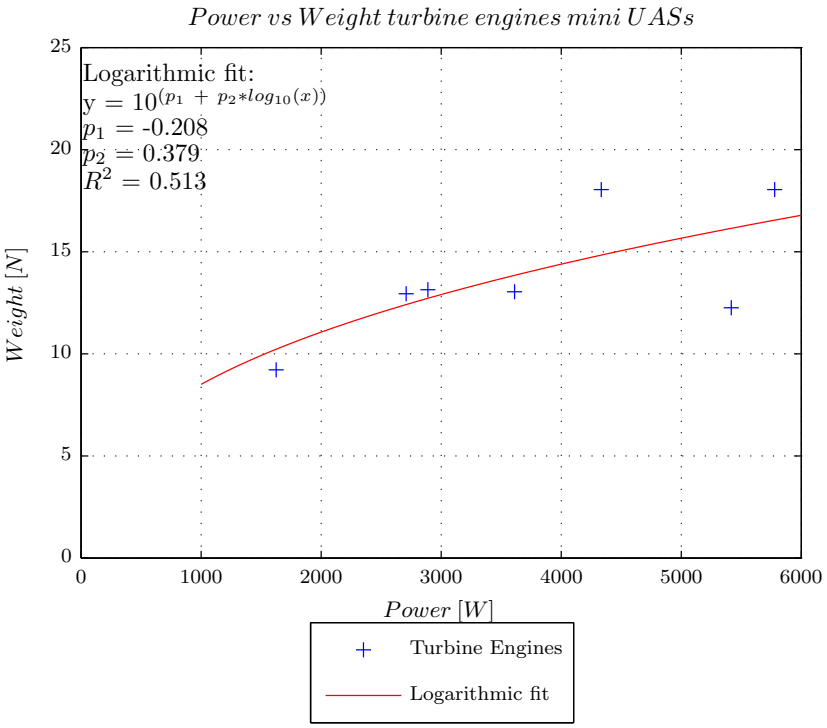

e: Engine weight vs Engine power turbine engine mini UAS

Figure D.1: Engine weight vs Engine power engines mini UAS (cont'd)

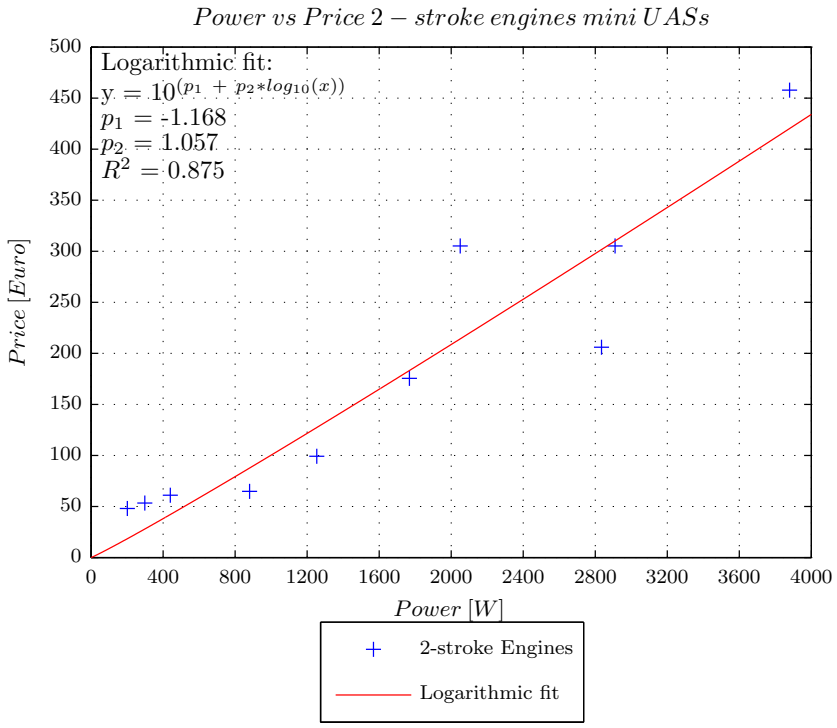

a: Engine price vs Engine power 2-stroke engine mini UAS

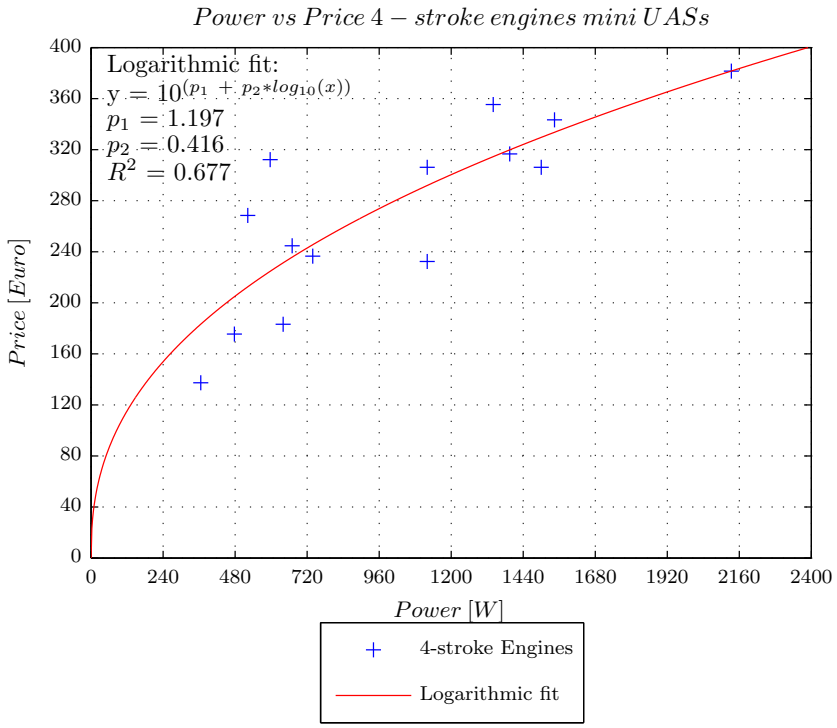

b: Engine price vs Engine power 4-stroke engine mini UAS

Figure D.2: Engine price vs Engine power engines mini UAS

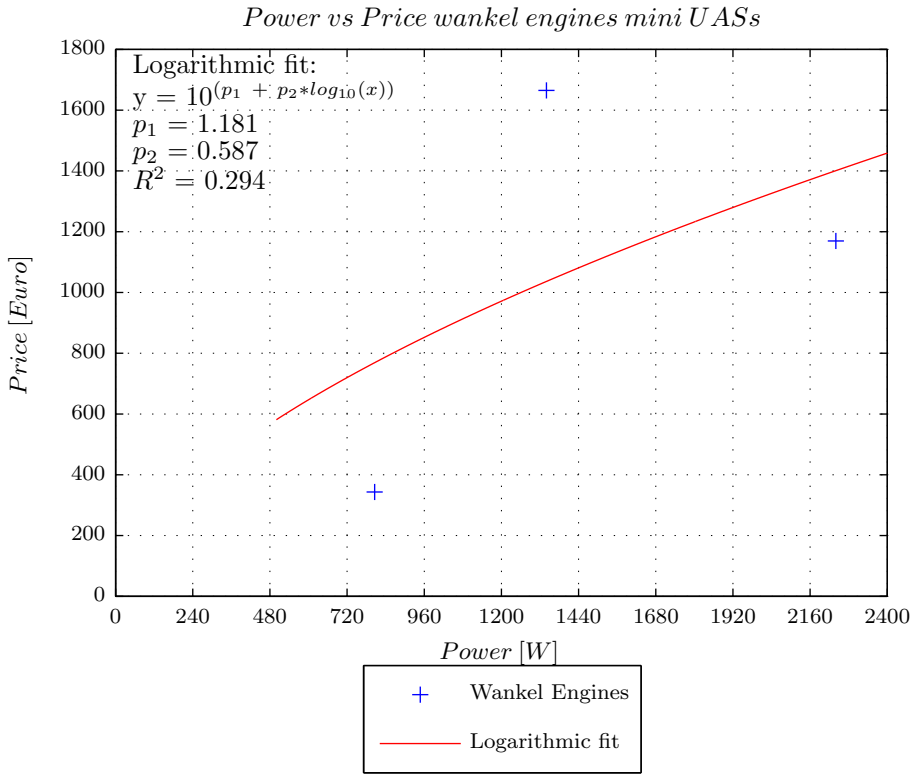

c: Engine price vs Engine power wankel engine mini UAS

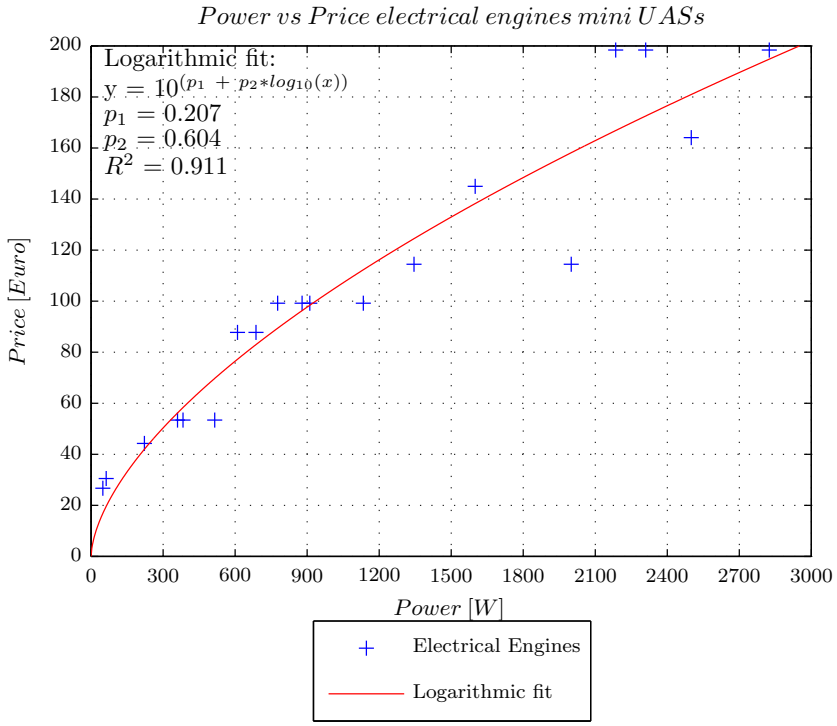

d: Engine price vs Engine power electrical engine mini UAS

Figure D.2: Engine price vs Engine power engines mini UAS (cont'd)

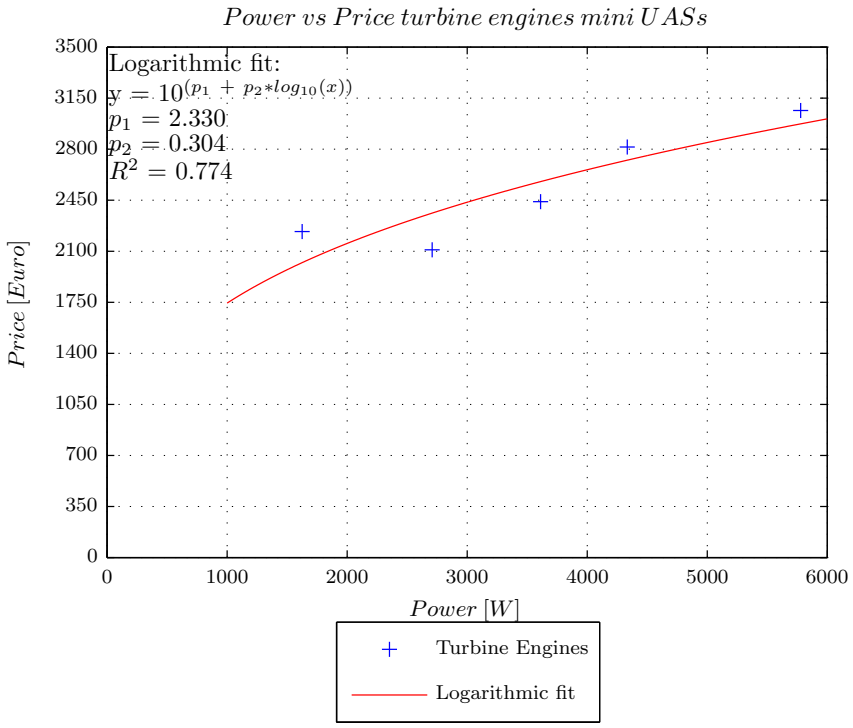

e: Engine price vs Engine power turbine engine mini UAS

Figure D.2: Engine price vs Engine power engines mini UAS (cont'd)

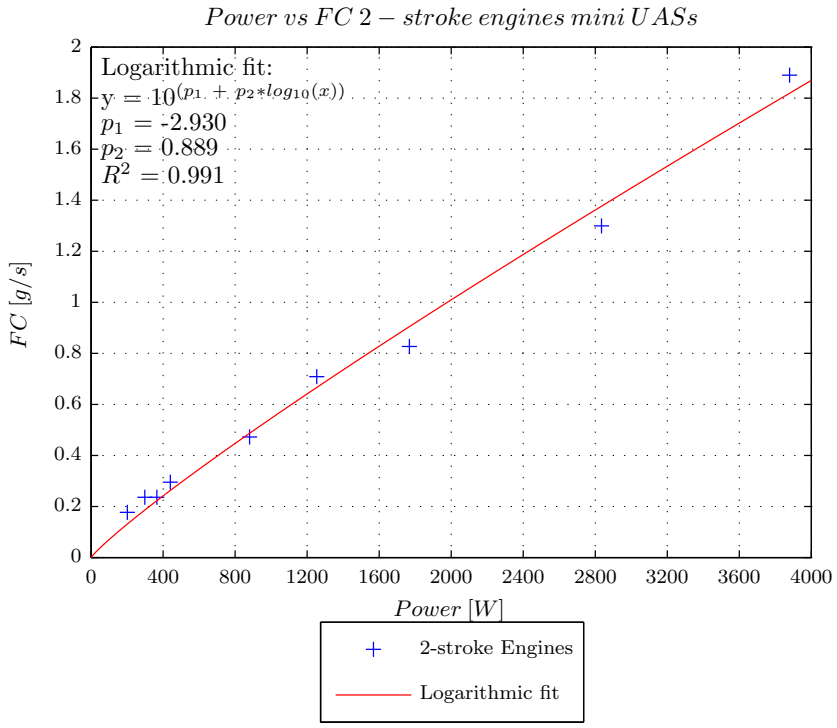

a: Engine FC vs Engine power 2-stroke engine mini UAS

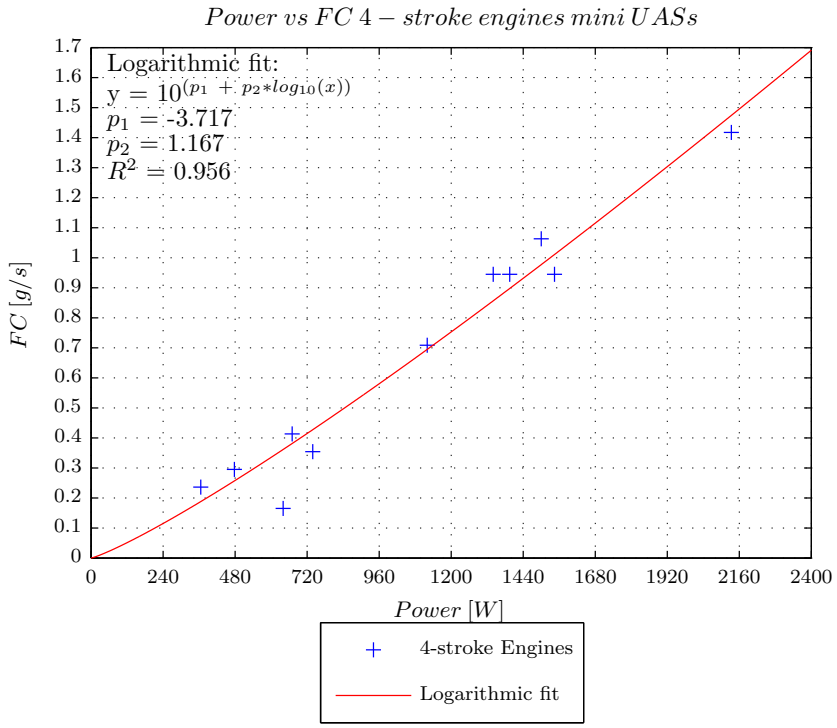

b: Engine FC vs Engine power 4-stroke engine mini UAS

Figure D.3: Engine FC vs Engine power engines mini UAS

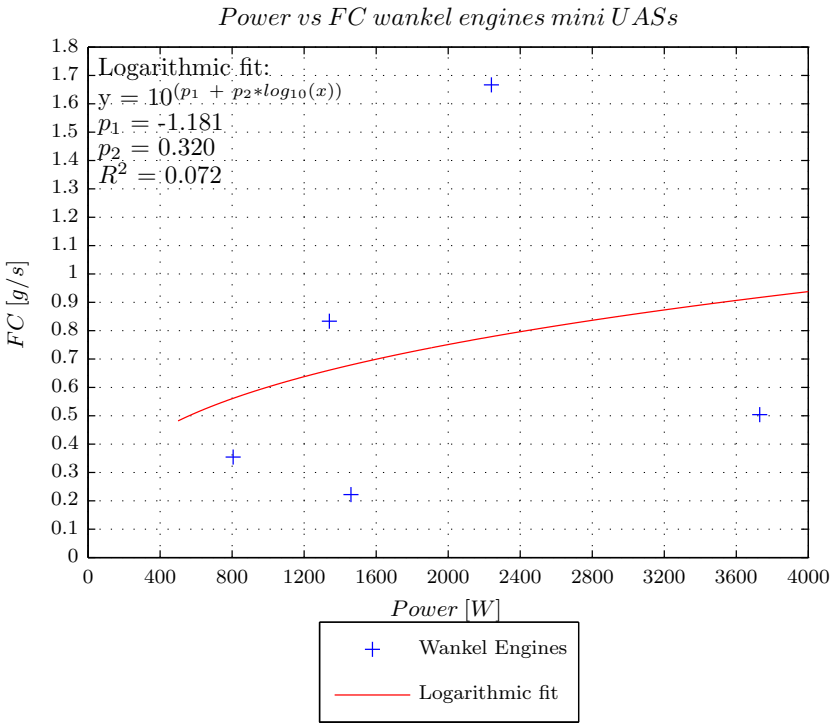

c: Engine FC vs Engine power wankel engine mini UAS

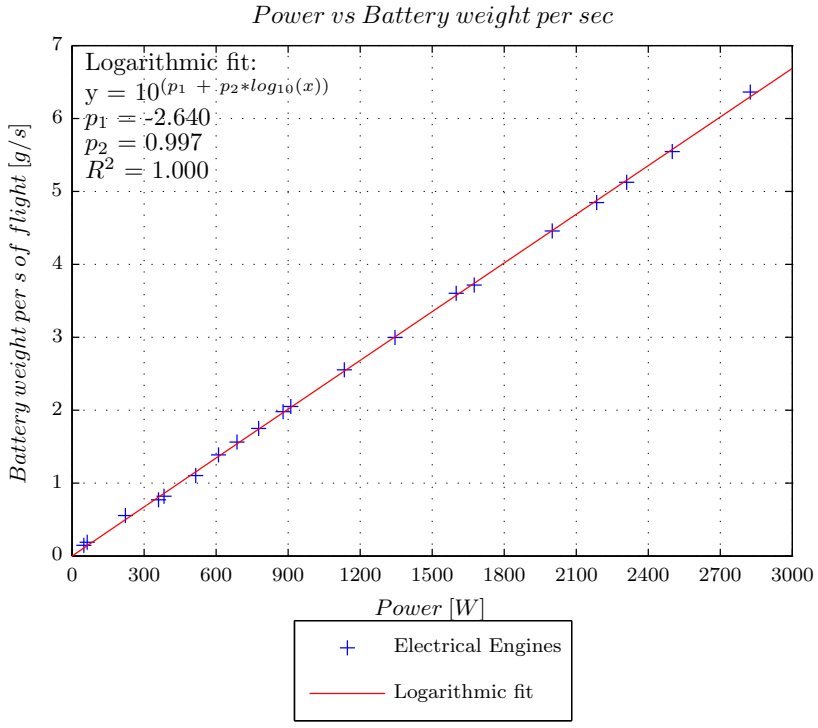

d: Engine FC vs Engine power electrical engine mini UAS

Figure D.3: Engine FC vs Engine power engines mini UAS (cont'd)

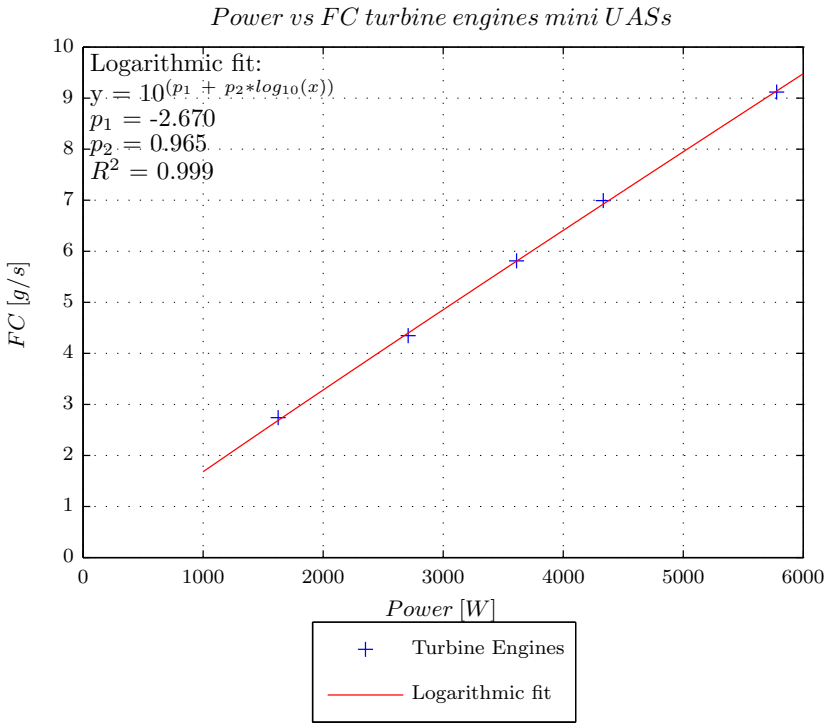

e: Engine FC vs Engine power turbine engine mini UAS

Figure D.3: Engine FC vs Engine power engines mini UAS (cont'd)

Appendix E

Fuel weight derivations electrical powered propeller aircraft

This chapter consists of two sections. Section one describes the derivation of the fuel weight for an electrical powered propeller aircraft based on the required range (Subsection E.1) The second section describes the derivation of the fuel weight for an electrical powered propeller aircraft based on the required endurance (Subsection E.2). The derivation of both sections is based on the method of Dennis Trips[78].

E.1 Derivation fuel weight electrical powered propeller aircraft based on range

$$\frac{dC}{dR} = \frac{\frac{dC}{dt}}{\frac{dR}{dt}} \tag{E.1}$$

with:

$$\frac{dC}{dt} = -I_e \quad and \quad \frac{dR}{dt} = V_\infty \tag{E.2}$$

Results in:

$$dR = -\frac{V_\infty}{I_e} dC \tag{E.3}$$

In Equation (E.3), I_e represents the electrical current, C the capacitance while R and V_∞ represent range and velocity. Equation (E.3) can be integrated resulting in:

$$R = \int_{C_1}^{C_2} -\frac{V_\infty}{I_e} dC \tag{E.4}$$

This can be rewritten as:

$$R = \int_{C_2}^{C_1} \frac{V_\infty}{I_e} dC \tag{E.5}$$

In Equation (E.5), C_1 represents the start capacity and C_2 represents the end capacity of the battery. The electrical current, I_e, can be split up into the electrical current of the motor, $I_{e_{motor}}$, and the electrical current of the remaining subsystems, $I_{e_{subsystems}}$. Equation (E.5) becomes:

$$R = \int_{C_2}^{C_1} \frac{V_\infty}{I_{e_{motor}} + I_{e_{subsystems}}} dC \tag{E.6}$$

$I_{e_{motor}}$ can be rewritten by using the following equations:

$$P_{r_{motor}} = D\, V_\infty \tag{E.7}$$

and:

$$P_{r_{motor}} = \eta_{tot}\, P_{e_{motor}} \tag{E.8}$$

Combining Equation (E.7) and Equation (E.8) leads to:

$$D\, V_\infty = \eta_{tot}\, P_{e_{motor}} \tag{E.9}$$

Rewriting Equation (E.9):

$$P_{e_{motor}} = \frac{D\, V_\infty}{\eta_{tot}} \tag{E.10}$$

with:

$$P_{e_{motor}} = U_{e_{motor}}\, I_{e_{motor}} \tag{E.11}$$

becomes:

$$U_{e_{motor}}\, I_{e_{motor}} = \frac{D\, V_\infty}{\eta_{tot}} \tag{E.12}$$

Rewriting Equation (E.12):

$$I_{e_{motor}} = \frac{D\, V_\infty}{\eta_{tot}\, U_{e_{motor}}} \tag{E.13}$$

Inserting Equation (E.13) in Equation (E.6):

$$R = \int_{C_2}^{C_1} \frac{V_\infty}{\frac{D\, V_\infty}{\eta_{tot}\, U_{e_{motor}}} + I_{e_{subsystems}}} dC \tag{E.14}$$

The first part of Equation (E.14) is not dependent on the capacity. This is true when the electrical tension is constant over time. Therefore this statement is true except for the beginning and end phase of the discharge. Equation (E.14) becomes:

$$R = \frac{V_\infty}{\frac{D\,V_\infty}{\eta_{tot}\,U_{e_{motor}}} + I_{e_{subsystems}}} \int_{C_2}^{C_1} dC \tag{E.15}$$

Equation (E.15) becomes:

$$R = \frac{V_\infty}{\frac{D\,V_\infty}{\eta_{tot}\,U_{e_{motor}}} + I_{e_{subsystems}}} (C_1 - C_2) \tag{E.16}$$

Drag can be written as:

$$D = \frac{C_D}{C_L}\,W_{TO} \tag{E.17}$$

Combining Equation (E.16) and Equation (E.17):

$$R = \frac{(C_1 - C_2)}{\frac{C_D}{C_L}\frac{W_{TO}}{\eta_{tot}\,U_{e_{motor}}} + \frac{I_{e_{subsystems}}}{V_\infty}} \tag{E.18}$$

In order to get the capacity in $[Ah]$ Equation (E.18) becomes:

$$R = 3600\,\frac{(C_1 - C_2)}{\frac{C_D}{C_L}\frac{W_{TO}}{\eta_{tot}\,U_{e_{motor}}} + \frac{I_{e_{subsystems}}}{V_\infty}} \tag{E.19}$$

Since fuel weight needs to be determined, Equation (E.19) must be rewritten in terms of capacity:

$$(C_1 - C_2) = \frac{R\left(\frac{C_D}{C_L}\frac{W_{TO}}{\eta_{tot}\,U_{e_{motor}}} + \frac{I_{e_{subsystems}}}{V_\infty}\right)}{3600} \tag{E.20}$$

E.2 Derivation fuel weight electrical powered propeller aircraft based on endurance

$$E = \int_{t_1}^{t_2} dt \tag{E.21}$$

with:

$$\frac{dC}{dt} = -I_e \tag{E.22}$$

Results in:

$$E = \int_{C_2}^{C_1} \frac{dC}{I_e} \tag{E.23}$$

with:

$$I_e = I_{e_{motor}} + I_{e_{subsystems}} \tag{E.24}$$

This becomes:

$$E = \int_{C_2}^{C_1} \frac{dC}{I_{e_{motor}} + I_{e_{subsystems}}} \tag{E.25}$$

$I_{e_{motor}}$ can be rewritten using the following equations:

$$P_{r_{motor}} = D\, V_\infty \tag{E.26}$$

and:

$$P_{r_{motor}} = \eta_{tot}\, P_{e_{motor}} \tag{E.27}$$

Combining Equation (E.26) and Equation (E.27) leads to:

$$D\, V_\infty = \eta_{tot}\, P_{e_{motor}} \tag{E.28}$$

Rewriting Equation (E.28):

$$P_{e_{motor}} = \frac{D\, V_\infty}{\eta_{tot}} \tag{E.29}$$

with:

$$P_{e_{motor}} = U_{e_{motor}}\, I_{e_{motor}} \tag{E.30}$$

becomes:

$$U_{e_{motor}}\, I_{e_{motor}} = \frac{D\, V_\infty}{\eta_{tot}} \tag{E.31}$$

Rewriting Equation (E.31):

$$I_{e_{motor}} = \frac{D\, V_\infty}{\eta_{tot}\, U_{e_{motor}}} \tag{E.32}$$

Inserting Equation (E.32) in Equation (E.25):

$$E = \int_{C_2}^{C_1} \frac{1}{\frac{D\, V_\infty}{\eta_{tot}\, U_{e_{motor}}} + I_{e_{subsystems}}}\, dC \tag{E.33}$$

The first part of Equation (E.33) is not dependent on the capacity. This is true when the electrical tension is again assumed to be constant over time. Therefore this statement is true except for the beginning and end phase of the discharge period. Equation (E.33) becomes:

$$E = \frac{1}{\frac{D\,V_\infty}{\eta_{tot}\,U_{e_{motor}}} + I_{e_{subsystems}}} \int_{C_2}^{C_1} dC \tag{E.34}$$

Equation (E.34) becomes:

$$E = \frac{\eta_{tot}\,U_{e_{motor}}}{D\,V_\infty + I_{e_{subsystems}}\,\eta_{tot}\,U_{e_{motor}}} (C_1 - C_2) \tag{E.35}$$

Drag can be written as:

$$D = \frac{C_D}{C_L}\,W_{TO} \tag{E.36}$$

Velocity can be written as:

$$V_\infty = \sqrt{\frac{2\,W_{TO}}{\rho\,S_{ref}\,C_L}} \tag{E.37}$$

Combining Equation (E.35) through Equation (E.37) gives:

$$E = \frac{\eta_{tot}\,U_{e_{motor}}}{\frac{C_D}{C_L}\,W_{TO}\,\sqrt{\frac{2\,W_{TO}}{\rho\,S_{ref}\,C_L}} + I_{e_{subsystems}}\,\eta_{tot}\,U_{e_{motor}}} (C_1 - C_2) \tag{E.38}$$

Rewriting Equation (E.38) becomes:

$$E = \frac{\eta_{tot}\,U_{e_{motor}}}{\sqrt{\frac{C_D^2}{C_L^3}\,\frac{2\,W_{TO}^3}{\rho\,S_{ref}}} + I_{e_{subsystems}}\,\eta_{tot}\,U_{e_{motor}}} (C_1 - C_2) \tag{E.39}$$

In order to get the capacity in $[Ah]$ Equation (E.39) becomes:

$$E = 3600\,\frac{\eta_{tot}\,U_{e_{motor}}}{\sqrt{\frac{C_D^2}{C_L^3}\,\frac{2\,W_{TO}^3}{\rho\,S_{ref}}} + I_{e_{subsystems}}\,\eta_{tot}\,U_{e_{motor}}} (C_1 - C_2) \tag{E.40}$$

Since fuel weight needs to be determined, Equation (E.40) must be rewritten in terms of capacity:

$$(C_1 - C_2) = E\,\frac{\sqrt{\frac{C_D^2}{C_L^3}\,\frac{2\,W_{TO}^3}{\rho\,S_{ref}}} + I_{e_{subsystems}}\,\eta_{tot}\,U_{e_{motor}}}{3600\,\eta_{tot}\,U_{e_{motor}}} \tag{E.41}$$

Appendix F

Additional XFOIL results

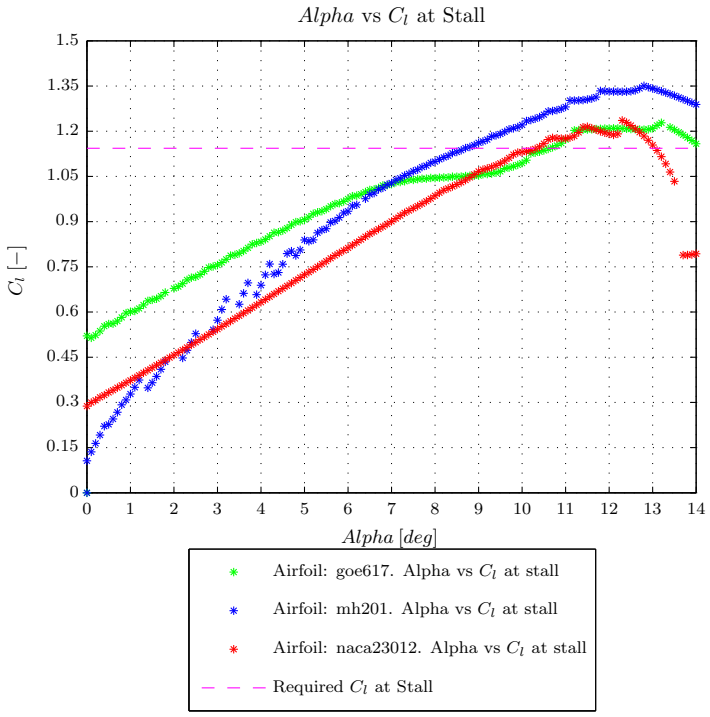

a: Alpha versus C_l

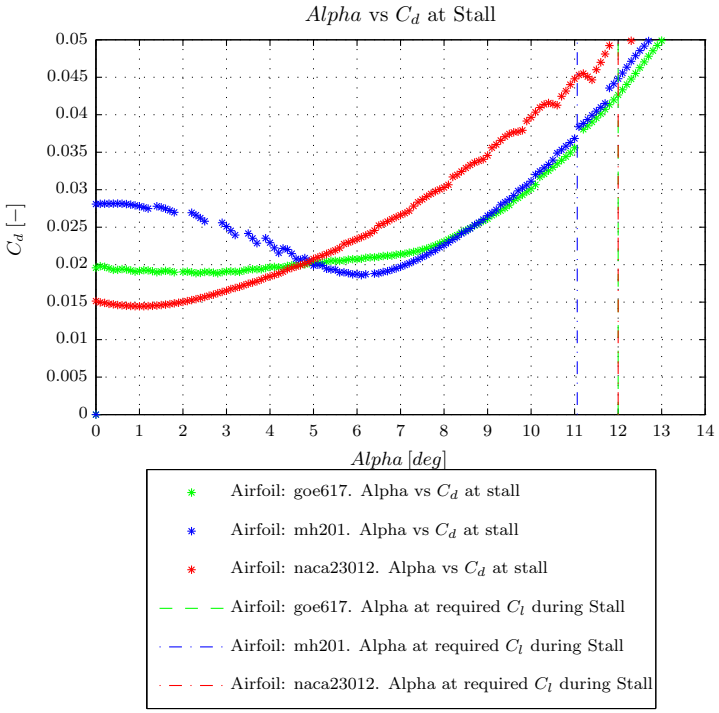

b: Alpha versus C_d

Figure F.0: XFOIL results selected airfoils during stall

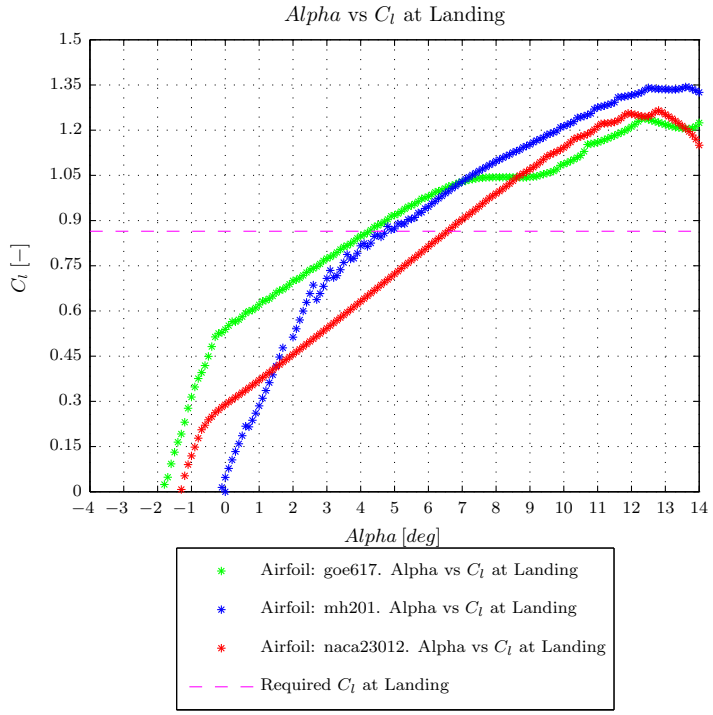

a: Alpha versus C_l

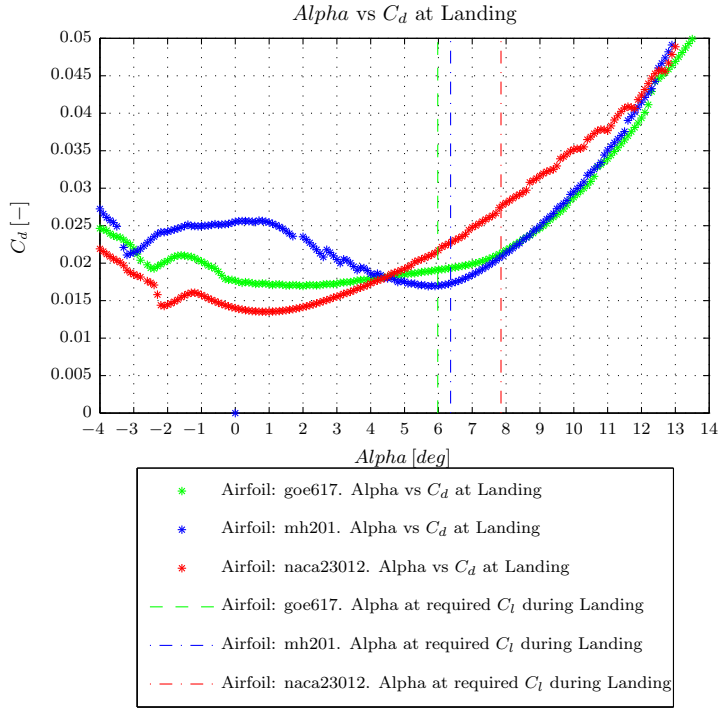

b: Alpha versus C_d

Figure F.1: XFOIL results selected airfoils during landing

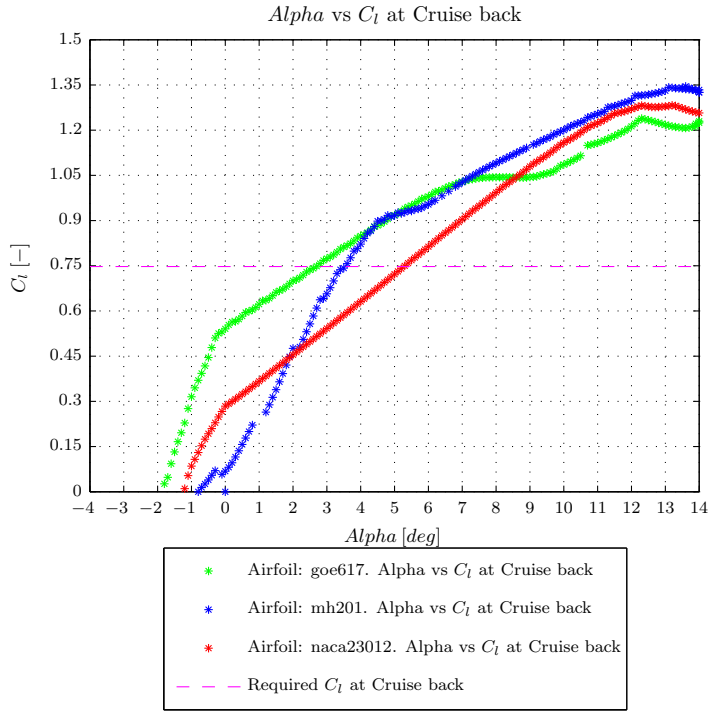

a: Alpha versus C_l

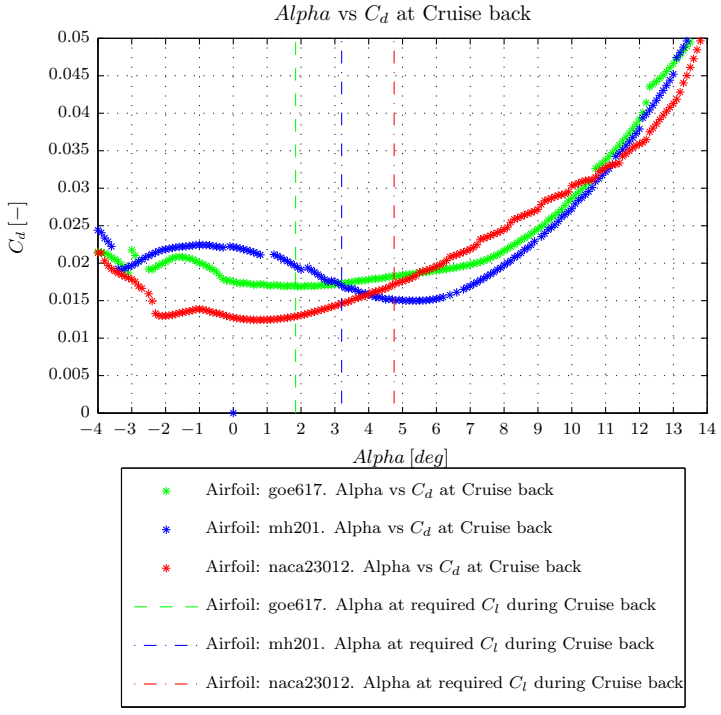

b: Alpha versus C_d

Figure F.2: XFOIL results selected airfoils during cruise back

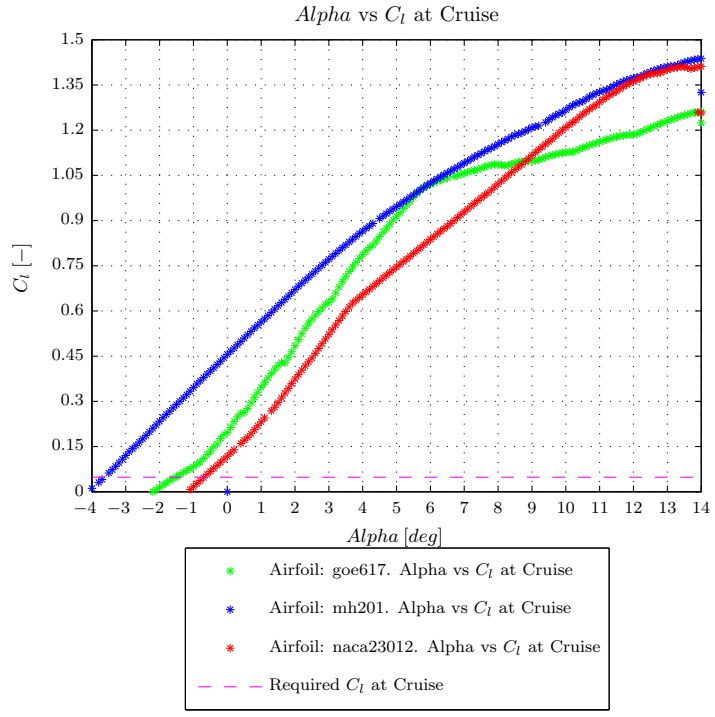

a: Alpha versus C_l

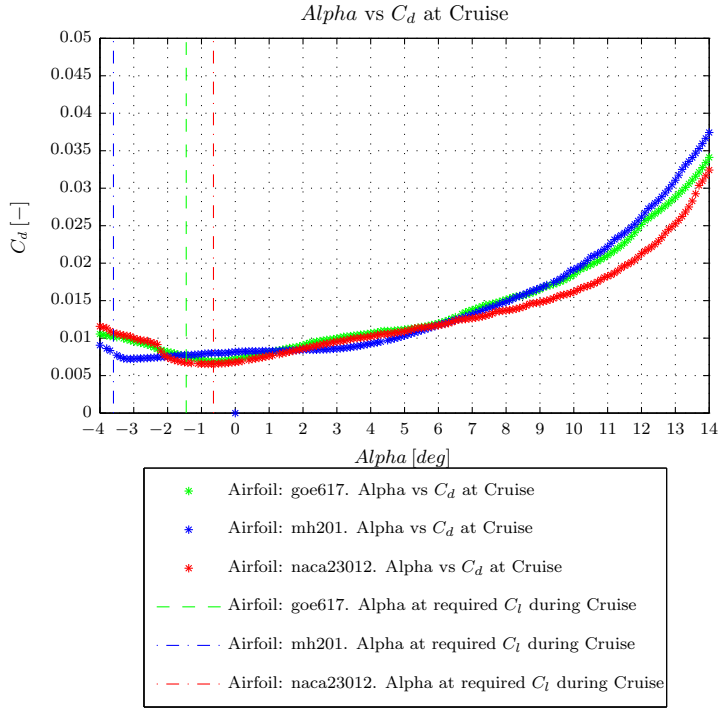

b: Alpha versus C_d

Figure F.3: XFOIL results selected airfoils during cruise

Appendix G

Software versions

Matlab version 7.10.0 (R2010a)
AVL version 3.27
XFOIL version 6.97
Wingoptimizer version 1.0
UDK version 1.0

All programming and analysis was run on a MacBookPro7,1 with an Intel Core 2 Due processor (2.66 GHz), 4 GB RAM, an OCZ-VERTEX2 SSD that was running on Mac OS X Version 10.6.8.

Appendix H

UDK engine and propeller file

H.1 UDK engine file

Listing H.1: UDK engine file

```
1  %% <?XDS v1.0 ?> %%
2  %
3  %
4  %       Hacker A30-22S
5  %      ----------------
6  %
7  %       Propeller definition file for UAV Development Kit 2012
8  %       All units according SI.
9  %       Filename Hacker A30-22S
10 %
11 %       (c) 2012 Jeroen Veerman & Stefan Otting
12 %
13
14 misc.name = 'Hacker A30-22S';
15 misc.version = '0.1';
16
17 %   The following part is considered the body of the file.
18 %   For some files this body is really large, and reading it would
19 %   be a burdon on your time.
20 %   If necessary, it could be ignored, therefore the following line
21 %   is added.
22
23 loader = {'misc'};
24 %BEGINBODY
25
26 meta.name = 'Hacker A30-22S';
27 meta.weight = 70.000000;
28 meta.Imax = 28.000000;
29 meta.Pmax = NaN;
```

```
30 meta.description = 'Angaben hacker-motor.com';
31 meta.I0 = NaN;
32 meta.price = NaN;
33 meta.nmax = NaN;
34 meta.Kv = NaN;
35 meta.R = 0.061568;
36 meta.ns = 1475.038293;
37
38 data(1,1).U = 8.4;
39 data(1,1).n = 0;
40 data(1,1).I = 1.4;
41 data(1,1).no_load = true;
42 data(1,1).M = NaN;
43 data(1,1).desc = '';
44
45 data(1,2).U = 8.5;
46 data(1,2).n = 10968;
47 data(1,2).I = 13.5;
48 data(1,2).no_load = false;
49 data(1,2).M = NaN;
50 data(1,2).desc = 'APC E';
51
52 data(1,3).U = 10.5;
53 data(1,3).n = 13344;
54 data(1,3).I = 19.5;
55 data(1,3).no_load = false;
56 data(1,3).M = NaN;
57 data(1,3).desc = 'APC E';
58
59 data(1,4).U = 12;
60 data(1,4).n = 14866;
61 data(1,4).I = 24.7;
62 data(1,4).no_load = false;
63 data(1,4).M = NaN;
64 data(1,4).desc = 'APC E';
65
66 data(1,5).U = 7.5;
67 data(1,5).n = 8960;
68 data(1,5).I = 19.1;
69 data(1,5).no_load = false;
70 data(1,5).M = NaN;
71 data(1,5).desc = 'APC E';
72
73 data(1,6).U = 9;
74 data(1,6).n = 10303;
75 data(1,6).I = 26.3;
```

```
76 data(1,6).no_load = false;
77 data(1,6).M = NaN;
78 data(1,6).desc = 'APC E';
79
80 meta.file = filename;
81
82 loader = { 'misc','meta','data'};
83 %     Finished flush to file succesfully
```

H.2 UDK propeller file

Listing H.2: UDK propeller file

```
%% <?XDS v1.0 ?> %%
%
%
%      APC Slowfly 10 x 4,7
%      ---------------------
%
%      Propeller definition file for UAV Development Kit 2012
%      All units according SI.
%      Filename APCSlowfly10x4,7.prop
%
%      (c) 2012 Jeroen Veerman & Stefan Otting
%

misc.name = 'APC Slowfly 10 x 4,7';
misc.version = '0.1';

%   The following part is considered the body of the file.
%   For some files this body is really large, and reading it would
%   be a burdon on your time.
%   If necessary, it could be ignored, therefore the following line
%   is added.

loader = {'misc'};
%BEGINBODY

f.name = 'APC Slowfly 10 x 4,7';
f.description = '';
f.foil_file = 'clarky.foil';
f.blades = 2;
f.diameter = 0.254;
f.variable_pitch = false;
f.folding = false;
f.r_beta_set = 0.7;
f.betad_set_min = 0;
f.betad_set_max = 0;
f.betad_set_std = 0;

f.geometry(1,1).r_ratio = [0.15 0.2 0.25 0.3 0.35 0.4 0.45 0.5 0.55
                           0.6 0.65 0.7 0.75 0.8 0.85 0.9 0.95 1;];
f.geometry(1,1).c = [0.013843 0.016764 0.019812 0.022352 0.024511
                     0.026162 0.027432 0.028321 0.028702 0.028575
                     0.027813 0.02667 0.025019 0.022733 0.019939
                     0.01651 0.011049 0.005334;];
```

```
44 f.geometry(1,1).betad = [21.11 23.9 24.65 24.11 22.78 21.01 19 17.06
45                          15.33 13.82 12.51 11.36 10.27 9.32 8.36 7.27
46                          6.15 5.04;];
47
48 f.r_hub = min(f.geometry.r_ratio) * f.diameter / 2;
49
50 f.file = filename;
51
52 loader = { 'misc','f'};
53
54 %     Finished flush to file succesfully
```

Appendix I

AVL input file

Listing I.1: AVL input file

```
naca23012
0.00                                    | Mach
0       0       0.0                     | iYsym   iZsym   Zsym

 4088.61814114   21.76491962   200.00   | Sref    Cref    Bref
 29.016      -0.000      3.143           | Xref    Yref    Zref
 0.0          0.0        0.0             | CDp  (optional)



#==============================================================
SURFACE                                 | (keyword)
naca23012  wing
#Nchord     Cspace    [ Nspan  Sspace ]
20          1.5          40          -1.5

# INDEX                                 | (keyword)
# 26578                                 | Lsurf

YDUPLICATE
0.0

SCALE
1.0   1.0   1.0

TRANSLATE
0.0   0.0   0.0

ANGLE
    3.4                                 | dAinc

```

```
32
33 #--------------
34 SECTION                                                    |
   (keyword)
35    0.0    0.0   0.0 29.44680135 0.0    40     -1.5    | Xle Yle Zle
   Chord Ainc   [ Nspan Sspace ]
36
37 AFIL 0.0 1.0
38 ../Airfoil_coord_lib/n.dat
39
40 #--------------
41 SECTION                                                    |
   (keyword)
42  0.0    100.0   0.0 11.43938006 0.0    40     -1.5    | Xle Yle Zle
   Chord Ainc   [ Nspan Sspace ]
43
44 AFIL 0.0 1.0
45 ../Airfoil_coord_lib/n.dat
46
47
48
49 #============================================================
50 SURFACE                          | (keyword)
51 naca23012 horizontal tail
52 #Nchord     Cspace    [ Nspan Sspace ]
53 20          1.5          10          -1.5
54
55 # INDEX                           | (keyword)
56 # 26580                           | Lsurf
57
58 YDUPLICATE
59 0.0
60
61 SCALE
62 1.0   1.0   1.0
63
64 TRANSLATE
65 0.0   0.0   0.0
66
67 ANGLE
68    -3.4412                        | dAinc
69
70
71 #--------------
72 SECTION                                                    |
   (keyword)
```

```
73 66.34   0.0     30.0    18.4    0.0    10    -1.5    | Xle Yle Zle
   Chord Ainc    [ Nspan Sspace ]
74
75 AFIL 0.0 1.0
76 ../Airfoil_coord_lib/naca0010.dat
77
78 #--------------
79 SECTION                                                    |
   (keyword)
80 69.62   37.50    30.0    9.2    0.0    10    -1.5    | Xle Yle Zle
   Chord Ainc    [ Nspan Sspace ]
81
82 AFIL 0.0 1.0
83 ../Airfoil_coord_lib/naca0010.dat
84
85
86
87 #============================================================
88 SURFACE                          | (keyword)
89 naca23012 vertical tail
90 #Nchord     Cspace    [ Nspan Sspace ]
91 11          1.0             10          -1.5
92
93 # INDEX                          | (keyword)
94 # 26581                          | Lsurf
95
96 SCALE
97 1.0   1.0   1.0
98
99 TRANSLATE
100 0.0   0.0   0.0
101
102 ANGLE
103     0.000                       | dAinc
104
105
106 #--------------
107 SECTION                                                    |
   (keyword)
108 55.42     0.0    0.0   30.7    0.0    10     -1.5    | Xle Yle Zle
   Chord Ainc    [ Nspan Sspace ]
109
110 AFIL 0.0 1.0
111 ../Airfoil_coord_lib/naca0010.dat
112
113 #--------------
```

```
114 SECTION                                                    |
    (keyword)
115 66.34    0.0    30.0    18.4    0.0    10      -1.5     | Xle Yle Zle
    Chord Ainc    [ Nspan Sspace ]
116
117 AFIL 0.0 1.0
118 ../Airfoil_coord_lib/naca0010.dat
```